Analysis of Strain Relaxation, Ion Beam Damage and Instrument Imperfections for Quantitative STEM Characterizations

Dissertation

zur
Erlangung des Doktorgrades
der Naturwissenschaften
(Dr. rer. nat.)

dem

Fachbereich Physik
der Philipps-Universität Marburg

vorgelegt von

Jürgen Belz, Dipl. Phys.

aus

Friedrichroda

Marburg (Lahn), 2019

Vom Fachbereich Physik der Philipps-Universität Marburg
als Dissertation angenommen am: 11.10.2019
Erstgutachter: Prof. Dr. Kerstin Volz
Zweitgutachter: Prof. Dr. Sangam Chatterjee
Tag der mündlichen Prüfung: 14.10.2019
Hochschulkennziffer: 1810

We strongly hope that the irradiated specimen resembles the pristine specimen the same way a grilled chicken is supposed to resemble rather a healthy chicken than a carbonized one.

Otto Scherzer, 1970

Danksagung

Ich danke: ...

... Prof. Kerstin Volz, die mir die Anfertigung dieser Arbeit ermöglicht hat, und zusammen mit Dr. Andreas Beyer stets unterstützend zur Seite stand.

... Prof. Dr. Sangam Chatterjee für die freundliche Übernahme des Zweitgutachtens.

... Prof. Dr. Florian Gebhard für die Vervollständigung der Prüfungskommission.

... Elke Vaupel, Marina Koch und Isabelle Kimmel für die Hilfestellung bei der Bewältigung des Bürokratie-Dschungels.

... Dr. Kahaber Jandieri für seine Unterstützung bei einer Vielzahl von Fragestellungen und die zahlreichen legendären *Kacha*-Momente.

... Dr. Jan Oliver Oelerich für STEMsalabim und exzessive Hilfestellung bei vielen, vielen technischen Problemen.

... Christian Fuchs, Eduard Sterzer, Lennart Duschek, Max Widemann, Pirmin Kükelhan und auch Rainer Straubinger für die vielen unvergesslichen und vollkommen fachfremden (Büro-)Momente.

... Ulrike Häuplik, Peter Ludewig, Antje Ruiz Perez und Johannes Zimmet für die unzähligen tiefsinnigen Gespräche während der Mittagspause.

... Allen Personen, insbesondere im Büro neben dem STEM, die während meiner zahlreichen Kaffee-Besuche meine geistigen Ergüsse ertragen durften.

... und insgesamt allen Kollegen für die angenehme Arbeitsatmosphäre.

... meinen Freunden und meiner Familie für ihre Unterstützung und Aufmunterung insbesondere in schwierigen Phasen.

... und insbesondere meiner Frau Viktoria für ihre unermessliche Geduld und ihre bedingungslose Unterstützung in guten und schlechten Tagen.

Contents

1 Introduction **1**

2 Physical background **3**

2.1 Materials . . . 3

2.1.1 Antiphase Domain Defect . . . 4

2.1.2 Elastic Theory . . . 5

2.2 Transmission Electron Microscopy . . . 6

2.2.1 Electron Matter Interaction . . . 6

2.2.1.1 Elastic Scattering . . . 6

2.2.1.2 Diffraction . . . 7

2.2.1.3 Thermal Diffuse Scattering . . . 8

2.2.1.4 Inelastic Scattering . . . 8

2.2.2 Electron Optics . . . 8

2.2.2.1 Aberrations . . . 9

2.2.2.2 Aberration Correction . . . 12

2.2.2.3 Beyond Geometrical Aberrations . . . 13

2.2.3 Scanning Transmission Electron Microscopy . . . 14

2.2.4 High Resolution Transmission Electron Microscopy . . . 17

3 Experimental Methods **21**

3.1 Sample Preparation . . . 21

3.2 Modeling of Elastic Relaxation . . . 25

3.3 The Transmission Electron Microscope . . . 27

3.4 Strain State Analysis . . . 28

3.4.1 Geometric Phase Analysis . . . 28

3.4.2 Zero-Loss Filtered HR-TEM . . . 29

3.5 Image Simulations . . . 29

4 Results **31**

4.1 (Sub-)Surface Damage . . . 31

4.2 Elastic Strain Relaxation 35
4.2.1 Atomic Force Microscopy of Cross-Section Specimens 35
4.2.2 High Resolution Strain State Analysis 36
4.2.3 Applications of Elastic Relaxation Modeling 38
4.3 Atomic-Scale 3D Reconstruction of APDs in GaP on Si by STEM 39
4.4 Effect of Depth Location of Bismuth Atoms on the Image Contrast 44

5 Summary 47

6 Scientific contributions 51
6.1 Main Contributions 51
6.1.1 Publication 1 51
6.1.2 Publication 2 65
6.1.3 Publication 3 76
6.1.4 Publication 4 86
6.1.5 Publication 5 96
6.2 Presentations and Further Publications 107

Bibliography 111

CHAPTER 1

Introduction

Most of modern worlds technology is based on solid state physics and to huge parts on semiconductor materials. These materials are very versatile since their optical and electrical properties can be modified by doping as well as ny chemical and structural engineering.
Albeit their optical and electrical properties are typically in focus of investigations, the actual fabrication of these materials and their atomic arrangements are of great relevance for current and future technologies where the scale of devices approaches the low nanometer regime. The functionality of such devices is based on only a few atoms and their particular arrangement. With the ongoing miniaturization of electronic and electromechanical structures the need for nano-scale and atomic-scale characterization has therefore been increasing continuously.
Over almost one century electron microscopes have been shown to be suitable devices to research all kinds of subjects. In particular, the transmission electron microscope (TEM) has been capable to resolve atomic structures on a regular basis for several decades. Nonetheless, the advent of spherical aberration correction has enabled researchers to use TEMs and their images more quantitatively. The resolutions achievable by modern (scanning) TEMs is in the order of 50 pm to 100 pm and therefore far below the binding distance of most solids. In addition, the increasing computational power has enabled the connection between sophisticated image simulations and precise experimental measurements.
Although the quantitative agreement between simulation and experiment is in good for simple systems of only a few nanometer size[1,2], many materials are experimentally more challenging. In practice, bulk materials have to be thinned to thicknesses of only a few tens of nanometers in order to be suitable for atomic resolution (S)TEM measurements. This procedure is very critical and great care has to be taken that the properties of a thin TEM specimen lead to the properties of the pristine bulk structure.
In this thesis several techniques have been developed, applied or extended that are connected to the intrinsic challenges that these thinning procedures imply. The investigations range from ion beam damage, to oxide layers to strain relaxations and their implications on

various imaging techniques as well the interpretation of measurement data. Furthermore, several aspects of practical microscopy with an aberration corrected (S)TEM have been investigated. The effects of finite electron emitter sizes, imperfect chromaticity as well as as their implications on data analysis are illustrated.

The inclusion of these features is shown to provide high quality agreement between experiment and simulation even for complex and thick specimens. The robustness is shown in the case of a three-dimensional structure restoration of the antiphase boundary defect seen in gallium phosphide on silicon to nearly atomic precision.

CHAPTER 2

Physical background

2.1 Materials

The material systems investigated in this thesis are inorganic semiconductor materials that are commonly used in various applications ranging from electronics to light emitting diodes. Many of these semiconductor materials consists of either group-IV elements like silicon, or are compound semiconductors made from a group-III and -V atom, respectively. These III/V-semiconductors share almost the same crystal symmetry as IV/IV-semiconductors. The latter is arranged in a so-called *diamond structure*, whereas the III/V semiconductors crystallize predominantly in *zincblende* structure. The only difference between these two structures is the basis atom set. Both can be composed from a face centered cubic lattice that is decorated by a two atomic basis. This basis contains two identical atoms in the diamond structure as e.g. in silicon (Si), and a group-III and group-V in zincblende as for e.g. in *gallium phosphide* (**GaP**). The two basis atoms are shifted by one forth of the unit cells diagonal with respect to each other.
The combination of different types of these inorganic semiconductors allows the design of optical and electronic properties as suited for a given application. One common method of creating complex material systems with different layer structures is the *metal-organic vapor phase epitaxy* (**MOVPE)** where gaseous precursor molecules are injected into a growth chamber where a heated substrate is located. The precursor molecules decompose at the surface of the substrate and the metallic elements form crystalline layers.
Albeit this monolithic growth of complex layer structures is possible, several aspects need to be taken into account. For one, even though the crystallographic symmetry of III/V and IV/IV semiconductors is nearly identical, the equilibrium bond lengths of various compounds can differ significantly. During heteroepitaxy – the growth of layers from different materials – the epitaxial layers are usually strained due to the need of in-plane lattice matching during growth. The mechanism of strain compensation in these systems is typically known as tetragonal distortion since the out-of-plane direction of the initially cubic crystal is either elongated or compressed. This distortion can be calculated from

basic linear elastic theory as shown by Hagen et al.[3]. A more detailed description of build-in strain and the boundary conditions will be given in sections 2.1.2 and 3.2 where the methodology of strain calculation and simulation is elucidated.
Although the crystallographic appearance of III/V- and elemental semiconductors is similar during growth, the two-atom basis of the zincblende structure can produce an antiphase boundary (APB). This APB is a planar defect that separates two crystal phases that terminate at either gallium or phosphorous atoms with respect to the surface silicon atoms.

2.1.1 Antiphase Domain Defect

The origin of this effect is the surface structure of the silicon surface[4]. As illustrated on the left hand side of figure 2.1 the zincblende structure starts to bind with a given type of element. In the case of a silicon monoatomic step terrace the GaP layer growth is shifted by an atomic layer. Due to its two-atomic basis the neighboring domains have to form P-P and Ga-Ga bonds. The phase with a majority of crystal coverage is called mainphase whereas the minority phase is called antiphase. The two domains are separated by a planar defect that is called antiphase boundary (APB).

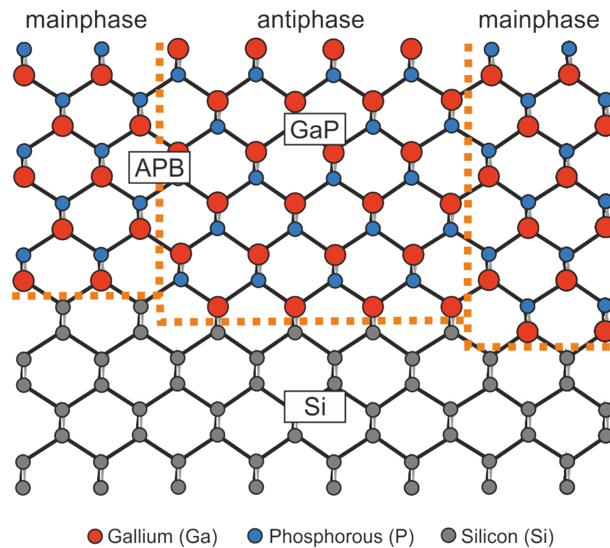

Figure 2.1: The mainphase crystal of GaP is separated from the APD by the APB. The origin of this defect is the monoatomic step on the silicon surface. The boundary contains P-P and Ga-Ga bonds that are not present in ideal binary crystals.

Figure 2.1 shows one type of possible APB formation. Depending on the lateral extension of the silicon terraces other geometries of APBs can occur. Previous studies[5,6] show that the exact silicon-(001) surfaces treated as described by Volz et al.[7] produces terraces that show a more complex triangular surface pattern. On these substrates the APBs form pyramidal structures.
Since the APBs consist of a given number of wrong bonds they accumulate charge that is dependent on the actual APD geometry and the resulting destibution of wrong bonds.

Purely energy based DFT calculations have been carried out by Rubel et al.[8] that indicate that some APB inclination angles are more favorable than others. Providing a framework of investigating the atomic configurations on these APBs is subject of the publication 6.1.2.

2.1.2 Elastic Theory

Since in heteroepitaxy built-in strain is almost inevitable and causes the tetragonal distortion commonly observed[3], its theoretical treatment will be introduced in the following. The strain that typically occurs by the lattice deformation during epitaxial growth of heterostructures is in the order of a few percent of the original lattice constant. Assuming the case of a perfectly coherent growth without plastic crystal relaxation and the resulting generation of defects, the linear elastic continuum theory can be applied.
The macroscopic form of the elastic theory of small elongations is known as *Hooke's law*, which relates the Force F needed to extend a spring with a given spring constant k by a length x in a linear way:

$$\vec{F} = k\,\vec{x}.$$

In the continuum elastic model that is applied to simulated elastic relaxation in the case of thin specimens the forces are typically shear and normal forces σ that occur as a result of bonding of atoms. The general form of the continuum elastic theory is therefore described by a matrix equation containing the so-called elasticity tensor $\underline{\underline{\mathbf{C}}}$ and the strain ε:

$$\vec{\sigma} = \underline{\underline{\mathbf{C}}}\vec{\varepsilon}$$

Although a TEM specimen is very thin and contains only a few tens to hundreds of atoms along the transmission direction, it is shown that the general concept of elastic theory can in principle be applied to nanoscale and micro structures[9]. Due to the different crystallographic orientations the strain state is altered depending on the length scale of different dimensions. In particular the thinning of TEM specimens causes an orientation depended deformation of multilayer structures that could be observed for conventional TEM investigations[10,11].
Since only simple systems can be treated analytically the elastic relaxation of built-in strain is carried out numerically. One of the most popular approaches for the calculation of strain states in complex geometries is called *finite elements analysis* (**FEA**). This technique is a numerical concept for solving systems of differential equations that is based on dividing the geometry into finite sections of simple blocks. It can be applied to various physical problems. These finite elements can be treated according to the relevant physical aspects by Ansatz-functions that include the response characteristic of the element considering the initial starting as well as boundary conditions[12]. The result of this treatment is a finite set of differential equations that can be solved to produce an approximation of the

ideal solution.
The practical implementation is discussed in more detail in section 3.2.

2.2 Transmission Electron Microscopy

In this thesis electron microscopy and in particular *transmission electron microscopy* (**TEM**) is primarily used. The basic principle involves a electron source and and high voltage electric field accelerating the emitted electrons towards the specimen. A complex system of magnetic lenses and auxiliary coils are utilized to deflect and focus the electron flux within the microscope column. A plethora of secondary signals is generated after the specimen interaction. Depending on the desired information various detection methods can be used to form images or spectra revealing different material properties.
At first the electron matter interaction will be discussed. Thereafter the electron optical system and aberrations are elucidated. Finally the conventional high resolution TEM mode as well as the *scanning* TEM (**STEM**) mode are explained.

2.2.1 Electron Matter Interaction

The interaction of high energy electrons with matter generates many different secondary signals. It is expedient to consider this interaction independently in either the electron particle framework or the electron wave description.
The scattering can be divided into elastic scattering ($\delta E \approx 0$) usually with the atom nucleus and inelastic scattering due to electron-electron interaction.

2.2.1.1 Elastic Scattering

Elastic scattering involves a negligible energy loss compared to the primary electron energy and is caused by the interaction with the (screened) electrostatic atomic potential. This scattering can be seen in the framework of the famous Rutherford scattering[13] – where α particles are scattered mainly by the atomic nuclei of a gold foil – since the deflection is caused by the atomic potentials as well. The differential scattering cross-section $\left(\frac{\mathrm{d}\sigma}{\mathrm{d}\Omega}\right)$ is the scattering probability (σ) per solid-angle element (Ω) and given by

$$\left(\frac{\mathrm{d}\sigma}{\mathrm{d}\Omega}\right)_{\text{Ruth}} = \left(\frac{1}{4\pi\epsilon_0}\frac{Z_1 Z_2 e^2}{4E_0}\right)^2 \frac{1}{\sin^4\left(\frac{\vartheta}{2}\right)},$$

with Z_1 and Z_2 being the charge of each particle and E_0 the energy of the projectile. However, this approximation is neither including the relativistic corrections needed for high energy electrons, the magnetic moment of the electron nor the screening of the *naked* atom core potential by its shell electrons. Based upon general scattering theory the differential scattering cross-section can be expressed in a general form including deviations from an

ideal Coulomb interaction

$$\left(\frac{\mathrm{d}\sigma}{\mathrm{d}\Omega}\right)_{\theta} = \left(\frac{\mathrm{d}\sigma}{\mathrm{d}\Omega}\right)_{\mathrm{Coul}} \cdot |F(\vec{q})|^2,$$

with an *atomic form factor* $F(\vec{q})$ which is the Fourier Transform of the atomic charge distribution. In practice the atomic potentials are derived from *ab-initio* relativistic *Hartree Fock* calculations[14]. There are several parameterizations[15–17] with the values provided by Doyle and Turner[15] being considered to be among the most accurate[14] especially for the commonly used high-angle scattering. Nonetheless, more recent calculations[17] show to be in better agreement with experiments than those of Doyle and Turner.
It is worth noting most methods are based on the first order perturbation approximation (Born-approximation) which is not applicable for either heavy elements or low kinetic energies[18]. A practical threshold is given by

$$Z_{valid} \approx 137 \cdot \left(\frac{v}{c}\right),$$

with the relativistic electron velocity v and the vacuum speed of light c. This criterion conveniently holds true for all stable elements in the case of 200 keV microscopes ($Z_{crit.} = 95$).

2.2.1.2 Diffraction

In crystals the elastic scattering is altered from the single scattering due to the periodic arrangement of atoms. In addition to the atomic form factor – the Fourier transform of the atomic charge distribution – the structure factor describes the shape of charge distributions, i.e. the atom positions, in the crystal. Due to the periodic arrangement, the structure factor shows high intensities based on the reciprocal lattice of the crystal where the scattered wavelets are in phase and therefore causing constructive interference.
In analogy to the constructive X-ray scattering condition described by Bragg[19] bright diffraction spots (parallel illumination, TEM mode) representing the crystal lattice are referred to as *Bragg spots*. The intensity of these spots is in general dependent on the crystal orientation with respect to the impinging beam and is furthermore complicated by the periodic occurrence of atom sites in transmission direction. In order to address this issue systematically, the concept of an extinction length ζ_g for each diffraction spot can be introduced. The extinction length describes the length where destructive interference of diffraction from a set of lattice planes leads to the extinction of the diffraction spots. It is worth noting that ζ_g is in the range of several tens of nm up to a few hundred nm and depends on the electron energy of the impinging beam[20]. This effect has strong implications for the image contrast in the conventional TEM as well as on all diffraction techniques. Its effect is noticeable as a depth dependent intensity variation even in STEM imaging as shown in section 4.4.

2.2.1.3 Thermal Diffuse Scattering

Since most (S)TEM experiments are carried out at room temperature the atoms are displaced from their equilibrium positions due to thermal vibrations. The vibration energies are expressed in terms of quantized energies called phonons. The electron-phonon interaction energy is in the order of several meV and its impact on electron energies can only be measured in very special (S)TEMs[21].
Nonetheless, the displacement of the atoms itself results in so-called thermal diffuse scattering (TDS). This displacement can be modeled as random displacement from the center position based on a normal distribution according to the so-called Debye-Waller factor (DWF)[22] given for many material systems[23]. These displacements are contributing to the scattering background especially for high angles[14,24]. Albeit the calculation of the interaction of electrons with real correlated lattice vibrations is complex[23] and difficult to calculate for alloys[25], the main impact on image contrast is the introduction of aforementioned TDS and is shown to be in good agreement with experiments[26].
The displacements are typically incorporated in the multi-slice approach within the so-called frozen lattice approximation that is based on independent movement according to the DWF. Further technical aspects of this procedure are described in section 2.2.3 and 3.5.

2.2.1.4 Inelastic Scattering

The inelastic scattering spectrum can be divided into the interaction with inner and outer shell electrons. The inner shell interactions can be identified in electron energy loss spectroscopy (EELS) by their characteristic appearance as *edges* closely related to the characteristic X-ray emission and are spread over a range of several keV energy losses depending on the binding energy of the respective electrons. The outer shell interactions, on the other hand, typically result in an energy loss of below 100 eV[20] and are by far the dominant inelastic scattering process of high energy electrons in matter.
The outer shell interaction is typically referred to as plasmon interaction. This scattering with the collective (nearly-)free outer shell electrons can be described most conveniently for metals in terms of a free electron gas of the jellium model[27].
The total mean free path of inelastic scattering is typically used to measure thicknesses of thin TEM specimens[20].

2.2.2 Electron Optics

Electron optics are based on the deflection of electrons by either magnetic or electric fields. In practice, most electron lenses for high voltage microscopes are based on electromagnetic focusing. The main lenses are strong electromagnetic round lenses whose magnetic field $\vec{B}$ deflects the trajectory of the incoming electrons with velocity $\vec{v}$ due to the Lorentz

force $\vec{F}$:

$$\vec{F} = -e\left(\vec{v} \times \vec{B}\right).$$

In a magnetic field the electron is therefore moving on a helical path within the pole piece. Since the magnetic field strength is proportional to the current applied to the winding the lenses have – in contrast to light optics – a variable focal length providing flexibility and simple switching of operation modii.
The general conception of electron microscopes can be treated in close analogy to light optics[28]. In fact, in both fields the wave properties can be neglected when considering the optical transfer system which is large compared to the wavelength of the particle. This is even more true for electron optics due to the much smaller wavelength of electrons. In fact, the whole optics of the microscope can be accurately described by so-called *geometrical electron optics* ignoring time dependence of propagation as well as all electron interference effects. Even in the case of electron matter interaction the particle picture can be used to describe a multitude of interaction properties. Nonetheless, accurate wave mechanics always include the results of geometrical optics but are much harder to simulate and comprehend due to the complex interference terms.
Similar to the geometric light optics the path of the electron is determined by the principle of *least action* which is formulated as *Fermat's principle*. It states that the light follows the shortest optical path. In analogy to *Snellius law* of light optics a refractive index can be derived for electromagnetic lenses[28]. It is worth noting that the refractive index for electrons in a magnetic field is in general both inhomogenous and anisotropic and therefore very different to the comparatively perfect glass lenses used in light optics.
With this analogy basically all concepts of geometrical light optics can be used for charged particle optics. It was shown that all symmetrical magnetic round lenses act as convergent lenses[29]. Hence, in later schematics electromagnetic lenses will be illustrated as double convex glass lenses.
It is clear that real imaging systems are never perfect and imperfections are affecting practical microscopy. This is in particular relevant to electron microscopes since the inhomogeneity of the magnetic fields is much more severe than for typical glass lenses. In the following paragraph the concept of aberrations will be introduced since its correction is key to quantitative atomic resolution microscopy.

2.2.2.1 Aberrations

In order to describe aberration correction it is useful to elucidate the origin and typical characteristics of magnetic lens aberrations. As shown by Busch[29] an impinging electron under a given angle is always deflected back to a point on the optical axis for a homogeneous magnetic field of sufficient strength. This distance l_z is determined by the electron rest mass m_0, the relativistic speed v, the electron charge e and the magnetic field component

along the optical axis B_z:

$$l_z = \tau v \cos\gamma = \frac{2\pi m_0 v}{eB_z} \cos\gamma.$$

Using the paraxial approximation the ideal Gaussian image plane can be introduced as the plane where electrons with flat trajectories (small γ) are focused to:

$$l_0 = \frac{2\pi m_0 v}{eB_z}.$$

Deviations of this paraxial approximation can be treated by utilizing series expansions of the angular dependence. In this simple rotational symmetric constant field a second order Taylor expansion is suitable.

$$l_z = \frac{2\pi m_0 v}{eB_z} \left(1 - \frac{1}{2}\gamma^2\right)$$

The deviation $\Delta_l = l_z - l_0$ is called longitudinal spherical aberration and results in image blurring at the Gaussian image plane of $r_S = \Delta_l \tan\gamma \approx -\frac{1}{2} l_0 \gamma^3$ as illustrated in 2.2. The spherical aberration r_S is determined by a lens dependent coefficient $-l_0/2$ as well as a angular dependence to the power of three. The aberration is therefore classified as a third-order aberration. This aberration was for decades the resolution limiting factor for transmission electron microscopy, since it was intrinsic to all magnetic round lenses. Only the invention and construction of modern aberration correctors removed the resolution constraints by introduction additional correction lenses. More details on the corrector design and the functioning will be given in section 2.2.2.2.

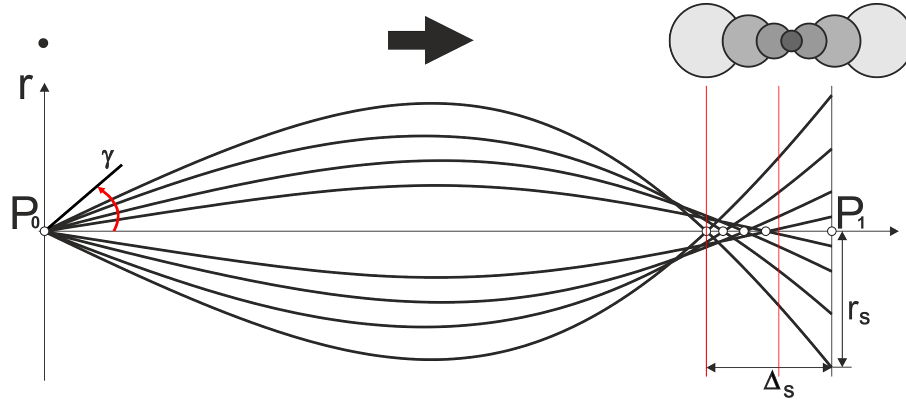

Figure 2.2: The longitudinal spherical aberration leads to a lateral blurring of the image from P_0 at the gaussian image plane P_1.

It is clear that a more systematic approach is necessary to characterize the total of aberrations in a complex lens system like a modern (S)TEM. Hereto, it is instructive to see a magnetic lens as a *black-box* which processes input into output. The rules of this transfer are subsumed by a (complex) characteristic transfer function t that affects amplitude and phase of the impinging electron. In a general form it can be shown that the resulting wave

$\Psi_i(\vec{r})$ can be described by a convolution of the initial wave with the transfer function in real space. Since electrons do not get lost in a strong magnetic lens the amplitude of the wave should not be affected. On the other hand the angular dependence of the impinging electrons and the shape of the magnetic field lead to different path lengths through the lens system. This path difference can be expressed as a phase difference and has the form

$$t_L(\vec{q}) = exp\left(-\frac{2\pi i}{\lambda}\chi\left(\vec{q}\right)\right)$$

in momentum space. The wave aberration function χ as well as the electron wavelength λ determine the phase shift ω:

$$\omega\left(\vec{q}\right) = \frac{2\pi}{\lambda}\chi\left(\vec{q}\right).$$

The wave aberration function can be written as a series expansion where each term represents aberration types. Theoretically, one has to distinguish between symmetry permitted aberrations of round lenses and parasitic aberrations due to mechanical imperfections of magnetic lenses. In practice both coexist and either type can be resolution limiting. The most prominent type of parasitic aberration is the twofold axial astigmatism that typically leads to elongated imaging points.

In total the wave aberration function is distorting the initially spherical wave front of a point source as illustrated in fig. 2.3.

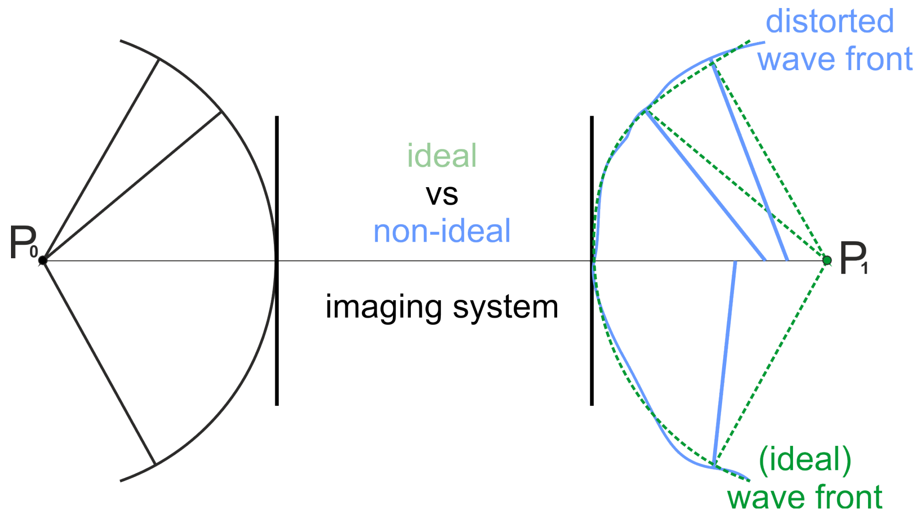

Figure 2.3: The wave aberration function leads to an imperfect wave front that leads to a image spread at P_1.

It is worth noting that the further description of aberrations will only be including so called axial aberrations. The off-axis aberrations can typically be neglected since the typical field of view of a transmission electron microscope is much smaller than the bore of the high resolution objective lens which leads to the the validity of the so-called isoplanatic approximation e.g. the flatness of the geometric wave front at the image plane.

The aforementioned aberrations are also called geometrical aberrations and are coherent

imaging errors that in principle only complicate the contrast transfer and do not reduce information content. On the other hand, it is usually necessary to consider the effect of incoherent aberrations as well. The most obvious of these is called chromatic aberration and is based on the difference in focusing power with respect to the electron velocity and hence wavelength. The consequence of this aberration is the incoherent overlap of different image planes for slightly different velocities. The practical result is a blurring of a point like feature and the loss of high frequency information e.g. small features.
The main factors that dominate the effect of chromatic aberration is the stability of the high tension, the current stability of the lens and the intrinsic energy width of the electron source. In addition, in the case of conventional broad beam illumination TEM, the sample itself acts as a source of inelastic scattering which therefore increases the energy spread of the exit wave.
Furthermore, the finite dimensions of the electron source introduce another contribution to the information loss. A real electron source cannot be a perfect point source. In fact, the image of the source consists of randomly emitted electrons that have a slightly different divergence angle and add up incoherently at the image plane.

2.2.2.2 Aberration Correction

In this section the concept of aberration correction will be briefly illustrated. In particular the correction of the (strictly positive) third order spherical aberration is relevant since it is the dominant aberration that is intrinsic to all magnetic round lenses[30]. Nonetheless, it is important to mention that the spherical aberration is only the limiting aberration when parasitic aberrations are compensated and the isoplantic approximation is valid.
Albeit the spherical aberration can be reduced by increasing the electron velocity as well as decreasing the focal length, for a broad variety of specimen types the introduction of additional aberration corrector lenses has been shown to be most useful[31,32].
Already in the early years of electron microscopy it was clear that the limiting positive spherical aberration could be compensated by introducing multiple lenses that are not strictly rotational symmetric[33]. Due to the additive characteristic of aberrations[34] it is not needed to build aberration-free lenses, but only a system with compensating aberrations. Two lens system designs are currently commercially available. The first is based on a set of quadrupole and octopole lenses, whereas the second utilizes hexapol (sectupol) lenses. The microscope used in this thesis uses the latter type of aberration corrector.
It can be shown that a pair of thin hexapol lenses can introduce a combination aberration that has a negative coefficient of spherical aberration. Alternatively, it can be shown[35,36] that a single extended hexapole field can replace a set of thin magnetic lenses without losing the negative spherical aberration. By using this additional hexapol fields the total sum of spherical aberration in the objective lens can therefore be set to nearly zero. On the other hand, the main effect of hexapol lenses is the introduction of (second order) threefold

astigmatism which can be resolution limiting itself. In principle the threefold astigmatism could be compensated by an appropriate design of the hexapol length itself. Nonetheless, the only practical solution up to date that provides the necessary degrees of fine tuning to compensate the threefold astigmatism as well as the residual parasitic aberrations consists of two extended hexapol fields coupled with four round telescopic transfer lenses[37]. This design ends up to be limited by a sixfold astigmatism that cannot be canceled out by this setup. It is worth noting that the practical implications due to parasitic aberrations and precise lens positioning are very severe and that their compensation necessitates additional stigmation coils at various locations within the corrector. The resulting resolution of a third-order aberration corrected microscope is therefore determined by its state of alignment. Only in a well aligned microscope are the fifth-order geometrical aberration as well as the first-order chromatic aberration resolution limiting. Further details about hexapole corrector can be found in[28,36,38]. Details regarding the quadrupole-octopole corrector can be found in[28,38,39].

In recent years further advances in instrumentation have lead to working fifth-order geometrical aberration correctors[40] as well as (combined) chromatic and geometrical aberration correctors[41,42].

2.2.2.3 Beyond Geometrical Aberrations

Albeit the geometrical third-order aberrations are in principle the limiting factor of conventional transmission electron microscopes, its compensation moves the limitation to other factors like incoherent chromatic aberration and higher-order geometrical aberrations. Furthermore, the statistical significance of measurements compared to the noise becomes increasingly relevant.

For STEM the correction of third-order spherical aberration leads to the geometrical limiting (residual) fifth-order aberrations introduced by the corrector system. With fifth-order aberrations of up to 2 mm the resolution limit would be in the about 50 pm[28] and the beneficial semi-convergence angle about 50 mrad. In fact, the achievable resolutions are in the range of 80 pm to 100 pm. This is mainly due to incoherent chromatic aberration. The chromatic aberration introduces amplified side lobes of the electron probe. This effect increases with the acceptance angle of the probe forming system and overcompensates the improvement the geometrical aberration correction up to third-order introduced[28]. Krivanek et al.[39] show that a chromatic aberration optimized semi-convergence angle α is given by

$$\alpha_{chrom} = 1.2\sqrt{\lambda\frac{E_0}{l_c}},$$

where λ is the electron wave length, E_0 its kinetic energy and $l_c = C_c\Delta E$ the energy length that is formed by the coefficient of chromatic aberration and the electron source energy

distribution ΔE. Typical values for ΔE for a Schottkey-type Field Emitter is in the range of 1.0 eV. A high resolution electron lens has a C_c value of about 2.0 mm. The resulting typical energy lengths of about 2.0 eV mm lead to a chromatic resolution limit δ_{chrom}

$$\delta_{chrom} = 0.51\sqrt{\lambda\frac{l_C}{E_0}}$$

of about 81 pm with a optimized convergence angle of about 19 mrad. It is noteworthy, that this value can be improved by optimization of the field emitter biasing voltages that reduce the effect of ΔE. For Schottky-type field-emitters the energy spread can be reduced to values of about 0.6 eV [43] leading to a beneficial semi-convergence angle of about 24.5 mrad leading to a resolution of about 63 pm. In total the resolution and the effect on overall imaging contrast is not trivial due to the interplay of geometrical and chromatic aberrations. Whereas the geometrical aberration modified the lateral dimensions of the electron probe, the chromatic aberration affects the axial probe spread along the beam direction.
Additional considerations and measurements regarding this interplay are presented in publication 6.1.5.

2.2.3 Scanning Transmission Electron Microscopy

In *scanning transmission electron microscopy* (**STEM**) the electron source is focused as a probe onto the specimen. In order to achieve this in a controlled manner, several condenser lenses are located after the illumination system which form the *condenser lens system.* Typically the electron cross-over of a FEG is wider than the desired probe size of a modern STEM. In order to create a finer probe the electron cross-over is projected into a plane where a mechanical aperture is located. In the JEOL JEM-2200FS the condenser system is set up to produce a constant acceptance angle in the aperture plane in a way that the probe current can be changed independently. The convergence (semi-)angle α is therefore determined by a set of mechanical apertures and matched to the aberration correction system. This setup assures that the additional aberration correction lenses can reliably reduce the probe spread due to geometrical lens aberrations, i.e. the dominant spherical aberration. Since the aberration correction is a key feature of a modern STEM, its principles are described in section 2.2.2.2. For now its effect can be seen as a reduction of the lateral beam spread increasing the resolution of the STEM significantly.

In order to generate an image in the scanning mode, the focused electron probe is moved across the specimen systematically and the position is correlated to the signal of a detector. The scanning itself is carried out by a pair of magnetic deflection coils that use a combination of tilts to translate the beam in a way that the optical axis is not tilted but only shifted. Since the electron probe is in the range of 70 pm after aberration correction

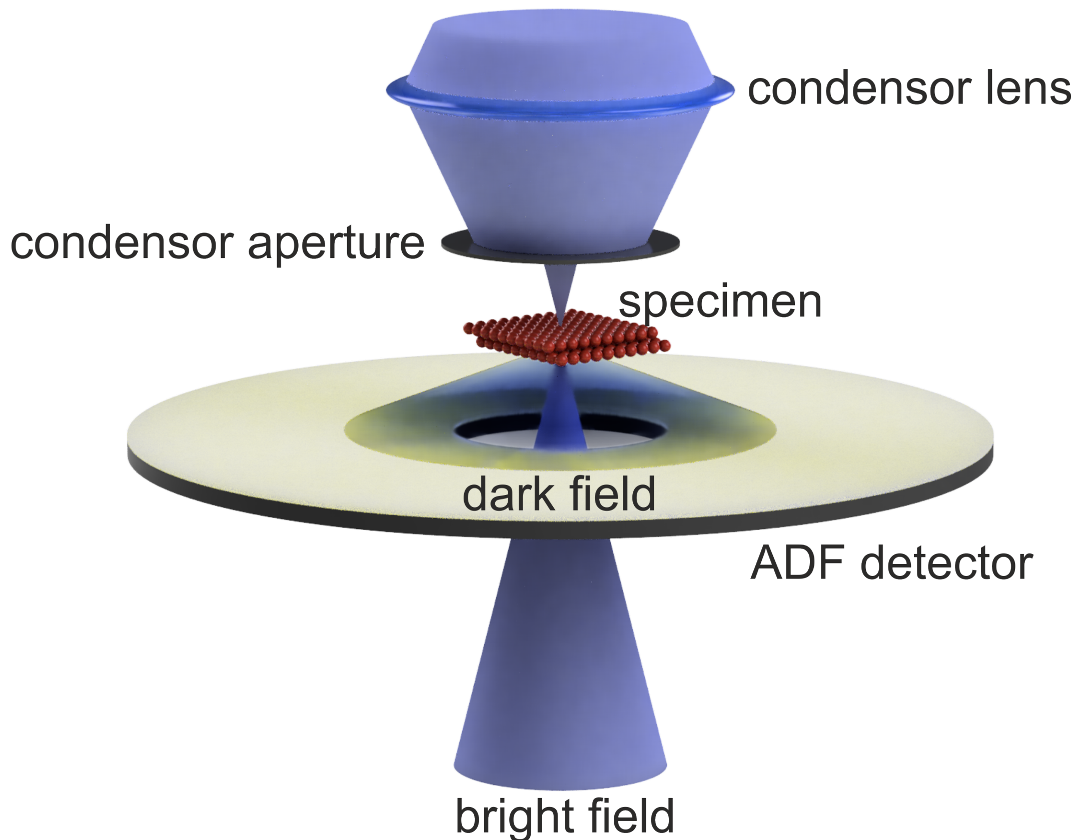

Figure 2.4: The electron beam is focused by the condensor lens (system) and the angular acceptance angle is limited by an aperture. The sharply focused beam is scanned across the specimen and the dark-field is integrated by an ADF detector. Each scan position is correlated to a digital image pixel representing this integrated intensity value.

the resolution is in principle constant. The scanning process and in particular its sampling causes the desired magnification of the specimen. In general the STEM is not tied to a particular detection system. Nonetheless, it is very common to use ring shaped detectors and utilizing annular dark-field (ADF) imaging[44]. Here, the integrating ring detector is located behind the specimen in such a way that the direct beam passes though the center hole. In combination with the projection lenses of the microscope, the (virtual) distance of this detector can easily be set up and is commonly referred to as the *camera length*. It is clear that this change of (virtual) distance enables the detection of different components of the initial scattering distribution. In the case of high angle ADF (HAADF) a typical collection inner angle θ_{in} is 70 mrad to 100 mrad with an outer angle determined by the physical geometry of the detector. In this work a detector is used that has a ratio of $4:1$ between the outer and the inner radius.
The final STEM image is generated by the digital synthesis of the detector measurements triggered at every scan point. It is noteworthy, that the signal conversion of the ADF detector includes an amplifier (*gain*) stage as well as an analog-to-digital conversion process.

The raw intensities of an ADF image are therefore only represented by *counts*. In practice, the amplifier gain curve is determined and the microscope is operated in the linear regime, which enables the quantitative correlation to incident electron numbers [45]. Furthermore, the detector sensitivity has to be taken into account [2].
It is clear that the lateral resolution of such a system is ultimately based on the ability to generate an extremely fine probe that is smaller than the length scale of interest. Since magnetic round lenses are fundamentally limited by the strictly positive spherical aberration coefficient [30], the resolution of a STEM can only be improved by more sophisticated aberration correction which is discussed in detail in section 2.2.2.2.

Image Formation The imaging process in STEM is quite different than for conventional STEM. Nonetheless, the of electron matter interaction is – in principle – identical.
In contrast to conventional imaging on a pixelated detector (e.g. a camera) with broad illumination, the STEM imaging is a serial process that correlates scattering with the beam position. In this thesis the utilized STEM detector are annular detectors that collect the total of electrons that were scattered in relatively high angles (several tens of milliradians). The primary forward scattering cone is typically not used. This kind of dark-field imaging is typically used due to its chemical sensitivity [44].
In order to derive quantitative information from STEM ADF measurements the scattering process is simulated using a so-called multi-slice approach [14]. This Ansatz is used to derive accurate scattering distributions from samples of *thick* specimens by slicing the simulated super cell into thinner sub-regions, i.e slices.
Since the electron speed is very high and the transmitted sample thickness is small, the electron sees a rather stationary snapshot of the crystal. Hence, it is sufficient to solve the electron wave function Ψ within the crystal using the time independent Schrödinger equation:

$$\left[-\frac{\hbar^2}{2m}\nabla^2 - eV\left(x,y,z\right)\right]\Psi\left(x,y,z\right) = E\Psi\left(x,y,z\right),$$

where $-eV$ is the electrostatic potential energy of the electron, m its relativistic mass. It can be shown [14] that the equation can be simplified in the case of fast electrons, where the main propagation direction z can be separated from the lateral interaction (xy):

$$\frac{\partial\Psi\left(x,y,z\right)}{\partial z} = \left[\frac{i\lambda}{4\pi}\nabla^2_{xy} + i\sigma V\left(x,y,z\right)\right]\Psi\left(x,y,z\right),$$

where λ is the incident electron wavelength and $\sigma = 2\pi me\lambda/h^2$ is called interaction parameter.
Furthermore, for fast electrons the interaction potential can be treated as a projected

potential v_s along the propagation direction:

$$v_s(x,y) = \sum_i \int V_i(x - x_i, y - y_i, z)\, dz. \tag{2.1}$$

The individual atomic potentials V_i are derived from tabulated atom scattering factors as described e.g. in Oelerich et al.[46].
For each of these slices the transmission function $t_s(x,y)$ can be expressed in the framework of a phase object approximation:

$$t_s(x,y) = \exp\left[i\sigma v_s(x,y)\right].$$

Following this interaction, the electron propagation is calculated by applying a Fresnel propagation $p(x,y)$ through free space:

$$p(k_x, k_y, dz) = \exp\left[-i|k|^2\lambda\ dz\right].$$

The total propagation through the crystal can then be calculated iteratively:

$$\Psi_{s+1}(x,y) = \mathcal{F}^{-1}\{p(k_x, k_y, dz)\,\mathcal{F}\left[t_s(x,y)\,\Psi_s(x,y)\right]\},$$

where $\mathcal{F}$ is the Fourier transform (FT) and $\mathcal{F}^{-1}$ the inverse FT.
The initial probe function Ψ_0 for a given scan point (x_p,y_p) is given by

$$\Psi_0(x,y,x_p,y_p) = B\mathcal{F}^{-1}\left(A(k_x,k_y)\exp\left[i\chi(k_x,k_y) + 2\pi i\,(k_x x_p + k_y y_p)\right]\right),$$

where B is a normalization factor, A the aperture function and χ the phase aberration function as introduced in chapter 2.2.2.1.
Besides this basic multi-slice algorithm, additional physical features are implemented. One of the most relevant implementations is the modeling of thermal excitation that cause a deviation of atom nuclei from the ideal lattice sites. In principle a full phonon treatment of the crystal is needed to model the correlated movement of lattice atoms[14,47]. Nevertheless, it can be shown[26] that the complete treatment of correlated phonons can be well approximated by the *frozen lattice* model especially for the case of high angle scattering that is typically measured by ADF STEM. In the frozen lattice approximation the lattice site vibrations are modeled by a perturbation of their ideal positions base on (room temperature) *Debye-Waller factors* (DWF) that are calculated for many materials[23,48,49].

2.2.4 High Resolution Transmission Electron Microscopy

Alternative, to the STEM mode with a very narrowly focused beam, the (conventional) TEM mode is utilizing a broad parallel illumination of the sample. This parallel illumi-

nation is interacting with the specimen, and its *exit wave field* (**EWF**) is captured by camera system.
The multi-slice formalism is valid as well, since the electron-matter interaction is identical but only the experimental setup is changed.
The TEM mode itself can be used in different operating modes. In the following the high resolution phase contrast mode will be introduced.
The basis of high resolution TEM is a parallel coherent illumination of the specimen. Hereto, the source is projected onto the target, and a angle limiting condenser aperture is used to assure an even and coherent illumination of the specimen. The condenser lenses and the objective pre-field are controlled in a way that the convergence angle is in the low mrad-regime.
The electron matter interaction – as described in section 2.2.1 – is analogous to the STEM mode. The major difference comes from the image formation that is utilized. In TEM the diffracted electrons form an image at the exit surface of the specimen. This exit wave field is then magnified by an objective lens onto the imaging plane and further on projected onto a detector i.e. camera.
A simplified derivation of the electron-matter interaction is called *phase object approximation* (**POA**)[28] and illustrates the interaction on a qualitative level. It is noteworthy, that more sophisticated theories include absorption i.e amplitude modulation in form of a complex electrostatic potential[28,50].
The impinging electron wave $\Psi_0(\vec{r}) \equiv 1$ is modulated by a weak perturbation due to the atomic potentials that results only in phase modulation $exp\{-i\Phi(\vec{r})\}$ due to the electrostatic interaction. The projected crystal potential $\Phi(\vec{r})$ can be formulated according to eq. 2.1. In the first order approximation – i.e. the *weak* POA (**WPOA**)[50] – the exit wave can be written as

$$\Psi_{exit}(\vec{r}) = 1 - i\psi(\vec{r}). \tag{2.2}$$

As emphasized by eq. 2.2 the initial wave field is modulated by the (weak) crystal potential that represents the atomic sites of the specimen. In addition, the diffracted partial beams form a diffraction pattern in the back focal plane of the (post-)objective lens that can be written as the Fourier-transform $\mathcal{F}$ of the EWF[28] with the spatial frequency vector $\vec{q}$ as the transformation of $\vec{r}$:

$$\Psi_{bfp}(\vec{q}) = \mathcal{F}[\Psi_{exit}(\vec{r})] = \Psi_{exit}(\vec{q}).$$

In a crystal the spatial frequencies that are non-zero are related to the reciprocal lattice vectors $\vec{g}$ of the crystal. The periodic pattern in the imaginary part of the EWF resembles therefore the symmetry of the transmitted crystal according to the Bragg diffraction angles.
The wave field at the imaging plane Ψ formed by the objective lens can now be written

in terms of the Fourier-transform of the diffraction plane convoluted with a instrument function t:

$$\Psi(\vec{r}) = \mathcal{F}^{-1}\left[\Psi_{exit}(\vec{q})\, t(\vec{q})\right],$$

and

$$\Psi(\vec{r}) = \Psi_{exit}(\vec{r}) \otimes t(\vec{r}).$$

The wave field at the imaging plane can therefore – within the WPOA – be written as[28]:

$$\Psi(\vec{r}) = 1 + \Phi(\vec{r}) \otimes \mathcal{I}\left[t(\vec{r})\right] - i\Phi(\vec{r}) \otimes \mathcal{R}\left[t(\vec{r})\right]$$

Since the intensity I is the absolute square of the wave function, it can be approximated up to first-order interference terms:

$$I(\vec{r}) \approx 1 + 2\left(\Psi(\vec{r}) \otimes \mathcal{I}\left[t(\vec{r})\right]\right).$$

The FT of $\mathcal{I}\left[t(\vec{r})\right]$ is describes how spatial frequencies transmitted and is commonly referred to as *phase contrast transfer* function (**PCTF**). This function would be frequency independent i.e. constant in a perfect transfer system. In reality the PCTF is a complicated function determined by various lens aberrations[51]. In the case of an aberration-corrected microscope the contrast transfer function is typically tailored to provide contrast even in focus conditions. The typical strong oscillations of the PCTF up to the information limit are typically removed in an aberration corrected microscope.

It is noteworthy, that albeit the WPOA is qualitatively representing the electron matter interaction in most cases the results do note agree with the measurements due to the very strong electron matter interaction and dynamical diffraction effects. A more advanced dynamic scattering theory can be found for example in Geuens et al.[52]. In addition, the linear transfer theory is usually inappropriate to describe the strong diffraction of thick specimens[53].

CHAPTER 3

Experimental Methods

3.1 Sample Preparation

In transmission electron microscopy the specimen thickness has to be in the range of several tens of nanometers in order to achieve atomic resolution. This is mainly due the strong electron matter interaction and the resulting multiple scattering during the transmission. The resulting energy loss leads to a significant loss of information and resolution.
In order to prepare samples for (S)TEM, different techniques are used depending on the properties of the specimen. For crystalline semiconductor materials a combination of mechanical and ion beam thinning is commonly applied. The mechanical grinding of material has the advantage of being fast. It can be carried out precisely down to material thicknesses in the low micro meter regime[54]. On the other hand, the final thinning is extremely difficult to control with mechanical grinding alone. Although there are results of mechanical thinning in combination with chemical etching[54], a more robust technique is the use of low energy ion beam polishing. The residual damage can be reduced by applying shallow angles of incidence and low ion energies. The resulting sample is intended to be free of artifacts and showing close resemblance of the pristine material.
There are two common geometries that are both used parts of this work. The first is the called cross-section (XS) geometry where the material is prepared in such a way that pieces of the material are glue together face-to-face by epoxy adhesive. The thinning direction is then perpendicular to the original surface, leading to a resulting transmission direction that shows the cross-section of the material stack under investigation.
The second geometry is called plan-view (PV) and prepared by removal of the backside of the specimen. In the case of epitaxial growth this is typically the substrate.
Depending on the desired geometry, different preparations are beneficial. Further details on the particular preparation type used in the respective measurements can be found in the respective sections of the publications presented in chapter 6.

Ion Beam Thinning In the following section the various ion beam techniques that were used throughout the research presented in this thesis will be introduced and elucidated one after another. Besides the main difference of broad beam argon ion thinning and focused gallium ion beam thinning, special preparation techniques will be elaborated.

Broad Ion Beam Technique The conventional type of ion beam preparation is carried out using a broad ion beam. In the Gatan PIPS system that was used in part for the preparation of specimens investigated in this work, argon ions with kinetic energies between about 1.0 keV to 6.0 keV were used. It is noteworthy, that the lateral extension of the argon ion beam is in the order of millimeters and huge amounts of materials are typically removed and potentially redeposited.
In order to reduce the final ion beam damage the kinetic energy is successively reduced during the thinning process. Depending on the details of the preparation geometry [55], the final specimen geometry typically has a center hole with the regions of interest close to its perimeter. In the case of the conventional double-sector (DS) milling the specimen show a thickness gradient that is correlated to the initial argon incident angle. The typical procedure is illustrated in figure 3.1. A more detailed analysis of this preparation is shown

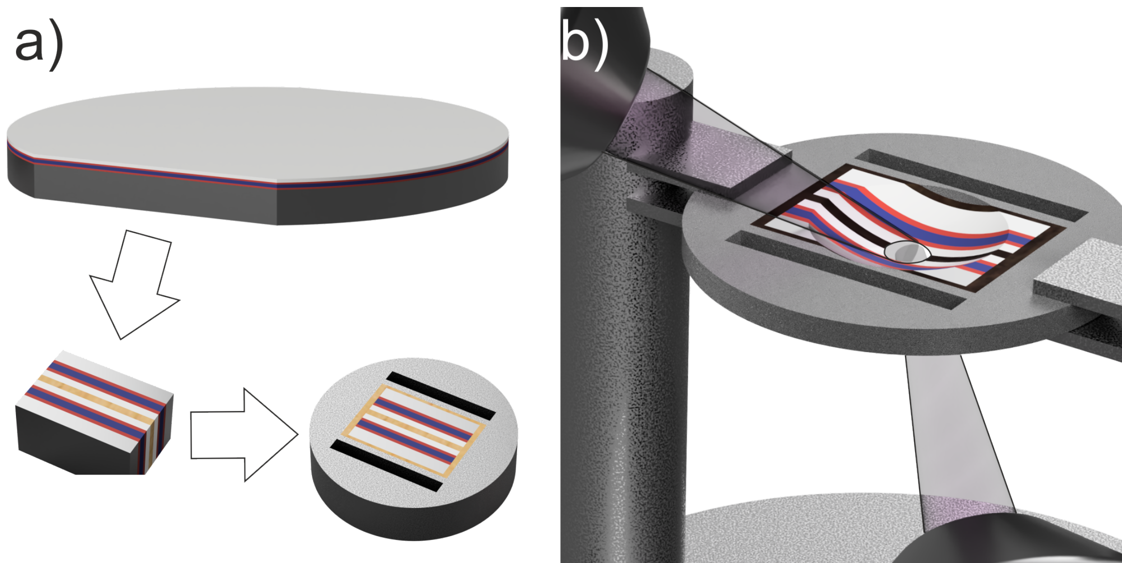

Figure 3.1: a) The conventional cross-section preparation of hard materials like inorganic semiconductors typically requires cutting of the initial bulk material (here: a wafer). Small pieces are then combined face-to-face with epoxy adhesive and put into a titanium support ring. This TEM specimen is then mechanically thinned to below about 100 microns and carefully polished to assure homogeneous ion beam etching. b) The polished specimen is introduced into the PIPS and etched by a broad argon ion beam from the bottom and top side until a small hole is created.

in the corresponding publication 6.1.1.

Focused Ion Beam Technique An alternative preparation technique uses a focused gallium ion beam to remove material. Its spatial resolution is of several nanometers up to a few micrometers.
The machine used in this work is a JEOL JIB-4601 that uses gallium ions accelerated between 1.0 keV to 30.0 keV. Furthermore, the tool has an additional electron column that is located at 53° with respect to the gallium column. With this dual column FIB target site preparations of features in the nanometer regime can be carried out conveniently.
The stages of a general lift-out process is exemplary shown for a target preparation as used for the investigations of (sub-)surface damage of broad argon ion beam preparation is published in Belz et al.[56] (Publ. 6.1.1). In general, a suitable target site is protected by several steps of electron and/or ion beam assisted depositions in order to prevent damage created by the gallium ion milling process itself (c.f fig. 3.2). The initial protection layers can be applied ex-situ by sputter coating or in-situ by electron beam induced decomposition of precursor gases. Since the electron beam assisted deposition is much slower than the ion beam assisted deposition the latter is used to great a huge volume of protective material that stays intact until the very last thinning steps to ensure an adequate specimen quality. The following steps b) and c) show the lift-out process by a manipulator transfer system. At first, the target site is cut free form surrounding material. At second, the transfer needle is attached to the specimen by soldering of tungsten that is created by decomposition of the tungsten precursor that is introduced to the preparation chamber by a gas injection system as seen in b). In figure 3.2 d) the thick specimen is soldered to a TEM compatible copper holder that is commonly referred to as a *grid*, and the manipulator needle is removed and retracted. After several steps of gallium ion beam milling the initial sample of few microns thickness is reduced to a few hundreds of nanometers (fig. 3.2 e). The final polishing steps are carried out by a reduced ion beam energy down to 1.0 keV, to ensure high quality surfaces and a final thickness of only a few tens of nanometers that is needed for high resolution (S)TEM investigations.

FIB Double-Cross Section (2XS) In order to investigate the initial damage of argon ions during the conventional broad beam thinning of multi-layer materials typically investigated in cross-section, the FIB was used to create a cross-section of these cross-section specimens. This double cross-section (2XS) preparation is the basis of the publication 6.1.1. In principle the preparation is identical to the well established FIB lift-out preparation as described above. Nonetheless, since the investigated specimen area is very small it can be considered to be a feature of only a few hundreds of nanometer lateral extension. The thinning is carried out symmetrically to keep the region of interest centered underneath the protective layers. The resulting specimen can be considered to be a buried *nanowire*, since two dimensions are considerably restricted to a few tens of nanometers.

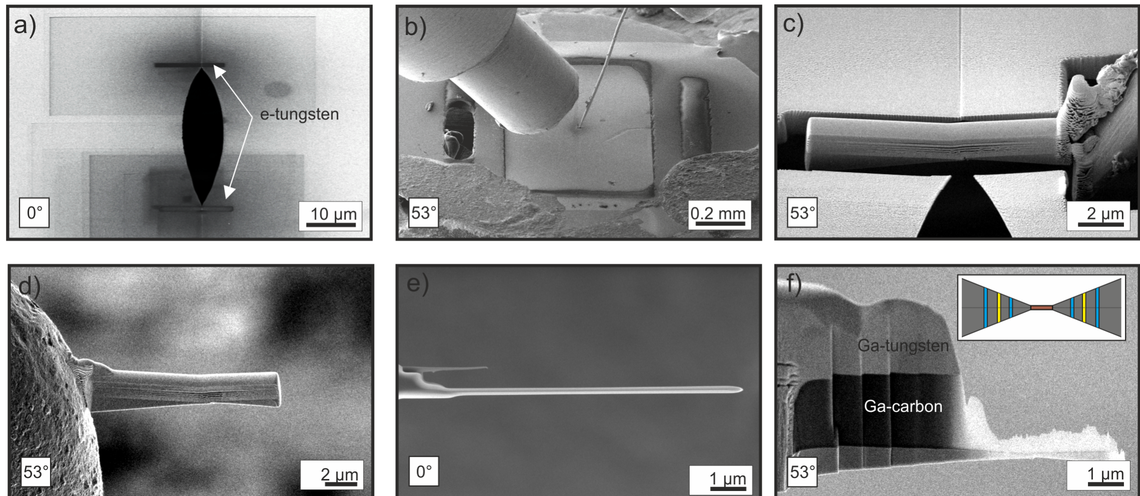

Figure 3.2: a) The target site (here: the thin edges of a conventionally prepared TEM specimen) are coated by electron beam deposition of tungsten and a following gallium ion deposition of additional protective layers. b, c) The target site is cut by ion beam milling and attached to a transfer manipulator by tungsten soldering. d) The thick lamella is transferred to a TEM compatible copper holder and e) thinned with successively reduced ion polishing steps until a thickness of less then 50 nm is reached f). Illustration modified from 6.1.1.

FIB Plan-View Preparation In order to prepare plan-view samples for (S)TEM investigations, in general broad ion beam thinning can be applied. Alternatively, in order to reduces the strain bending of large thin areas and excessive amounts of material re-deposition, the FIB target site preparation can be applied to plan-view samples as well. Hereto, a mechanically thinned piece of the target material is attached to a modified support ring in a way that the thin edge can be milled by the gallium ion beam (c.f. figure 3.3 a). In order to reduce the amount of strain induced foil bending, only small regions are thinned from the side of the substrate exclusively. Since the top surface needs to be intact, it cannot be ion polished. Hence it has to be cleaned carefully and tilted in a way that the incident gallium beam does not hit these regions.

Similar to the aforementioned lift-out procedure the thinning is done by reducing the incident ion beam energy down to 1.0 keV in several steps. Albeit its not necessary to create a hole, it is often inevitable due to the lack of thickness control in the sub-100 nm region.

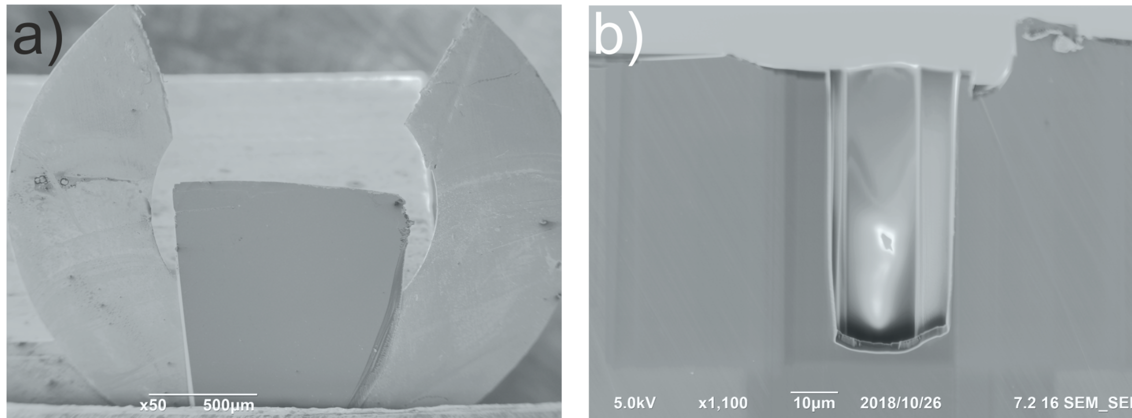

Figure 3.3: a) The secondary electron image shows a mechanically thinned wedge of material glued onto a copper support ring. b) After ion beam milling with successivly lower ion energies the resulting specimen contains electron transparent regions for high resolution microscopy.

3.2 Modeling of Elastic Relaxation

The built-in strain elaborated in section 2.1 can be treated analytically only for simple geometries and boundary conditions as shown e.g. by Hagen[3]. Therein, the special geometry of infinite lateral extension is assumed which is valid for the case of the growth process at wafer scale during MOVPE. As briefly explained in section 2.1.2 the continuum elastic theory can be numerically solved for arbitrary structures utilizing the finite element (FE) formalism. In this work the COMSOL Multiphysic™ Suite[57] has been used to create, solve and post-process the strain relaxation of various material systems.
In a first stage the geometry is modeled as a 3D model using computer-aided design (CAD) tools that are available in COMSOL Multiphysic™. The geometry can be modeled as either a wedge with a given geometric wedge angle as been used for the investigations shown in chapter 4.1, or as a stack of blocks as been used for the investigations of uniaxial strain on scattering distributions (Publ. 6.1.4 and 6.1.3). This modeling was initially done manually, but has been automatized to generate geometries from parameter files that can be generated by an in-house MATLAB™-based[58] software. This software provides an interface to create multilayer systems of a large variety of multi-element compound semiconductors of arbitrary compositions. The composition and thicknesses of these heterostructures layers determine the elastic properties of the respective layer. The layer is treated as a uniform homogeneous continuum with properties derived from linear interpolation of elasticity tensor components and lattice parameters that are tabulated for binary material systems[8,59–64].
The total geometrical structure is automatically divided into finite elements that represent (multiples) of primitive unit cells. The simulation of elastic strain state relaxation for the CAD model is done by initializing the boundary conditions with an isotropic compression/dilatation that is corresponding to the relative lattice mismatch of the deformed

layer with its substrate layer. The parameters needed to calculate the initial mismatch are derived from tabulated values of binary components (c.f. tab. 3.1) and their linear interpolation according to chemical compositions. This approach is justified due to the fact that the coherent growth of of epitaxial layers without plastic deformations is conserving the total strain energy i.e. is elastic.

In the following the numerical solver that is provided by the COMSOL suite automatically optimizes the system and solves the differential equations for according to the linear elastic continuum theory. It is noteworthy, that this relaxation can be carried out using either the isotropic material approximation that utilizes Poisson's ratio as well as the fully anisotropic case where the elasticity components C_{11}, C_{12} and C_{44} are used. The latter approach is computationally more demanding but more suitable to reality.

Depending on the type of simulation needed appropriate boundary conditions are set. The COMSOL post-processor provides access to various results relevant to the strain relaxation. In particular the displacement field is used to calculate the sample deformation for a given super cell that is used in actual image formation simulations (c.f. section 3.5). For these simulations the (deformed) continuum material model is decorated with the corresponding atom types according to the initial compositions.

In addition to the mesoscopic strain deformation field the samples can be relaxed locally by atomistic methods like the valence force field (VFF) approach[65]. This local relaxation of impurity atoms is typically needed to reproduce the realistic static atomic displacements (SAD) in multi-elemental compound semiconductors[8,66–68]. In addition, the software provides an interface to substitute specific atoms in a systematic way and to do strain state analysis.

Specific details about the geometries used, can be found in the corresponding sections of the publications 6.1.1, 6.1.3 and 6.1.4.

	III	V	a_0 [nm]	ν	C_{11} [GPa]	C_{12} [GPa]	C_{44} [GPa]	Source
GaN	Ga	N	0.45	0.35177	293	159	155	[59]
GaP	Ga	P	0.54505	0.30617	140.5	62	70.3	[59]
GaAs	Ga	As	0.56532	0.31673	122.1	56.6	60	[59]
GaSb	Ga	Sb	0.60959	0.3126	88.4	40.2	43.2	[59]
GaBi	Ga	Bi	0.633	0.30937	73	32.7	35.3	[60]
BN	B	N	0.36	0.18007	817.8	179.6	469.9	[61,62]
BP	B	P	0.4497	0.19369	358	86	196.7	[8,62]
BAs	B	As	0.47373	0.22404	284	82	157.9	[8,62]
BSb	B	Sb	0.512	0.23364	205	62.5	112.1	[60]
BBi	B	Bi	0.5529	0.24327	160.2	51.5	87.4	[60]
AlN	Al	N	0.438	0.34483	304	160	193	[59]
AlP	Al	P	0.54672	0.32143	133	63	61.5	[59]
AlAs	Al	As	0.56611	0.29933	125	53.4	54.2	[59]
AlSb	Al	Sb	0.61355	0.33107	87.69	43.4	40.76	[59]
AlBi	Al	Bi	0.646	0.33395	72.2	36.2	33.4	[60]
InN	In	N	0.498	0.40064	187	125	86	[59]
InP	In	P	0.58687	0.35687	101.1	56.1	45.6	[59]
InAs	In	As	0.60583	0.35202	83.2	45.2	39.5	[59]
InSb	In	Sb	0.647	0.35296	68.47	37.35	31.11	[59]
InBi	In	Bi	0.66107	0.3503	60.31	32.52	27.5	[69]
TlN	Tl	N	0.498	0.37079	194.3	114.5	103.2	[63]
TlP	Tl	P	0.58697	0.33085	107.6	53.2	53.6	[63]
TlAs	Tl	As	0.60583	0.33258	88.5	44.1	44.1	[63]
TlSb	Tl	Sb	0.64794	0.32685	69.2	33.6	34.1	[63]
TlBi	Tl	Bi	0.5	0.35647	54.7	30.3	26.8	[63]
SiSi	Si	Si	0.54312	0.28	166	64	79.6	[64]

Table 3.1: Material databases used for continuum elastic strain relaxation by COMSOL.

3.3 The Transmission Electron Microscope

In the framework of this thesis almost all measurements were carried out using a image- and probe-corrected JEOL JEM-2200FS. This microscope is capable of being operated in the conventional parallel beam TEM mode (section 2.2.4) as well as in the scanning probe mode (section 2.2.3) and has spherical aberration correctors for either mode. In addition, the microscope is equipped with an *Ω*-type energy filter, that can create an energy spectrum that can be truncated or recorded depending on the requirements of the experiment.

In the JEM-2200FS the electron source is thermally assisted field emitting gun (Schottky-FEG). In the FEG assembly the extracted electrons are accelerated up to 200 keV with an electron energy spread of about 1.0 eV. The resulting electron distribution is very narrow and the de-Broglie wavelength of the emitted electrons is about 2.51 pm.

The accelerated high energy electrons are directed towards the specimen in an evacuated

column with a residual pressure of about 10^{-5} to 10^{-6} Pa. The crossover of the initial gun assembly is typically demagnified by the illumination system consisting of multiple so called condenser lenses. In the case of TEM, a parallel illumination is desired, whereas a convergent probe is formed in the STEM mode. The detection system of the STEM mode is usually a annular dark-field detector that integrates the scattered electrons within a given angular range. In contrast, the TEM mode uses a camera and acquires images in parallel, whereas the STEM records images sequentially.

3.4 Strain State Analysis

The strain state of a specimen can be partially reconstructed from its projected lattice investigated by (S)TEM techniques. It can be shown that a real space approach [70] that measures distances between image features, as well as a reciprocal wave approach called *geometrical phase analysis* (**GPA**) [71] can lead to the information about the strain state with respect to a reference system. Nonetheless, in large scale micrographs where high resolution information can be found, but –due to pixelation of the camera – hardly be used for peak finding, the latter approach is more viable [71]. It is worth mentioning, that with sufficiently stable conditions and sufficient scan point density both methods can be used to measure strain by using STEM as demonstrated e.g. by Guo et al. [72].

3.4.1 Geometric Phase Analysis

The GPA method is based on inverse Fourier filtering of images and processing of only specific spatial frequencies (i.e. *Bragg spots*) in the further process.
Since the Bragg spots belong to specific lattice planes of the crystal (c.f. section 2.2.4) and Hÿtch et al. [71]) they represent the *geometric wave* of lattice planes in the corresponding real space direction $\vec{r}$. The complete image $I(\vec{r})$ can be decomposed into a Fourier series:

$$I(\vec{r}) = \sum_g H_g \exp\{2\pi i \vec{g} \cdot \vec{r}\},$$

where $H_g = A_g \exp\{iP_g\}$ is the Fourier component of frequency $\vec{g}$ with the (geometric) phase P_g and Amplitude A_g. As shown in Hÿtch et al. [?] selecting a given Bragg-spot g an image can be calculated from the (masked) complex Fourier-transform which is connected to the geometric phase as a real function:

$$B_g(\vec{r}) = 2A_g(\vec{r}) \cos(2\pi \vec{g} \cdot \vec{r} + P_g)$$

Surrounding the Bragg condition g are spatial frequency components that contain information about the deviations from the main (corresponding) real space distance $\vec{r}$. Extending

eq. 3.4.1 $\vec{g} \mapsto \vec{g} + \Delta\vec{g}$ results in

$$B_g(\vec{r}) = 2A_g(\vec{r})\cos\left(2\pi\vec{g}\cdot\vec{r} + 2\pi\Delta\vec{g}\cdot\vec{r} + P_g\right).$$

It can be seen that the phase $P_g(\vec{r}) = 2\pi\Delta\vec{g}\cdot\vec{r}$ changes uniformly with the small change $\Delta\vec{g}$ of the reciprocal lattice vector $\vec{g}$.
Takeing the gradient of this geometric phase leads to

$$\bigtriangledown P_g(\vec{r}) = 2\pi\Delta\vec{g}.$$

It can be seen that this gradient is directly proportional to the change of the corresponding spatial frequency. By extending the analysis to multiple Bragg spots, the distortions in various directions can be measured.
Further details can be found in the corresponding literature by Hÿtch et al.[71].
The algorithm is implemented as a commercial software plugin for the microscope control software.

3.4.2 Zero-Loss Filtered HR-TEM

In section 2.2.4 the image formation process is explained in terms of fully coherent elastic diffraction. In reality especially thick specimens create a significant amount of inelastic low angle scattering due to electron-electron interaction. This inelastic scattering does not follow the coherent imaging mechanism that is providing contrast in HR-TEM. Its effect is typically the loss of contrast and is therefore detrimental to high quality imaging.
The JEOL JEM-2200FS is therefore equipped with an Ω-type energy prism[20] that is capable of dispersing the transmitted electron beam. The energy spectrum is magnified and projected onto a mechanical slit that physically blocks electrons with an energy loss of typically >1 eV.
This technique is typically called *zero-loss filtered* (**ZLF**) HR-TEM.

3.5 Image Simulations

Based on the general multi-slice approach illustrated in section 2.2.3 the computation of (S)TEM images is straight forward: At first, the material under investigation is constructed using several in-house utility tools partly incorporated in the STEMsalabim[46] package. Depending on the particular type of investigation these so-called *super cells* can be relaxed – as discussed in 3.2 – or left as a unrelaxed crystal.
In the following the simulation parameters are passed over to the STEMsalabim code located on the highly parallelized computation cluster *Marburger RechenCluster 2* (**MaRC2**) where the main STEMsalabim code is located.
The original super cell is divided into various slices, and the 3D potentials are projected

on the respective slices. The pixels in the scan grid – that is set up by the parameter file – are treated individually and can therefore be calculated in parallel for every image point of every frozen lattice configuration.

Typically, the individual phonon configurations are not relevant for the final image contrast. The individual results are therefore averaged on the final stage for all phonon simulations. For practical reasons all slices are stored and can be used for different simulated sample thicknesses.

The angular scattering distribution is averaged radially which is most suitable to the typical ADF detection setup used for STEM.

The partial temporal coherence and its effect on defocus are treated as defocus series as discussed in [73–75]. The partial spatial coherence and its effect on the effective virtual source size are typically treated at the final stage as a convolution with a point spread kernel [74]. Further aspects of its technical implementation are described in detail in Oelerich et al [46].

CHAPTER 4

Results

In this section the main results of this thesis and related publications are being elaborated. In the first part quantification of damage layers as well as additional artifacts of TEM specimens are presented. By carrying out the measurement and modeling of elastic relaxation of strained crystalline semiconductor materials, the viability of the finite elements method is demonstrated. Thereafter the implications of amorphous layers and elastic strain relaxation on STEM ADF image contrast are elucidated in conjunction with the effects of focal spread and a finite source size. Finally, a scheme for three-dimensional data retrieval from STEM HAADF images of GaP antiphase domains (APD) is presented utilizing the previous findings.
In addition, simulation studies of gallium phosphide bismide (Ga(P,Bi)) are presented to show implications of atomic arrangements as well as focus variations on electron channeling. These effects are shown to have a significant role in the quantitative evaluation of STEM ADF imaging.

4.1 (Sub-)Surface Damage

The HAADF STEM imaging mode is an invaluable tool providing information on composition due to its relatively simple elemental contrast (*Z-contrast*)[76] (c.f. 2.2.3). However, in reality the contrast is affected by several other factors. These aspects will be outlined in the following and their relevance and possible compensation schemes will be elaborated. One of the most apparent features is the damage introduced to a specimen during the preparation process. Especially for crystalline semiconductor materials the preparation of thin TEM specimens results in damaged surfaces due to the material removal process. In addition to this inevitable surface damage, ion beam thinning can cause a complex geometry, surface roughness as well as a material dependent etching rate. Since conventional (S)TEM measurements rely on assumptions about the material along the transmission direction, accurate knowledge about its fundamental appearance is of great relevance to

any quantitative (S)TEM measurement. Figure 4.1 illustrates a typical (over-)simplified model that includes basic geometrical assumptions as for example a constant thickness gradient. On the other hand it is clear that this model can only hold true for very gentle and homogeneous sample preparation and is not necessarily close to the physical reality. The complex model includes various deviations from this simplified model that need to be considered for most material systems. In the following the surface quality will be investigated.

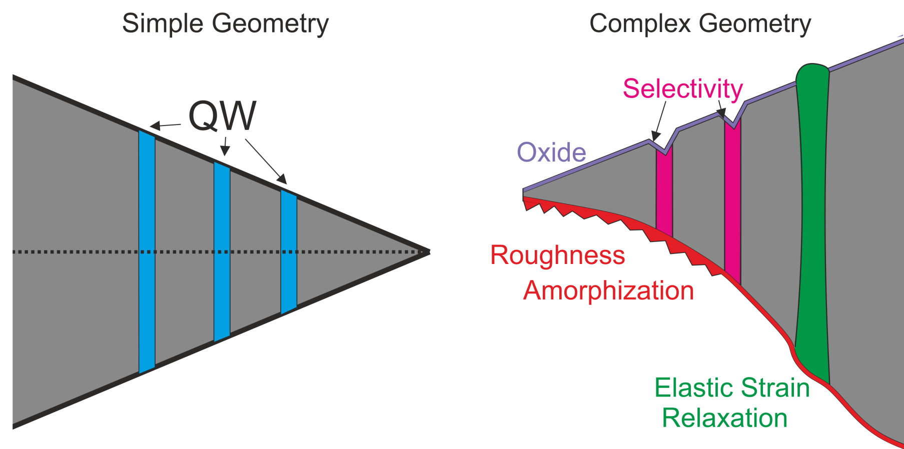

Figure 4.1: Comparison between an idealized sample geometry of a typical cross-section preparation and an more realistic model with added complexity.

Albeit ion polishing can be considered to be a more gentle approach to thinning samples for electron microscopy than mechanical grinding alone, several aspects have to be taken into account. One of the most decisive factors is the kinetic energy and mass of the ions hitting the sample surface. It is clear that less energy equates to a reduction of the damage depth but also to a significantly reduced sputtering rate. The extend and quality of such ion beam damage caused by argon ions is elaborated in Belz et al.[56]. Herein, the residual damage of a typical argon polishing energy of about 1.7 keV is investigated by creating a cross-section of a conventional TEM specimen.
The following paragraph will describe the method used for the investigation of the residual damage introduced by such ion beam polishing.
Since these specimens are cross-sections of semiconductor hetero-structures cross-sections they can be referred to as as *double cross-sections* (**2XS**). The preparation of these specimens utilizes the FIB lift-out technique and is described in more detail in section 3.1 as well as in the according publication 6.1.1. Since the 2XS-specimens show the surface affected by the initial (original) ion beam thinning in cross-section the damage depth can be analyzed.

A region of pure GaAs of a 2XS-specimen measured under HAADF conditions is shown in Figure 4.2a. The protective electron beam deposited tungsten (*e-tungsten*) layer is on top of the ion treated surface and the depth profile normal to this surface (red arrow) is the

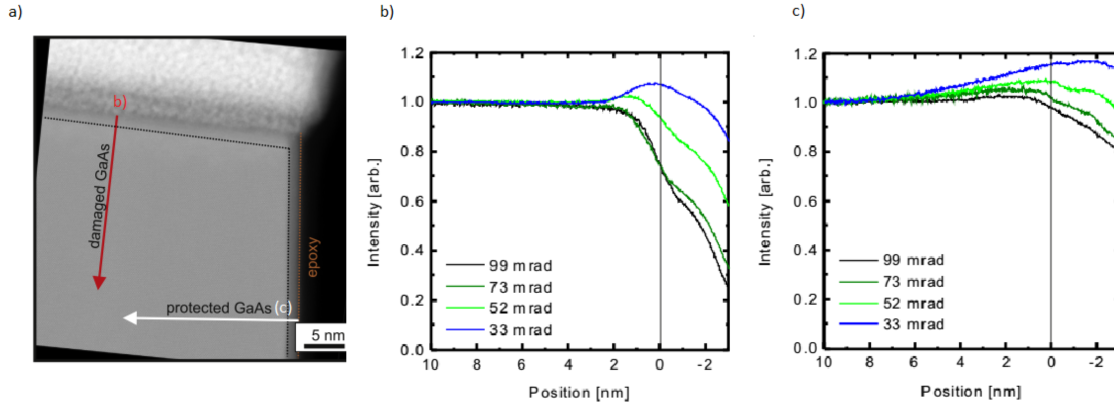

Figure 4.2: a) The high resolution ADF image of a 2XS that shows the initially thinned surface (vertical) and the unaffected surface that was protected by an excessive epoxy layer throught the preparation (horizontal). Their respective intensity profiles along the b) protected GaAs material as well as c) the damaged GaAs regions indicate a significant difference of these regions regarding crystal quality. Both profiles are shown for different acquisition angles (from an image series) and are aligned to each other.

basis of the intensity plots shown in Figure 4.2c. In contrast an undamaged depth profile can be retrieved from the region protected by epoxy during the whole argon ion beam thinning (c.f. Figure 4.2b).
Both profiles are aligned with respect to the onset of crystalline contrast (0 nm mark) , where the negative coordinates are within the crystalline bulk and positive regions belong to the damage and oxide region.
The thickness and basic structure of the native oxide can be derived from figure 4.2b. Comparing the four inner detection angles in fig. 4.2b it can be seen that the LAADF regime shows profiles with obviously different character. These profiles are dominated by the different scattering distribution of amorphous and disordered materials in contrast to crystalline media and are therefore less useful for the determination of the oxide layer thickness. In the scattering regime from 73 mrad onward the intensity profiles are simpler and are therefore used to measure the oxide thickness. In these profiles two distinct regions can be identified that are attributed to the oxide/epoxy interface and the oxide/crystal interface. Their thickness is measured by taking the distance between their inflection points leading to a GaAs oxide thickness of about 3.0 nm to 3.5 nm. It is noteworthy that the transition regions are widened due to the finite thickness and a small geometrical wedge in transmission direction. Nonetheless, since the thickness of the FIB lamella can be estimated from the bulk crystal intensities to about 20 nm the latter effects are considered to be of minor relevance.
This oxide layer can be considered almost inevitable for any practical measurements due to the sample transfer in ambient air [77]. Nevertheless, it is worth mentioning that for some materials wet chemical etchants [54] and/or inert gas transfer can be utilized to avoid or reduce the oxidation layer formation [54].

In contrast to the formation of a native oxide layer, the damage layer can be divided into different regions with intermixing interfaces: The very surface is a complex oxide that is either partially or fully formed during preparation and transfer into the microscope. The underlying layer is also highly amorphous and can be considered to be the actual damage layer due to ion bombardment. Its appearance is changing from fully amorphous to partially crystalline. This can be seen in figure 4.2c where the integrated line profiles under different ADF conditions are shown. The *Z-contrast* dominated HAADF profiles (and their respective micrographs) show a less intense scattering of the amorphous damage layer (neg. x-coordinate) that is followed by a small increase and a rapid phase-out towards the pristine GaAs crystal. It can be seen, that for the very high ADF regime 99 mrad this initial increased level ends at about 4.0 nm below the crystalline onset. This behaviour can be attributed to a small amount of argon implantation increasing the total scattering power.

By comparison of the different ADF profiles it can be seen that intensity change can be measured ranging into the crystal about 7.5 nm. This effect can be understood in terms of increasingly rare ion cascade damage introduced by the initial sputtering process where the GaAs matrix atoms are themselves knocking GaAs atoms from their respective lattice sites. The crystal has therefore a disorder gradient that causes a deviation from perfect crystalline scattering conditions. This disorder scattering is known to cause an increase in LAADF intensities with only minor impact on very HAADF imaging[78].

This is consistent with simple Monte Carlo ion stopping and transport simulations carried out with the *SRIM*-Software[79]. Additionally,[80,81] have shown by atom probe tomography in conjunction with time-of-flight measurements that the implantation of 2.0 keV gallium ions in silicon results in a decreasing exponential implantation profile up to an extend that is comparable to the findings in this thesis.

In order to estimate the ion beam damage in more complex materials the analysis is extended to the ternary GaAs-compounds gallium indium arsenide ((Ga,In)As) and gallium nitride arsenide (Ga(N,As)). It can be seen that the penetration depth and the relative intensity deviation due to ion implantation and damage induced disorder is material dependent and not identical for GaAs and its ternary compounds[56]. Nonetheless, it is clear that the partial amorphization and the ion implantation depths are significantly higher then the pure amorphous surface layer. In the case of Ga(N,As) the damage layer is also shorter than for GaAs, which can attributed to a nitrogen induced hardening effect[82] as well as a reduced ion channeling power due to the intrinsic local strain and disorder in this material system. In general it is expected that pure well aligned crystals amplify the range of ion transport as opposed to amorphous materials as described for example in Schaffer et al.[83].

Further preparation induced artifacts are discussed in the corresponding publication 6.1.1. Therein it is shown that there is no evidence of a strong selective quantum well etching for neither Ga(N,As) nor (Ga,In)As with respect to the surrounding GaAs matrix when

using the argon broad ion beam thinning procedure. Furthermore, there is no significant variation of damage layer thickness across the same material. For further details the reader is referred to the respective publication 6.1.1 and the images therein.

4.2 Elastic Strain Relaxation

4.2.1 Atomic Force Microscopy of Cross-Section Specimens

In addition to the aforementioned extrinsic artifacts introduced by the thinning process, STEM measurements can also be affected by inherent properties causing deviations from the simplified specimen model. The most pronounced artifact considered in this thesis is the elastic relaxation of pseudomorphically grown layers. Since the built-in strain of these layers is not restricted to the growth direction in the case of thin STEM specimens these strained layers cause a deformation of the crystal leading to a locally varying lattice plane bending (c.f. section 2.1.2). This deformation due to elastic strain relaxation produces several measurable features complicating the evaluation of bulk material properties and can therefore be considered to be measurement artifacts.

One feature of this deformation is the bulging of a strained quantum well that can be

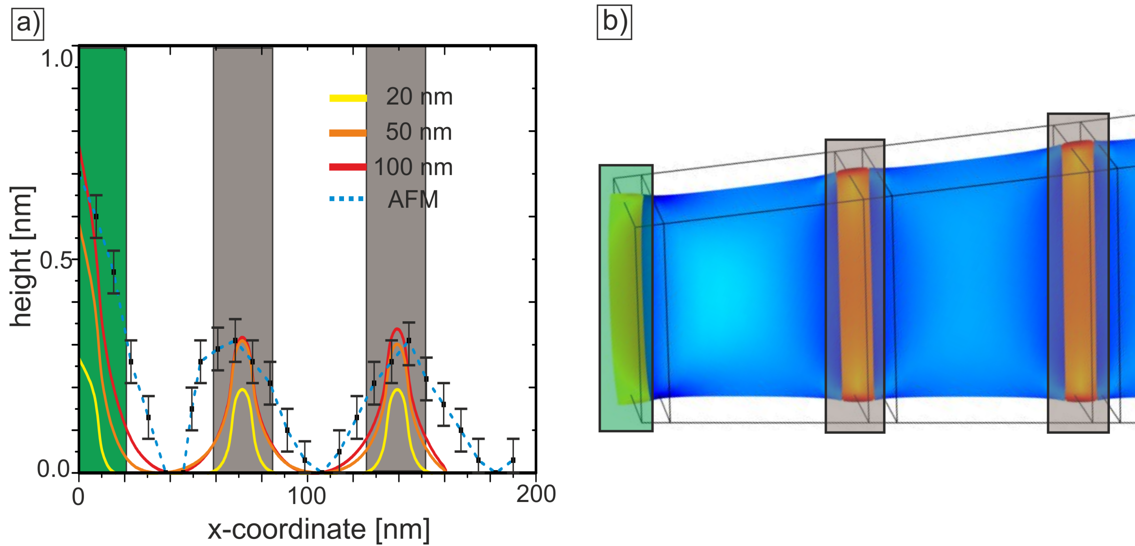

Figure 4.3: a) The simulated topological profile for cross-sections of (Ga,$In_{30\%}$)($N_{1.5\%}$,As) QWs in a GaAs matrix with a thickness of 20 nm, 50 nm and 100 nm and the corresponding AFM data are shown. The green region indicates the free surface whereas the grey regions show embedded quantum wells. b) Illustration of the different strain contents causing the bulging effect in different regions as shown in a).

noticed as a change in the surface topology when a cross-section of a strained layer is investigated. This property is readily accessible by atomic force microscopy (AFM) which can measure the height differences in the (sub-)Å regime.

Although this effect can be seen in principle already on the edges of complete wafers e.g.

by AFM measurements[84] their nearly infinite in-plane dimensions are distinctly different from the low thickness of (S)TEM specimens. Hence, the investigations were carried out on actual cross-section specimens prepared for high resolution (S)TEM investigations. An additional benefit of this approach is that the surface roughness is accessible simultaneously from AFM measurements.

The thickness dependence of the surface bulging due is demonstrated in figure 4.3a. Therein, the AFM measurement is compared to the simulated effect for different specimen thicknesses. From the simulation studies it is clear that the bulging effect converges to a maximum for increasing thicknesses. This thick sample limit leads to an elevation of an embedded quantum well region of about 0.3 nm in the case of (Ga,$In_{30\%}$)($N_{1.5\%}$,As) that is compressively strained by 2 % with respect to the GaAs substrate.
The embedded quantum well regions are highlighted in fig. 4.3 by grey shading. Whereas the difference between 50 nm and 100 nm thick TEM specimens shows little variation for these embedded regions, the situation is different for the edge of the sample with its different geometrical constraints (light green background). The simulated topology for a 100 nm thick specimen is clearly in better agreement with the experimental AFM data then either the 20 nm or the 50 nm thick specimen. It is noteworthy, that the simulated elevation profile has significantly less lateral spread than the AFM measurement which can be easily explained by the much lower lateral resolution of the AFM probe which is convoluted with the real z-profile.
These findings show that the finite elements relaxation model is in very good agreement with experimentally derived data. Unfortunately it is apparent that the measurement of the areas that are relevant for (S)TEM analysis are not easily accessible by AFM due to the difficult alignment and the tiny electron transparent regions. Nonetheless, it can be shown that the finite elements method is capable of accurately modeling the elastic strain relaxation mechanism.

4.2.2 High Resolution Strain State Analysis

Another experimentally accessible tool for the strain state analysis is the evaluation of HR-TEM/HR-STEM images with crystal lattice resolution. As described in chapter 3.4 the sample deformation can be calculated from the atomic lattice positions. Utilizing the geometric phase analysis[71](GPA)(c.f. 3.4.1) method the strain state of a thin TEM specimen can be derived by measuring the difference in the lattice periodicity between a strained region(the quantum well) and a reference system (GaAs barriers).
Figure 4.4a shows a zero-loss energy filtered conventional TEM micrograph of a (Ga,$In_{30\%}$)($N_{1.5\%}$,As) multi quantum well structure prepared as (2XS)-specimen. This specimen can be considered to be a one-dimensional structure – or nanowire – and therefore

shows a further amplified lattice deformation due to elastic relaxation.
The displacement field of a magnified region of figure 4.4a is shown color coded in figure 4.4b. In this figure the estimated sample thickness of about 55 nm is implicitly averaged along the transmission direction due to the projection nature of transmission microscopy.
This averaged displacement field in growth direction (left to right) is normalized to the value of the built-in tetragonal distortion. In order to compare the experimental data three sub-regions have been averaged to reduce the experimental fluctuations due to imperfect imaging, local damage and thickness variations. The averages range from 58 nm to 75 nm which illustrates the significant degree of strain relaxation in thin TEM sample geometries. By knowing the transmitted sample thickness the complete geometry is known and can therefore be compared to a equivalent computer model strain state analysis. Hereto, the geometry was build according to the measurement parameters and the final strain state was calculated according to the procedure elaborated in section 3.2. The displacement field was further on averaged along the TEM transmission directiof n using natural interpolation in order to provide comparable data to the experimental data.

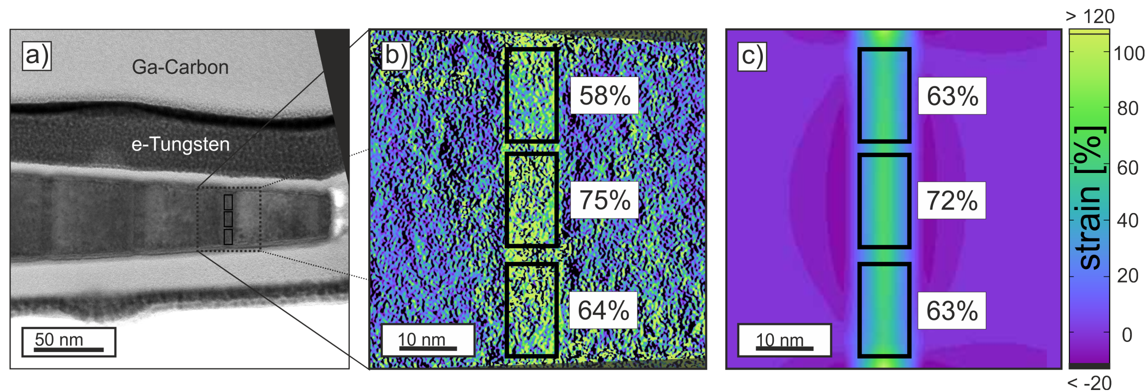

Figure 4.4: a) Overview TEM micrograph showing a 2XS specimen. b) The (projected) strain of several regions within a QW is shown as measured by GPA. The strain is shown as a fraction of its value for infinitely thick samples. c) Shows the calculated values for projected strains derived by a *nanowire* simulation with geometries derived from the overview micrograph in a).

The direct comparision of fig. 4.4b and c shows a remarkable agreement between the simulation model and the experimental data. The relative deviation between related regions of both images is below $10\%_{\mathrm{rel.}}$. It is noteworthy, that the experimental data is acquired over a relatively large field of view of a strained and inevitably bent specimen. The high resolution lattice image is therefore slightly under-sampled. In addition, the HR-TEM imaging conditions are very sensitive to thickness, tilt and orientation [11] of the specimen. It is therefore only possible to compare larger sample regions as an averaged entity.
A similar strain measuring characterization with adaptation to HR-STEM measurements

was carried out in the framework of strain relaxation in high aspect-ratio epitaxy [72]. In this publication the strain state was investigated by using HR-TEM and HR-STEM. It is shown that the strain profile measurements are in very good agreement with well established X-ray diffraction techniques.
These measurements show the validity of the finite elements method for calculation of strain states for structures with lateral extensions of a few tens of nanometers for both HR-STEM and HR-TEM. Furthermore, it is shown that the model can be used to incorporate material features that are known for bulk structures and be adapted to the lower dimensionality of TEM specimens.

4.2.3 Applications of Elastic Relaxation Modeling

As a further refinement step of the relaxation technique a combination of atomistic lattices and continuum mechanics is established. Hereto, the finite elements model is generated from first order approximations like supporting X-ray data about the structure. The computer model is then generated based on a-priory knowledge from these experimental measurements. These provide layer thicknesses and average layer compositions. It is noteworthy that this is not necessarily the case for complex compound semiconductors since the XRD measurements usually model the total strain as well as the layer thickness which is not uniquely possible in multinary materials.
Since the thickness determination is a very crucial parameter several techniques can be considered. In Beyer at al. [73] the through focus method is shown to accurately measure the thickness of a sample on the scale of the probe spread. Therein, it is additionally shown that the method is in close agreement with alternative methods like the electron energy loss spectroscopy (EELS). Besides these techniques also HAADF measurements have been shown to provide accurate results when combined with image simulations [2,74,85] and statistical computer modeling [86,87]
With a geometrical thickness model the (S)TEM specimen can be modeled in three dimensions allowing for the strain relaxation of any built-in strain.
Since compound crystalline semiconductor materials consist of several elements the strain can only be modeled from an average material. To overcome these limitations, the expansion of the continuous relaxation model is carried out by an additional atomistic valence force field relaxation (VFF) step. The VFF approach models local distortions due to impurities with good accuracy [66] and is used as a local refinement step for the result of elastic strain relaxation.
Hereto, a region of the fully relaxed model is decorated with the corresponding elements at lattice sites and the total system energy is minimized according to the VFF algorithm.

In the following results the atomic resolution measurements of strained semiconductor layers are elaborated. The influence of strain and lattice plane deformation on quantitative atomic resolution STEM image intensities is investigated by simulation studies on strained GaAs quantum wells embedded in GaP[74]. Therein, a simulation matrix of geometries with 22, 37 and 74 atomic monolayers (ML) widths and 80, 184 and 376 MLs thickness are elastically relaxed using the FE formalism. In this publication the mean square displacement (MSD) of the atoms from the average column location is considered as the decisive metric to connect local displacements with changes to the scattering intensities. It is shown by profile plots that the MSD is directly correlated to the relative change of ADF intensities. The findings are furthermore analyzed in terms of sub-lattice intensities. We find that the relative intensity change between the simple tetragonally deformed and the FE relaxed model is similar for both sub-lattice types and up to $8.5\%_{\mathrm{rel.}}$ in the case of high angle scattering. The difference between the (artificially) unstrained GaP/GaAs interface is up to $15\%_{\mathrm{rel.}}$. Consequent considerations for LAADF intensities show similar trend for the on-column positions.
In addition, the background level in between atomic columns was investigated. It was observed that although the HAADF background is hardly affected by strain, the LAADF background shows a significant intensity increase. This trend is similar to the findings of[66,78] for static atomic displacements due to impurity atoms.
Following the above simulations, experimental measurements of an embedded $\mathrm{Ga(P,As_{65.6\%})}$ quantum film were compared to these simulations. Hereto, the simulations where done using the FE formalism as well as the additional VFF refinement step in order to include the impact of static order displacement. The results are in good agreement with the strain relaxation model and emphasize the need for strain modeling when chemical information of interfaces is required. It is pointed out that the intensity change due to strain causes artificial contrast implying non-existing composition gradients. It is clear, that the distinction between measurement artifacts and specimen properties need careful separation when quantitative measurements are desired.

4.3 Atomic-Scale 3D Reconstruction of APDs in GaP on Si by STEM

In the case of homoepitaxy or epitaxial growth of materials with a very similar lattice constant the built-in strain is generally much lower than in most other cases. In particular GaP and silicon have nearly identical lattice constants and are hence mismatched by only 0.356 % with respect to the silicon substrate.
As described in chapter 2.1 various challenges occur due to the polar atomic basis of zincblende materials in combination with mono- and bilayer steps of silicon-(001) surfaces.

These APBs are defects that in general degrade electric and structural properties in devices. They also complicate the growth of flat layers during epitaxy[5,7]. In order to correlate growth conditions with APB creation and their termination formation HR-STEM is utilized. Since classical cross-section (XS) samples usually show projections of 3D structures, where in parts of the depth information are obscured and inaccessible. In the case of III/V semiconductors the plan view (PV) geometry has several benefits over XS's since the projected lattice is cubic and elemental columns are in an simple alignment with a large spacing.
In the GaP/Si system investigated the lateral extension of the APD is in the range of 50 nm to 100 nm which is relatively large in the framework of lattice resolved STEM. Therefore, the thickness variation across the region of interest (ROI) as well as the ion beam damage have to be minimized at an atomic scale. A special preparation combining mechanical grinding and low energy FIB milling was undertaken. This method is similar to a classical *H-bar*[88] XS sample preparation commonly utilized for FIB preparations but with special precautions to ensure a minimal surface modification on the pristine GaP side of the specimen. Most of the material is removed by fast mechanical thinning down to a few microns thickness. The final thinning is carried out in the FIB with ion energies down to 1.0 keV on spatially well separated locations (*trenches*). This technique provides many high quality trenches of several microns width where only one side has been ion polished. It is worth appreciating that this alone halves the total damage layer thickness. Further details about the preparation steps can be found in the respective publication 6.1.2 as well as in chapter 3.1.
Another important aspect beneficial for the retrieval of atomic 3D information from STEM projections are image simulations on an absolute intensity scale. Multiple microscope parameters that play a significant role are incorporated in order to match experimental measurements conditions. As elucidated in publication 6.1.5 the commonly neglected parameters in quantitative STEM image simulations are the partial temporal and spatial coherence of the microscopes electron source as well as the amorphous layers formed due to ion damage and oxidation. The implications on image contrast and the compensation schemes involve the simulation of an effective probe spread in transmission direction and the convolution of an effective source size in the lateral directions. The inclusion of amorphous layers is difficult and is done heuristically by applying a pseudo-oxide layer that is fully amorphized. For simplicity, this material contains only disordered GaP and the actual oxidation configuration is neglected. More details on the quantification and characterization of these features can be found in publication 6.1.5.
Furthermore, the effect of electron channeling on the scattering has to be accounted for in detail. The channeling of electrons along well aligned atom columns is known to cause a significant deviation to the scattering distribution compared to single scattering and amorphous scattering distributions[89]. A further complication implied by this effect is that the elemental decoration of lattice sites within an atomic column has significant impact

on the scattering distribution since the scattering power is approximately proportional to Z^1 *to* Z^2 for annular dark-field imaging[1,76]. This is particularly relevant in the case of GaP where the atomic basis consists of elements with very dissimilar atomic numbers ($Z_{Ga} = 31$, $Z_P = 15$).
In order to account for these effects and the complicated scattering distribution due to multiple scattering, a systematic forward simulation series of image intensities was carried out. Hereto, the PV geometry was modeled up to a thickness matching the specimen under investigation (ca. 65 nm). In the PV geometry every atomic column contains a given amount of gallium and phosphorous atoms depending of the ratio between mainphase (MP) and antiphase (AP). Figure 4.5 illustrates this arrangement where the MP (white background) is stacked ontop of the AP (grey background) along the electron beam transmission direction [001]. From left to right the MP to AP ratio increases resulting in a gallium dominated column which represents the natural decoration of the group-III sub-lattice.

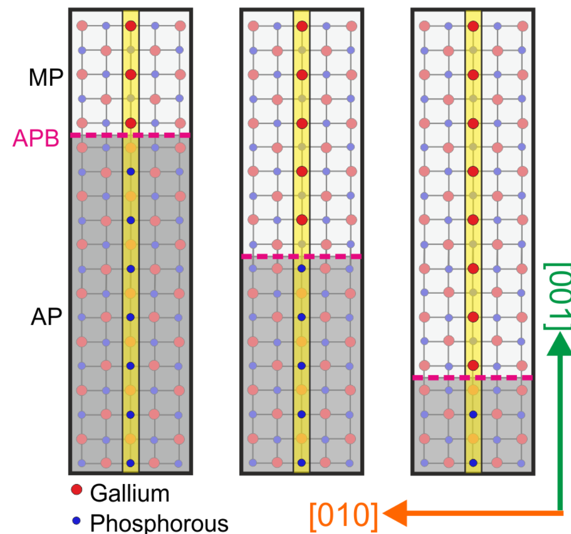

Figure 4.5: Illustration of a cross-section of simplified APBs. The location is changed from left to right revealing the different chemical compositions of each individual column as usually measured along the [001] direction.

For the complete simulation a stack of total 118 super cells is needed where an artificial APB is generated by inverting the column decoration for only one central column. The image simulation was carried out including a finite source size, a focus spread, thermal vibrations and amorphous pseudo-oxide layers. The respective values are determined from previous experiments and fitted to the experimental data derived for pure GaP. Further details are given in the respective publication 6.1.2. The product of these seven independent focus values in addition to the 15 different phonon configurations lead to a total of 12 390 different image simulations that are weighted and combined as elucidated in chapter 3.5.

For a given thickness a HAADF image according to experimental conditions is created for

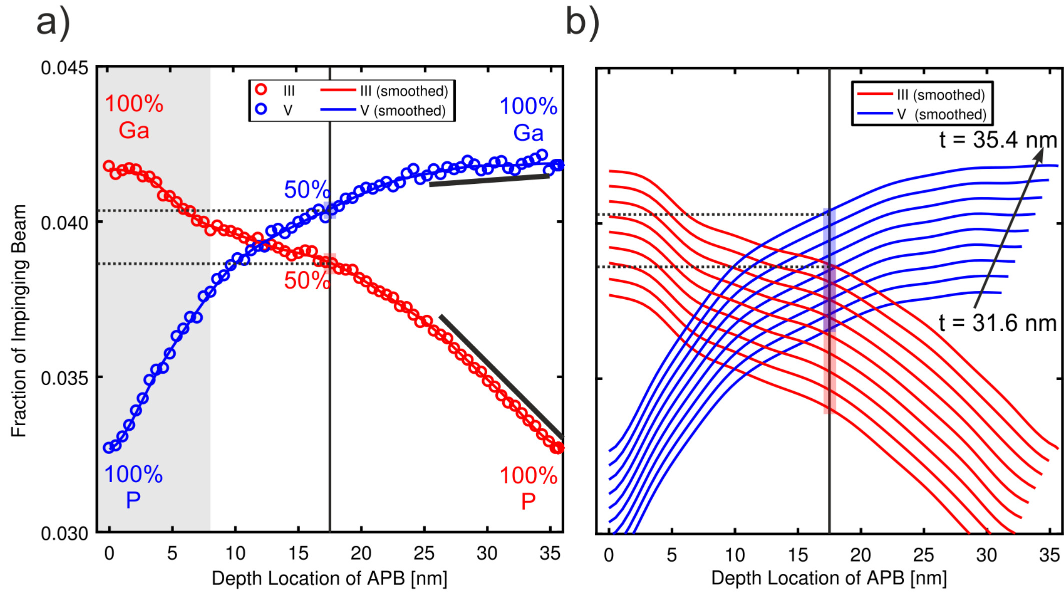

Figure 4.6: The averaged intensities from all simulations of group-III and -V sub-lattice positions with a MP/AP ratio from 0% to 100% are shown for a) a single thickness of about 35 nm and b) a set of different thicknesses.

every simulation and the column intensity for the group-III and group-V sub-lattice is then extracted. The normalized average intensity is shown in figure 4.6a as a fraction of the initial impinging beam plotted versus the depth within the super cell. Without an APB the group-III column is occupied purely by gallium atoms and the group-V column purely by phosphorous. Whereas the intensities are completely inverted in a pure antiphase domain (APB location equals total thickness). It is noteworthy that both intensity curves are not mirror symmetric with respect to each other which is attributed to the defocus region (grey background) as well as the difference due to different channeling conditions. This is particularly apparent in the case of an equal gallium/phosphorous ratio where the total column intensity is significantly higher with gallium atoms on top of phosphorous atoms and vice versa.

For the 3D reconstruction of the spatial extend of an APB within a crystal an accurate thickness determination is needed. For the analysis of high magnification images a bilinear thickness gradient is applied that is measured from the surrounding pure phases. Whereas a local thickness is estimated by using the surrounding column intensities for images with a larger field-of-view.
Since the graphs shown in fig. 4.6a are thickness dependent, a complete series of curves are needed for practical considerations as illustrated in fig. 4.6b. Therein the intensity curves are plotted for a thickness ranging from 31.6 nm to 35.4 nm.

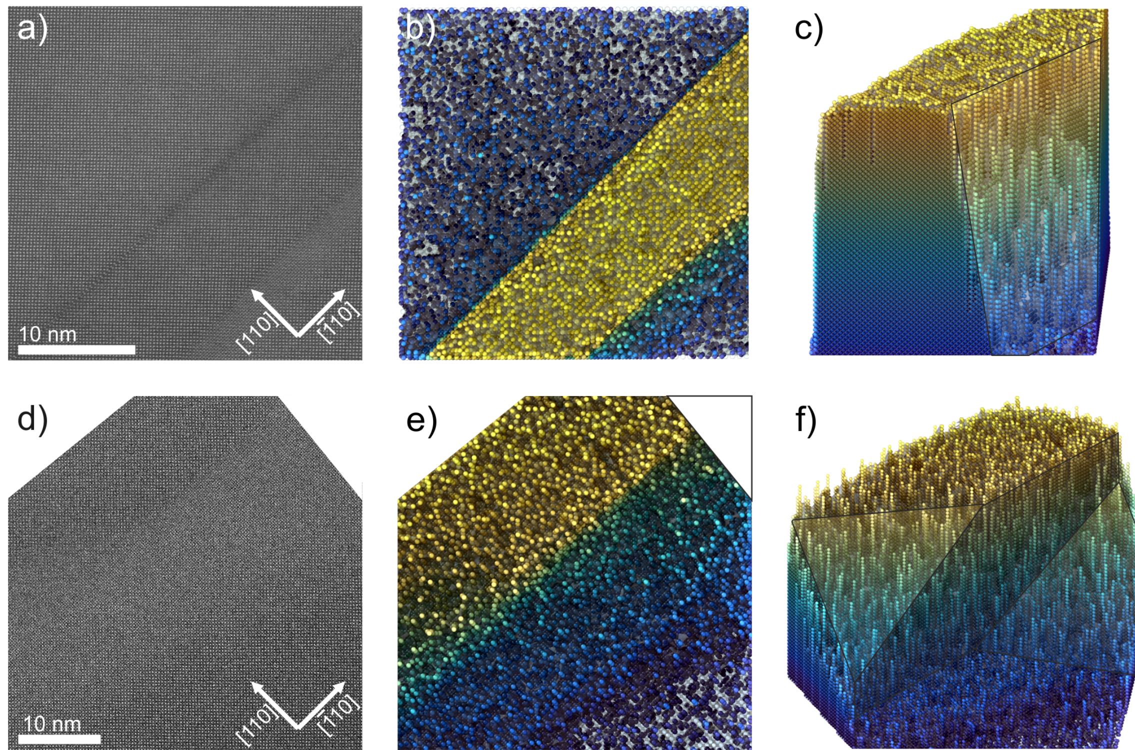

Figure 4.7: The reconstruction of two APBs from two HAADF images (a&d) with containing about 22 000 and 55 000 atom columns, respectively. The reconstructed atom positions are shown in b) and e) in plan view. The depth location of the APB ranging from 0 nm to 35 nm is color coded from blue to yellow, respectively. Another perspective on the reconstructed volume is shown in c and f, where the mainphase atoms are removed for visual clarity.

Apart from the generation of universal lookup table for the GaP system, experimental data extraction has been carried out. The experimental images were normalized to the intensity of the direct beam using a known CCD conversion efficiency as well as data from detector response measurements (c.f. Publ. 6.1.2 and therein). By doing so the simulation and the experiment are on the same absolute intensity scale without any further relative scaling.

The column positions are determined by peak finding using contour thresholding of *Bragg-filtered* images where only a portion of the Fourier transform of an image is used to select strong components of the lattice periodicity. This is closely connected to the reciprocal lattice representation of a crystal structure (c.f sec. 3.4.1). This technique equalizes the column intensity of dark and bright columns. These initial peak positions are further refined by two-dimensional Gaussian fitting of the raw data.

Finally, after image segmentation into columns, the algorithm translates the column intensity based on the determination of local thicknesses into the location of the APB. By applying it to all lattice points the missing depth information is retrieved from the 2D projection measured in the STEM.

Figure 4.7a-f show the reconstruction of two APBs from two HAADF images (a&d) with

a very large field of view that contain about 22 000 and 55 000 columns, respectively. Figure 4.7b and e) show the plan view of the final reconstructed image. For clarity the mainphase component is omitted and the APB depth location is color-coded. Another perspective on the reconstructed volume is shown in fig. 4.7c and f. Therein different planes with specific angles can be distinguished with significant fluctuation across these interfaces.
As described in more detail in Publ. 6.1.2 for well-sampled high magnification images the mapping error is strongly correlated to the contrast between column and background. In addition, it is clear that the lack of sampling for larger field-of-view images leads to a higher error rate as well. For practical uses it is therefore needed to reduce specimen drift in order to provide high sampling in combination with low image distortions.
As shown for the investigations of antiphase boundaries the location of scattering centers along a column can have a significant impact on the detected intensities. In the following section this effect will be investigated for a more isolated model system.

4.4 Effect of Depth Location of Bismuth Atoms on the Image Contrast

In the framework of depth information in (S)TEM data, the dependence of impurity atoms at varying depth locations on the scattering distribution were carried out for the ternary alloy gallium phosphide bismide (Ga(P,Bi)). In this material the atomic number difference of $Z_{Bi} = 83$ to $Z_P = 15$ is extremely high. It is therefore very suitable to analyze the (maximum) effect of (heavy) impurity atoms within a crystal with respect to their depth location within an atomic column.
Hereto, in a systematic simulation series a Ga(P,Bi) crystal was generated with only one bismuth atom incorporated into a phosphorous column of a GaP crystal with a thickness of about 20 nm. Hereto, the z-coordinate of the bismuth atom was changed from top to bottom.

From these series of super cells image simulations were carried out and the columnar contrast was analyzed by averaging a circular area of about 50 pm diameter centered on the bismuth containing column. This intensity value (without partial coherence effects) plotted against the respective z-position of the bismuth atom is shown in figure 4.8. In addition to the simulated Ga(P:1Bi) data – where only one single atom of bismuth is added into a group-V column – the pure phosphorous column intensity (with no bismuth atom) is shown as a reference (blue). It can be seen that the scattering intensity of the bismuth containing column is strongly correlated to the focus of the STEM probe. This effect causes a significant increase of intensity that is up to about three times the intensity of a deep bismuth atom.

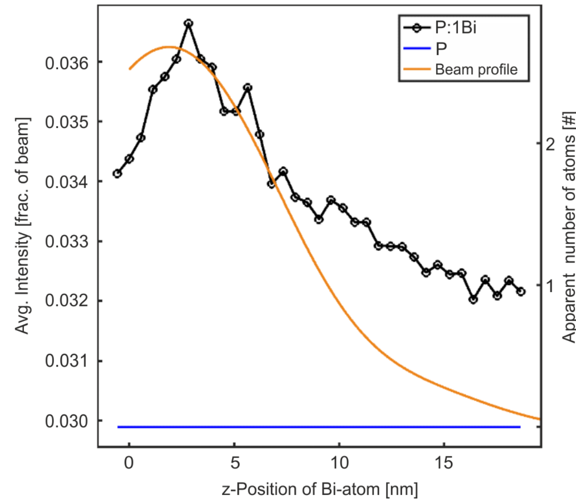

Figure 4.8: a) The average intensity of a simulated phosphorous column with the addition of a single bismuth atom is plotted over the position of this single impurity with respect to the top surface (black). The blue line references a pure phosphorous column without bismuth substitution. Additionally, the depth profile of the simulated electron probe is shown (orange).

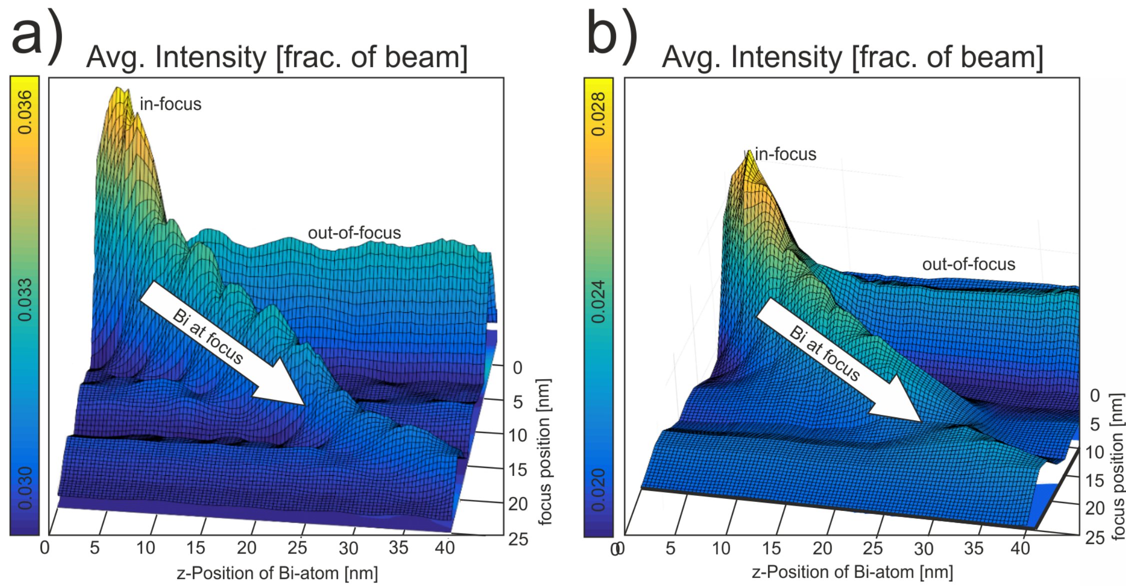

Figure 4.9: a) The intensity profile with an extension of varying defocus positions for a source with perfect coherence b) only partial coherence is shown. The pronounced ridge of intensity with optimum defocus (as depicted in fig. 4.8 is included at around −2 nm defocus.

The simulation of the z-dependence can be extended towards the inclusion of through-focus conditions. The results of this simulation grid are shown in fig. 4.9a. The simulations include the findings of fig. 4.8 as a profile along the −2 nm defocus position across the data-set but in addition show another strong correlation with the electron probe z-position. The local maxima coincide with the z-position of the bismuth atoms.

These results show that the alteration of scattering intensities is the strongest when heavy scattering centers are in focus conditions and/or near the top surface of a specimen. The propagation of electrons along the column direction is hence affected by the elemental arrangement. This effect is extremely significant in the case of heavy scatter centers like bismuth atoms. The near surface bismuth atoms generate a scattering that is almost up to three times the scattering power of a (typical) buried bismuth atom (c.f. fig. 4.8. From the view-point of chemical composition analysis, this effect creates the impression of local increase of apparent bismuth concentration although only a single atom is close to the top surface.

Finally, simulations including the effects of partial coherence were carried out. The results are shown in figure 4.9b and show a significant reduction of the intensity variation between in focus and out-of-focus conditions as well as the z-dependence of the scattering intensity. Nonetheless, the general trend is unaffected but the degree of deviation is reduced due to the additional blurring.

In conclusion it is worth noting that the out-of-focus condition is statistically much more likely and therefore in the case of chemical analysis much closer to the (mean) intensity for a ternary alloy of a given composition. This confines the significance of such strong deviations to local intensity distributions as opposed to large scale composition analyses where the averaging removes the rarer features.

CHAPTER 5

Summary

It is illustrated that the preparation of thin specimens from bulk materials can have significant influence on the interpretability of (S)TEM data. The results of the presented measurements show that and the elastic strain relaxation in low dimensional structures alters the overall strain state of the material – and hence affects strain measurements – as well as the contrast of STEM measurements and is generally needed to be incorporated in comparative simulation studies that involve strained structures. Furthermore, the ion beam thinning process itself can introduce – even with relatively low energies – a serious alteration of the surface which can affect the contrast of STEM measurements. Hence, the correlation to thickness measurements is complicated due to the distinct difference in scattering behaviour between (partially) amorphized surface layers in comparison with crystalline material. Although parts of these effects cannot be avoided the inclusion of amorphous pseudo-oxide layers in simulations has been shown to provide reasonable agreement with the experimental data.
Furthermore, the impact of a finite electron source with limited coherence has been investigated. It can be shown that a reproduction of experimental contrast by simulation can only be achieved by the inclusion of an additional focus spread as well as an lateral point spread due to partial spatial coherence.
Finally, the previous results are combined to reconstruct the three-dimensional shape of several antiphase domains within gallium phosphide grown on silicon-(001). At first the concept was demonstrated for a simple but highly strained interface and second for large structures with thousands of atomic columns.
It is shown that although the contrast mechanism for annular dark-field imaging is in principle straight forward and mathematically simple, the details of atomic resolution microscopy are still very challenging. Realistic assumptions about the specimen properties and the electron optics have been shown to be of great relevance for data evaluation.
It is clear that the research should be extended to the regime of low angular dark-field imaging where strain and inelastic scattering play a even more relevant role. Furthermore, it is of great importance to investigate the aforementioned practical aspects of damage

layers and optical imperfections for other advanced imaging techniques like diffraction imaging. In addition, it is worth investigating in how far through focus depth section can be utilized to increase the reliability of structure restoration along the transmission direction.

It is expected that the improvement of accuracy and robustness of atomic counting techniques will greatly increase the power of a (S)TEM by providing simultaneously lateral and depth information about arrangement and composition. Furthermore, it is clear that the role of high performance simulations will have an even more important role in the future.

Zusammenfassung

Es wurde gezeigt, dass die Präparation von dünnen Proben aus Volumenmaterial erheblichen Einfluss auf die Interpretierbarkeit von (S)TEM Daten haben kann. Die gezeigten Messungen legen dar, dass die elastische Relaxation von Verspannungen niedrigdimensionaler Strukturen den Gesamtverspannungszustand des Materials verändert, und sowohl Verspannungsmessungen als auch den Kontrast aus STEM Messungen beeinflusst, und daher im Allgemeinen in vergleichenden Simulationsstudien an solchen Strukturen einbezogen werden muss. Weiterhin wurde gezeigt, dass die Ionenstrahldünnung selbst – auch bei vergleichsweise niedrigen Energien – zu erheblichen Veränderungen der Oberflächen führen und den STEM Kontrast beeinflussen kann. Daher wird auch die Messung von Probendicken aufgrund der unterschiedlichen Streuverteilungen zwischen (partiell) amorphisierten Oberflächenlagen und kristallinem Material beeinflusst. Obwohl Teile dieses Effektes nicht vermeidbar sind, wurde gezeigt, dass die Einführungen amorpher Pseudo-Oxidlagen bei Simulationen zu guten übereinstimmung mit dem experimentellen Daten führt.
Im Weiteren wurde der Einfluss einer Elektronenquelle mit endlicher Größe und eingeschränkter Kohärenz untersucht. Es wurde gezeigt, dass experimenteller Kontrast durch Simulationen reproduziert werden kann, wenn eine zusätzliche Fokusaufweitung und eine laterale Punktaufweitung aufgrund der partiellen Kohärenz eingeführt wird.
Abschließend wurden die zuvor genannten Resultate kombiniert um die dreidimensionale Struktur einiger Antiphasen Domänen von Galliumphosphid auf Silizium-(001) zu rekonstruieren. Zum einen wurde das Konzept an einer einfachen jedoch hochverspannten Grenzfläche, und zum anderen an großen Strukturen mit tausenden von Atomsäulen demonstriert.
Es wurde gezeigt, dass auch wenn die Entstehung des ADF STEM Bildkontrasts im Prinzip einfach ist, die Details der atomar auflösenden Mikroskopie hingegen anspruchsvoll sein können. Es wurde dargelegt, dass realistische Annahmen der Probeneigenschaften und der Elektronenoptik im Hinblick auf die Datenanalyse von großer Bedeutung sind. Es ist klar, dass die Untersuchungen auf niedrigere Streuwinkel ausgedehnt werden sollten, in denen Verspannungen und unelastische Streuung eine größere Rolle spielen. Weiterhin ist es von großer Relevanz die zuvor genannten Aspekte der Schadschichten und optischen Mängel auf andere Bildgebende Verfahren auszudehnen. Zusätzlich ist die Untersuchung von Durchfokussierungstechniken zur Strukturrekonstruktion entlang der Transmissions-

richtung eine vielversprechende Verbesserungsmöglichkeit.
Es ist zu erwarten, dass die Verbesserung der Genauigkeit und Robustheit von Techniken zum Zählen von Atomen die Leistungsfähigkeit von (S)TEM erheblich verbessern wird, und Zugang zu der dreidimensionalen Struktur und Komposition ermöglichen wird. Weiterhin ist ersichtlich, dass die Rolle von Hochleistungsrechnungen zum Bildsimulation eine noch größere Rolle in der Zukunft einnehmen wird.

CHAPTER 6

Scientific contributions

The following section lists the scientific contributions of Jürgen Belz. In the first part the main publications that are the basis of this thesis are listed. Subsequently a list of publications directly related to the results presented in chapter 4 is presented. The last section will contain a list of further scientific contributions only partially related to key results of this thesis.

6.1 Main Contributions

6.1.1 Publication 1

Citation

Direct investigation of (sub-) surface preparation artifacts in GaAs based materials by FIB sectioning
J. Belz, A. Beyer, T. Torunski, W. Stolz , K. Volz, Ultramicroscopy **163**, p.19–30, 2016, DOI: 10.1016/j.ultramic.2016.01.001.

Abstract

The introduction of preparation artifacts is almost inevitable when producing samples for (scanning) transmission electron microscopy (**(S)TEM**). These artifacts can be divided in extrinsic artifacts like damage processes and intrinsic artifacts caused by the deviations from the volume strain state in thin elastically strained material systems. The reduction and estimation of those effects is of great importance for the quantitative analysis of (S)TEM images. Thus, optimized ion beam preparation conditions are investigated for high quality samples. Therefore, the surface topology is investigated directly with atomic force microscopy (**AFM**) on the actual TEM samples. Additionally, the sectioning of

Reprinted from *Ultramicroscopy **163**,19–30,2016*, Copyright 2016, with permission from Elsevier.

those samples by a focused ion beam (**FIB**) is used to investigate the damage depth profile directly in the TEM. The AFM measurements show good quantitative agreement of sample height modulation due to strain relaxation to finite elements simulations. Strong indications of (sub-)surface damage by ion beams are observed. Their influence on high angle annular dark-field (**HAADF**) imaging is estimated with focus on thickness determination by absolute intensity methods. Data consolidation of AFM and TEM measurements reveals a 3.5 nm surface amorphization, negligible surface roughness on the scale of angstroms and a sub surface damage profile in the range of up to 8.0 nm in crystalline gallium arsenide (**GaAs**) and GaAs-based ternary alloys. A correction scheme for thickness evaluation of absolute HAADF intensities is proposed and applied for GaAs based materials.

Contributions

Jürgen Belz carried out the FIB preparations, (S)TEM imaging and computer modeling presented. Torsten Torunski realized the AFM measurement. Andreas Beyer and Jürgen Belz designed the experiment focused on the double cross-section technique. Jürgen Belz wrote the manuscript that was reviewed by all authors. Kerstin Volz supervised the research and secured the funding.

Ultramicroscopy 163 (2016) 19–30

Contents lists available at ScienceDirect

Ultramicroscopy

journal homepage: www.elsevier.com/locate/ultramic

Full length article

Direct investigation of (sub-) surface preparation artifacts in GaAs based materials by FIB sectioning

Jürgen Belz, Andreas Beyer, Torsten Torunski, Wolfgang Stolz, Kerstin Volz *

Materials Science Center and Faculty of Physics, Philipps-Universität Marburg, 35032 Marburg, Germany

A R T I C L E I N F O

Article history:
Received 10 July 2015
Received in revised form
27 December 2015
Accepted 23 January 2016
Available online 27 January 2016

Keywords:
HAADF
FIB, AFM
Quantitative STEM
Finite elements analysis
Sample preparation
Novel semiconductors

A B S T R A C T

The introduction of preparation artifacts is almost inevitable when producing samples for (scanning) transmission electron microscopy ((S)TEM). These artifacts can be divided in extrinsic artifacts like damage processes and intrinsic artifacts caused by the deviations from the volume strain state in thin elastically strained material systems. The reduction and estimation of those effects is of great importance for the quantitative analysis of (S)TEM images. Thus, optimized ion beam preparation conditions are investigated for high quality samples. Therefore, the surface topology is investigated directly with atomic force microscopy (AFM) on the actual TEM samples. Additionally, the sectioning of those samples by a focused ion beam (FIB) is used to investigate the damage depth profile directly in the TEM. The AFM measurements show good quantitative agreement of sample height modulation due to strain relaxation to finite elements simulations. Strong indications of (sub-) surface damage by ion beams are observed. Their influence on high angle annular dark field (HAADF) imaging is estimated with focus on thickness determination by absolute intensity methods. Data consolidation of AFM and TEM measurements reveals a 3.5 nm surface amorphization, negligible surface roughness on the scale of angstroms and a sub-surface damage profile in the range of up to 8.0 nm in crystalline gallium arsenide (GaAs) and GaAs-based ternary alloys. A correction scheme for thickness evaluation of absolute HAADF intensities is proposed and applied for GaAs based materials.

© 2016 Elsevier B.V. All rights reserved.

1. Introduction

In the vast field of material sciences aiming for nanoscale resolution transmission electron microscopes (TEM) have been working horses for over 50 years. In particular the investigations of crystalline materials like metals, semiconductors and superconductors have been an ongoing task for TEM. Within the last decade the experimental instrumentation for investigations on the nanoscale down to the atomic scale have been improved enormously. Especially the invention and commercialization of C_s-aberration correction for electron optics mainly used in (scanning) (S)TEM has boosted the accuracy and reliability of experimental data up to a level where atom counting becomes feasible [1].

In parallel, sample preparation techniques have been improved to avoid the inherent damaging process which is (usually) necessary for the investigation of bulk materials in the TEM. The strong electron–matter interaction implies that even with very high energy electrons the sample thickness for quantitative analysis has to be below several hundred nanometers. In the case of high resolution investigations the demands are even higher. In conventional transmission electron microscopy simple structural contrast can only be acquired for crystalline materials up to thicknesses of around 15 nm. Similar demands are valid for high accuracy measurements by high angle annular dark field (HAADF) STEM when atomic resolution is sought [2]. Despite its incoherent nature – providing straight forward structural images [3] – the dynamical scattering as well as the beam divergence have to be taken into account with increasing thickness.

Thus, especially in high resolution investigations of atomic configurations thinning artifacts have to be considered.

Common techniques for the preparation of TEM samples from hard bulk materials are either mechanical grinding, ion beam thinning or most commonly the combination of both approaches.

The effects of energetic ions impinging the target material have been investigated for many years [4–9]. Their surface damage can most likely be recognized as full amorphization of the target material but the dynamics of those ion–matter interactions are known to be of respectable complexity in particular for crystalline materials [10,11]. In contrast to the easily detectable amorphous layers the sub-surface damage and the inclusion of ion beam atoms as dopants can only be investigated with much effort. In the recent years various methods like atomic probe tomography (APT)

* Corresponding author.

http://dx.doi.org/10.1016/j.ultramic.2016.01.001
0304-3991/© 2016 Elsevier B.V. All rights reserved.

[12] and electron holography [13] have been applied to quantify these effects with focus on gallium ion incorporation during focused ion beam (FIB) processing.

Especially for very thin samples the influence of the surfaces becomes increasingly relevant and it is important to consider that a 10 nm sample is almost exclusively consisting of surfaces. The effects of surface damage become increasingly pronounced although the absolute damage is not changed when comparing identical samples with different thicknesses.

A suitable method to investigate the depth profile of a conventional (S)TEM sample is by cross-sectioning it with the FIB [14]. This method has been carried out and applied in various ways and has shown to provide valuable insights. Nevertheless, previous researches aimed at the investigation of gallium incorporation by FIB processing [13] as well as the resulting sidewall damage [8,15] in FIB geometries. In addition argon milled wedge samples were investigated with respect to the shape and geometry by Suess et al. [16].

One aim of this work is the quantitative investigation of surface amorphization and sub-surface damage by low kV argon ions. Therefore we characterize the sample morphology as well as their depth profile. It becomes apparent that the quantitative analysis of complex material systems like semiconductor heterostructures composed of several multinary materials require accurate knowledge about the sample under investigation in order to avoid misinterpretations due to artifacts be they extrinsic by the preparation or (practically) intrinsic like the surface oxidation layers or elastic strain relaxation of thin foils.

Much work in the field of thin film relaxation [17,18] and selective material etching by ion beam bombardment [7,11,15,19] has been carried out. Nevertheless, with improved instrumentation the need for better sample quality becomes obvious especially when information on the (sub-) angstrom scale is sought.

Obviously, the exact sample geometry is of great interest for such ambitious tasks and has to be considered for quantitative investigations. An illustration of various artifacts is shown in Fig. 1. On the left hand side of this illustration a simplified wedge sample model with the semi-angle α is shown. On the right hand side a more realistic model including the microscale geometry with changing thickness and a smooth long range curvature is shown. Further large scale effects are microscopic scratches, ion shadowing effects and selective etching of different compounds. The nano- and atomicscale roughness due to the stochastical thinning process, amorphous damage and oxide layers and redeposition of sputtered material is affecting the whole sample whereas for example elastic strain relaxation with its effect on the crystalline zone axis [20,21] and the bulging out into the vacuum at the surface have a more localized nature. For a high precision measurement of atomic compositions those effects have to be measured or estimated and if needed incorporated into modeling for computer simulations.

Aiming for the characterization of those artifacts the quaternary material (GaIn)(NAs) and its ternary constituents (GaIn)As and Ga(NAs) provide suitable complexity and thus provide access to most of aforementioned effects. The investigation of those materials is furthermore of great interest in the development of high efficiency multi junction solar cells [22] and infrared laser diodes [23].

These material systems are studied as multilayer quantum well structures alternating with pure gallium arsenide (GaAs) layers on GaAs substrates epitaxially grown by metal organic vapor phase epitaxy (MOVPE) [24]. The material system is considered to be coherently strained which was verified by high resolution x-ray diffraction (HRXRD) beforehand. Despite the high quality of those layers compositional inhomogeneities are possible due to the extreme non-equilibrium growth conditions applied and are topic of current research [25,26].

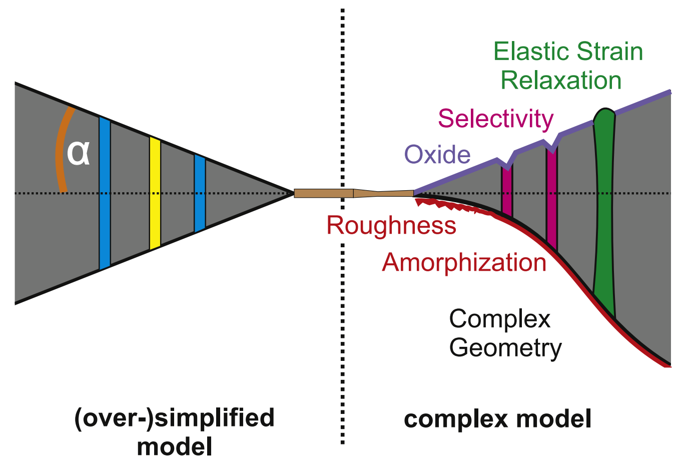

Fig. 1. Illustration of the difference between an (over-) simplified model (left) and a more complex geometry (right) of a wedge shaped cross-section TEM sample.

Due to the great effect of dilute amounts of nitrogen on (GaIn) As the material properties of this system are distinctly different from the barrier material GaAs [27]. Furthermore, the amount of different elements in this compound adds to the complexity of ion beam etching [19,28]. Additionally, the overall material hardness is significantly increased by the incorporation of nitrogen atoms in the ternary compound [29].

The difference in etching rates is known for inappropriate thinning conditions but it is assumed to be severely reduced for low angle and low energy milling as indirectly investigated in the TEM [30].

In contrast to this indirect method a direct approach by utilizing the atomic force microscope (AFM), focused ion beam (FIB) and TEM techniques is used in the present work. The AFM provides valuable information about the sample surface quality as well as the elastic strain relaxation [31,32] but the material below the very surface is not accessible. Therefore, the double cross-section method [14] of ion beam sectioning actual TEM samples is employed. This method allows for the investigation of (sub-) surface artifacts like deep ion beam damage which was caused – in our case – by the argon ions. This is achieved by preparing a high quality FIB lamella from a very thin region of the TEM sample which directly represents the cross-section of the TEM depth profile.

2. Methods

In order to directly investigate the intrinsic and extrinsic artifacts of thin TEM samples several steps have to be employed.

Firstly, conventional TEM wedge samples of good quality are produced and measured in the AFM. Secondly, the FIB lamella from the sample cross-section has to be prepared and finally investigated in the TEM.

Therefore, this section is divided into three parts describing the steps of investigation in chronological order.

Furthermore, we decided to omit an “in-between” investigation of the samples in order to avoid additional (high energy) electron beam damage and contamination of the sample surfaces.

2.1. Conventional sample preparation

In order to distinguish the geometric effect of strain relaxation from material properties, samples containing epitaxial quantum well (QW) structures of different composition have been grown by

MOVPE. By doing so, lattice matching as well as straining of the quantum wells could be achieved.

The strained multi quantum well (MQW) sample consists of 8 nm thick $(GaIn_x)(N_yAs)$ layers with $x=30\%$ and $y=1.5\%$ whereas a lattice matched (LM) sample was grown with $x=8.0\%$ and $y=2.9\%$. Growth details can be found elsewhere [24].

The lattice matching was assured by carrying out $\omega/2\vartheta$- scans around the (004) reflection of GaAs by HRXRD.

The TEM samples were prepared in standard cross-section geometry with two pieces of the wafer glued face-to-face on each other applying modest pressure in order to guarantee glue lines usually in the order of several hundred nanometers. Small pieces of these sandwiches were put into titanium support rings, and ground to a final thickness of about 50 μm. In each grinding step the grain size was successively reduced and a thickness of at least three times the grain size of the previous step was removed in order to guarantee the full removal of prior damage layers. The plan parallel samples were thinned down to approximately 10–20 μm final thickness by double side dimple grinding. The final polishing step was carried out using 0.25 μm diamond polishing compound. Light microscopy was used to ascertain the absence of scratches around the center region. The low thickness ensures a fast ion beam milling under low angles and with low initial energies.

Traditional double sector milling was carried out in the PIPS System (GATAN Inc.) by argon ions with energies ranging from 3.0 kV to 1.7 kV. Initially the argon ion guns were aligned to match the height of the sample and adjusted to be centered as well as possible. It is noteworthy, that the final polishing with 1.7 kV is not the state-of-the-art but was long considered to be “good enough” in the pre-aberration correction era and was chosen therefore.

The broad argon ion beam with an ion flux full width at half magnitude (FWHM) of no better than 650 μm hits the center of the sample under an angle of incidence of nominally $\pm 3^{\circ}$ which is expected to produce wedge shaped samples with a wedge semi-angle of about this value and a center hole of several micrometers in diameter. The final polishing steps were carried out under a slight increase of angle in order to optimize the sputtering yield of low kV (down to 1.7 kV) argon ions. Despite the ion current readout of the PIPS system (0–1 μA) visual inspection with a fluorescence screen in a dark room shows a noticeable ion flux under appropriate pressure conditions.

This optimization was aided by empirically fitting the ion flux to a suitable model curve and extrapolation of the total beam current and beam width. Furthermore, sputtering rate estimations were carried out for GaAs with the Monte Carlo simulation “Stopping and Range of Ions in Matter” (SRIM) [28].

In addition to this optimized preparation a significantly faster ion milling set up was used for comparison. The angle of ion incidence was set to $\pm 6^{\circ}$ and the ion energy was set to 4.5 keV.

It is expected that this kind of preparation will induce significant preferential thinning resulting in a bad sample quality.

2.2. Surface investigation of TEM samples

After these initial preparation steps the actual measurements were carried out in two steps:

For the direct investigation of the sample surface height profiles in the vicinity of the central hole of the TEM sample were acquired by AFM (Digital Instruments NanoScope IIIa Scanning Probe Microscope) in intermittent contact mode (“tapping mode”) thus reducing the probability of destroying the thin TEM samples.

For the investigation and comparison of elastic strain relaxation computer simulations are employed in order to account for the complex geometry. In the present work the numerical relaxation of suitable geometric models by means of finite elements (FE) analysis is used. The sample geometry was therefore modeled and relaxed within the COMSOL Multiphysics® suite.

The FE relaxation is based on the concept of “Vegards Rule” - which describes a linear interpolation of material properties like the lattice parameter from a mixture of binary materials - and the solution of the continuum linear elastic theory which provides comfortable access to large scale displacements as well as the local strain state. The lattice mismatch of the composition dependent virtual crystal (GaIn)(NAs) to GaAs is used to apply hydrostatic pressure on the MQW layers. The TEM sample is then modeled by applying periodic boundary conditions in the foil plane and neglecting the actual wedge shape for the FE simulation, due to the shallow wedge semi-angle of about 3°. A more pronounced wedge shape would presumably cause a slight asymmetric strain relaxation.

2.3. Cross-section profiles from TEM samples

The second step after the plain surface investigation is the direct observation of e.g. the (sub-) surface damage introduced by ion beam bombardment.

The samples were sectioned with a dual column FIB (JEOL JIB-4601F) in order to create cross-sections from the actual TEM samples.

In order to protect the top surface from damage by the gallium ions an in-situ protective coating is applied to regions of interest (ROI) near the center hole by electron beam induced decomposition of a metal organic tungsten precursor gas [33]. This protective step is carried out in-situ by the scanning electron microscope (SEM) which is furthermore essential for feedback and alignment of the sample for FIB processing. In the following this protection layer will be referred to as “e-tungsten”. Additionally, an initial protective ex-situ layer by sputter coating might be considered. Nevertheless, the adhesion to the glue line might be problematic.

Fig. 2a shows a SEM image whose perspective of 0° with respect to the surface normal is similar to a low magnification TEM image. Around the center hole of this TEM sample two protective layers of about 20 μm × 2 μm lateral dimension and several hundred nanometer thickness are located at the upper and lower apex of the elliptically shaped hole. The large rectangle areas show charging effects and carbon contamination induced by the SEM.

The thickness of the initial protection layer was chosen such that damage from the subsequent rapid deposition of several microns of protective coating by gallium ion assisted decomposition of a carbon (“Ga-carbon”) and a tungsten precursor gas (“Ga-tungsten”) is unlikely. The low magnification SEM image in Fig. 2b shows the process of coating with assistance of gallium ions which has to be carried out under a sample tilt of 53° with respect to the electron optic. The wafer sandwich with its titanium support ring as well as the gas injection system on the left hand side is clearly visible. On the right hand side the micro-manipulator needle can be seen. It is later used in the lift-out process which is shown in Fig. 2c. The protective coating of several microns mainly consisting of metallic tungsten shows bright contrast on top of the greyish wafer material.

Prior to the lift-out most of the perimeter around the ROI is removed by gallium ion milling. After soldering the almost freestanding lamella to a manipulator needle the remaining connection to the PIPS sample is removed.

The lamella is lifted out (Fig. 2c) and carefully transferred to a TEM compatible copper grid. Fig. 2d shows the freestanding cross-section profile lamella which was soldered to the grid and after the removal of the manipulator needle. The connection between both wafer sides is provided by the protective coating and the epoxy.

Roughly following the “wedge pre-milling” procedure suggested by Schaffer et al. [34] and employing an early decrease in

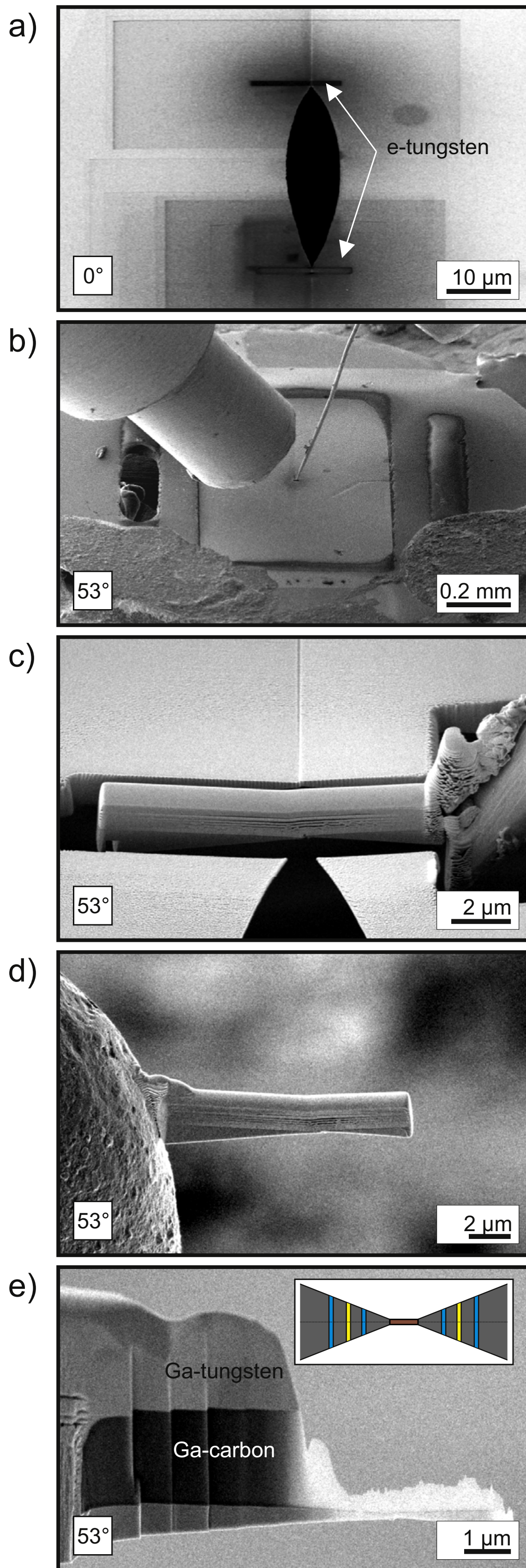

Fig. 2. (a) SEM image of the TEM sample after e-tungsten deposition for protective coating prior to further (rapid) gallium assisted deposition of several microns of carbon and tungsten. (b) A low magnification side view SEM image taken during the deposition of such layers. (c) The TEM cross-section sample is shown prior to the lift-out process. The bright tungsten protective layer on top of the wedge sample is connected to the lift-out manipulator. After transfer and fixation to a copper grid the lamella is separated from the manipulator needle (d) and can be thinned to electron transparency by increasingly gentle ion milling. (e) Finally, the protective coatings consisting of Ga-carbon (black) followed by Ga-tungsten (bright) are revealed. The initial e-tungsten deposition cannot be seen at this scale.

ion energy down to 1.0 keV produces suitably thin lamellas of good quality for (S)TEM investigations. The final lamella is shown in Fig. 2e where the different layers of protective coating can be seen. In between the topmost tungsten layer and the bottom wafer material the dark carbon layer becomes visible. It is mainly used for rapid growth of thick protection layers and additionally provides suitably thin amorphous regions for the alignment of the aberration corrector which is a great use for (S)TEM investigations. With a final thickness of only a few nanometers the SEM contrast is reversed and all materials show strong bright contrast (nearly independent of the material).The inset illustrates the sample geometry presented in the introduction.

The sample thickness in transmission and the lateral geometry were taken from quantitative comparison of absolute STEM-HAADF intensities to multi-slice simulations [35]. This approach is frequently used in high resolution work [36–41].

For the STEM investigation of the lamellas a C_s corrected STEM (JEOL JEM-2200FS) is used in ADF imaging mode with different detection ranges ("camera lengths"). The standard ADF inner detector angle which is used – unless stated otherwise – is 73 milliradians (mrad). This high angle ADF imaging condition is considered to predominantly reflect the atomic species because of the high Z-dependence of the Rutherford-like scattering mechanism (Z-contrast) [3].

Despite this dominant contrast mechanism some minor yet important amendments have to be considered. The first is the "Huang-like" scattering due to disorder which generally increases the low to mid-range scatter contribution. The second mechanism is usually called de-channeling and is commonly observed in low order zone axis STEM-ADF images of (crystalline) strained multilayer structures. Due to the column bending the channeling condition along atomic columns is disturbed and thus lower HAADF intensity is observable. Both processes are somewhat complementary due to their different effect on the intensity distribution over the scattering angle [42].

3. Results

In the following the results from the aforementioned surface investigations of the heterostructure with the quaternary (GaIn)(NAs) MQW system will be laid out. Furthermore, the results of the cross-section of a heterostructure containing alternating layers of Ga(NAs)/GaAs/(GaIn)As will be shown. The focus will be set on the evaluation of the binary compound semiconductor GaAs. In addition, the damage depth profile of its two ternaries will be shown.

3.1. Surface damage and preparation

In Fig. 3a the AFM measurement of a TEM sample using the fast ion milling set up ($\alpha = \pm 6°$, $E = 4.5$ keV) with a single lattice matched (GaIn)(NAs) QW is shown. The AFM scan was carried out over $(2\ \mu m)^2$ and a standard two dimensional linear background subtraction was applied. At the very left side the amorphous epoxy shows strong height modulation and is thus overlaid (black rectangle) for better visualization. To its right a line of increased height can be seen which is parallel to the glue line and resembles the single QW. This elevation of several nanometers is a result of inappropriate thinning conditions which can be easily seen from direct comparison with Fig. 3b.

Therein an AFM area scan of a twin sample prepared under optimized thinning conditions is shown. A tremendous increase in surface quality was achieved and there are no surface features of noteworthy magnitude. In particular, there is hardly any height abnormality along the QW its position is judged from the distance

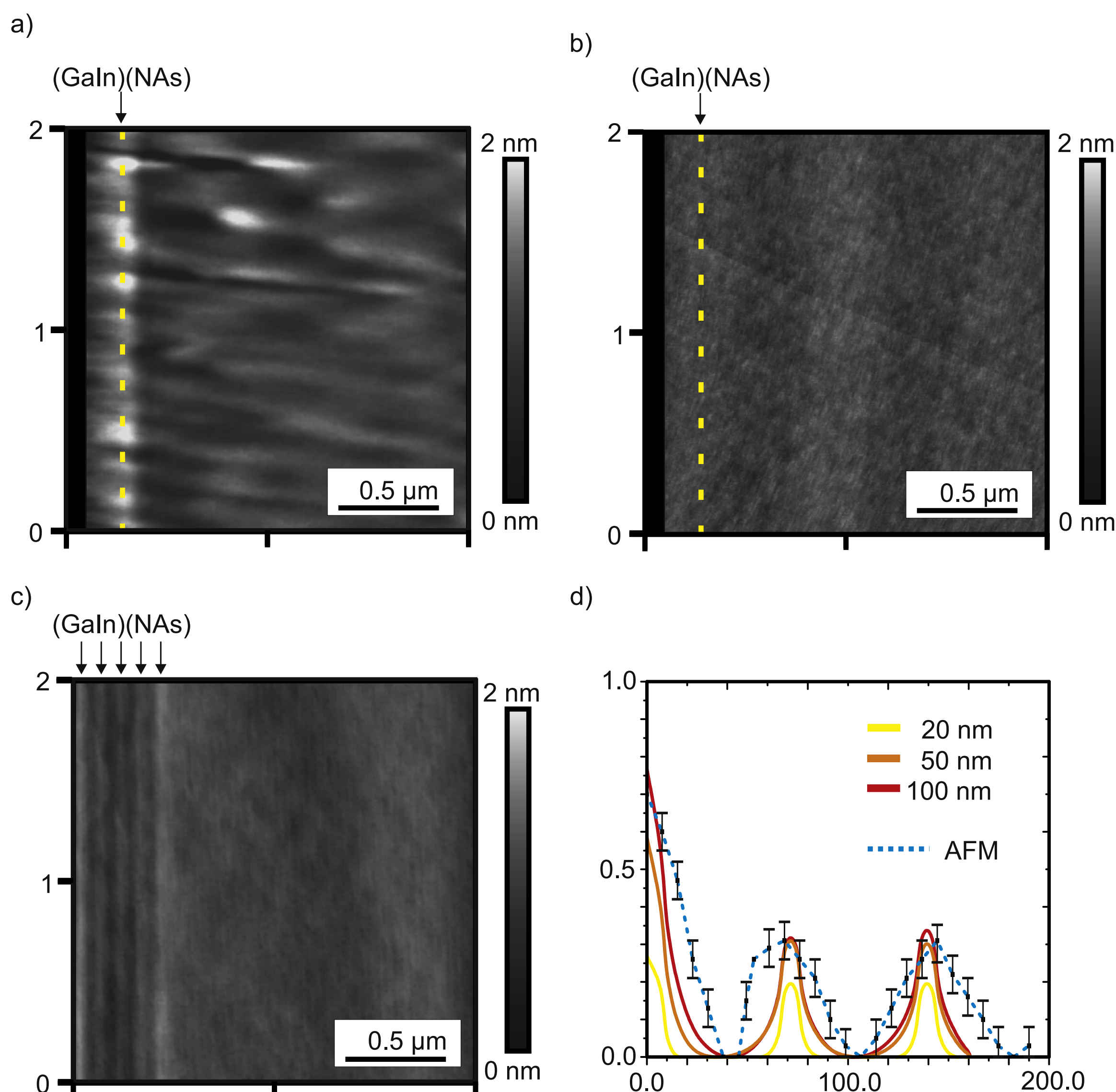

Fig. 3. AFM measurements show that (a) inappropriate preparation conditions lead to a pronounced visibility of a lattice matched GaIn)(NAs) QW due to selective etching of GaAs. (b) Optimized conditions result in nearly atomically flat surfaces without height differences between the lattice-matched QW and the surrounding material. (c) Applying the optimized preparation to a strained MQW system shows surface height features only as a result of elastic strain relaxation. (d) The bulging out is in excellent agreement with FE simulations approaching the thick sample limit.

to the epoxy and indicated by a yellow dash-dotted guide to eye. This absence of surface features actually identifying the quantum well region is an indication of a homogenous oxidation layer of GaAs and (GaIn)(NAs) which was experimentally verified for the (GaIn)As/GaAs system [32].

Fig. 3c shows the AFM measurement of a strained MQW sample which was prepared under aforementioned optimized conditions. The height profile of the five MQWs can be seen clearly. In this case the height profile directly reflects the elastic strain relaxation at free surfaces. This is illustrated in Fig. 3d. The plot shows the comparison of the AFM measurement with results from FE simulations. The AFM measurement represents the average height profile parallel to the glue line of the region between the epoxy and the fourth strained QW (excluded). Additionally, the corresponding simulated height profiles for three different sample thicknesses are added. The error bars indicate the measured root mean square (RMS) roughness of the surface which is about 0.1 nm and nearly constant over the whole scan area of Fig. 3c.

Considering the lateral resolution of the AFM the simulation and the measurement are in excellent agreement (cf. Fig. 3d) thus proving the validity of the assumed mixture model and the suitability of the thinning procedure. It is noteworthy that an increased bulging out at the uncapped top QW can be seen in both the experiment and the simulation.

The thickness dependent bulging out of the strained quantum well region rapidly converges to the infinite thickness limit and is in good agreement with the AFM data over a rather large thickness range.

These results of the surface investigation show that the sample quality is excellent over a large sample area. The small RMS roughness indicates – within the lateral precision of the AFM – nearly atomic flatness and could be fully attributed to the oxidation layer which is expected to be amorphous and thus not necessarily atomically flat.

With AFM being a surface sensitive technique of limited lateral precision the damage cannot be fully characterized. Additionally, everything below the very surface is not accessible with this technique.

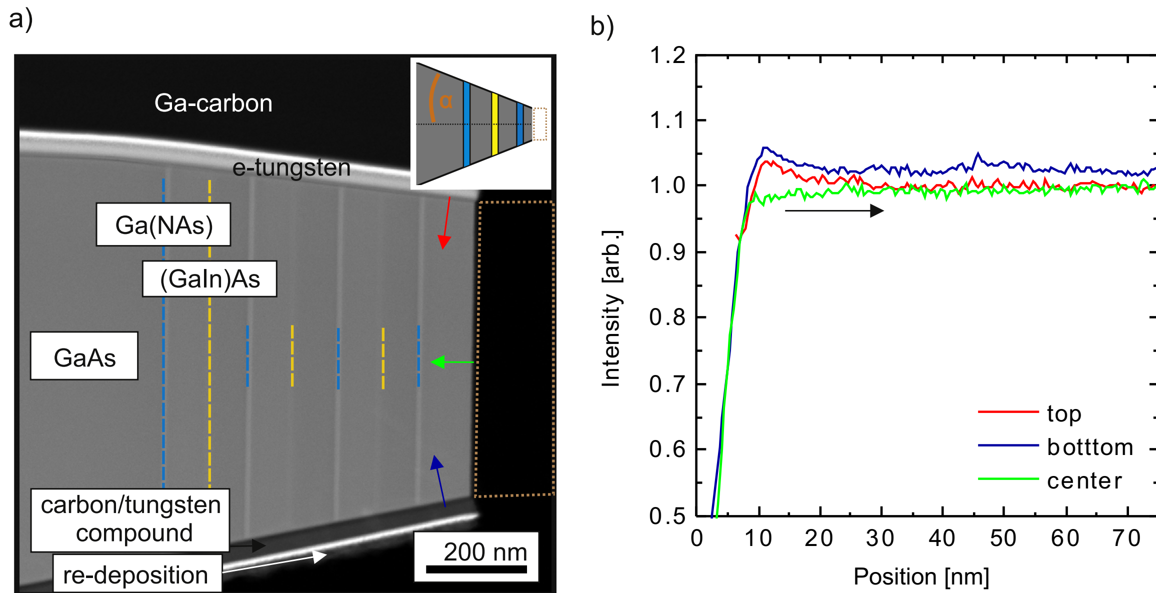

Fig. 4. The low magnification HAADF image shows the left side of a double wedge sample illustrated in the inset. The sample contains alternating ternary alloy QWs on GaAs seperated by GaAs barriers. (a) The normalized GaAs intensity of three different regions marked with colored arrows in Fig. 4a shows a significant rise near the initial surfaces. This is in contrast to the center profile where no rise in intensity is observerable. (For interpretation of the references to color in this figure, the reader is referred to the web version of this article.)

3.2. (Sub-) Surface damage in GaAs

In order to characterize the (sub-) surface sample quality after broad argon ion beam thinning which would usually be hidden in traditional transmission geometries, the cross-sectional FIB sample of an alternating (GaIn)As/GaAs/Ga(NAs) structure is investigated with ADF-STEM. Fig. 4a shows a low magnification HAADF image of the left sample wedge shown in Fig. 2e. For illustration purposes the initial epoxy area is overlaid by a brown rectangle and an inset is shown to clarify the sample geometry of the sample under investigation.

In the upper part of Fig. 4a the fully intact e-tungsten and Ga-carbon depositions can be seen. It is noteworthy, that the initially applied e-tungsten deposition was considerably thicker when measured in the SEM/FIB. We assume that this is due to the dynamic etching and growth process during gallium assisted coating. On the bottom side a much thinner Ga-carbon and a Ga-tungsten layer can be seen. These layers are probably deposited by transmitted electrons in the SEM/FIB that reach the backside of the TEM sample - despite the fact that the initial gallium ions are completely stopped in the protective layers - where the surrounding precursor gas can be decomposed. Owing to the thickness of the sample this process is less likely than the decomposition at the top surface. This explains the absence of a distinct e-tungsten layer at the bottom surface. However, this is unproblematic because these layers were always protected from the ion beam due to its direction heading from top to bottom. Energy dispersive x-ray spectroscopy (EDS) shows that the dark gray “gap” region on top of the bottom surface (cf. Fig. 4a) is carbon and tungsten containing without any significant gallium signal. It is followed by a tungsten layer which forms after the initial contact compound (carbon-rich) was created. The arrangement indicates the re-deposition of material during the lamella thinning on top of this carbon/tungsten.

As a guide to the eye the (GaIn)As quantum well and the Ga(NAs) are emphasized by blue and yellow dot-dashed lines respectively. At the former top and bottom sample surfaces a faint bright contrast can be seen which is absent at the initial wafer surface (right hand side, center region) that was covered by the epoxy glue line (400 nm) during the conventional broad beam thinning.

Fig. 4b shows line profiles averaged (width of about 10 nm) along the three sample surfaces which are normalized to the intensity plateau in the core regions of the sample. The direction and color corresponds to the regions indicated by arrows in Fig. 4a. It can be clearly seen from the red and blue profile that at both surfaces hit by argon ions a significant increase of the (normalized) HAADF intensity occurs. This effect is not seen for the scan along the untreated (wafer) surface.

Despite the minor deviation presumably originating from slightly different thicknesses the relative increase of the intensity at both surfaces is about 4%. This is in strong contrast to the slight decrease near the center (wafer) surface which was protected by the epoxy during argon ion milling (PIPS).

Due to the coarse sampling of low magnification STEM images smaller areas have to be investigated for quantitative evaluation to improve the contrast localization in each pixel avoiding severe under-sampling. Additionally, the focus of the subsequent study will be set on the top surface because of its similarity to the lower surface (see Fig. 4) which indicates that there are no severe artifacts introduced by FIB preparation and that the in-situ e-tungsten deposition was indeed sufficient. On the contrary, the effect of an insufficient deposition can be seen in Fig. 5. In this conventional HRTEM micrograph the stopping power of the e-tungsten layer was too little and therefore caused severe damage to the top side of a similar sample clearly showing full amorphization of that area with subsequent partial amorphization of the sample.

Nevertheless, there is certainly also damage introduced by the gallium ions during FIB processing of well protected samples. However, this will very likely only be nearly homogeneous sidewall damage across the whole lamella. A minor thickness gradient which is almost inevitable is also expected.

Fig. 6a exemplarily shows the top surface of Fig. 4a (red arrow) at higher magnification. The dotted lines guide the eye to the onset of crystallinity (black) and the epoxy glue line (brown).

The horizontal direction (white arrow) crosses the epoxy coated (wafer) surface. This epoxy layer presumably prevents argon ions from hitting the sample thus it is considered to be a

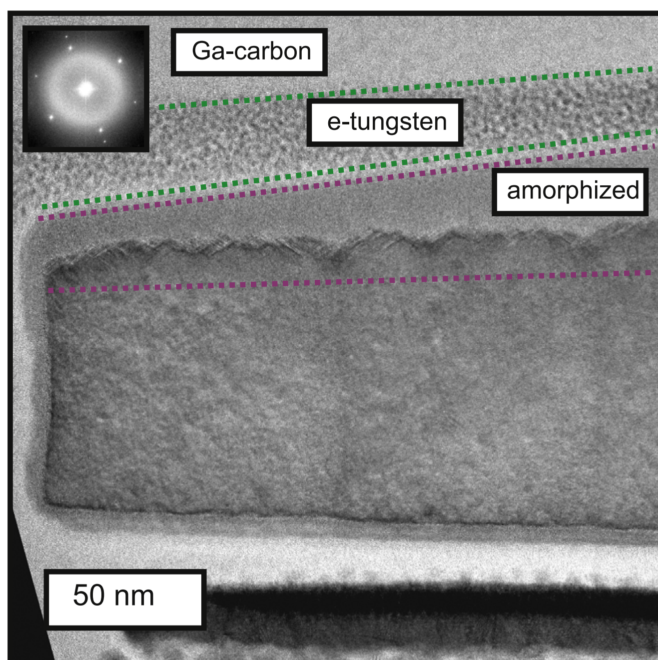

Fig. 5. The HRTEM micrograph of a different sample shows the effect of high energy (30 keV) Ga ions impinging on the sample with insufficient coating during the ion beam assisted deposition. The thin (residual) e-tungsten layer (dotted, green) did not fully stop the incoming gallium ions which caused full material amorphization of the top surface. The gallium ions were finally stopped in the samples causing severe damage to the crystalline regions (dotted, purple). (For interpretation of the references to color in this figure legend, the reader is referred to the web version of this article.)

protected surface. In contrast, the surface opposed to the argon ion guns during the conventional preparation is considered to be damaged.

In order to acquire information on the (native) oxidation layer the protected interface was investigated in more detail.

In Fig. 6b a HAADF image of the protected interface is shown. A rather unsharp transition from amorphous to crystalline can be observed which can be fully attributed to the amorphous GaAs-Oxide [43].

An averaged line profile towards this interface is shown in Fig. 6c. Therein the origin of the x-axis is set to the onset of atomic column contrast for better comparability. It is noteworthy that this position is not the GaAs intensity plateau of the bulk several nanometers from the surfaces. This is presumably due to the intermixing layers of the crystalline GaAs phase (c-GaAs) and the amorphous oxide layer (a-GaAs-ox). Further towards the epoxy the run of the curve is less steep for about 2 nm and falls rapidly to the epoxy level at about -4 nm.

The intensity behavior can be explained in terms of intermixing of different rough layers. First, there is the c-GaAs/(a-GaAs-ox) intermixing which leads to the onset of dumbbell contrast at 0 nm and the biased plateau to the right. The second steep slope resembles the intermixing of the rough (a-GaAs-ox) and the epoxy material. Overall, judging from the inflection points of aforementioned slopes the amorphous oxide spreads over about 3.5 nm. This value is in good agreement with conventional TEM measurements of this sample (Fig. 7b) and in fair agreement with the thickness of the native passivation oxide of the wafer material [44].

Additionally, the crystalline material shows a small decrease in intensity over a range of about 5 nm which can be also seen in Fig. 4b.

For clarification of this ambiguity a series of STEM images with different camera lengths has been acquired. The results for the protected surface shown in Fig. 8a indicate a slight decrease in intensity for large detector inner angles (99 and 73 mrad) and an increase for mid and low angle detection ranges.

This might indicate a strain driven effect which is mentioned e.g. for the a-Si/c-Si interface by Yu et al. [45].

In contrast, the normalized intensity curve of the damaged surface (cf. Fig. 8b) shows a tremendous increase in intensity for all scattering angles. It can be seen that the effect has a lateral extension of about 8 nm which is similar for all but the highest detection angle. The intensity increase ranges from about 2.5% at 99 mrad to 15% for 33 mrad and decreases to the core plateau nearly linearly.

The absence of contrast reversals indicates a static disorder which points to deep damage by argon ions and the creation of lattice imperfections due to those damage cascades.

3.3. *(Sub-) Surface Damage in ternary material systems*

In the following the quantification of the damage induced contrast is extended to the ternary material systems (GaIn)As and Ga(NAs). For the sake of illustration the collage of two ADF images of each ternary QW and the separating barrier shown in Fig. 9a is rotated by 90° with respect to the former images. Additionally, the ADF inner angle is chosen to 52 mrad revealing the “cloudiness” of the damage layer. Fig. 9b–d show line scans through the quantum well layers and the separating GaAs barrier.

The GaAs barrier shows the strongest relative increase in intensity (cf. Fig. 9c) compared to the other material systems (cf. Fig. 9b and d). Furthermore, the effect has a significantly longer range for GaAs (8.0 nm) than for Ga(NAs) (5.5 nm) and (GaIn)As (6.0 nm) . Despite the obvious measurement uncertainties a significant decrease in ion straggle range can thus be assumed for the ternary alloys. The relative intensity increase is much smaller for the alloy systems which can be seen for any camera length in direct comparison. The overall trend with respect to scattering angles is the same for all material systems except for 99 mrad detection angle. For this angle a significant increase can be seen only for pure GaAs.

Additionally, there are no signs of elastic strain relaxation like (obvious) lattice plane bending or bulging out on the surface. The former can be explained by the STEM imaging mode which is in fact a time series with a lateral precision dependent on the scan unit. Thus, fine lateral displacements (in the picometer regime) are extremely hard to quantify with scanning TEM. This is also the case for the bulging-out effect of strained QWs at surfaces. Furthermore, this effect is at maximum in the range of a few hundred picometers for thin samples as can be seen in Fig. 2d where the average height profile of an AFM measurement is shown.

The overall surface roughness of about 100 pm (taken from AFM) additionally applies a strong hindrance for the direct imaging of these bending effects.

It has been shown that the damage effect and the oxide have a considerable effect on the mean intensity with respect to the absolute GaAs bulk value. Furthermore, it should be noted that additionally the atomic arrangement and the composition in these damaged regions are presumably severely altered and thus atomic compositional evaluation on an absolute scale might be hindered. Thus it can be concluded that the alteration of the damaged surfaces might influence many if not every high resolution investigations. Especially for thin samples the ratio of (damaged) surface areas to the undisturbed volume-material is drastically increased which results in a pronounced impact of aforementioned damage layers.

Exemplary, influences on the HAADF thickness measurement of GaAs will be investigated.

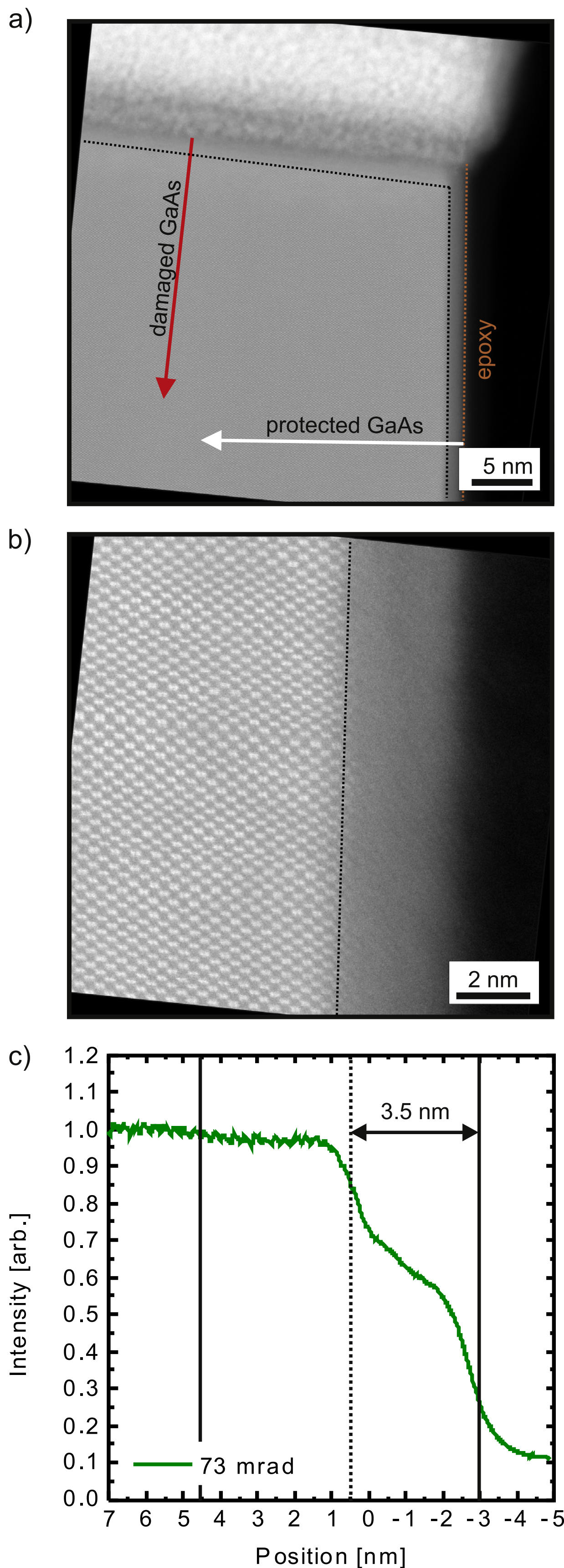

Fig. 6. The HAADF image of the upper surface near the epoxy shows two distinctly different types of surfaces namely a protected GaAs profile and a damaged surface. Dotted lines are added to guide the eye to the onset of crystallinity (black) and the onset of the epoxy glue line (brown). (a) The protected surface at a higher magnification shows a fading atomic column contrast near the amorphous/crystalline interface. (b) The normalized HAADF intensity over the position relative to the onset of atomic contrast shows a steady decrease with several stages due to layer intermixing of the c-GaAs and a-GaAs-ox as well as the a-GaAs-ox and the epoxy. (For interpretation of the references to color in this figure legend, the reader is referred to the web version of this article.)

3.4. Effect on thickness measurements

Assuming the case of a crystalline phase with a passivation oxide thickness measurements can give significantly different results depending on the method employed and the surface-to-volume ratio.

Measurements based on crystalline signals more or less ignore the amorphous oxides whereas e.g. electron energy loss spectroscopy (EELS) measurements account for the total transmitted volume. As stated in Beyer et al. [46] the thickness values derived from through-focal HAADF-STEM are systematically lower than those derived by EELS which presumably reflects this trend. Thus, for the estimation of thickness from mean HAADF intensities two main effects have to be considered. First, the finite thickness of the native oxide layer and second, the extension of the surface- as well as the deep damage.

In order to quantify these effects we first consider the impact of an oxide layer on the mean intensity in the conventional STEM-ADF setup. Therefore, we measure the intensity profile towards the GaAs surfaces which can be translated into the total ADF intensity of usual ADF-measurements. In the case of perfect c-GaAs the thickness can be related to the total collected intensity (considering the full beam propagation in the sample and the detection system as well as the beam current). On the other hand, the interpretation of this mean intensity ignores any a-GaAs or an a-GaAs-oxide (presumably a-Ga_2O_3). From simulation studies it can be seen, that a fully disordered a-GaAs does not scatter as strongly as c-GaAs into high angles presumably due to the missing channeling effect. Furthermore, the oxide is much more complex due to its low-Z component and the different density in addition to its amorphous state. Hence, a realistic simulation study is hard to carry out. Instead the intensity profile of the presented double-cross sections can be used to derive the necessary data.

From the integration towards the protected surface (cf. Fig. 6b) the intensity of the pure oxide layer can be determined and this intensity can be recalculated in a c-GaAs intensity equivalent.

This excess intensity with respect to the pure c-GaAs phase would result in a correction of the TEM sample thickness (usual transmission geometry) of about 2×2.1 nm (each surface) whereas the real physical thickness of the oxide is about 7.0 nm (2×3.5 nm). Therefore, the sample thickness would be underestimated by a constant thickness of about 2.8 nm if the surface damage was completely neglected.

It is noteworthy, that in addition to this a thickness measurement by position averaged convergent electron beam diffraction would presumably provide only the c-GaAs thickness.

When considering the line profile towards the c-GaAs/a-GaAs-ox interface (cf. Fig. 6c) the drop of intensity might be attributed to a strain driven de-channeling [20,42]. In this case the asymmetric loss of intensity would not contribute to the mean intensity in the conventional sample geometry. This might be illustrated in terms of shear stress which causes a local tilt from the STEM optic axis in

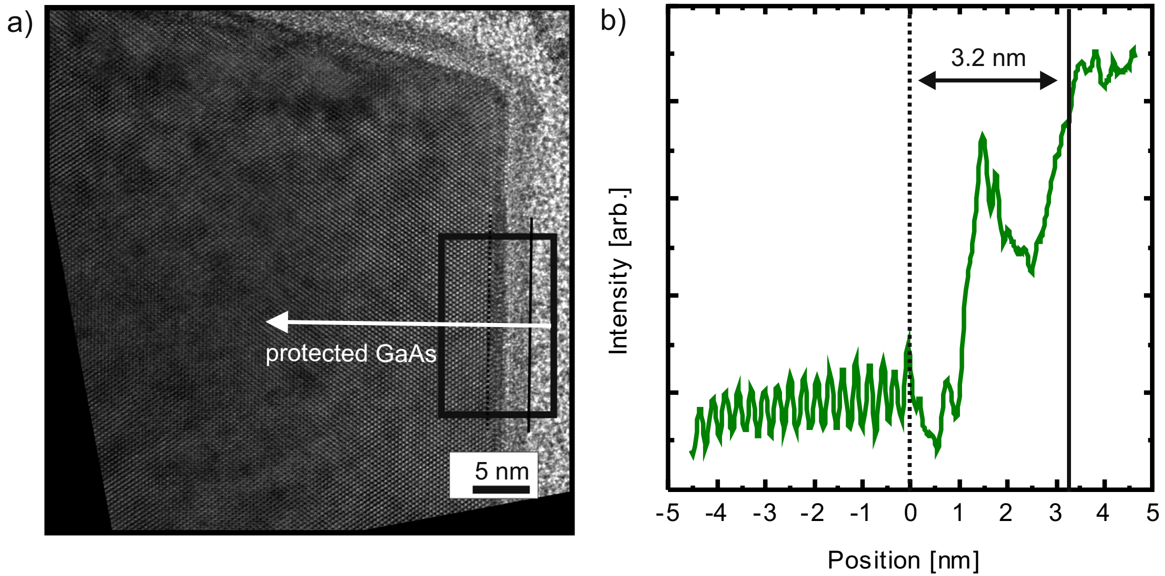

Fig. 7. (a) The HRTEM micrograph of the protected GaAs surface shows good agreement with the ADF-STEM observations indicating an interconnection between the pure crystal and the oxide. (b) The line profile along the interface reveals an approximately 3.2 nm thick oxidation layer.

thin TEM foils. This shear component would be absent in the normal transmission setup except for the edges of the material under investigation. Additionally, the systematic error would be almost negligible compared to ignoring the oxide.

Finally, the excess intensity caused by the ion beam damage is an additional source of error.

Comparing the first 3.5 nm of the protected and the damaged surface (cf. Fig. 6a) reveals a significant difference. Whereas the excess intensity (from the oxide) equals to about 2.1 nm c-GaAs intensity for the protected surface the excess intensity of the damaged surface equals to 3.3 nm c-GaAs. Hence, these layers are mainly heavily disordered GaAs with some contributions from an oxide layer.

In general, the cumulative effect of damage and oxide has a TEM specimen thickness dependence due to the overlap of damaged regions of constant thickness and the changing TEM specimen thickness. Hence, an error estimation has to be made for every given thickness. With decreasing physical sample thickness the constant thickness damage/oxide layer becomes increasingly relevant which leads to huge relative errors when using mean HAADF intensities for thickness evaluations.

For example, a measured intensity equal to 10 nm would be wrong by +10% giving a (damage) corrected thickness of about 9 nm. Additionally, the c-GaAs volume would just be about 3 nm due to the a-GaAs layer. These estimates of course change when HAADF imaging is not performed at “standard” angles but at lower detector inner angles, where the contrast is more sensitive to static atomic displacements.

4. Discussion

The increase of HAADF intensity close to TEM specimen surfaces is attributed to the argon ion beam damage of the surfaces during conventional broad ion beam sample thinning. The contrast mechanism proposed is the local static atomic displacement [47]

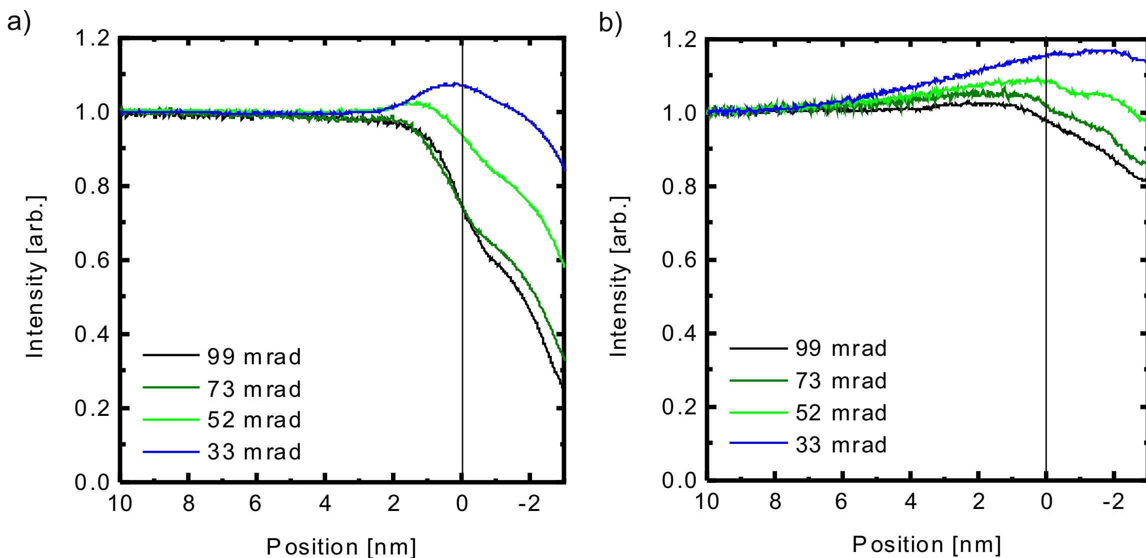

Fig. 8. (a) The normalized HAADF intensity of the protected intensity over the position is plotted for different detection (inner-) angles. An angle dependant contrast is observable between the high angle regime and the mid angle regime. (b) The normalized HAADF intesity of the damaged intensity over the position is plotted for different detection (inner-) angles. The curve shows significant deviations from the line profile along the unprotected surface without contrast reversals near the interface.

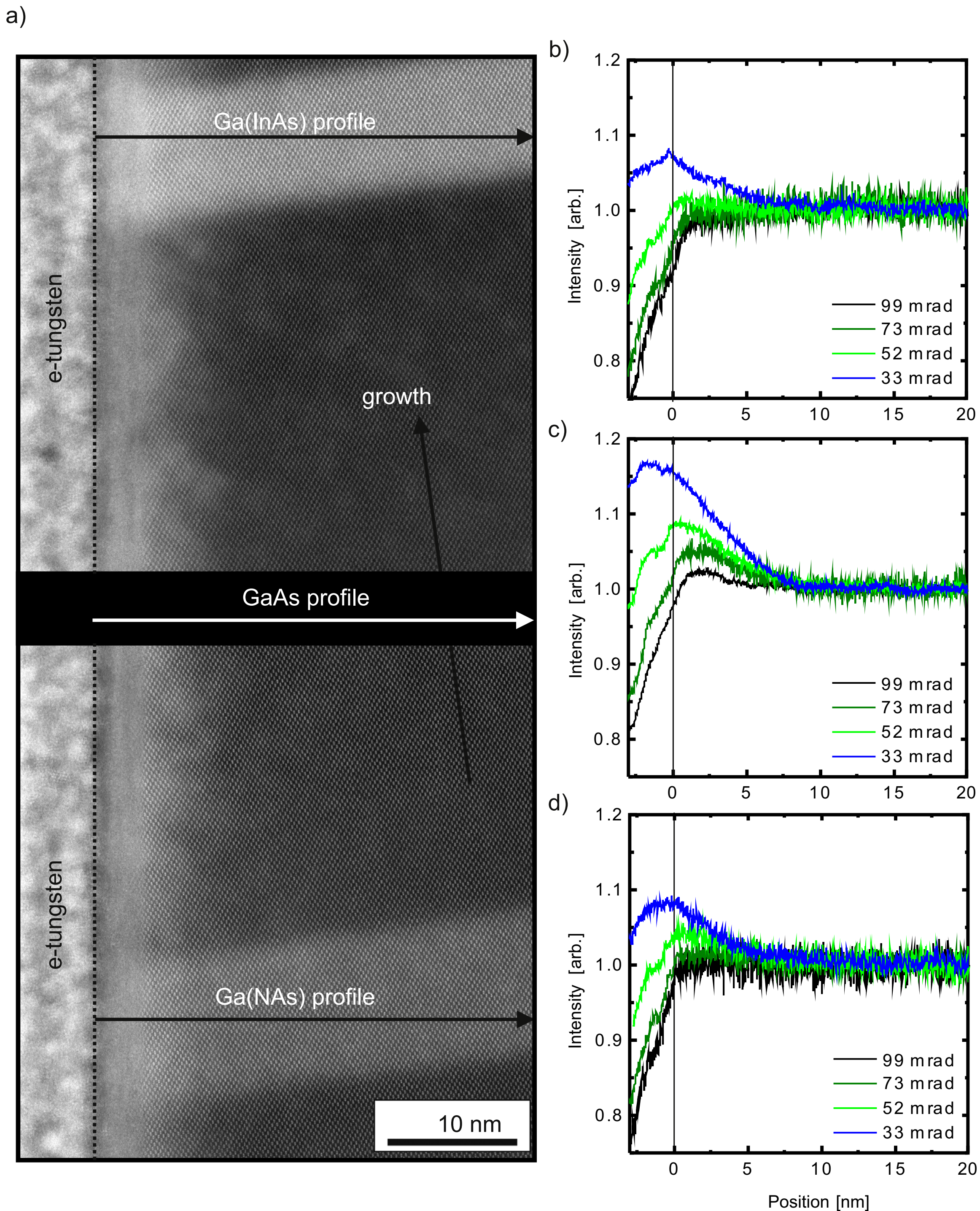

Fig. 9. (a) A collage from two mid angle STEM images shows the GaAs barrier separating two different ternary compound QWs. The arrows indicate line scans towards the surface into the volume material. The cloudy contrast near the surface can be readily seen. (b)–(d) The normalized HAADF intensity of the damage depth profiles over the position is plotted for different detection (inner-) angles. The curves are set to match the associated region in (a). The range of ambigous contrast increase is lower for the ternary materials than for pure GaAs. The magnitude of the normalized signal rises with decreasing scattering angle for all cases but is strongest for the c-GaAs material.

(with respect to pure materials). These displacements are presumably caused by ion impact damage cascades which introduce crystal disorder and/or alloy fluctuations. In addition, argon ion incorporation and point defect creation are possible. The overlay of those effects is complex because of their unknown contributions to the overall signal but leads to an intensity increase especially for small and medium detection angles with a linear decreasing magnitude from the very surface towards the inner sample region.

The amorphous layer thickness of 3.5 nm is in good agreement with the proposed fully amorphous layers from SRIM simulations giving an amorphization range of 3.5 nm and an ion straggle of 2.1 nm (for the material system investigated here). It is a well-known effect that the ion range for crystalline materials is severely underestimated by the plain SRIM due to the ion channeling of charged particles in periodic structures. This effect is well known for electrons [48] and for ions [49] and in the latter case increases the direct and indirect damage range in crystals.

The apparent decrease of the ion straggle range in the ternary compound materials might be attributed to the internal disorder of a random alloy and the different binding energies with respect to the pure GaAs which is highly ordered.

Another possible explanation could be the strain caused by the adhesion of the protective coatings. Despite the fact that HAADF-STEM is very sensitive to changes in the atomic number (Z-contrast), strain causes a bending of atomic columns in thin samples and thus acts as a source of de-channeling from the low index zone axis condition usually applied.

Nevertheless, neither in low magnification nor in high magnification images did the contrast at the surfaces change with moderate tilting, which strongly favors the damage layer scenario. Furthermore, nearly the same intensity increase can be seen for the top and bottom surface where – as described before – the adhering compound is obviously very different.

Finally, the cloudiness of the near surface areas cannot be explained by long range strain fields and thus strongly favor the discrete damage scenario with statistically distributed damage cascades.

Both, the amorphous surface and the gradually decreasing sub-surface damage have influence on (S)TEM imaging. The impact of these effects is very much depending on the sample thickness and was investigated for ADF-STEM elsewhere [50–55]. The role of amorphous surface layers on conventional HRTEM imaging was investigated for Boothroyd et al. [56–58] and is considered to be a significant contribution to the deviation between simulated and measured contrast levels ("Stobbs factor").

Because of the presumably complex damage mechanisms during ion beam thinning a complete modeling of the actual (gradually) degraded surface layers is very challenging and beyond the scope of this work. Nevertheless, the sub-surface damage could be considered as a disordered crystal and first order corrections to image evaluations might be derived from such an approach. Additionally, simulation studies [42,59] and experimental studies on disorder are found in the literature [40,41,60].

5. Conclusions

It could be shown that a combination of surface sensitive measurements like AFM and a novel cross-section FIB/TEM approach are able to quantify most of the artifacts associated with STEM specimen preparation. Especially the (sub-) surface damage from ion beam thinning is of great magnitude and reaches down to about 11.5 nm below the (final) surface even for considerably low argon ion energies. Its effect is readily seen as a diffuse cloudy dot-like contrast modulation in HAADF STEM images which indicates a local disordering without full amorphization. It is worth mentioning that this effect can be observed by conventional TEM samples as well, if inappropriate thinning conditions are applied.

Its effect on the HAADF intensity is evaluated for ternary alloys and pure GaAs for various scattering angles. The results indicate a material dependence on the ion damage range without showing significant selective etching.

Additional effects like oxide layer thickness, selective etching, surface roughness and elastic deformation can in principle be investigated but are hindered by the comparatively large amount of damage to the initial surfaces.

The systematic error introduced due to these intensity changes by damage and oxidation is estimated for GaAs proposing a systematic correction scheme which can be applied with relative ease and subsequent to a conventional sample investigation.

Finally, it is shown that despite the optimized preparation which produces almost atomically flat surfaces without significant selective etching the damage below the final surface is completely hidden but of considerable magnitude.

It is noteworthy that the FIB sectioning technique of cross-section TEM samples might help to clarify ambiguities in conventional (S)TEM measurements when precise modeling is needed.

Acknowledgments

This work was supported by the German Science Foundation (GRK 1782: "Functionalization of Semiconductors" and SFB 1083: "Structure and Dynamics of Internal Interfaces").

References

[1] A. De Backer, G.T. Martinez, A. Rosenauer, S. Van Aert, Atom counting in HAADF STEM using a statistical model-based approach: methodology, possibilities, and inherent limitations, Ultramicroscopy 134 (2013) 23–33, http://dx.doi.org/10.1016/j.ultramic.2013.05.003.

[2] G.T. Martinez, A. Rosenauer, A. De Backer, J. Verbeeck, S. Van Aert, Quantitative composition determination at the atomic level using model-based high-angle annular dark field scanning transmission electron microscopy, Ultramicroscopy 137 (2014) 12–19, http://dx.doi.org/10.1016/j.ultramic.2013.11.001.

[3] S.J. Pennycook, D.E. Jesson, High-resolution Z-contrast imaging of crystals, Ultramicroscopy 37 (1991) 14–38, http://dx.doi.org/10.1016/0304-3991(91)90004-P.

[4] D.J. Barber, Radiation damage in ion-milled specimens: characteristics, effects and methods of damage limitation, Ultramicroscopy 52 (1993) 101–125, http://dx.doi.org/10.1016/0304-3991(93)90025-S.

[5] Á. Barna, B. Pécz, M. Menyhard, TEM sample preparation by ion milling/amorphization, Micron 30 (1999) 267–276, http://dx.doi.org/10.1016/S0968-4328(99)00011-6.

[6] L. Dieterle, B. Butz, E. Müller, Optimized Ar(+)-ion milling procedure for TEM cross-section sample preparation, Ultramicroscopy 111 (2011) 1636–1644, http://dx.doi.org/10.1016/j.ultramic.2011.08.014.

[7] J.P. McCaffrey, M.W. Phaneuf, L.D. Madsen, Surface damage formation during ion-beam thinning of samples for transmission electron microscopy, Ultramicroscopy 87 (2001) 97–104, http://dx.doi.org/10.1016/S0304-3991(00)00096-6.

[8] N.I. Kato, Reducing focused ion beam damage to transmission electron microscopy samples, J. Electron Microsc. (Tokyo) 53 (2004) 451–458, http://dx.doi.org/10.1093/jmicro/dfh080.

[9] N.I. Kato, Y. Kohno, H. Saka, Side-wall damage in a transmission electron microscopy specimen of crystalline Si prepared by focused ion beam etching, J. Vac. Sci. Technol. A Vacuum Surf. Film 17 (1999) 1201, http://dx.doi.org/10.1116/1.581795.

[10] W.M. Lau, I. Bello, L.J. Huang, X. Feng, M. Vos, I.V. Mitchell, Argon incorporation in Si(100) by ion bombardment at 15–100 eV, J. Appl. Phys. 74 (1993) 7101–7105, http://dx.doi.org/10.1063/1.355024.

[11] S.J. Pearton, C.R. Abernathy, F. Ren, J.R. Lothian, Ar+-ion milling characteristics of III-V nitrides, J. Appl. Phys. 76 (1994) 1210–1215, http://dx.doi.org/10.1063/1.357849.

[12] M.K. Miller, K.F. Russell, K. Thompson, R. Alvis, D.J. Larson, Review of atom probe FIB-based specimen preparation methods, Microsc. Microanal. 13 (2007) 428–436, http://dx.doi.org/10.1017/S1431927607070845.

[13] A. Pantzer, A. Vakahy, Z. Eliyahou, G. Levi, D. Horvitz, A. Kohn, Dopant mapping in thin FIB prepared silicon samples by off-axis electron holography, Ultramicroscopy 138 (2014) 36–45, http://dx.doi.org/10.1016/j.ultramic.2013.12.001.

[14] W. Boxleitner, G. Hobler, V. Klüppel, H. Cerva, Simulation of topography evolution and damage formation during TEM sample preparation using focused ion beams, Nucl. Instrum. Methods Phys. Res. Sect. B Beam Interact. Mater. Atoms 175–177 (2001) 102–107, http://dx.doi.org/10.1016/S0168-583X(01)00334-2.

[15] E. Montoya, S. Bals, M.D. Rossell, D. Schryvers, G. Van Tendeloo, Evaluation of top, angle, and side cleaned FIB samples for TEM analysis, Microsc. Res. Technol. 70 (2007) 1060–1071, http://dx.doi.org/10.1002/jemt.20514.

[16] M.J. Süess, E. Mueller, R. Wepf, Minimization of amorphous layer in Ar+ ion milling for UHR-EM, Ultramicroscopy 111 (2011) 1224–1232, http://dx.doi.org/10.1016/j.ultramic.2011.03.004.

[17] S. Kret, T. Benabbas, C. Delamarre, Y. Androussi, A. Dubon, J.Y. Laval, et al., High resolution electron microscope analysis of lattice distortions and In segregation in highly strained $In_{0.35}Ga_{0.65}As$ coherent islands grown on GaAs (001), J. Appl. Phys. 86 (1999) 1988–1993, http://dx.doi.org/10.1063/1.370998.

[18] M.M.J. Treacy, The effects of elastic relaxation on transmission electron microscopy studies of thinned composition-modulated materials, J. Vac. Sci. Technol. B Microelectron. Nanom. Struct. 4 (1986) 1458–1466, http://dx.doi.org/10.1116/1.583473.

[19] J.P. McCaffrey, A. Barna, Preparation of cross-sectional TEM samples for low-angle ion milling, Microsc. Res. Technol. 36 (1997) 362–367, http://dx.doi.org/10.1002/(SICI)1097-0029(19970301)36:5 < 362::AID-JEMT3 > 3.0.CO;2-N.

[20] V. Grillo, The effect of surface strain relaxation on HAADF imaging, Ultramicroscopy 109 (2009) 1453–1464, http://dx.doi.org/10.1016/j.ultramic.2009.07.010.
[21] K. Tillmann, M. Lentzen, R. Rosenfeld, Impact of column bending in high-resolution transmission electron microscopy on the strain evaluation of GaAs/InAs/GaAs heterostructures, Ultramicroscopy 83 (2000) 111–128, http://dx.doi.org/10.1016/S0304-3991(99)00175-8.
[22] D.J. Friedman, J.F. Geisz, S.R. Kurtz, J.M. Olson, 1-eV solar cells with GaInNAs active layer, J. Cryst. Growth 195 (1998) 409–415, http://dx.doi.org/10.1016/S0022-0248(98)00561-2.
[23] M. Kondow, S. Natatsuka, T. Kitatani, Y. Yazawa, M. Okai, Room-temperature continuous-wave operation of GaInNAs/GaAs laser diode, Electron. Lett. 32 (1996) 2244–2245, http://dx.doi.org/10.1049/el:19961480.
[24] K. Volz, J. Koch, F. Höhnsdorf, B. Kunert, W. Stolz, MOVPE growth of dilute nitride III/V semiconductors using all liquid metalorganic precursors, J. Cryst. Growth 311 (2009) 2418–2426, http://dx.doi.org/10.1016/j.jcrysgro.2008.09.210.
[25] O. Rubel, K. Volz, T. Torunski, S.D. Baranovskii, F. Grosse, W. Stolz, Columnar [001]-oriented nitrogen order in Ga(NAs) and (GaIn)(NAs) alloys, Appl. Phys. Lett. 85 (2004) 5908–5910, http://dx.doi.org/10.1063/1.1829801.
[26] K. Volz, D. Lackner, I. Németh, B. Kunert, W. Stolz, C. Baur, et al., Optimization of annealing conditions of (GaIn)(NAs) for solar cell applications, J. Cryst. Growth 310 (2008) 2222–2228, http://dx.doi.org/10.1016/j.jcrysgro.2007.11.199.
[27] A. se Erol, Dilute III-V Nitride Semiconductors and Material Systems : Physics and Technology, 2008, doi: 10.1007/978-3-540-74529-7.
[28] J.F. Ziegler, M.D. Ziegler, J.P. Biersack, SRIM - The stopping and range of ions in matter (2010), Nucl. Instrum Methods Phys. Res. Sect. B Beam Interact. Mater. Atoms 268 (2010) 1818–1823, http://dx.doi.org/10.1016/j.nimb.2010.02.091.
[29] K. Momose, H. Yonezu, Y. Fujimoto, K. Ojima, Y. Furukawa, A. Utsumi, et al., Hardening effect of $GaP_{1-x}N_x$ and $GaAs_{1-x}N_x$ Alloys by adding nitrogen atoms, Jpn. J. Appl. Phys. 41 (2002) 7301–7306, http://dx.doi.org/10.1143/JJAP.41.7301.
[30] A. Strecker, J. Mayer, B. Baretzky, U. Eigenthaler, T. Gemming, R. Schweinfest, et al., Optimization of TE M Specimen Preparation by Double-Sided Ion Beam Thinning under Low Angles, 48, 1999, pp. 235–244.
[31] F. Lelarge, O. Dehaese, E. Kapon, C. Priester, Strain relaxation at cleaved surfaces studied by atomic force microscopy, Appl. Phys. A Mater. Sci. Process. 69 (1999) 347–351, http://dx.doi.org/10.1007/s003390051012.
[32] F. Lelarge, C. Priester, C. Constantin, a Rudra, K. Leifer, E. Kapon, Strain mapping of V-groove InGaAs/GaAs strained quantum wires using cross-sectional Atomic Force Microscopy, Appl. Surf. Sci. 166 (2000) 290–294, http://dx.doi.org/10.1016/S0169-4332(00)00410-4.
[33] P.C. Hoyle, Electron beam induced deposition from $W(CO)_6$ at 2 to 20 keV and its applications, J. Vac. Sci. Technol. B Microelectron. Nanom. Struct. 14 (1996) 662, http://dx.doi.org/10.1116/1.589154.
[34] M. Schaffer, B. Schaffer, Q. Ramasse, Sample preparation for atomic-resolution STEM at low voltages by FIB, Ultramicroscopy 114 (2012) 62–71, http://dx.doi.org/10.1016/j.ultramic.2012.01.005.
[35] A. Rosenauer, M. Schowalter, STEMSIM—a New Software Tool for Simulation of STEM HAADF Z-Contrast Imaging, Springer, Netherlands, Dordrecht (2008) http://dx.doi.org/10.1007/978-1-4020-8615-1.
[36] J.M. LeBeau, S.D. Findlay, L.J. Allen, S. Stemmer, Standardless atom counting in scanning transmission electron microscopy, Nano Lett. 10 (2010) 4405–4408, http://dx.doi.org/10.1021/nl102025s.
[37] J. LeBeau, S. Findlay, L. Allen, S. Stemmer, Quantitative atomic resolution scanning transmission electron microscopy, Phys. Rev. Lett. 100 (2008) 206101, http://dx.doi.org/10.1103/PhysRevLett.100.206101.
[38] A. Rosenauer, K. Gries, K. Müller, A. Pretorius, M. Schowalter, A. Avramescu, et al., Measurement of specimen thickness and composition in AlxGa($1-x$)N/GaN using high-angle annular dark field images, Ultramicroscopy 109 (2009) 1171–1182, http://dx.doi.org/10.1016/j.ultramic.2009.05.003.
[39] G. Möbus, G. Necker, M. Rühle, Adaptive fourier-filtering technique for quantitative evaluation of high-resolution electron micrographs of interfaces, Ultramicroscopy 49 (1993) 46–65, http://dx.doi.org/10.1016/0304-3991(93)90212-G.
[40] T. Grieb, K. Müller, R. Fritz, M. Schowalter, N. Neugebohrn, N. Knaub, et al., Determination of the chemical composition of GaNAs using STEM HAADF imaging and STEM strain state analysis, Ultramicroscopy 117 (2012) 15–23, http://dx.doi.org/10.1016/j.ultramic.2012.03.014.
[41] T. Grieb, K. Müller, E. Cadel, A. Beyer, M. Schowalter, E. Talbot, et al., Simultaneous quantification of indium and nitrogen concentration in InGaNAs using HAADF-STEM, Microsc. Microanal. 20 (2014) 1740–1752, http://dx.doi.org/10.1017/S1431927614013051.
[42] V. Grillo, K. Mueller, K. Volz, F. Glas, T. Grieb, A. Rosenauer, Strain, composition and disorder in ADF imaging of semiconductors, J. Phys. Conf. Ser. 326 (2011) 012006, http://dx.doi.org/10.1088/1742-6596/326/1/012006.
[43] G. Hollinger, R. Skheyta-Kabbani, M. Gendry, Oxides on GaAs and InAs surfaces: an x-ray-photoelectron-spectroscopy study of reference compounds and thin oxide layers, Phys. Rev. B 49 (1994) 11159–11167, http://dx.doi.org/10.1103/PhysRevB.49.11159.
[44] H. Bluhm, U.D. Schwarz, F. Herrmann, P. Paufler, Study of the influence of native oxide layers on atomic force microscopy imaging of semiconductor surfaces, Appl. Phys. A Solids Surf. 59 (1994) 23–27, http://dx.doi.org/10.1007/BF00348415.
[45] Z. Yu, D.A. Muller, J. Silcox, Study of strain fields at a-Si/c-Si interface, J. Appl. Phys. 95 (2004) 3362–3371, http://dx.doi.org/10.1063/1.1649463.
[46] A. Beyer, R. Straubinger, J. Belz, K. Volz, Local sample thickness determination via scanning transmission electron microscopy defocus series, J. Microsc. (n. d.). doi:10.1111/jmi.12284.
[47] V. Grillo, E. Carlino, F. Glas, Influence of the static atomic displacement on atomic resolution Z-contrast imaging, Phys. Rev. B 77 (2008) 054103, http://dx.doi.org/10.1103/PhysRevB.77.054103.
[48] A. Howie, Diffraction channelling of fast electrons and positrons in crystals, Philos. Mag. 14 (1966) 223–237, http://dx.doi.org/10.1080/14786436608219008.
[49] D.S. Gemmell, Channeling and related effects in the motion of charged particles through crystals, Rev. Mod. Phys. 46 (1974) 129–227, http://dx.doi.org/10.1103/RevModPhys.46.129.
[50] T. Yamazaki, K. Watanabe, N. Nakanishi, I. Hashimoto, Role of surface amorphous film in high-resolution high-angle annular dark field STEM imaging, Ultramicroscopy 99 (2004) 125–135, http://dx.doi.org/10.1016/j.ultramic.2003.12.001.
[51] K.A. Mkhoyan, S.E. Maccagnano-Zacher, E.J. Kirkland, J. Silcox, Effects of amorphous layers on ADF-STEM imaging, Ultramicroscopy 108 (2008) 791–803, http://dx.doi.org/10.1016/j.ultramic.2008.01.007.
[52] S.E. Maccagnano-Zacher, K.A. Mkhoyan, E.J. Kirkland, J. Silcox, Effects of tilt on high-resolution ADF-STEM imaging, Ultramicroscopy 108 (2008) 718–726, http://dx.doi.org/10.1016/j.ultramic.2007.11.003.
[53] Z. Yu, D. a Muller, J. Silcox, Effects of specimen tilt in ADF-STEM imaging of a-Si/c-Si interfaces, Ultramicroscopy 108 (2008) 494–501, http://dx.doi.org/10.1016/j.ultramic.2007.08.007.
[54] T. Walther, C.B. Boothroyd, C.J. Humphreys, Strain relaxation induced local crystal tilts at Si/SiGe interfaces in cross-sectional transmission electron microsco pe specimens, in: MSM-9, Inst. Phys. Conf. Ser. 146, 1995, pp. 11–16.
[55] T. Walther, C.J. Humphreys, Quantification of the composition of silicon germanium/silicon structures by high-angle annular dark field imaging, in: Proc. EMAG-97, Inst. Phys. Conf. Ser. 153, 1997, pp. 303–306.
[56] C.B. Boothroyd, W.M. Stobbs, The contribution of inelastically scattered electrons to high resolution images of (Al, Ga)As/GaAs heterostructures, Ultramicroscopy 26 (1988) 361–376, http://dx.doi.org/10.1016/0304-3991(88)90235-5.
[57] C.B. Boothroyd, Why don't high-resolution simulations and images match? J. Microsc. 190 (1998) 99–108, http://dx.doi.org/10.1046/j.1365-2818.1998.2910843.x.
[58] C.B. Boothroyd, Quantification of High-Resolution Electron Microscope Images of Amorphous Carbon, 83, 2000, pp. 159–168.
[59] E. Carlino, V. Grillo, Atomic-resolution quantitative composition analysis using scanning transmission electron microscopy Z-contrast experiments, Phys. Rev. B 71 (2005) 235303, http://dx.doi.org/10.1103/PhysRevB.71.235303.
[60] T. Grieb, K. Müller, R. Fritz, V. Grillo, M. Schowalter, K. Volz, et al., Quantitative chemical evaluation of dilute GaNAs using ADF STEM: avoiding surface strain induced artifacts, Ultramicroscopy 129 (2013) 1–9, http://dx.doi.org/10.1016/j.ultramic.2013.02.006.

6.1.2 Publication 2

Citation

Atomic-scale 3D reconstruction of antiphase boundaries in GaP on (001)silicon by STEM
J. Belz, A. Beyer, K. Volz, Micron **114**, p.32 - 41, 2018, DOI: 10.1016j.micron.2018.07.008.

Abstract

In order to overcome the limitations of silicon-based electronics, the integration of optically active III V compounds is a promising approach. Nonetheless, their integration is far from trivial and control as well as understanding of corresponding growth kinetics, and in particular the occurrence and termination of antiphase defects, is of great relevance. In this work, we focus on the three-dimensional reconstruction of such boundaries in gallium phosphide from single scanning transmission electron microscopy images. In the high angle annular dark-field imaging mode, the appearance of these antiphase boundaries is strongly determined by the chemical composition of each atomic column and reflects the ratio of transmitted anti- to mainphase. Therefore it is possible to translate measured intensities to the depth location of these boundaries by utilizing simulation data. The necessary spatial resolution for these column-by-column mappings is achieved via electron optical aberration correction within the microscope. Hence, the complete 3D orientation of these defects can be measured at atomic resolution and correlated to growth related parameters. Finally, we present a method to reconstruct large areas from well sampled images and retrieve information about complex embedded nanoscale structures at the atomic scale.

Contributions

Jürgen Belz carried out the experiments, programmed the majority of the algorithm and wrote the manuscript. Andreas Beyer provided parts of the programming code, contributed to the interpretation and evaluation. Kerstin Volz supervised the research and secured the funding to support the study. All authors reviewed the manuscript.

Reprinted from *Micron **114**,32 - 41,2018*, Copyright 2018, with permission from Elsevier.

Micron 114 (2018) 32–41

Contents lists available at ScienceDirect

Micron

journal homepage: www.elsevier.com/locate/micron

Atomic-scale 3D reconstruction of antiphase boundaries in GaP on (001) silicon by STEM

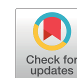

Jürgen Belz*, Andreas Beyer, Kerstin Volz

Faculty of Physics and Materials Science Center, Philipps-Universität Marburg, Hans-Meerwein-Straße 6, Marburg, Hessen, 35032, Germany

ARTICLE INFO

Keywords:
Scanning transmission electron microscopy
3D reconstruction
Interfaces
Compound semiconductors

ABSTRACT

In order to overcome the limitations of silicon-based electronics, the integration of optically active III–V compounds is a promising approach. Nonetheless, their integration is far from trivial and control as well as understanding of corresponding growth kinetics, and in particular the occurrence and termination of antiphase defects, is of great relevance. In this work, we focus on the three-dimensional reconstruction of such boundaries in gallium phosphide from single scanning transmission electron microscopy images. In the high angle annular dark-field imaging mode, the appearance of these antiphase boundaries is strongly determined by the chemical composition of each atomic column and reflects the ratio of transmitted anti- to mainphase. Therefore it is possible to translate measured intensities to the depth location of these boundaries by utilizing simulation data. The necessary spatial resolution for these column-by-column mappings is achieved via electron optical aberration correction within the microscope. Hence, the complete 3D orientation of these defects can be measured at atomic resolution and correlated to growth parameters. Finally, we present a method to reconstruct large areas from well sampled images and retrieve information about complex embedded nanoscale structures at the atomic scale.

1. Introduction

Silicon-based semiconductor devices are extremely wide spread and – even up to now – almost inevitable when thinking of the near-future development in computer technology (Wang et al., 2017). The research is branched into several different technologically relevant directions ranging from improved channel materials for transistors to the direct monolithic integration of III–V lasers on silicon for data transmission (del Alamo, 2011; Desplanque et al., 2012; Liebich et al., 2011).

Nonetheless, it is well known that the monolithic integration of III–V materials into silicon is challenging and antiphase domains (APDs) can be formed during heteroepitaxy of polar materials on nonpolar layers due to monoatomic surface steps. Although the reduction and suppression of APDs for the interesting and equally important gallium phosphide (GaP) on silicon has seen great progress, their occurrence is still a severe issue and can affect the performance of many devices adversely due to local strain and charge effects (Beyer et al., 2012, 2011; Desplanque et al., 2012; Feifel et al., 2017; Kroemer, 1987; Kunert et al., 2008; Németh et al., 2008; Volz et al., 2011). Therefore, a detailed understanding of their formation, appearance and ultimately termination is of great relevance to the integration of III–V optoelectronic materials onto exact silicon as it is used in the current complementary metal–oxide–semiconductor (CMOS) based technology.

Up to now, the detailed bonding characteristics within such antiphase boundaries (APBs) are not well understood. Although theoretical investigations have been carried out for a limited number of interfaces like GaAs/Ge and GaP/Si, experimental atomic resolution studies by Beyer et al. show the occurrence of more complex geometries than initially anticipated (Beyer et al., 2013; Cho and Carter, 2001; Rubel and Baranovskii, 2009). Due to this complex situation, the effects of APBs on many devices need careful modelling for example by atomistic simulations like density functional theory (DFT) where the resulting charge distribution is dependent on the actual geometry. Hence, the actual geometry of these APBs is important due to the charge accumulated by wrong bonds.

In order to resolve the structure of APDs with atomic resolution we use quantitative high angle annular dark-field (HAADF) scanning transmission electron microscopy (STEM). While other techniques like (S)TEM (tilt-series) electron tomography (Midgley, 2003; Midgley and Weyland, 2003) or atomic probe tomography (APT) (Kelly and Miller, 2007; Seidman, 2007) provide a reasonable resolution with an accuracy of up to 1 nm (and even below for APT), the lateral resolution of aberration corrected STEM is in the sub-Ångstrom regime. This is in particular aiding the determination of complex binding geometries as

* Corresponding author.
E-mail address: juergen.belz@physik.uni-marburg.de (J. Belz).

https://doi.org/10.1016/j.micron.2018.07.008
Received 15 May 2018; Received in revised form 19 July 2018; Accepted 19 July 2018
Available online 23 July 2018
0968-4328/ © 2018 Elsevier Ltd. All rights reserved.

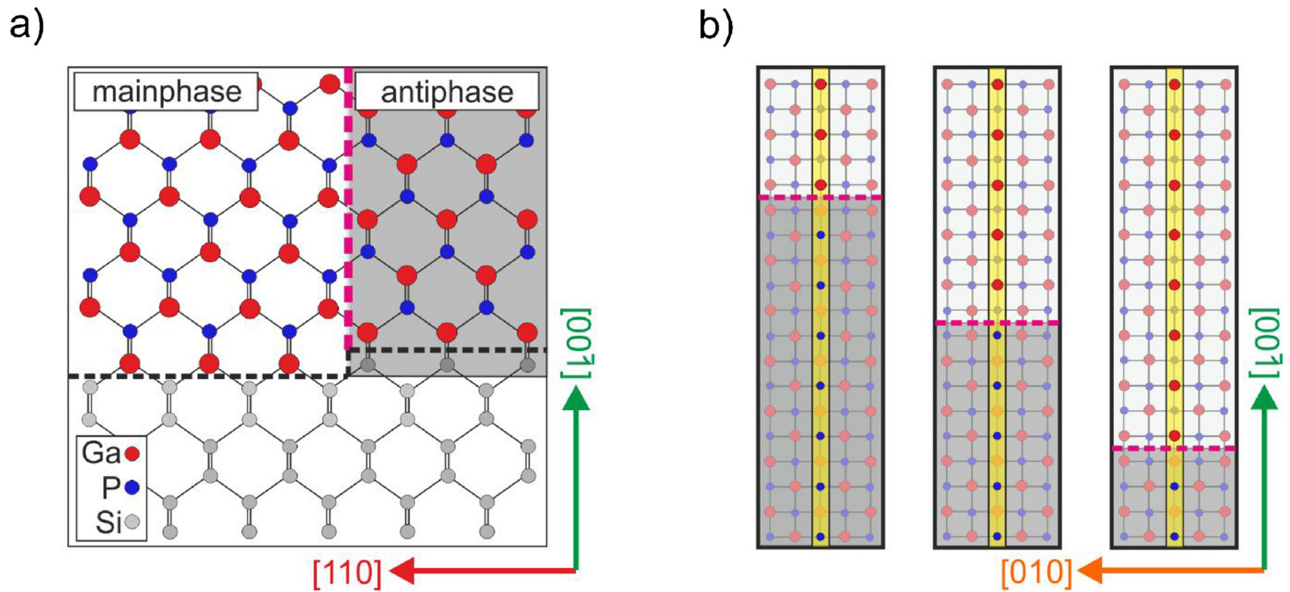

Fig. 1. (a) Cross-section view illustrating the origin of the antiphase defect (simplified) seen along [−110]. (b) The APB (magenta) divides the MP from the AP resulting in a varying ratio of Ga to P in each column.

seen for extended structural defects like APBs.

Another common disadvantage of many tomography methods is that the reconstruction relies on the acquisition of multiple images taken under different conditions and usually implies a difficult sample preparation. The latter point makes these tomography techniques impractical if either the region of interest is not representing the majority of the material or hard to find during the process of preparation.

On the other hand, quantitative STEM investigations have come a long way since the term "Z-Contrast" was coined in the early 90s of the last century (Pennycook and Jesson, 1991). The advance of instruments in the field of electron microscopy, especially the advent of commercialized aberration correctors for TEM and STEM, opened the doors for quantitative sub-Ångstrom microscopy on a daily basis (Haider et al., 1998; Krivanek et al., 1997; Uhlemann and Haider, 1998). Since then, quantifying the HAADF signal on an absolute scale at atomic resolution has become increasingly popular.

While there are many occasions where STEM measurements with qualitative match to simulations are already sufficient, the demand for quantitative match to simulations has led to a more detailed understanding of (S)TEM contrast in terms of thermal diffuse scattering (Howie, 2004; Loane et al., 1991), inelastic scattering (Allen et al., 2015; Bleloch et al., 1994; Mkhoyan et al., 2008), as well as the development of various implementations of image simulation algorithms like the STEMsalabim code (Oelerich et al., 2017) used in this work. A comprehensive list of image simulation software can be found in (Oelerich et al., 2017). In addition, the characterization of experimental equipment has led to remarkable agreement between experiment and simulation (Beyer et al., 2016a; Jones et al., 2014; LeBeau et al., 2008, 2010; Martinez et al., 2014). Especially the confocal nature of the STEM technique has been shown to truly deliver 3D information on a nearly atomic scale (Alania et al., 2016; Gonnissen et al., 2016; Muller et al., 2004). Nonetheless, even single STEM HAADF images can be used on their own to retrieve three-dimensional data in many cases as will be shown in this manuscript.

Since STEM images are generally projections of 3D entities, a direct interpretation of such images demands specific knowledge about the sample under investigation. Conventionally, in analytical STEM measurements local material compositions can be derived by considering the TEM sample geometry as being either flat or wedge shaped. On the other hand, by considering a-priori knowledge about the sample chemistry measured intensities can be used to retrieve geometrical structures on the atomic scale. In particular, it is possible to derive the evolution of the APB with respect to one of the surfaces of a STEM specimen. This becomes clear when one considers the case of GaP on silicon where the constituents are known but the geometry of the crystal defect is to be investigated. Since the HAADF STEM signal is related to the atomic number Z, one can directly correlate the scattering strength to a chemical composition. This is in particular applicable in the case of GaP since the pure GaP mainphase (MP) is separated from the pure GaP antiphase (AP) only by their inner interface (APB). The compositional transition from the MP to the AP is illustrated in Fig. 1a, as cross-section along the [−110] direction. Due to the polar basis of GaP, single steps of the silicon substrate cause the creation of APBs. In contrast to the simplistic illustration in Fig. 1a the actual geometry of APBs is rather complex but can be considered to be monotonously changing from the MP to the AP as can be seen from previous experimental results (Beyer et al., 2012; Volz et al., 2011). Generally, a single crystal column seen in transmission can contain different fractions of MP and AP. Here, the boundary can be considered within every single column independently. Connecting these single column boundaries results in the overall appearance of the APB. This situation is illustrated in Fig. 1b where a cross-section along the [100] direction shows the chemical transition from MP to AP on a single column with an increasing fraction of the AP (gray shaded). On an atomic scale, this corresponds to a changing group-III and group-V sub-lattice decoration from gallium (Ga) to phosphorous (P) and from P to Ga respectively. Since this behavior is identical for any shape of the overall APB, the composition of each column can be used to map the z coordinate of the APB.

Seen along a low order zone axis like [001] as in the case of a plan-view (PV) investigation the atoms are aligned in columns along the z direction. The imaging plane of the microscope is therefore the xy plane.

2. Material and method

For the recording of high quality STEM measurements, several prerequisites were carried out in order to reduce the effects of beam damage and bending for a sufficiently large field of view. In the following, the preparation procedure will be explained and the STEM ADF measurements will be elucidated.

2.1. Sample preparation

An about 65 nm thick layer of GaP epitaxially grown on silicon (001) was prepared for PV investigations using mechanical pre-thinning with the *Allied MultiPrep™ Polishing System*. The grinding procedure was carried out while introducing a small angle that guarantees a thin region of interest as well as a thick supporting region for easy handling. For the final thinning steps, a dual column focused ion beam machine (*JEOL JIB-4601F*) was used to remove the backside material leading to thicknesses in the nanometer range. In order to create high quality regions, a 30 kV Ga^+ beam was used to etch several "windows" into the sample with an angle approximately compensating the residual wedge angle of 2° introduced by the mechanical grinding steps. The notion behind this is to reduce the thickness gradient and the resulting defocus variations in the later STEM measurements. The windowing procedure is aimed to stabilize the regions of interest by reducing scrolling and bending effects due to the intrinsic strain energy of this material system. These initial regions are further thinned by using successively reduced ion beam energies down to the last polishing step with only 1 kV acceleration voltage therefore reducing excessive damage.

2.2. Image acquisition

The STEM investigations were carried out with a *JEOL JEM-2200FS* image and probe corrected microscope operated at 200 kV using annular dark-field (ADF) imaging. Using a semi-convergence angle of 24 mrad, the geometrical probe correction leads to a sub-Ångstrom sized electron probe with a current of about 25 pA. In order to acquire a strong chemical contrast the HAADF regime in the range from 86 to 344 mrad is chosen for image evaluation (Pennycook and Jesson, 1991). In addition, the low angle ADF (LAADF) regime of 35–140 mrad is used for detection, orientation and visualization of APBs due to strain and disorder contrast (Beyer et al., 2017a; Grillo et al., 2008, 2011). For the purpose of quantitative high resolution HAADF investigations, the experimental micrographs were normalized to the intensity of the direct beam imaged onto an *Ultrascan 1000XP* CCD camera following an approach similar to He and Li (2014). Hereto, a "detector scan "has been used to account for the inhomogeneous response of the ADF (He and Li, 2014; LeBeau et al., 2008). It is noteworthy that the electron scattering in STEM is affected by the transfer system after the interaction with a sample especially when TEM image correctors are present (Krause et al., 2016). Hence we deactivated the strong lenses in the image corrector in the case of STEM imaging.

In order to assure close to ideal imaging conditions, the measurements were carried out soon after a complete corrector alignment and with manual fine tuning of low order aberrations using the Ronchigram method. Furthermore, the defocus was set to provide the maximum contrast by using a through-focus sweep as described for example in Beyer et al. (2016a,b). This leads to a defocus value of about −2 nm with respect to the top surface.

For a robust quantitative chemical analysis of single columns, HAADF imaging is used in the following high magnification measurements. In order to overcome the challenges imposed by the relatively low intensity scattered into high angles, the signal-to-noise ratio has to be increased. This is especially relevant for the dark P columns which are merely above the background level and often hardly visible (Beyer et al., 2016a). We therefore utilized the *Smart Align* tool for the registration and scan noise correction of 32 high resolution images rapidly captured one after another (Jones et al., 2015). These $512 \times 512\,px^2$ images were recorded with a pixel dwell time of 3 µs each resulting in a frame time of about 32×1 s. The rapid acquisition leads to a highly efficient image registration due to reduced drift effects and only small low residual noise (Jones and Nellist, 2013). After careful inspection of the pair registration between images, the individual recordings have been averaged into one single high quality STEM image.

After transferring the sample into the microscope, the sample is aligned along the [001] direction. Utilizing the aforementioned LAADF imaging, the boundary separating the MP and the AP can be recognized in STEM images at low magnification if a sufficient sampling is chosen (Fig. 2a). It is noteworthy that for most of the sample the resulting thickness is less than 65 nm. Therefore, the complete sample is consisting of pure GaP since the silicon has been removed from the backside.

Upon closer inspection, it can be seen that the basic shape of the boundary is generally triangular or "needle-shaped" pointing towards the [110] direction. The orthogonal [−110] direction can be seen to be the predominant direction of the triangle basis. The shape of the APB can be shown to be closely related to the silicon surface during the metalorganic vapour phase epitaxy (MOVPE) growth as shown by Volz et al. (2011). These findings are also in agreement with earlier findings of Beyer et al. using conventional TEM dark-field techniques (Beyer et al., 2012).

With increasing magnification, it can be seen that the APBs show abrupt and continuous transition regions indicating different lattice plane orientations. This fact can easily be appreciated as illustrated in Fig. 2b where the high resolution image taken from a region significantly thinner than those of in Fig. 2a is shown. For visualization purposes, the "{200}-Bragg-filtered" inverse Fourier transform is shown as it highlights the intensity irregularity at the APB. In this "virtual dark-field" image one can see different dark fading regions with an extension over several nanometers, as well as very abrupt transitions (dashed frame, white). These abrupt boundaries are located on {110}-planes and run perpendicular to the imaging plane along the electron beam direction.

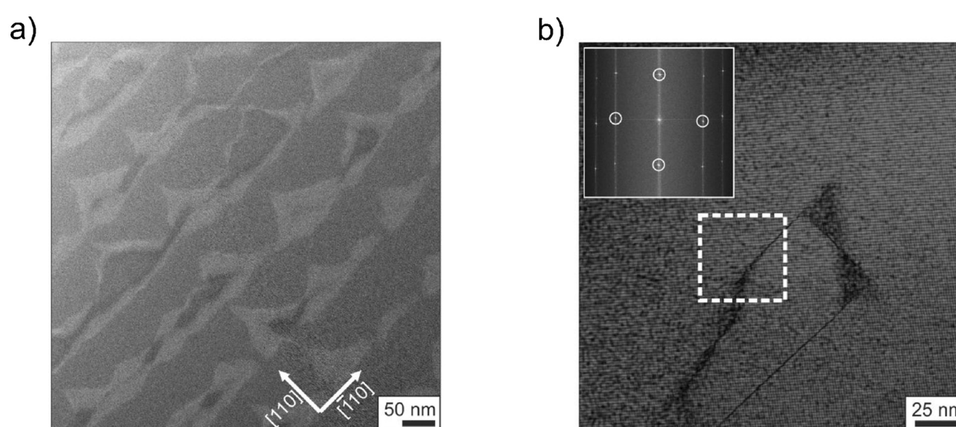

Fig. 2. (a) STEM image from a PV sample at low magnification showing the approximate alignment of the APB defect with the silicon surface steps. (b) For a better illustration the higher magnification image of a region of (a) is shown as the inverse Fourier transform of a {200} Bragg filtered HRSTEM micrograph.

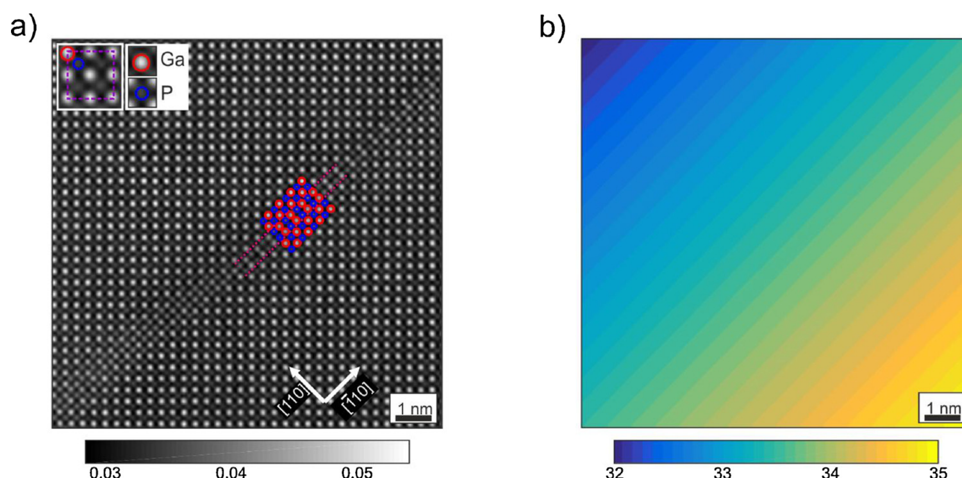

Fig. 3. (a) Shows the intensity normalized HAADF image of a {110} dominated boundary. Over a short segment the boundary is apparently almost perfectly located on the {110} plane, whereas the shape is deviating from those planes on both sides of the micrograph. The experimental thickness in nm across the image is shown in (b). Here a bi-linear approximation is used to interpolate the local thickness for each column position.

The dashed region of Fig. 2b recorded at higher magnification by using high angle ADF for an increased chemical contrast is shown in Fig. 3. In this image, the phase separating boundary can be readily seen in the center, where the initial group-III sub-lattice decoration by (exclusively) Ga atoms (III_{Ga}) switches from the MP region to the AP region (III_P) partly within a single atom plane. Analogously, also the group-V sub-lattice decoration is inverted ($V_P \rightarrow V_{Ga}$). It is worth mentioning that albeit the choice of defining the group-III sub-lattice might seem arbitrary, the MP is known from the overview images by comparing the area ratio.

As a guide to the eye, color markers are set at Ga (red) and P (blue) columns and the magnification of an elementary (projected) unit cell is shown as an inset. The green lines enclose a part of the two adjacent crystal planes that form the {110} boundary. In this region, the sub-lattice decoration with Ga and P is overlaid by the corresponding color code highlighting the abrupt interface consisting of a multitude of Ga-Ga and P-P wrong bonds.

Upon closer inspection of the boundary shown in Fig. 3, it can be seen that the “simple” {110}-dominated boundary shows signs of contrast irregularities on the right hand side, as well as on the left hand side. In order to investigate this kind of APB in detail, such “fading contrasts” have been analysed with the aid of image simulations. With these the shape of the APB can be ultimately reconstructed by quantitatively mapping the column composition using HAADF intensities.

The transcription from STEM HAADF column intensities to actual chemical column compositions and therefore ultimately the depth position of the APB, is carried out by a series of image simulations. A detailed description is given in the following section.

2.3. Image simulations

For the reconstruction of 3D information, the scattered intensity has to be connected to the column decoration and ultimately the depth position of the APB where the column decoration becomes inverted. In order to account for every column decoration of the transition from one to the other phase, multiple supercells were created where the atomic column decoration is inverted at different heights therefore creating different chemical compositions of that particular atomic column (cf. Fig. 1b).

Image simulations were carried out for all of these 118 supercells (maximum GaP thickness of 65 nm) utilizing our new high performance cluster computer implementation of STEMsalabim (Oelerich et al., 2017) based on the so called multislice method (Kirkland, 2010) and the frozen lattice approximation (Loane et al., 1991) finished within a few days on the Marburg Computation Cluster *MaRC2*. It is worth noting that once the simulations are carried out for a given material system for all thicknesses up to the thickness of interest, the simulations do not need to be carried out again unless microscope parameters are significantly altered.

In order to reduce the self-interference of the simulated probe, the lateral extension of the supercell was chosen to be 5 × 5 unit cells (UCs) where only the innermost unit cell was used for image simulation. The k-space was sampled by 982 × 982 px^2 for each of the real space image points (22 × 22 px^2). The microscope parameters where chosen to match our aberration corrected *JEOL JEM-2200FS* with a probe convergence semi angle of 24 mrad at 200 keV. The defocus value was set to be −2 nm measured from the top surface and the residual 5th order spherical aberration was set to 2 mm. Further geometric aberrations were neglected in the image simulations. However, the chromatic aberration was modeled as described in Beyer et al. (2016a,b) as a weighted sum of differently focused probes and reflects the characteristics of the aforementioned microscope. Each defocus contains a set of 15 phonon configurations leading to 105 independent configurations in order to stabilize the intensity variation for low sample thicknesses on single columns. The real space sampling was chosen to have a density of 40 $px\,nm^{-1}$ sufficiently sampling the simulation data. In order to account for the experimental sampling density ranging from 30 to 140 $px\,nm^{-1}$, the simulation data has been rescaled accordingly.

3. Data processing

3.1. Experimental data

In order to match the experimental recordings with the simulated data, several image data processing steps were carried out. At first, the experimental sampling was determined and the image normalization to the direct electron beam as described earlier was applied. We therefore show high resolution images in units of the fraction of the impinging electron flux (cf. Fig. 3a). In the following, the peak positions are determined by a combination of Fourier filtering and contour thresholding. As a follow up, the atomic on-column positions (“peaks”) are refined by fitting a two-dimensional paraboloid to every peak in order to increase the accuracy of position determination.

Despite the experimental counter-measurements, a small residual thickness gradient is almost inevitable and can be usually observed as an intensity gradient across the micrographs. In order to account for its effect, we apply a two dimensional model compensating the sample wedge angles. Hereto, we use the mean average image intensity to simulation data of pure GaP since the mean intensity of pure GaP is directly correlated to the thickness of the transmitted crystal. This intensity is then approximated by a bi-linear fit mapping the simulated thickness (c.f. Fig. 3b) to local column positions. It is worth mentioning that the field-of-view in our images usually is large enough to record the two phases of GaP. Alternatively, the intensity of the local “unit cell

equivalent environment" surrounding each atomic column can be used to account for more localized thickness variations and is applied for the large field of view images evaluated in the latter part of this work.

3.2. Reconstruction procedure

As elucidated before, the actual image contrast in experimental images is usually worse than the one of simulations due to effects like limited temporal and spatial coherence, as well as residual aberrations, vibrations and small defocusing errors. Another source of discrepancy between simulations and experiment is the occurrence of amorphous layers by either the native oxidization or the thinning procedure itself. In this study, we treated the amorphous layer as a constant background level and implicitly include its effect in the (effective) source size value. We consider the amorphous background to be 2 nm for the top layer (derived from cross section images) where the original oxidized sample surface is located and another 3.5 nm for the lower surface where ion milling was carried out. Since the actual composition of the oxide and damaged layer are generally unknown, we consider amorphous GaP as a reasonable substitute. A detailed description of the generation of these amorphous layers and their impact on the image contrast can be found in Beyer et al. (2016a).

Additionally, a two dimensional Lorentzian distribution accounting for the finite source size is found to be suitable for accurately matching the experimental data measured at our *JEOL JEM-2200FS* (Beyer et al., 2016a,b). Following this approach, only a minor additional blurring has to be applied to fit the experimental with the simulation contrast. Hereto, a small region in the pure mainphase is periodically averaged and used to measure the column shape and hence the probe shape. The experimental intensity profile of such an averaged unit cell is shown in Fig. 4a. The best match between experiment and simulation can be found for a total combined blurring σ_{total} of 61 pm for e.g. the image (cf. Fig. 4a). It can be seen that the levels for bright Ga columns and the (very) dark P columns are well reproduced. Additionally, the simulated intensities for thicknesses of ± 4 *atoms* (± 2 nm) around the optimum are shown as red shading.

Since the column intensity is a two-dimensional quantity, the background substracted on-column contrast between Ga and P columns with respect to the average limiting radius has been analysed as depicted in Fig. 4b. Herein, the contrast is normalized to the maximum value (i.e. peak intensity ratio). It can be seen that the experimental column contrast is matching the simulated contrast over the full range of possible "column radii" therefore strongly underlining the accuracy of the model proposed by Beyer et al. (2016a). It is worth mentioning that these graphs are very sensitive to changes of amorphous layer thicknesses and changes in the PSF and hence very useful to match experimental conditions with simulation data.

After the optimum point spread function is found, the simulation data is blurred accordingly and the data extraction can be carried out.

3.3. Data extraction from experiment and simulation

Since the column shape is fitted accurately the further treatment of data extraction does not highly depend on the integration radius around a particular atomic column, as long as simulation and experiment are treated identically. For the purpose of chemical investigations, we focus on large non-overlapping integration radii close to the nearest neighbour (NN) distance in order to increase the robustness against noise.

The data extraction is carried out automatically for the whole simulation data ensemble and the column intensities are extracted analogously to the experimental data. This procedure leads to curves translating the intensity of either group-III or group-V columns to the depth location of the APB. As an example Fig. 5a shows the resulting curve derived from the simulated images. Herein, for each simulation the averaged column intensity (red and blue circles respectively) is plotted.

Since the position of the domain inversion (APB) is known for the simulated sample database, the measured intensity can be directly related (black dashed lines, as a guide to the eye). Upon closer inspection, one can see that these curves can be divided into distinct regimes. For about the first 7 nm – 10 nm, the slopes of both curves are steeper. This is indicating that the domain inversion is influencing the image formation the most for the regions with the phase inversion focus. It is noteworthy that although both curves are more pronounced in this region, the initially darker group-V sub-lattice is almost twice as responsive to compositional changes than the already bright Ga

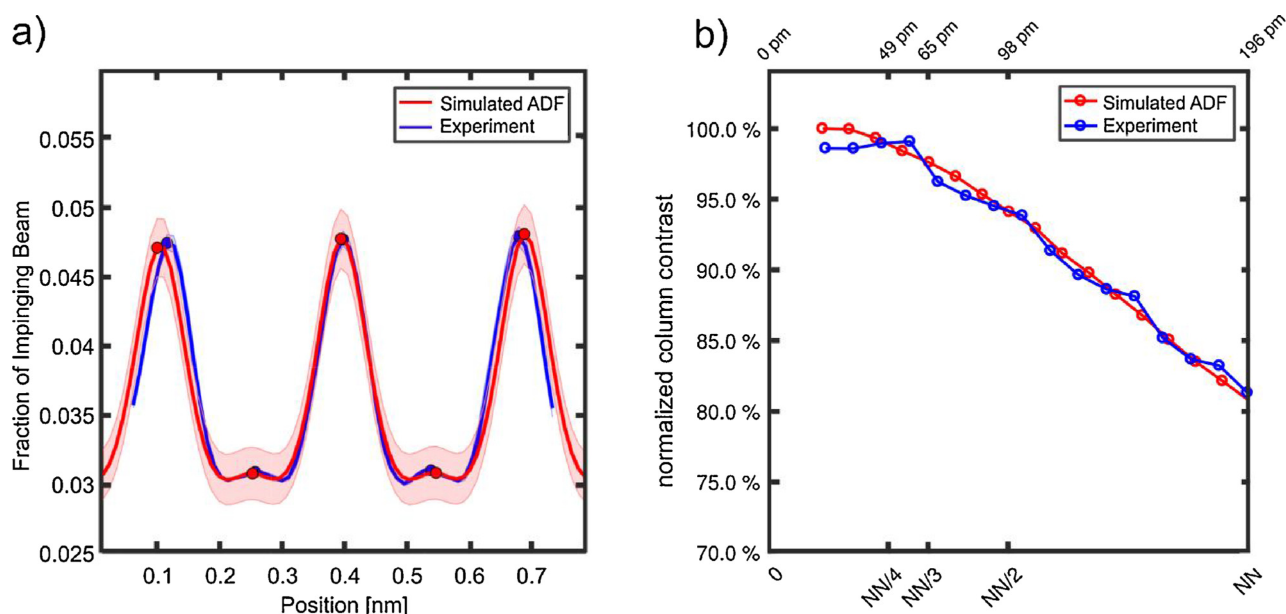

Fig. 4. (a) A line profile over the averaged unit cell in the reference mainphase domain of GaP is shown experimentally (blue), as well as a proper contrast matched simulation (red). (b) Alternatively, the (normalized) column contrast is evaluated using two dimensional circular masks of different sizes. It is clearly seen that the experiment is well represented by the simulated curves when proper parameters for the PSF and amorphous layers are used. (For interpretation of the references to color in this figure legend, the reader is referred to the web version of this article).

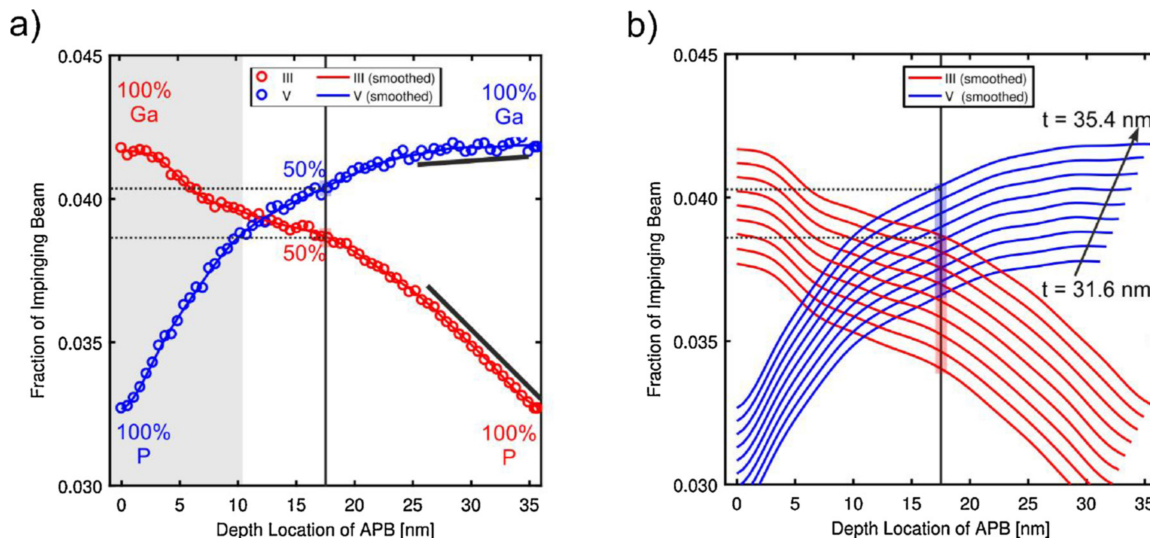

Fig. 5. (a) The on-column intensities of both a initially Ga containing group-III and a P containing group-V column extracted from a simulation database are shown for a specific thickness. With an increasing AP/MP ratio the intensity changes gradually towards a full inversion (100% AP). It is noteworthy that the turning point is not identical due to channeling effects. (b) The corresponding array of curves for all relevant thicknesses is needed for the mapping of APB locations in an actual micrograph due to thickness variations. (For interpretation of the references to color in the text, the reader is referred to the web version of this article).

dominated group-III column. On the other hand, if the domain inversion takes place far underneath the top surface, the intensity change of the group-V column becomes very low. The opposite is the case for the initial group-III sub-lattice, where the decrease is continuously progressive even for very deep positions of the APB. It is noteworthy, that the column intensities is depending on whether the MP or the AP is transmitted first as can be seen for the case of 50% Ga and 50% P (c.f. Fig. 5a). This issue can be accounted for by taken good care of the sample orientation in the microscope which is in particular easy for a PV geometry used in this work. In combination with the knowledge that the APB forms due to single steps at the silicon interface, the APB depth can be determined uniquely.

Taking into account the different thicknesses within the experimental image, a complete set of curves is calculated (Fig. 5b). Herein, it is clearly seen that the thicker the crystal the stronger the scattering power. This effect is very significant especially considering the low slopes for the initial group-V lattice. This amplifies the relevance of carefully measuring and correctly accounting for local thicknesses.

After processing the stack of simulated images as described above, the mapping from intensities into APB location value becomes straight forward as long as the local thickness is considered. Fig. 6a shows the position of the APB measured from the top surface in nanometers. It is clearly seen that the anticipated APB for the MP is – per definition – close to zero. In contrast, the MP is almost perfectly set to the local thickness value in terms of APB position. It is worth mentioning that neither scaling nor data fitting is applied. The image is the direct mapping from column intensity to best matching APB position. The only constraint is the thickness value associated to each column. The same image region is shown for visualization as a 3D model (Fig. 6b) with aspect ratios of 1:1:3 for x:y:z. Herein, a thickness gradient from

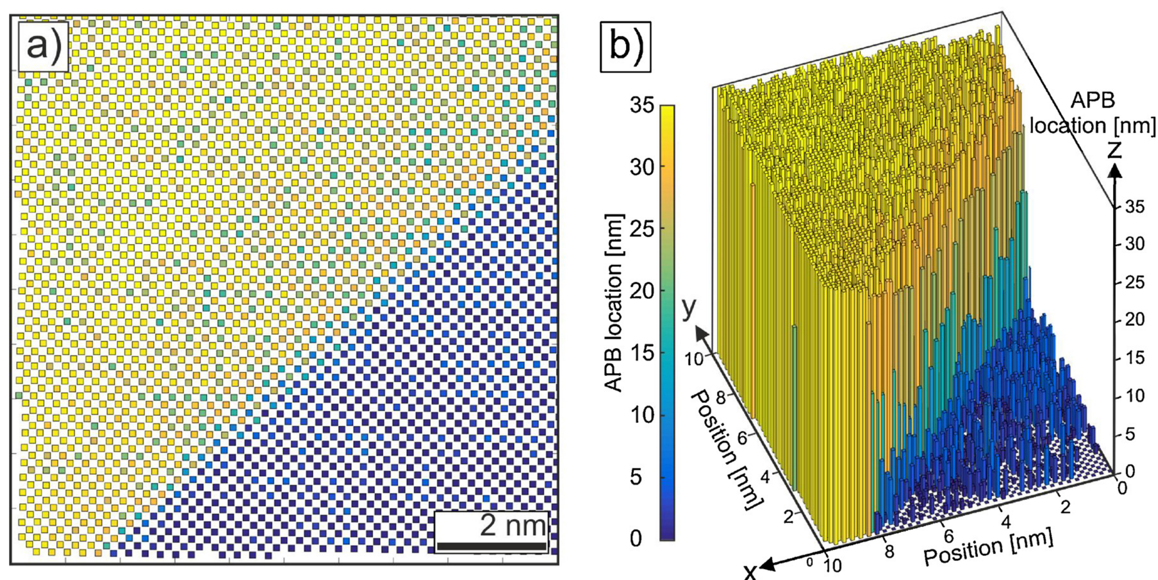

Fig. 6. (a) After the calculation APB positions from experimental intensities their value can be shown color-coded. In addition, the boundary can be illustrated as a 3D entity effectively suppressing the visibility of the mainphase domain (b). (For interpretation of the references to color in the text, the reader is referred to the web version of this article).

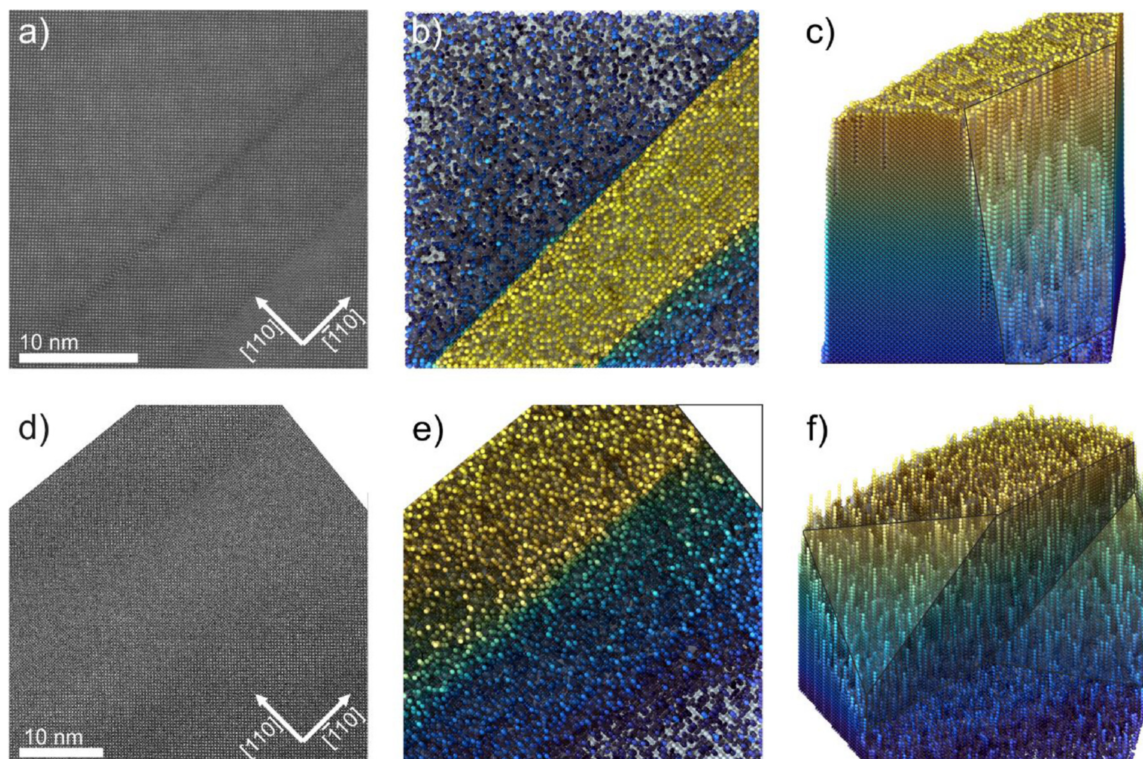

Fig. 7. (a, d) High resolution HAADF STEM micrographs showing different APB boundaries under rapid acquisition conditions over a moderately large field of view. (b, e) Reconstructed 3D models of (a) and (d) respectively, are shown with additional supportive color coding of the calculated APB position. The models are furthermore mapped into a rigid zinc blende structure. These 3D structures are shown with perspective (c, f) and contain several kinked interfaces. (For interpretation of the references to color in the text, the reader is referred to the web version of this article).

the top right to the bottom left edge can be anticipated. Taking a look to the blueish MP region, the measurement error due to image intensity variations can be recognized.

In addition, one can notice a slight broadening of the {110}-boundary of about three lattice planes directly at the interface. Considerations about this finding and the scope of validity and accuracy will be discussed in more detail in the following section.

Besides this initial high magnification benchmarking with fast acquisition and stack alignment, we applied the analysis scheme to images showing APBs on a much larger scale.

Fig. 7a and d shows high resolution micrographs with $(4096\ \text{px})^2$ and a sampling of about 100 px nm^{-1} and 140 px nm^{-1} respectively providing an imaging field of view of about $(43\ \text{nm})^2$ and $(32\ \text{nm})^2$ respectively. Both images were acquired with a dwell time of about 1 µs reducing the image drift as well as possible.

The first STEM HAADF image shows a part of a bigger APD enclosed by a {110} boundary and a kinked boundary on the top right hand side. Mapping the estimated APB location for all ~22,000 columns is carried out in such a way that a valid zinc blende crystal is generated. Using the *Open Visualization Tool* (*OVITO*) a 3D file is rendered and shown in PV perspective (Fig. 7b). Herein, the APB height value is additionally color-coded with a maximum APB position corresponding to the pure AP region (yellow region) with a thickness of about 32 nm (Stukowski, 2009).

Besides the previously discussed straight {110}-boundary, the second boundary is approximately parallel to the [1-10] direction with a small slope in [110] direction. The resulting angle shown in Fig. 7c indicates an approximate stepwise increase of the APB position from low to high. The angle between the interface plane and the APB is about 81° and appears to be consisting of strong {110} components. The overall resulting APB plane is highlighted by a semi-transparent guide to the eye (dark frame).The second image (cf. Fig. 7d) shows a clearly more complex course of the APB. In this image, it is obviously hard to estimate the transition behavior of the two phases only by eye. After mapping the calculated APB positions to the 55,000 atomic columns of a 3D crystal model, it is already possible to anticipate two distinct features of this particular APB (cf. Fig. 7e). Firstly, a clearly abrupt transition region is noticeable where a strong amount of {110} planes form the APB. In contrast to this straight APB course there are two regions showing a similar inclination towards the sample surface (cf. Fig. 7f). The left region shows a main angle of about 52°. A similar angle of about 53° is found at the region at the upper right hand side of the image. Besides these material features, it is worth mentioning that two scan distortions cause erratic mapping seen as horizontal lines in Fig. 7e.

4. Discussion

As mentioned before, the buried interface between the AP and the MP can be remarkably well reconstructed. Nonetheless, some irregularities are striking and will be discussed in the following.

At first, it is seen in Fig. 6a that there are several single columns significantly deviating from the respective base level of either the AP or MP domain. Their values are in the order of 10 nm therefore considerably high. Although some of the features near the interface might be actual features, the vast majority is located in the "bulk" parts of the phases. In order to identify the erratic mappings more carefully, the corresponding sublattices haven been separated (Fig. 8a, d) and statistically evaluated (Fig. 8b, c, e, f).

The reconstruction from group-V column positions only (Fig. 8a) (defined with respect to the MP) and from group-III columns (Fig. 8d) respectively, shows a very visual cause of the aforementioned mapping errors. While in Fig. 8a the MP group-V columns are occupied by the dark P atoms (V_P), the AP is decorated by Ga (V_{Ga}). An analogue

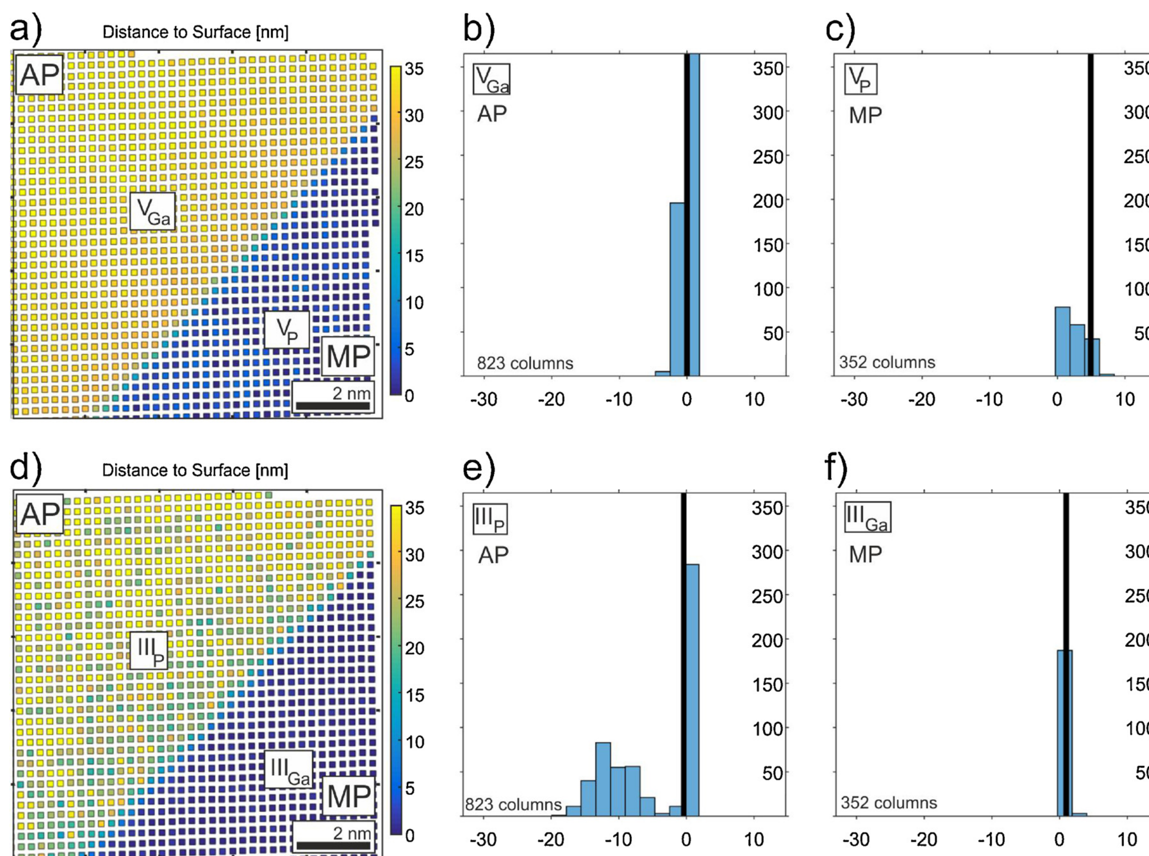

Fig. 8. (a, d) The lattice columns are split into the respective sub lattices (III and V) and the calculated APB position in [nm] is color coded. (b–c) Show the deviation from the respective pure phase for group V lattice sites and group-III lattice sites (e, f), respectively.

situation holds true for the group-III sub-lattice where the MP group-III sub-lattice (III_{Ga}) is almost without any outliers. In contrast, the AP domain shows a significant fluctuation (Fig. 8e). We can therefore conclude that the sub-lattice reconstructions of regions where P is located is deviating the most. To estimate the magnitude of this error in the pure phases, we calculated the distribution of the deviation with respect to the anticipated true APB value. Hence, the denoted values for the AP region are measured as deviation from the full thickness value (Fig. 8b, c), while the MP regions are deviating from the zero value (Fig. 8e, f). Due to the small numbers, all histograms show the deviation (abscissa) measured in the number of deviating atoms. The conversion is easily carried out since the projected column increases by one atom every unit cell spacing.

These histograms clearly show that the deviation is the highest for where the column intensity is low. On the other hand, it is seen in Fig. 6a that the "mapping curve" on its own shows no such trend. The fact that the slope steepness is significantly lower for the blue curve (V_{XY}) than for the red curve (III_{XY}) has no apparent effect on the accuracy of the reconstruction procedure. On the contrary, it is clearly shown that the experimental contrast between column and background is the most crucial aspect. In fact, it is not surprising that the mapping becomes erratic when the column intensity comes down to the very level of the background.

It is worth mentioning that this kind of analysis is not fully accounting for all deviations that affect the reconstruction. Firstly, the way the error estimation is carried out is causing a high peak at the "correct" APB location which is caused by the constraints of the analysis. Since the thickness estimation is approximating the specimen with linear gradients there is additional error included. This thickness limitation leads to a clipping most prominent in Fig. 8e causing a strong peak around zero. Alternatively, negative APB positions could be used which is equally artificial. Nonetheless, it is quite clear that a broader error distribution must be appreciated for all cases and in particular those of (dark) P dominated columns.

Albeit the rather simple appearance of the {110}-boundary, it is the extreme case in terms of a benchmarking sample due to several aspects. Firstly, the mapping of dark atoms due to high APB values is shown to be affected the strongest. Secondly, the projected bond strain in these APBs is the highest, since the strain caused by the so called Ga-Ga and P-P "wrong bonds" at the very interface of both phases has a maximum component orthogonal to the electron trajectory in the microscope. Therefore, the distortion of the columnar arrangement has the highest impact on the on-column intensities since these are shifted from their ideal crystal positions the most (Beyer et al., 2017b). Hence, the {110}-boundary is the worst case scenario in terms of accuracy. The influence of column bending can be noticed – even in these HAADF images (Grillo, 2009) – as a discrepancy between the estimated APB position mapped from the group-III and group-V sub-lattices (cf. Fig. 6a) at the very interface. It should be mentioned that the actual modelling of such bond strain is not trivial. Whereas accurate DFT calculations can be carried out for small periodic supercells the elastic relaxation of the actual supercells used in this work is unfeasible due to their size and a simple derivation of empirical potentials (i.e. Keating VFF) for such strongly charged wrong bonds is challenging, too. In addition it is clear from the findings of this work that the situation of actual APB formation can be much more complex. The actual strain therefore depends on the existing structure and could be best modelled as a iterative refinement using e.g. results derived from our technique.

Alternatively, there is the possibility although generally neglected that the interface structure is affected by selective etching during the sample preparation.

Deviating from these more ideal imaging conditions into the regime

of higher noise as for the images shown in Fig. 7a and d, we can generally see a trend to higher fluctuation on a per column basis. This is presumably due to the unfavorable signal-to-noise ratio compared to aligned stack averages. In addition, it is obvious that experimental challenges like any kind of scan noise and drift have larger relevance if the acquisition time is generally higher. Nonetheless, we can show that with careful interpretation the data derived from such a reconstruction is still very valuable. The easiest approach to improve the image quality would presumably to balance the increase in dwell time at the cost of sample drift.

Regarding the experimental findings of the APD formation in GaP on exact Si(001), we can see a significant contribution of {110} boundaries, as well as various different kinked planes. These findings are in good agreement with the calculations of Rubel et al. where the {110}-boundaries are shown to be the most energetically favorable configuration (Rubel and Baranovskii, 2009). Nevertheless, judging from the relatively small subset presented in this manuscript there is no clear preference for a specific inclined lattice facet. It is also worth mentioning that this result agrees with a thermally driven APB formation corresponding to high growth temperatures without a specific preference of resulting lattice planes.

As a final remark, we want to point out that albeit comprehensive measurements have been taken in order to reduce the effects of amorphous damage layers caused by oxidation and ion beam milling their effects are modelled in a very simplistic way. The details of these layers are beyond the scope of this work, but are highlighted elsewhere (Belz et al., 2016). In addition, as seen in Fig. 5b the thickness mapping is a very crucial process and a linear model (although reasonable) might be oversimplifying the situation. As a further refinement, we find that local (gliding) averaging is a useful tool for measuring the thickness variations more accurately on an atomic scale.

In total, we show that the reconstruction is generally precise and the sources of error as e.g. the lack of contrast with respect to the background level as well as the saturation effect seen for thick samples can be identified and treated correspondingly.

5. Conclusion

We have shown that the atomic scale 3D reconstruction of APDs by means of quantitative HAADF STEM measurements is not only feasible but remarkably accurate as benchmarked for the reconstruction error in both phases under ideal imaging conditions (cf. Figs. 6,8). The presented approach is capable of doing so by using only a single HAADF image with or without stack averaging and the chemical simplicity of the binary material GaP. As elaborated before, no scaling or fitting is applied except of an additional blurring of the simulated images in order to match the experimental *on-column* contrast for both sub-lattice sites. It is noteworthy that this additional blur is strongly related to the finite source size which is not explicitly included in our current multislice simulations. In addition, we find that the handling of the experimental thickness is a decisive factor and show that a bi-linear interpolation, as well as a local averaging approach provide accurate results for a field of view of at least $(42\ nm)^2$.

Various APBs were successfully reconstructed up to about 35 nm by means of quantitative HAADF measurements in combination with a set of frozen lattice multi-slice simulations proofing the principle of this particular reconstruction technique for general APB planes.

We anticipate that the method can be used for various other material systems and tasks like e.g. the characterisation of structural defects in crystals, facetting of nanoparticles and determination of nanostructures. In addition, we expect that the depth information can most easily be retrieved if a large atomic contrast between the constituents is existing.

Nonetheless, the possibilities for application of such reconstructions are manifold and only the test case of GaP APBs is shown in this study.

As a future improvement, especially for materials with less contrast, the inclusion of through-focus series can be considered as the shift of focus emphasizes the scattering response to some degree.

Acknowledgements

The authors acknowledge support from the German Science Foundation (SFB 1083: “Structure and Dynamics of Internal Interfaces”) and the German Federal Ministry of Education and Research through the project “MehrSi 03SF0525C”.

References

Alania, M., Altantzis, T., De Backer, A., Lobato, I., Bals, S., Van Aert, S., 2016. Depth sectioning combined with atom-counting in HAADF STEM to retrieve the 3D atomic structure. Ultramicroscopy 177, 36–42. https://doi.org/10.1016/j.ultramic.2016.11.002.

Allen, L.J., D'Alfonso, A.J., Findlay, S.D., 2015. Modelling the inelastic scattering of fast electrons. Ultramicroscopy 151, 11–22. https://doi.org/10.1016/j.ultramic.2014.10.011.

Belz, J., Beyer, A., Torunski, T., Stolz, W., Volz, K., 2016. Direct investigation of (sub-) surface preparation artifacts in GaAs based materials by FIB sectioning. Ultramicroscopy 163, 19–30. https://doi.org/10.1016/j.ultramic.2016.01.001.

Beyer, A., Németh, I., Liebich, S., Ohlmann, J., Stolz, W., Volz, K., 2011. Influence of crystal polarity on crystal defects in GaP grown on exact Si (001). J. Appl. Phys. 109. https://doi.org/10.1063/1.3567910.

Beyer, A., Ohlmann, J., Liebich, S., Heim, H., Witte, G., Stolz, W., Volz, K., 2012. GaP heteroepitaxy on Si(001): correlation of Si-surface structure, GaP growth conditions, and Si-III/V interface structure. J. Appl. Phys. 111. https://doi.org/10.1063/1.4706573.

Beyer, A., Haas, B., Gries, K.I., Werner, K., Luysberg, M., Stolz, W., Volz, K., 2013. Atomic structure of (110) anti-phase boundaries in GaP on Si(001). Appl. Phys. Lett. 103. https://doi.org/10.1063/1.4815985.

Beyer, A., Belz, J., Knaub, N., Jandieri, K., Volz, K., 2016a. Influence of spatial and temporal coherences on atomic resolution high angle annular dark field imaging. Ultramicroscopy 169, 1–10. https://doi.org/10.1016/j.ultramic.2016.06.006.

Beyer, A., Straubinger, R., Belz, J., Volz, K., 2016b. Local sample thickness determination via scanning transmission electron microscopy defocus series. J. Microsc. 262, 171–177. https://doi.org/10.1111/jmi.12284.

Beyer, A., Duschek, L., Belz, J., Oelerich, J.O., Jandieri, K., Volz, K., 2017a. Influence of surface relaxation of strained layers on atomic resolution ADF imaging. Ultramicroscopy 181, 8–16. https://doi.org/10.1016/j.ultramic.2017.04.019.

Beyer, A., Duschek, L., Belz, J., Oelerich, J.O., Jandieri, K., Volz, K., 2017b. Surface relaxation of strained Ga(P,As)/GaP heterostructures investigated by HAADF STEM. J. Microsc. 268, 239–247. https://doi.org/10.1111/jmi.12622.

Bleloch, A.L., Castell, M.R., Howie, A., Walsh, C.A., 1994. Atomic and electronic Z-contrast effects in high-resolution imaging. Ultramicroscopy 54, 107–115. https://doi.org/10.1016/0304-3991(94)90109-0.

Cho, N.H., Carter, C.B., 2001. Formation, faceting, and interaction behaviors of antiphase boundaries in GaAs thin films. J. Mater. Sci. 36, 4209–4222. https://doi.org/10.1023/A:1017981324721.

del Alamo, J.A., 2011. Nanometre-scale electronics with III–V compound semiconductors. Nature 479, 317–323. https://doi.org/10.1038/nature10677.

Desplanque, L., El Kazzi, S., Coinon, C., Ziegler, S., Kunert, B., Beyer, A., Volz, K., Stolz, W., Wang, Y., Ruterana, P., Wallart, X., 2012. Monolithic integration of high electron mobility InAs-based heterostructure on exact (001) Silicon using a GaSb/GaP accommodation layer. Appl. Phys. Lett. 101, 142111. https://doi.org/10.1063/1.4758292.

Feifel, M., Ohlmann, J., Benick, J., Rachow, T., Janz, S., Hermle, M., Dimroth, F., Belz, J., Beyer, A., Volz, K., Lackner, D., 2017. MOVPE grown gallium phosphide-silicon heterojunction solar cells. IEEE J. Photovolt. 7, 502–507. https://doi.org/10.1109/JPHOTOV.2016.2642645.

Gonnissen, J., De Backer, A., den Dekker, A.J., Sijbers, J., Van Aert, S., 2016. Atom-counting in high resolution electron microscopy: TEM or STEM - that's the question. Ultramicroscopy 174, 112–120. https://doi.org/10.1016/j.ultramic.2016.10.011.

Grillo, V., 2009. The effect of surface strain relaxation on HAADF imaging. Ultramicroscopy 109, 1453–1464. https://doi.org/10.1016/j.ultramic.2009.07.010.

Grillo, V., Carlino, E., Glas, F., 2008. Influence of the static atomic displacement on atomic resolution Z-contrast imaging. Phys. Rev. B 77, 054103. https://doi.org/10.1103/PhysRevB.77.054103.

Grillo, V., Mueller, K., Volz, K., Glas, F., Grieb, T., Rosenauer, A., 2011. Strain, composition and disorder in ADF imaging of semiconductors. J. Phys. Conf. Ser. 326, 012006. https://doi.org/10.1088/1742-6596/326/1/012006.

Haider, M., Rose, H., Uhlemann, S., Schwan, E., Kabius, B., Urban, K., 1998. A spherical-aberration-corrected 200kV transmission electron microscope. Ultramicroscopy 75, 53–60. https://doi.org/10.1016/S0304-3991(98)00048-5.

He, D.S., Li, Z.Y., 2014. A practical approach to quantify the ADF detector in STEM. J. Phys. Conf. Ser. 522, 012017. https://doi.org/10.1088/1742-6596/522/1/012017.

Howie, A., 2004. Hunting the Stobbs factor. Ultramicroscopy 98, 73–79. https://doi.org/10.1016/j.ultramic.2003.08.002.

Jones, L., Nellist, P.D., 2013. Identifying and correcting scan noise and drift in the scanning transmission electron microscope. Microsc. Microanal. 1050–1060. https://doi.org/10.1017/S1431927613001402.

Jones, L., Macarthur, K.E., Fauske, V.T., Van Helvoort, A.T.J., Nellist, P.D., 2014. Rapid estimation of catalyst nanoparticle morphology and atomic-coordination by high-resolution Z-contrast electron microscopy. Nano Lett. 14, 6336–6341. https://doi.org/10.1021/nl502762m.

Jones, L., Yang, H., Pennycook, T.J., Marshall, M.S.J., Van Aert, S., Browning, N.D., Castell, M.R., Nellist, P.D., 2015. Smart Align—a new tool for robust non-rigid registration of scanning microscope data. Adv. Struct. Chem. Imaging 1 (8). https://doi.org/10.1186/s40679-015-0008-4.

Kelly, T.F., Miller, M.K., 2007. Invited review article: atom probe tomography. Rev. Sci. Instrum. 78. https://doi.org/10.1063/1.2709758.

Kirkland, E.J., 2010. Advanced Computing in Electron Microscopy. Springer Science & Business Mediahttps://doi.org/10.1007/978-1-4419-6533-2.

Krause, F.F., Schowalter, M., Grieb, T., Müller-Caspary, K., Mehrtens, T., Rosenauer, A., 2016. Effects of instrument imperfections on quantitative scanning transmission electron microscopy. Ultramicroscopy 161, 146–160. https://doi.org/10.1016/j.ultramic.2015.10.026.

Krivanek, O.L., Dellby, N., Spence, A.J., Camps, R.A., Brown, L.M., 1997. Aberration correction in the STEM. Inst. Phys. Conf. Ser. EMAG97, vol. 153, 35–40. https://doi.org/10.1142/9781848167902_0009.

Kroemer, H., 1987. Polar-on-nonpolar epitaxy. J. Cryst. Growth 81, 193–204. https://doi.org/10.1016/0022-0248(87)90391-5.

Kunert, B., Németh, I., Reinhard, S., Volz, K., Stolz, W., 2008. Si (001) surface preparation for the antiphase domain free heteroepitaxial growth of GaP on Si substrate. Thin Solid Films 517, 140–143. https://doi.org/10.1016/j.tsf.2008.08.077.

LeBeau, J., Findlay, S., Allen, L., Stemmer, S., 2008. Quantitative atomic resolution scanning transmission electron microscopy. Phys. Rev. Lett. 100, 206101. https://doi.org/10.1103/PhysRevLett.100.206101.

LeBeau, J.M., Findlay, S.D., Allen, L.J., Stemmer, S., 2010. Position averaged convergent beam electron diffraction: theory and applications. Ultramicroscopy 110, 118–125. https://doi.org/10.1016/j.ultramic.2009.10.001.

Liebich, S., Zimprich, M., Beyer, A., Lange, C., Franzbach, D.J., Chatterjee, S., Hossain, N., Sweeney, S.J., Volz, K., Kunert, B., Stolz, W., 2011. Laser operation of Ga(NAsP) lattice-matched to (001) silicon substrate. Appl. Phys. Lett. 99. https://doi.org/10.1063/1.3624927.

Loane, R.F., Xu, P., Silcox, J., 1991. Thermal vibrations in convergent-beam electron diffraction. Acta Crystallogr. Sect. A 47, 267–278. https://doi.org/10.1107/S0108767391000375.

Martinez, G.T., Rosenauer, A., De Backer, A., Verbeeck, J., Van Aert, S., 2014. Quantitative composition determination at the atomic level using model-based high-angle annular dark field scanning transmission electron microscopy. Ultramicroscopy 137, 12–19. https://doi.org/10.1016/j.ultramic.2013.11.001.

Midgley, P.A., 2003. Energy filtered transmission Electron microscopy (EFTEM) and the use of. Microsc. Microanal. 9, 1574–1575. https://doi.org/10.1017/S1431927603447879.

Midgley, P.A., Weyland, M., 2003. 3D electron microscopy in the physical sciences: the development of Z-contrast and EFTEM tomography. Ultramicroscopy 96, 413–431. https://doi.org/10.1016/S0304-3991(03)00105-0.

Mkhoyan, K.A., MacCagnano-Zacher, S.E., Thomas, M.G., Silcox, J., 2008. Critical role of inelastic interactions in quantitative electron microscopy. Phys. Rev. Lett. 100, 1–4. https://doi.org/10.1103/PhysRevLett.100.025503.

Muller, D.A., Voyles, P.M., Kirkland, E.J., 2004. Depth-dependent imaging of individual dopant atoms in silicon. Microsc. Microanal. 10, 291–300. https://doi.org/10.1017/S1431927604040012.

Németh, I., Kunert, B., Stolz, W., Volz, K., 2008. Heteroepitaxy of GaP on Si: correlation of morphology, anti-phase-domain structure and MOVPE growth conditions. J. Cryst. Growth 310, 1595–1601. https://doi.org/10.1016/j.jcrysgro.2007.11.127.

Oelerich, J.O., Duschek, L., Belz, J., Beyer, A., Baranovskii, S.D., Volz, K., 2017. STEMsalabim: a high-performance computing cluster friendly code for scanning transmission electron microscopy image simulations of thin specimens. Ultramicroscopy 177, 91–96. https://doi.org/10.1016/j.ultramic.2017.03.010.

Pennycook, S.J., Jesson, D.E., 1991. High-resolution Z-contrast imaging of crystals. Ultramicroscopy 37, 14–38. https://doi.org/10.1016/0304-3991(91)90004-P.

Rubel, O., Baranovskii, S.D., 2009. Formation energies of antiphase boundaries in GaAs and GaP: an ab initio study. Int. J. Mol. Sci. 10, 5104–5114. https://doi.org/10.3390/ijms10125104.

Seidman, D.N., 2007. Three-dimensional atom-probe tomography: advances and applications. Annu. Rev. Mater. Res. 37, 127–158. https://doi.org/10.1146/annurev.matsci.37.052506.084200.

Stukowski, A., 2009. Visualization and analysis of atomistic simulation data with OVITO–the Open Visualization Tool. Model. Simul. Mater. Sci. Eng. 18, 015012. https://doi.org/10.1088/0965-0393/18/1/015012.

Uhlemann, S., Haider, M., 1998. Residual wave aberrations in the first spherical aberration corrected transmission electron microscope. Ultramicroscopy 72, 109–119. https://doi.org/10.1016/S0304-3991(97)00102-2.

Volz, K., Beyer, A., Witte, W., Ohlmann, J., Nmeth, I., Kunert, B., Stolz, W., 2011. GaP-nucleation on exact Si (0 0 1) substrates for III/V device integration. J. Cryst. Growth 315, 37–47. https://doi.org/10.1016/j.jcrysgro.2010.10.036.

Wang, Z., Abbasi, A., Dave, U., De Groote, A., Kumari, S., Kunert, B., Merckling, C., Pantouvaki, M., Shi, Y., Tian, B., Van Gasse, K., Verbist, J., Wang, R., Xie, W., Zhang, J., Zhu, Y., Bauwelinck, J., Yin, X., Hens, Z., Van Campenhout, J., Kuyken, B., Baets, R., Morthier, G., Van Thourhout, D., Roelkens, G., 2017. Novel light source integration approaches for silicon photonics. Laser Photonics Rev. https://doi.org/10.1002/lpor.201700063.

6.1.3 Publication 3

Citation

Surface relaxation of strained Ga (P, As)/GaP heterostructures investigated by HAADF STEM
A. Beyer, L. Duschek, J. Belz, J.O. Oelerich, K. Jandieri, K. Volz, Journal of Microscopy **268**, p.239–247, 2017, DOI: 10.1111/jmi.12622

Abstract

The surfaces of thin transmission electron microscopy (**TEM)** specimens of strained heterostructures can relax. The resulting bending of the lattice planes significantly influences high angle annular dark-field (**HAADF**) measurements. We investigate the impact by evaluating the intensities measured at the atomic columns as well as their positions in high-resolution HAADF images. In addition, the consequences in the diffraction plane will be addressed by simulated position averaged convergent beam electron diffraction (**PACBED**) patterns. The experimental column intensities and positions acquired from a strained Ga(P,As) quantum well (**QW)** embedded in a GaP matrix agree very well with frozen phonon contrast simulations , if the surface relaxation is taken into account by finite element relaxation. Neglecting the surface relaxation the As content of the QW can be significantly underestimated. Taking the effects into account correctly, we find the lower interface of the investigated Ga(P,As) QW is atomically abrupt whereas the upper one is smeared out.

Contributions

Andreas Beyer wrote the majority of the manuscript and carried out and designed the STEM measurements and programmed most of the image processing tools. Lennart Duschek did data processing , super cell image simulations as well as programming of data evaluation tools and wrote the respective parts of the manuscript. Jürgen Belz programmed the FE relaxation software and a parametric super cell construction interface in addition to the corresponding text paragraphs. Jan Oliver Oelerich wrote the multi-slice code and implemented most of the computation cluster utilities. Kakhaber Jandieri, Lennart Duschek and JÃ¼rgen Belz integrated the VFF code with the FE code and created utilities for a consistent work flow. Kerstin Volz supervised the work and secured the funding to support this study.

Reprinted from *Journal of Microscopy **268**,239–247,2017*, Copyright 2017, with permission Elsevier.

Journal of
Microscopy

Journal of Microscopy, Vol. 268, Issue 3 2017, pp. 239–247 doi: 10.1111/jmi.12622
Received 23 May 2017; accepted 7 August 2017

Surface relaxation of strained Ga(P,As)/GaP heterostructures investigated by HAADF STEM

ANDREAS BEYER, LENNART DUSCHEK, JÜRGEN BELZ, JAN OLIVER OELERICH, KAKHABER JANDIERI & KERSTIN VOLZ
Materials Science Center and Faculty of Physics, Philipps-Universität Marburg, Marburg, Germany

Key words. Atomic resolution, frozen phonon simulations, scanning transmission electron microscopy, strained interfaces, surface relaxation.

Summary

The surfaces of thin transmission electron microscopy (TEM) specimens of strained heterostructures can relax. The resulting bending of the lattice planes significantly influences high-angle annular dark field (HAADF) measurements. We investigate the impact by evaluating the intensities measured at the atomic columns as well as their positions in high-resolution HAADF images. In addition, the consequences in the diffraction plane will be addressed by simulated position averaged convergent beam electron diffraction (PACBED) patterns.
The experimental column intensities and positions acquired from a strained Ga(P,As) quantum well (QW) embedded in a in a GaP matrix agree very well with frozen phonon contrast simulations, if the surface relaxation is taken into account by finite element relaxation. Neglecting the surface relaxation the As content of the QW can be significantly underestimated. Taking the effects into account correctly, we find that the lower interface of the investigated Ga(P,As) QW is atomically abrupt whereas the upper one is smeared out.

Introduction

Aberration corrected scanning transmission electron microscopy (STEM) has become an essential method in the field of materials science (Nellist *et al.*, 2004; Krivanek *et al.*, 2010). In particular, the high-angle annular dark field (HAADF) technique was proven to be a valuable tool in addressing complex heterostructures due to the easily interpretable Z contrast (Pennycook, 1989). Such heterostructures consist of various materials and therefore are usually strained (Tan *et al.*, 2016; Wang *et al.*, 2016; Xu *et al.*, 2016).

When an electron transparent transmission electron microscopy (TEM) sample is prepared from such a strained heterostructure, the strain partially relaxes at the free surface (Gibson & Treacy, 1984; Treacy *et al.*, 1985; De Caro *et al.*, 1995). This leads to a deformation at the surface and more importantly, a bending of the lattice planes. The strength of the bending depends on the sample geometry, that is the sample thickness and the widths of the constituent layers (Treacy *et al.*, 1985). The finite element (FE) formalism can be used to model the displacement fields for a given sample geometry (Rosenauer *et al.*, 2006; De Caro *et al.*, 1997). The mistilt angle of the lattice planes with respect to perfect zone axis conditions can serve as a measure for the strength of the lattice plane bending (Grillo, 2009) as well as the lateral mean square displacement M of the atomic columns. The value M_i for the i-th column is determined via:

$$M_i = \sum_{k=1}^{N} \frac{(x_k - \bar{x}_i)^2}{N} + \sum_{k=1}^{N} \frac{(y_k - \bar{y}_i)^2}{N}, \qquad (1)$$

where $\bar{x}_i$ and $\bar{y}_i$ are the mean x and y coordinates of the respective atomic column, x_k and x_k are the coordinates of the k-th atom in this column and N denotes the number of atoms in this column.

This bending significantly influences the intensity in conventional high-resolution (HR) TEM imaging (De Caro *et al.*, 1997) as well as the positions of the atomic columns in the HR image, which influences strain mapping of strained quantum wells (Bierwolf *et al.*, 1993; Jouneau *et al.*, 1994; Walther *et al.*, 1995; Tillmann *et al.*, 2000) and islands (Tillmann *et al.*, 1996). Because the atoms along a column are no longer perfectly aligned, the channelling conditions change and the HAADF intensity will be influenced as well (Grillo, 2009). More to the point, the dechannelling effect of the electrons (Amali *et al.*, 1997; Perovic *et al.*, 1993; Cowley & Huang, 1992; Huang, 1947; Grillo, 2009) leads to a clear intensity deterioration at a strained interface (Yu *et al.*, 2004; Beyer *et al.*, 2017; Grillo, 2009). The intensity change observed in simulated HAADF images across a strained GaP/GaAs interface perfectly correlates with the lateral displacement M (Beyer *et al.*, 2017). This can impede the characterisation of a sample,

Correspondence to: Andreas Beyer, Materials Science Center and Faculty of Physics, Philipps-Universität Marburg, Hans-Meerweinstraße 6, 35032 Marburg, Germany. Tel +49 6421 28 25704; fax +49 6421 28935; e-mail: andreas.beyer@physik.uni-marburg.de

© 2017 The Authors
Journal of Microscopy © 2017 Royal Microscopical Society

because the intensity change introduced by the surface relaxation can easily be misinterpreted as change of the chemical composition.

Often, the effect of surface relaxation is counter-balanced by averaging the intensity of an atomic column over a certain area, for example the Voronoi cell of each column, and therefore attributing the dechannelled intensity back to the respective column (Rosenauer *et al.*, 2011; E *et al.*, 2013). However, because surface relaxation not only leads to a redistribution of the intensity in real space but also in reciprocal space, some intensity is scattered into lower angles. Therefore, even applying an averaging approach, intensity dips at the interface are observed (Grieb *et al.*, 2012), which could be compensated by combining measurements with different angular scattering ranges (Grieb *et al.*, 2013).

However, all averaging approaches may hide some information, which was present in atomic resolution HAADF images. Especially for materials consisting of elements with different properties, for example covalent radius or electronegativity, the introduced displacements of the atoms and the resulting change in intensity of the atomic columns are important. The correct treatment of the surface relaxation effects allows the investigation of the interfaces in more complex materials, where such additional static atomic displacements (SADs) are present, for example Ga(N,As) in GaP, (Ga,In)(N,As) in GaAs (Grieb *et al.*, 2014) or (Ga,In)N in GaN (Rosenauer *et al.*, 2011). Recently we examined the effects of surface relaxation theoretically by simulated atomic resolution HAADF and low-angle annular dark field (LAADF) images (Beyer *et al.*, 2017).

Here we use the example of Ga(P,As) quantum wells (QWs) embedded in GaP to visualise these effects in experiments. We will show the influence of surface relaxation in real space by investigating the atomic column intensities as well as their positions in HAADF measurements. The impact on the scattering distribution in reciprocal space will be discussed via simulated position averaged convergent beam electron diffraction (PACBED) patterns. Furthermore, we will discuss the implications of the surface relaxation for different (S)TEM methods. We will show that the contrast simulations, taking into account the bending of the lattice planes, resemble the experiment very well.

Experimental

Ga(P,As) multi-QWs were grown via metalorganic vapour phase epitaxy (MOVPE) on GaP(100) substrate. The layer width of 11.7 nm and the As content of 65.5% were determined by modelling the 400 X-ray diffraction (XRD) rocking curves acquired in a Panalytical X′Pert Pro system (PANalytical GmbH, Kassel-Waldau, Germany). The elastic constants and lattice parameters used were taken from (Vurgaftman *et al.*, 2001).

The TEM specimens were prepared by mechanical polishing utilising an Allied MULTIPREP system (Allied High Tech Products, Inc., Rancho Dominguez, California, United States). The crystallographic [001] direction was chosen as viewing direction. Subsequent argon ion milling was carried out in a GATAN PIPS (Gatan, Pleasanton, California, United States) until electron transparency was achieved. Hereby, the voltage was progressively reduced from 5 kV to a final value of 1.2 kV to minimise amorphous surface layers and damage of the thin specimens.

HAADF measurements were carried out in a double C_S-corrected JEOL JEM 2200FS (JEOL [Germany] GmbH Freising, Germany) operating at 200 kV. An annular detector range from 73 to 174 mrad and a probe semiconvergence angle of 24 mrad were used. Series of 20 individual images were acquired and aligned nonrigidly using the Smart-Align software (Jones *et al.*, 2015) to improve the signal-to-noise ratio. The image intensity was normalised to the intensity of the impinging beam applying the approach described in (He & Li, 2014). The TEM sample thickness was determined to be 22 nm by comparing the normalised intensity in reference regions sufficiently far away (>20 nm) from the bent QW with adequate image simulations, as successfully performed for example in Beyer *et al.* (2016b).

In order to account for the effect of surface relaxation, super cells modelling the sample geometry were created and relaxed via FE applying linear elastic theory. In these cells abrupt interfaces between barrier and QW were assumed. Within the QW the two different elements present on the group V sublattice, that is P and As, were distributed randomly. Due to the discrete number of atoms in the super cell, the As content is 65.9% instead of the 65.5%, which was determined via XRD. Additional SADs, caused by the two different elements, were taken into account by a subsequent valence force field (VFF) relaxation (Keating, 1966). A model of the central part of the surface relaxed super cell is shown in Figure 1(A). Periodic boundary conditions were applied along the y axis, whereas the cell was allowed to expand along the x and z directions. For the given sample geometry this results in a bulging out of the QW of $\Delta z \sim 0.35$ nm and a mistilt $\alpha \sim 10$ mrad of the formerly straight lattice planes. In the right half of Figure 1(A), the calculated displacements were multiplied by a factor of 5 for better visualisation. Because the sample thickness (22 nm) and the QW width (12 nm) are in a similar range, the surface relaxation is very prominent, as predicted for this case (Treacy *et al.*, 1985).The lateral mean square displacement of each lattice plane was calculated according to Eq. (1). The variation of the displacement across the QW is drawn in Figure 1(B). In the centre of the QW the lateral displacement is zero, because the forces of the two opposing interfaces cancel out. Across the interfaces the displacements rise to a maximum of $\sim 6 \times 10^{-4}$ nm^2 at a distance of ∼4 nm away from the respective interface. Far away from the interfaces (>10 nm) the displacements decrease to zero again, which cannot be seen in the smaller section shown here. For the purely tetragonally distorted super cell, periodic boundary conditions were applied

© 2017 The Authors

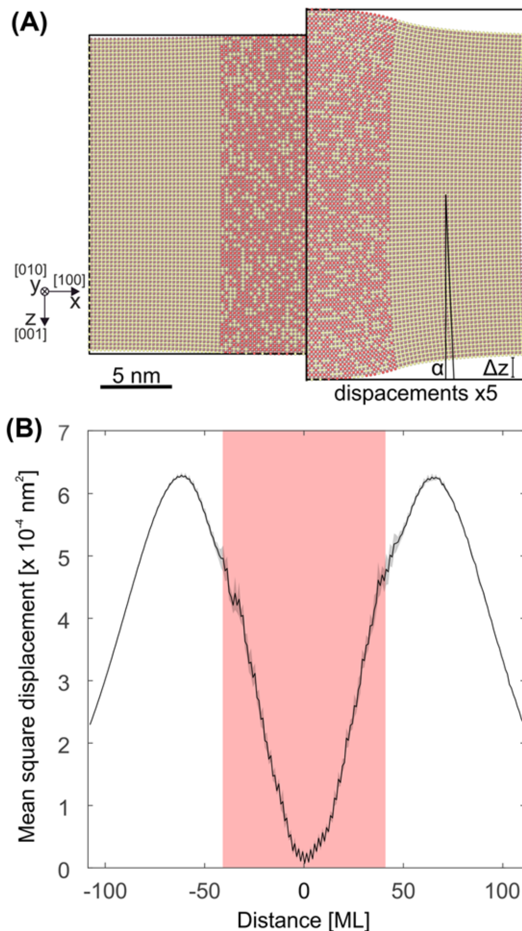

Fig. 1. Model of the surface relaxed super cell (A). In the right half of the image, the calculated displacements are multiplied by a factor of 5 for visualisation purposes. The derived displacements across the quantum well calculated according to Eq. (1) are drawn in (B).

along *y* and *z*, only expansion along the *x* axis was allowed. Both constructed super cells, a purely tetragonally distorted one as well as an additionally surface relaxed one, served as input for multislice simulations. To this end, we used the frozen phonon approach implemented in the STEMsalabim package (Oelerich *et al.*, 2017). Hereby, 7 different defoci with 10 independent phonon configurations were calculated to account for chromatic aberration and thermal diffuse scattering. The simulated images were convoluted by a Lorentzian source distribution with a width of 45 pm. Performing this simulation procedure, a nearly perfect agreement between simulation and experiment could be achieved for GaP (Beyer *et al.*, 2016a). Theoretical PACBED patterns were derived by averaging 400 simulated CBED patterns from one unit cell of the respective super cell.

Results

Here, we will illustrate the occurring effects using an experimental HAADF image. We will show that the experimental features are also found in the simulated images with good quantitative agreement. A quantitative comparison between simulation and experiment will be carried out for the intensities as well as the strain. In addition, we will discuss the scattering redistribution in the reciprocal space.

Figure 2 shows a high-resolution HAADF image of the Ga(P,As) QW grown on GaP substrate. The [100] growth direction is oriented along the *x* axis and the electron beam transmits through the sample along the *z* axis, that is the crystallographic [001] direction. The As containing layer can be identified by its brighter contrast with respect to the surrounding GaP barriers due to its larger mean atomic number. The centre of the QW was tilted into zone axis condition utilising the convergent diffraction pattern. It is worth noting that the orientation alignment has to be carried out carefully, because the bending of the lattice planes results in apparent changes of the sample orientation across the field of view. A TEM sample thickness of 22 nm was derived by comparing the experimental intensity of the GaP barrier to thickness dependent frozen phonon simulations. At a sufficiently large distance from the QW (>10 nm), the Ga columns appear nearly circular symmetric with some residual astigmatism and the image exhibits a high contrast, which can be seen in more detail in the enlarged section shown in Figure 2(B) and in false colour in Figure 2(C), where the low-intensity features are better visible. The positions of the group III and V atomic columns are marked by circles. Due to the lower scattering power, the P atomic columns are barely visible. Two positions situated horizontally between two group III or two group V columns are marked by B_{III} and B_V, respectively. In this part of the image B_{III} and B_V appear equivalent. In contrast to this region, the Ga columns in the direct vicinity of the interface (<3 nm) appear blurred and elongated along the *x* direction. In combination with the aforementioned residual astigmatism, the atomic columns appear slightly inclined with respect to the *x* axis. An enlarged view of a unit cell from this region is depicted on a greyscale and in false colour in Figures 2(D) and (E), respectively. The 4-fold symmetry seems to be broken and the B_{III} and B_V positions are no longer equivalent. Taking a closer look at the QW itself reveals that the atomic columns appear blurred close to the upper and the lower interface, whereas the central part appears sharp. This change in the image contrast across the interface (i.e. sharp at a large distance from the QW (>10 nm)⇔ blurred at the interface⇔ sharp in the centre of the QW) follows the variations in displacements which are expected across the structure (c.f. Fig. 1B).

However, in the experimental image it is not possible to prove that the changing image contrast and the elongated lattice planes are introduced by the lattice plane bending, because the surface relaxation will always be present. Complementary simulations, however, allow this because both purely tetragonally distorted and surface relaxed structures can be used as inputs. For illustration a model of the surface relaxed super cell is shown in Figure 1(A).

© 2017 The Authors

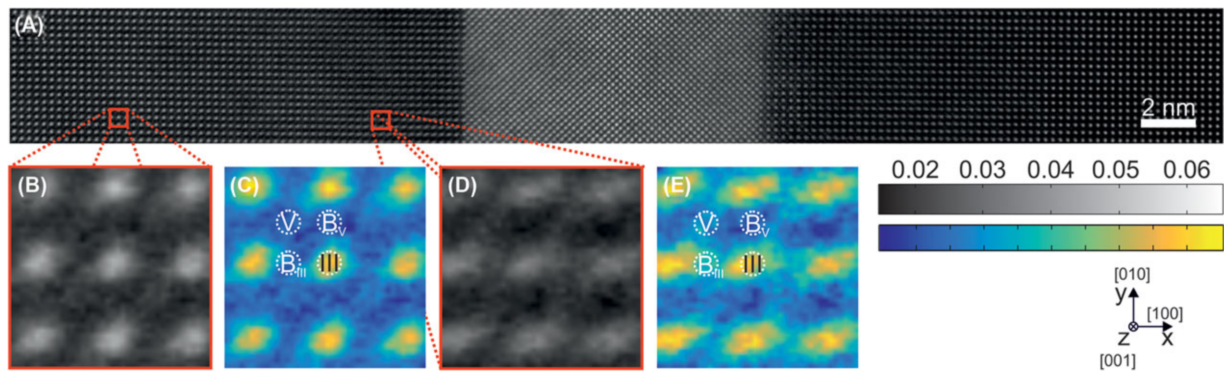

Fig. 2. Experimental high-resolution HAADF image of Ga(P,As) quantum well framed by GaP in [001] projection (A). A unit cell of the undistorted region far away (>10 nm) from the interface is shown in (B). The same section is shown in false colour in (C). An analogous region close to the interface is shown in greyscale and false colour in (D) and (E), respectively. The positions of the group III and V atomic columns are marked by circles. In addition, the positions that are situated horizontally between two group III or two group V columns are marked by B_{III} and B_V, respectively

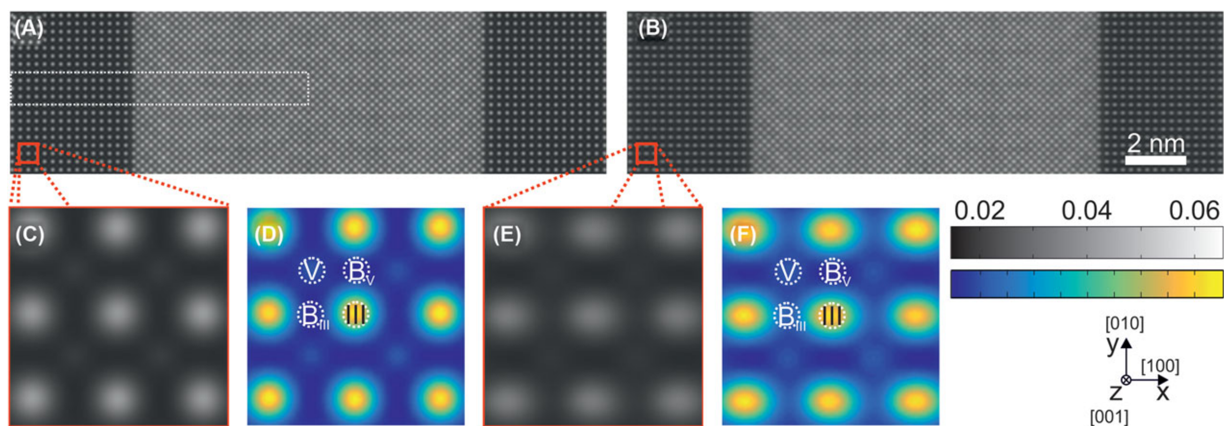

Fig. 3. Simulated HAADF images derived from a purely tetragonally distorted and the additionally surface relaxed super cell are shown in (A) and (B), respectively. Enlarged regions from both images are depicted in greyscale and false colour in (C) and (D) and (E) and (F), respectively. The positions of the group III and V atomic columns are marked by circles. In addition, the positions that are situated horizontally between two group III or two group V columns are marked by B_{III} and B_V, respectively

The simulated images derived from the purely tetragonally distorted and the surface relaxed cell with a sample thickness of 22 nm are shown in Figures 3(A) and (B), respectively. The white rectangle in Figure 3(A) indicates the simulated region, the simulations were mirrored vertically and repeated along the y axis for better resemblance of the experimental data.

Comparing Figures 3(A) and (B), the reduced contrast in the latter becomes obvious. This can be seen in more detail in the enlarged unit cells shown in Figures 3(C) and (E) and the corresponding false colour images in Figures 3(D) and (F). Again, the positions which are situated horizontally between two group III or two group V columns are marked by B_{III} and B_V, respectively. Although the atomic columns of the purely tetragonally distorted cell in Figures 3(C) and (D) appear perfectly round, the columns of the surface relaxed cell in Figures 3(E) and (F) appear significantly elongated along the x direction. The two different background positions B_{III} and B_V show different intensity. Comparing the simulations of Figure 3 to the experimental data presented in Figure 2 yields a very good qualitative agreement.

In the following, the simulation and experiment will be compared quantitatively using intensity profiles across the QW. Figure 4 depicts the respective profiles for the different positions within a unit cell, that is the group III atomic columns (Fig. 4A), the group V atomic columns (Fig. 4B) and the background positions in between the columns (Fig. 4C). The intensity value of each atomic column is derived by averaging the intensity across a circular region with a diameter of 25 pm around the column centre, to compensate for inaccuracies in the determination of the peak centres. The size of the averaging circles is indicated by dashed circles depicted for example in Figure 3(D). Subsequently the intensity of a lattice plane is derived by averaging the intensities of the associated atomic columns. The shaded area indicates the standard deviation of the intensity across the atomic columns of a lattice plane.

© 2017 The Authors

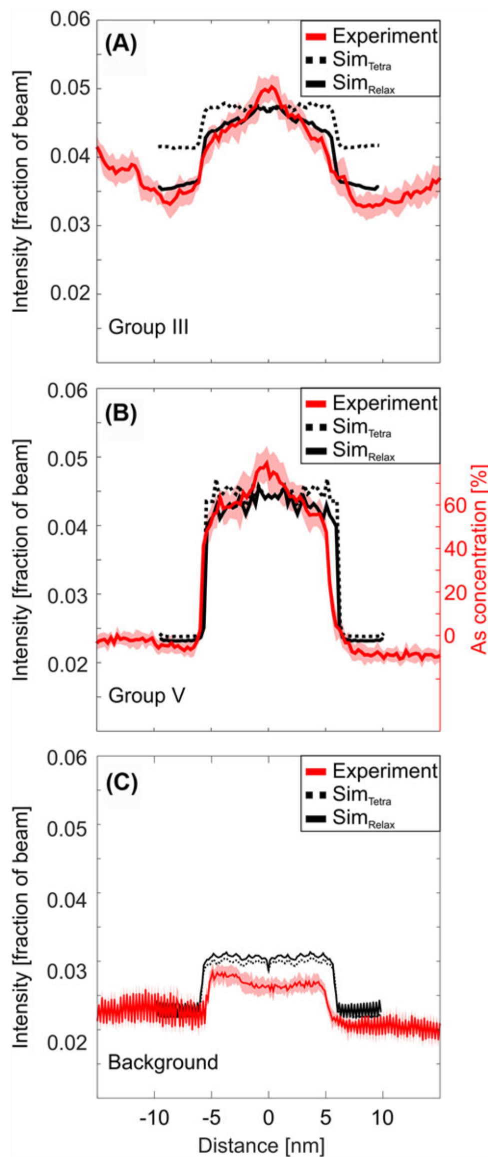

Fig. 4. The red lines indicate the experimental intensity profiles across the quantum well derived at the positions of the group III atomic columns (A), the group V atomic columns (B) and the background positions in between the columns (C). The simulated intensities for the surface relaxed case are drawn as a solid black lines. The simulated intensity derived from the purely tetragonally distorted cell is drawn as dashed black line for comparison.

The intensity profiles of the group III sublattice in Figure 4(A) illustrate the influence of the lattice plane bending best, because the lattice sites are occupied by Ga only throughout the whole structure. Because the chemical composition remains constant across the QW, the changes in intensity are caused by the plane bending mainly. We find that the simulated intensity derived from the surface relaxed super cell (solid black line) is up to 20% reduced compared to the intensity derived from the purely tetragonally distorted cell (dashed black line). The maximum deviation can be found in the barrier, ∼10 nm away from the centre of the QW, where the atoms are displaced the most (c.f. Fig. 1B). The displaced atoms lead to dechannelling of the electron beam (Huang, 1947; Cowley & Huang, 1992; Perovic *et al.*, 1993; Amali *et al.*, 1997; Grillo, 2009) and accordingly to a reduced HAADF intensity at the positions of the atomic columns (Yu *et al.*, 2004; Grillo, 2009; Beyer *et al.*, 2017). Additionally, the displaced atomic columns lead to increased Huang scattering into low angles (Huang, 1947; Cowley & Huang, 1992). The influence of the surface relaxation on the angular dependence of the scattering will be discussed in more detail below. The experimental curve (red line) closely resembles surface relaxed simulation (solid black line). The lack of correspondence between the experiment and the simulation at the upper interface is not caused by missing factors in the simulation but actual properties of the sample and will be discussed later.

The simulated intensity of the group V sublattice derived from the purely tetragonally distorted super cell (dashed black line in Fig. 4B) nearly resembles a box profile. The slight intensity variations within the QW region are due to the fact that the chemical composition fluctuates around the mean As content of 65.9%. The right y axis indicates the corresponding As concentration. For reasons of simplicity a linear dependence of the intensity on the composition was assumed, which has shown to be valid for thin samples (Van Aert *et al.*, 2009). In contrast, the profile derived from the surface relaxed super cell (solid black line in Fig. 4B) significantly differs from a box profile. Close to the interfaces the intensity is clearly reduced because of the displaced atomic columns. The resulting intensity gradient could be misinterpreted as a composition gradient. According to the right y axis an As content of only ∼50% would be present at the interface. We emphasise that there are procedures to partially compensate for the observed intensity loss, for example the probe integrated scattering cross sections (PICS) approach (E *et al.*, 2013). Nevertheless, in this manuscript we want to highlight the influences of the surface relaxation. As stated in the introductory section, averaging approaches can fail for materials, in which additional SADs are present, for example Ga(N,As).

Also on the group V sublattice, the profile derived from the surface relaxed super cell (solid black line) resembles the experimental curve (red line) very well and shows some sample related deviations at the upper interface.

The intensity in the background is strongly influenced by the surface relaxation as well (Fig. 4C). The intensity of the purely tetragonally distorted simulation (dashed black line) follows a box profile following the different amounts of thermal diffuse scattering in GaP and Ga(P,As). The surface relaxation and the resulting bent lattice planes break the 4-fold symmetry, therefore there are two different intensity values of the background depending on whether there are two neighbouring Ga or P atomic columns along the x direction (compare e.g. Fig. 2F).

© 2017 The Authors

This manifests as intensity oscillations in the simulated background profile (solid black line) as well as the experimental profile (red line). Additionally, a slight intensity increase is observable at the edges of the QW in the simulation as well as in the experiment.

In general there is a very good agreement between the experiment and the simulations taking into account the lattice plane bending for all three observed positions. However, some distinct discrepancies can be found. First, a small intensity gradient is present in the experimental profiles, which is due to the wedge shape that is caused by the sample preparation. Second, at the upper interface the experimental profile is less steep than the simulation, where an abrupt composition profile was assumed. This might be caused by the thickness gradient and a corresponding asymmetric surface relaxation. However, we think that the change in thickness (<2 nm across the >25 nm field of view) is not sufficient to significantly alter the intensity profiles. This means that the upper interface is not atomically abrupt but intermixed. Both factors contribute to the notable asymmetry of the experimental profiles. It is worth noting that this asymmetry was not retrieved by the XRD measurements, where also a prefect box-like profile was assumed. Assuming a composition gradient in the simulated XRD profile could improve the fit to the experimental data.

The surface relaxation may not only influence the HAADF intensities, but also the positions of the atomic columns. The magnitude of this effect is investigated in the following.

To this end, the positions of the atomic columns in the simulated data were derived directly from the respective super cell by omitting the z coordinate and averaging the x and y coordinates of the atoms belonging to one atomic column. In the case of the experimental images, the corresponding positions were determined via the Peak Pairs software (Galindo *et al.*, 2007).

In each case the distances to the four next neighbour columns were determined, averaged and split into the components along the x and y axis, respectively. The distances were calibrated using the 4 0 0 spots in the FFT of the GaP region below the QW. We decided to only use the spots along the x direction because this is the fast scan direction in the experimental images which is less influenced by sample drift and scan distortions (Grieb *et al.*, 2012). The resulting curves utilising the positions of the group III and the group V atomic column are shown in Figures 5(A) and (B), respectively. As expected the determined lattice constants are almost identical for both sublattices, therefore we will discuss the observations on the basis of the group III lattice only. The right y axis indicates the As content, which was derived by combining Vegard's law with the tetragonal distortion due to pseudomorphic growth.

In analogy to the previous intensity evaluation, the lattice constant evaluation of the purely tetragonally distorted simulation (dashed black line in Fig. 5A) nearly follows a box profile. The lattice constant of 0.57 nm in the QW is in good agreement with the values derived from the XRD measurement. The small indents before and after the QW are caused by atom displacements at the interface due to the VFF relaxation, which was carried out for all simulated super cells, to account for the SADs introduced by the mixture of As and P atoms on the group V sublattice.

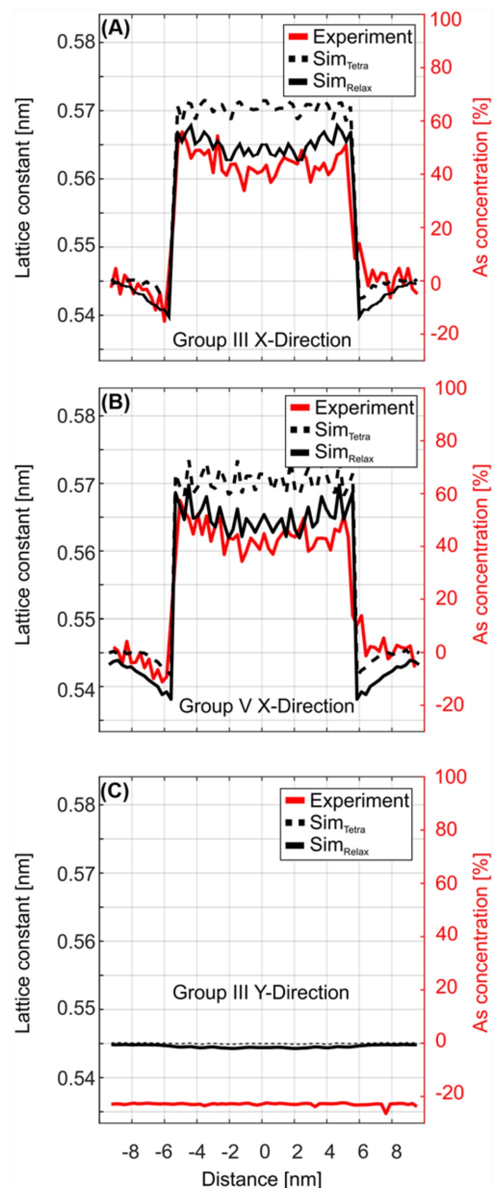

Fig. 5. Variation of the out-of-plane lattice constant across the QW derived from the group III (A) and group V (B) atomic column positions of the experimental image (red lines) and the surface relaxed simulation (solid black lines). The values derived from the purely tetragonally distorted cell are drawn as dashed black lines. The corresponding evaluation of the in-plane lattice constant is shown in (C).

The lattice constants derived from the surface relaxed cell (solid black curve) are significantly altered. The previously observed dip at the interfaces becomes more pronounced. Additionally, the lattice constant in the centre of the QW is drastically reduced. This is due to the fact that a fraction of

© 2017 The Authors

the strain energy stored in the system is relaxed due to the additional free surface. Similar to the case of the intensity evaluation this change can be misinterpreted as a change of composition. According to the right y axis, the As content in the centre of the QW would be around 50% instead of the actual content of 65.9%. Again, the agreement between experiment (red curve) and surface relaxed simulation (solid black curve) is very good except for the upper interface. As discussed for the intensity curves, this discrepancy is caused by the intermixed upper interface.

We emphasise that the standard deviation of the experimental lattice constant is in the range of 15 pm, which is rather high compared to the difference in lattice constant between GaP and Ga(P,As), which is around 25 pm. The accuracy could be improved by increasing the sampling in the images to improve peak finding and by averaging over a larger number of images to reduce the impact of drift and scan distortions. Recently, accuracies in the range of 1% were reported in the determination of lattice constants via STEM (Yankovich *et al.*, 2014; Jones *et al.*, 2017). Here we did not add error bars to the graphs to retain clarity. As stated before, the evaluation of the out-of-plane lattice constant using the group V lattice (Fig. 5B) leads to similar results.

The analogue evaluation of the perpendicular y direction is shown in Figure 5(C). As expected for pseudomorphic growth, the in-plane lattice constant remains constant across the QW. In the simulations the absolute value is 0.545 nm, that is that of the GaP substrate. The value derived from the experiment is reduced by ~8 pm which is most likely caused by a compression of the y axis due to sample drift. To compensate for this the image could be rectified or the effect of drift could be reduced by intentionally varying the fast scan direction during the STEM measurements (Sang & LeBeau, 2014; Jones *et al.*, 2015). However, this small discrepancy is not important in our case, because the lattice constant along y is constant over the field of view.

After discussing the influences of the surface relaxation in the real space we finally address the reciprocal space as well. We do this via simulated PACBED patterns. The simulated patterns derived from a unit cell of the purely tetragonally distorted and a unit cell of the surface relaxed super cell for a specimen thickness of 22 nm are depicted in Figure 6(A) (top and bottom halves, respectively). The angular range is from 0 to 300 mrad. The bright field disc with a radius of 24 mrad is distinctly visible in the centre as well as the Kikuchi bands expected from the [001] crystal orientation. Comparing the two simulations, it becomes apparent that the surface relaxed PACBED (bottom) is blurred with respect to the purely tetragonally distorted one (top). Because the bending of the lattice planes induced by the surface relaxation is not isotropic, the PACBED pattern is no longer 4-fold symmetric. This can be seen faintly at the bright field disc as well as at the first-order Laue zone (FOLZ). The FOLZ is clearly visibly as a bright ring in the lower segment of the surface relaxed pattern (highlighted by white arrow), whereas it vanishes in the left segment of the pattern (highlighted by dark arrow). The observable asymmetry between the left and right half of the pattern could be used in experiments to judge whether significant lattice plane bending is present. This break of symmetry can also be very important for differential phase contrast (DPC) measurements, because the effects caused by the surface relaxation can be misinterpreted as electric fields at the interface.

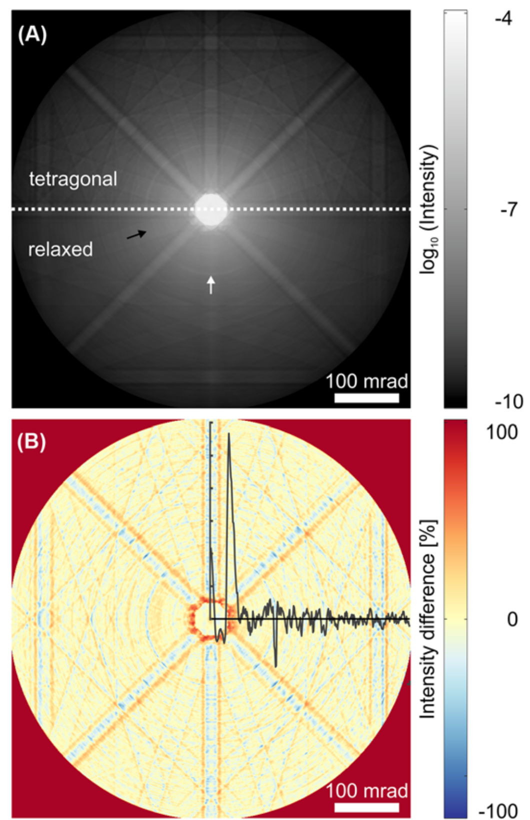

Fig. 6. Simulated PACBED patterns derived from one unit cell of the purely tetragonally distorted (top) and the surface relaxed (bottom) super cell (A). The difference between the two simulations is shown in false colour in (B). The black line represents the radial average of the difference.

The blurring of the pattern becomes even more obvious in the difference plot, which is shown in false colour in Figure 6(B). The difference values I_{Diff} were derived via $I_{\mathrm{Diff}} = (I_{\mathrm{Surf}} - I_{\mathrm{Tetra}})/I_{\mathrm{Surf}}$, where I_{Surf} and I_{Tetra} are the intensities from the surface relaxed and the purely tetragonally distorted simulation, respectively. The broadening of the Kikuchi bands is clearly visible by the red edges and blue centre of each band. The horizontal bands do not show up in the difference plot at all which implies they are not affected by the surface relaxation. Because periodic boundary conditions still apply along the y direction, no lattice plane bending is present. In the centre of the pattern an increased intensity is observable. This is caused by additional Huang scattering (Huang, 1947) and agrees well with the 'expansion of the diffraction pattern' for

© 2017 The Authors

example observed at dislocations (Cowley & Huang, 1992). The asymmetry of the pattern can be seen in the difference plot as well.

The radial average across the difference plot is shown as black line in Fig. 6(B). Most prominently the increased intensity at low scattering angles is visible. In LAADF images, where this angular region is detected, the increased intensity leads to a bright line at the strained interfaces (Grillo *et al.*, 2011; Grieb *et al.*, 2012; Beyer *et al.*, 2017). Additionally, the reduced intensity at FOLZ is visible in the radial average as well. So far we only addressed the reciprocal space via simulations, however, our theoretical findings could be compared to nanobeam diffraction experiments (Müller-Caspary *et al.*, 2015) or to actual CBED patterns acquired across the strained QW due to the recent developments in the field of fast pixelated detectors (Chen *et al.*, 2016).

In summary, there is a significant influence of the surface bending on the different STEM measurements presented. There are several possibilities to address these effects and minimise their impact. First, an optimum sample thickness can be chosen according to the QW width (Treacy *et al.*, 1985; Beyer *et al.*, 2017). For a fixed sample geometry, adequate evaluation schemes have to be applied, which attribute the dechannelled intensity back to the respective atomic column, for example the PICS approach (E *et al.*, 2013), or make use of measurements with different angular scattering ranges (Grieb *et al.*, 2013). Last but not least, the expected displacements can be modelled, for example by FE, to decide whether the surface relaxation will be crucial and to localise the distorted regions. Moreover, the displacement fields can be used to compensate the deteriorated intensity or to create super cells which reflect the actual sample geometry (Rosenauer *et al.*, 2006; Beyer *et al.*, 2017).

Conclusion

The surface relaxation of thin TEM specimens of commensurately strained heterostructures leads to a bending of the lattice planes. In HR HAADF measurements the intensities of the atomic columns are decreased wherever bending is present. In the case of a compressively strained QW, the distances of the atomic columns in the quantum well are reduced by the relaxation in comparison to the purely tetragonally distorted crystal. FE can be used to model the bending. The simulated HAADF images of a Ga(P,As) QW embedded in GaP are in good agreement with the experiments. Ignoring the effect of surface relaxation can lead to misinterpretation of data. Taking it into account, we find that the lower interface of the investigated sample is atomically abrupt, whereas the upper one is smeared out. The simulated PACBED patterns verify that the surface relaxation leads to additional scattering into low angles. Moreover, the Kikuchi bands belonging to bent planes broaden and the 4-fold symmetry is broken. The latter effect can be utilised to detect the presence of lattice plane bending. The occurring effects can be accounted for by the appropriate choice of the sample geometry and the evaluation schemes or by the modelling of the surface relaxation.

Acknowledgements

This work was supported by the German Research Foundation (GRK 1782: 'Functionalization of Semiconductors' and SFB 1083: 'Structure and Dynamics of Internal Interfaces').

References

Van Aert, S., Verbeeck, J., Erni, R., Bals, S., Luysberg, M., van Dyck, D. & van Tendeloo, G. (2009). Quantitative atomic resolution mapping using high-angle annular dark field scanning transmission electron microscopy. *Ultramicroscopy* **109**, 1236–1244.

Amali, A., Rez, P. & Cowley, J.M. (1997). High angle annular dark field imaging of stacking faults. *Micron* **28**, 89–94.

Beyer, A., Belz, J., Knaub, N., Jandieri, K. & Volz, K. (2016a). Influence of spatial and temporal coherences on atomic resolution high angle annular dark field imaging. *Ultramicroscopy* **169**, 1–10.

Beyer, A., Duschek, L., Belz, J., Oelerich, J.O., Jandieri, K. & Volz, K. (2017). Influence of surface relaxation of strained layers on atomic resolution ADF imaging. *Ultramicroscopy* **181**, 8–16.

Beyer, A., Straubinger, R., Belz, J. & Volz, K. (2016b). Local sample thickness determination via scanning transmission electron microscopy defocus series. *J. Microsc.* **262**, 171–177.

Bierwolf, R., Hohenstein, M., Phillipp, F., Brandt, O., Crook, G.E. & Ploog, K. (1993). Direct measurement of local lattice distortions in strained layer structures by H R E M. *Ultramicroscopy* **49**, 273–285.

De Caro, L., Giuffrida, A., Carlino, E. & Tapfer, L. (1995). Elastic stress relaxation in HRTEM specimens of strained semiconductor heterostructures and its influence on the image contrast. *Microsc. Microanal. Microstruct.* **6**, 465–472.

De Caro, L., Giuffrida, A., Carlino, E. & Tapfer, L. (1997). Effects of the elastic stress relaxation on the HRTEM image contrast of strained heterostructures. *Acta Crystallographica Sect. A Found. Crystallogr.* **53**, 168–174.

Chen, Z., Weyland, M., Ercius, P. *et al.* (2016). Practical aspects of diffractive imaging using an atomic-scale coherent electron probe. *Ultramicroscopy* **169**, 107–121.

Cowley, J.M. & Huang, Y. (1992). De-channelling contrast in annular dark-field STEM. *Ultramicroscopy* **40**, 171–180.

E, H., MacArthur, K.E., Pennycook, T.J., Okunishi, E., D'Alfonso, A.J., Lugg, N.R., Allen, L.J. & Nellist, P.D. (2013). Probe integrated scattering cross sections in the analysis of atomic resolution HAADF STEM images. *Ultramicroscopy* **133**, 109–119.

Galindo, P.L., Kret, S., Sanchez, A.M. *et al.* (2007). The Peak Pairs algorithm for strain mapping from HRTEM images. *Ultramicroscopy* **107**, 1186–1193.

Gibson, J.M. & Treacy, M.M.J. (1984). The effect of elastic relaxation on the local structure of lattice-modulated thin films. *Ultramicroscopy* **14**, 345–349.

Grieb, T., Müller, K., Cadel, E., Beyer, A., Schowalter, M., Talbot, E., Volz, K. & Rosenauer, A. (2014). Simultaneous quantification of indium and nitrogen concentration in InGaNAs using HAADF-STEM. *Microsc. Microanal.* **20**, 1740–1752.

© 2017 The Authors

Grieb, T., Müller, K., Fritz, R., Grillo, V., Schowalter, M., Volz, K. & Rosenauer, A. (2013). Quantitative chemical evaluation of dilute GaNAs using ADF STEM: avoiding surface strain induced artifacts. *Ultramicroscopy* **129**, 1–9.

Grieb, T., Müller, K., Fritz, R., Schowalter, M., Neugebohrn, N., Knaub, N., Volz, K. & Rosenauer, A. (2012). Determination of the chemical composition of GaNAs using STEM HAADF imaging and STEM strain state analysis. *Ultramicroscopy* **117**, 15–23.

Grillo, V. (2009). The effect of surface strain relaxation on HAADF imaging. *Ultramicroscopy* **109**, 1453–1464.

Grillo, V., Mueller, K., Volz, K., Glas, F., Grieb, T. & Rosenauer, A. (2011). Strain, composition and disorder in ADF imaging of semiconductors. *J. Phys.: Conf. Ser.* **326**, 1–10.

He, D.S. & Li, Z.Y. (2014). A practical approach to quantify the ADF detector in STEM. *J. Phys.: Conf. Ser.* **522**, 1–4.

Huang, K. (1947). X-ray reflexions from dilute solid solutions. *Proc. R. Soc. A: Mathemat., Phys. Eng. Sci.* **190**, 102–117.

Jones, L., Wenner, S., Nord, M., Ninive, P.H., Løvvik, O.M., Holmestad, R. & Nellist, P.D. (2017). Optimising multi-frame ADF-STEM for high-precision atomic-resolution strain mapping. *Ultramicroscopy* **179**, 57–62.

Jones, L., Yang, H., Pennycook, T.J., Marshall, M.S.J., Van Aert, S., Browning, N.D., Castell, M.R. & Nellist, P.D. (2015). Smart Align—a new tool for robust non-rigid registration of scanning microscope data. *Adv. Struct. Chem. Imag.* **1**, 1–16.

Jouneau, P.H., Tardot, A., Feuillet, G., Mariette, H. & Cibert, J. (1994). Strain mapping of ultrathin epitaxial ZnTe and MnTe layers embedded in CdTe. *J. Appl. Phys.* **75**, 7310–7316.

Keating, P.N. (1966). Effect of invariance requirements on the elastic strain energy of crystals with application to the diamond structure. *Phys. Rev.* **145**, 637–645.

Krivanek, O.L., Chisholm, M.F., Nicolosi, V. *et al.* (2010). Atom-by-atom structural and chemical analysis by annular dark-field electron microscopy. *Nature* **464**, 571–574.

Müller-Caspary, K., Oelsner, A. & Potapov, P. (2015). Two-dimensional strain mapping in semiconductors by nano-beam electron diffraction employing a delay-line detector. *Appl. Phys. Lett.* **107**, 1–4.

Nellist, P.D., Chisholm, M.F., Dellby, N. *et al.* (2004). Direct subangstrom imaging of a crystal lattice. *Science (New York, N.Y.)* **305**, 1741.

Oelerich, J.O., Duschek, L., Belz, J., Beyer, A., Baranovskii, S.D. & Volz, K. (2017). STEMsalabim: a high-performance computing cluster friendly code for scanning transmission electron microscopy image simulations of thin specimens. *Ultramicroscopy* **177**, 91–96.

Pennycook, S.J. (1989). Z-contrast stem for materials science. *Ultramicroscopy* **30**, 58–69.

Perovic, D.D., Rossouw, C.J. & Howie, A. (1993). Imaging elastic strains in high-angle annular dark field scanning transmission electron microscopy. *Ultramicroscopy* **52**, 353–359.

Rosenauer, A., Gerthsen, D. & Potin, V. (2006). Strain state analysis of InGaN/GaN – sources of error and optimized imaging conditions. *Physica Status Solidi (a)* **203**, 176–184.

Rosenauer, A., Mehrtens, T., Müller, K. *et al.* (2011). Composition mapping in InGaN by scanning transmission electron microscopy. *Ultramicroscopy* **111**, 1316–1327.

Sang, X. & LeBeau, J.M. (2014). Revolving scanning transmission electron microscopy: correcting sample drift distortion without prior knowledge. *Ultramicroscopy* **138**, 28–35.

Tan, H., Furlan, A., Li, W. *et al.* (2016). Highly efficient hybrid polymer and amorphous silicon multijunction solar cells with effective optical management. *Adv. Mater.* **28**, 2170–2177.

Tillmann, K., Lentzen, M. & Rosenfeld, R. (2000). Impact of column bending in high-resolution transmission electron microscopy on the strain evaluation of GaAs/InAs/GaAs heterostructures. *Ultramicroscopy* **83**, 111–128.

Tillmann, K., Thust, A., Lentzen, M. *et al.* (1996). Determination of segregation, elastic strain and thin-foil relaxation in InxGa-1-x As islands on GaAs(001) by high resolution transmission electron microscopy. *Philos. Magaz. Lett.* **74**, 309–315.

Treacy, M.M.J., Gibson, J.M. & Howie, A. (1985). On elastic relaxation and long wavelength microstructures in spinodally decomposed InxGa1−x.AsyP1−y epitaxial layers. *Philos. Magaz. A.* **51**, 389–417.

Vurgaftman, I., Meyer, J.R. & Ram-Mohan, L.R. (2001). Band parameters for III–V compound semiconductors and their alloys. *J. Appl. Phys.* **89**, 5815–5875.

Walther, T., Boothroyd, C.B. & Humphreys, C.J. (1995). Strain relaxation induced local crystal tilts at Si/SiGe interfaces in cross-sectional transmission electron microscope specimens. *Inst. Phys. Conf. Ser.* **146**, 11–16.

Wang, N., Cheng, L., Ge, R. *et al.* (2016). Perovskite light-emitting diodes based on solution-processed self-organized multiple quantum wells. *Nat. Phot.* **10**, 699–704.

Xu, Q., Ji, Y., Krut, D.D., Ermer, J.H. & Escarra, M.D. (2016). Transmissive concentrator multijunction solar cells with over 47% in-band power conversion efficiency. *Appl. Phys. Lett.* **109**, 1–4.

Yankovich, A.B., Berkels, B., Dahmen, W. *et al.* (2014). Picometre-precision analysis of scanning transmission electron microscopy images of platinum nanocatalysts. *Nat. Commun.* **5**. http://www.nature.com/doifinder/10.1038/ncomms5155

Yu, Z., Muller, D.A. & Silcox, J. (2004). Study of strain fields at a-Si/c-Si interface. *J. Appl. Phys.* **95**, 3362–3371.

© 2017 The Authors

6.1.4 Publication 4

Citation

Influence of surface relaxation of strained layers on atomic resolution ADF imaging
A. Beyer, L. Duschek, J. Belz, J.O. Oelerich, K. Jandieri, K. Volz, Journal of microscopy **181**, p8–16, 2017, DOI: 10.1016/j.ultramic.2017.04.019

Abstract

Surface relaxation of thin transmission electron microscopy(**TEM**) specimens of strained layers results in severe bending of lattice planes. This bending significantly displaces atoms from their ideal channeling positions which has a strong impact on the measured annular dark-field (**ADF**) intensity.
With the example of GaAs quantum wells (**QW**) embedded in a GaP barrier, we model the resulting displacements by elastic theory using the finite element (**FE**) formalism. Relaxed and unrelaxed super cells served as input for state of the art frozen phonon simulation of atomic resolution ADF images.
We systematically investigate the dependencies on the samples geometric parameters, i.e. QW width and TEM sample thickness, by evaluating the simulated intensities at the atomic columns positions as well as at the background positions in between. Depending on the geometry the ADF intensity can be affected in a range several nm from the actual interface.
Moreover, we investigate the influence of surface relaxation on the angular distribution of the scattered intensity. At high scattering angles we observe an intensity reduction at the interface as well as in the GaP barrier due to de-channeling. The amount of intensity reduction at an atomic column is directly proportional to its mean square displacement . On the contrary we find clearly increased intensity at low angles caused by additional diffuse scattering. We discuss the implications for quantitative evaluations as well as strategies to compensate for the reduced intensities.

Contributions

Andreas Beyer and Lennart Duschek wrote the manuscript in addition to the data processing and image simulations. Jürgen Belz carried out the FE relaxation as well as the integration with Kakhaber Jandieris VFF code. Jan Oliver Oelerich wrote the image simulation code and supervised the integration of super cells. Kerstin Volz supervised the work and secured the funding to support this study.

Reprinted from *Ultramicroscopy **181**,8–16,2017*, Copyright 2017, with permission from Elsevier.

Ultramicroscopy 181 (2017) 8–16

Contents lists available at ScienceDirect

Ultramicroscopy

journal homepage: www.elsevier.com/locate/ultramic

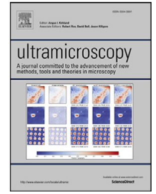

Influence of surface relaxation of strained layers on atomic resolution ADF imaging

Andreas Beyer*, Lennart Duschek, Jürgen Belz, Jan Oliver Oelerich, Kakhaber Jandieri, Kerstin Volz

Materials Science Center and Faculty of Physics, Philipps-Universität Marburg Hans-Meerweinstraße 6, 35032 Marburg, Germany

ARTICLE INFO

Article history:
Received 2 December 2016
Revised 24 April 2017
Accepted 28 April 2017
Available online 29 April 2017

ABSTRACT

Surface relaxation of thin transmission electron microscopy (TEM) specimens of strained layers results in a severe bending of lattice planes. This bending significantly displaces atoms from their ideal channeling positions which has a strong impact on the measured annular dark field (ADF) intensity.

With the example of GaAs quantum wells (QW) embedded in a GaP barrier, we model the resulting displacements by elastic theory using the finite element (FE) formalism. Relaxed and unrelaxed super cells served as input for state of the art frozen phonon simulation of atomic resolution ADF images.

We systematically investigate the dependencies on the samples geometric parameters, i.e. QW width and TEM sample thickness, by evaluating the simulated intensities at the atomic columns positions as well as at the background positions in between. Depending on the geometry the ADF intensity can be affected in a range several nm from the actual interface.

Moreover, we investigate the influence of the surface relaxation on the angular distribution of the scattered intensity. At high scattering angles we observe an intensity reduction at the interface as well as in the GaP barrier due to de-channeling. The amount of intensity reduction at an atomic column is directly proportional to its mean square displacement. On the contrary we find a clearly increased intensity at low angles caused by additional diffuse scattering. We discuss the implications for quantitative evaluations as well as strategies to compensate for the reduced intensities.

© 2017 Elsevier B.V. All rights reserved.

1. Introduction

Modern devices often consist of multilayer structures, see e.g. [1–3]. Therefore, interfaces between different materials become increasingly important as their actual structure and chemical composition can determine the physical properties and efficiency of devices.

Aberration corrected high angle annular dark field (HAADF) scanning transmission electron microscopy (STEM) has become one of the leading techniques in the investigation of nanoscale materials [4,5], since a spatial resolution below one Angstrom is feasible. Moreover, quantitative agreement between simulation and experiment can be achieved if all decisive parameters are taken into account [6]. The dominant factors are the sensitivity of the annular dark field (ADF) detector [7,8], the partial spatial [9,10] and temporal coherences [6,11] and artefacts introduced by the sample preparation, e.g. amorphous layers [12].

At the interface of two materials additional challenges arise, as the lattice constants of the two materials forming the interface are commonly different. This is particularly relevant in the case of heteroepitaxy. In the special case of cubic materials, pseudomorphic growth takes places and the lattice mismatch results in the well-known tetragonal distortion, as long as a critical layer thickness is not exceeded. When a thin transmission electron microscopy (TEM) sample of a strained heterostructure is prepared, the stress can be relieved elastically, due to the additional free surface [13,14]. Depending on the lattice mismatch and the elastic constants, this results in the deformation of the TEM sample and the bending of the previously straight lattice planes [15]. This effect can be modeled by elastic theory [16]. Utilizing finite element (FE) calculations this model can be used to calculate the deformation fields occurring for actual sample geometries [13,16,17]. The tremendous effect of the bent lattice planes on conventional high resolution (HR) TEM imaging was studied e.g. in [13,16,18]. Although STEM, and especially high angle ADF, are regarded as less sensitive towards strain compared to conventional TEM, a distinct intensity deterioration at strained interfaces was found for uncorrected STEM microscopy [15,19] and explained by a de-channeling effect of the electrons [15,20–23]. Therefore, composition profiles

* Corresponding author.
E-mail address: andreas.beyer@physik.uni-marburg.de (A. Beyer).

http://dx.doi.org/10.1016/j.ultramic.2017.04.019
0304-3991/© 2017 Elsevier B.V. All rights reserved.

across interfaces and the actual interface structure cannot be determined straight forwardly. An accepted scheme to encounter this effect in HAADF measurements is to sum the scattered intensity over a certain lateral area e.g. the Voronoi cells of the atomic columns [24] like in the probe integrated scattering cross sections (PICS) method [25]. This method attributes the intensity scattered away from the atomic columns back to the column positions and therefore partially compensates for the effect of de-channeling.

In this paper we systematically study the influence of the lattice plane bending on simulated atomic resolution ADF images. To this end we intentionally choose evaluation schemes to visualize the occurring effects, i.e. evaluating the column intensities rather than Voronoi averaged intensities. To model the surface relaxation, we use super cells of heterostructures that are relaxed via an FE method using linear elastic theory. In addition, the actual interfaces are relaxed using Valence Force Field (VFF) [26] routine, minimizing the total energy of the cell. The resulting cells are then used as input for STEM multislice simulations. As material system we choose a 2 dimensional GaAs quantum well (QW) embedded in a GaP matrix. Yet the relaxation procedure could also be adapted for non-planar structures like e.g. embedded quantum dots.

We choose this system for the simplicity of having two binary constituents with fixed compositions. Therefore, no additional static atomic displacements (SADs) resulting from different properties of the constituents are expected and we can focus on the macroscopic relaxation rather than elemental distribution, because the whole group III sublattice is occupied by Ga atoms only. Additionally, the lattice mismatch between GaP and GaAs is 3.7%, which is a rather high value for actual pseudomorphically grown layers. Nevertheless, thin pseudomorphic layers can indeed be successfully grown [27]. A profound understanding of the occurring effects on the basis of this simple model system allows to address the interfaces in more complex materials, where additional SADs are present, like e.g. Ga(NAs) in GaP, (GaIn)(NAs) in GaAs [28] or (GaIn)N in GaN [24].

Since the elastic surface relaxation is a geometrical effect, we will systematically vary the geometrical parameters, i.e. the QW width and the sample thickness. In order to quantify the effect on actual imaging we will vary the angular detection range resembling high and low angle ADF measurements. Finally, we will propose conditions allowing for the quantification of the chemical composition across the interface of a strained heterostructure at the atomic scale.

2. Materials and methods

In this study several super cells with different geometries were created. The structure of the super cells is exemplarily depicted in Fig. 1 and will be described in the following. The two materials considered, GaP and GaAs, crystallize in zinc blende structure and therefore exhibit cubic symmetry. At first a GaP layer with a width of 376 monolayers (ML) (i.e. ~50 nm) along the "growth" direction x was created. Please note that here we regard group III and group V as individual ML, which might differ from the literature where often the bilayer of GaP is regarded as one ML. Since the absolute lengths in nm will change due to the subsequent relaxation, we will stick to monolayers as a length scale, which simplifies comparing data derived from relaxed and unrelaxed cells, respectively. On top of this virtual GaP substrate, a GaAs QW with a width w of either 22, 37 or 74 ML is created, which translates to a width of approximately 3, 5 and 10 nm, respectively. The QW is followed by another 376 ML of GaP. One has to keep in mind that the Ga columns at the interface have neighboring P columns as well as As columns and therefore could be ambiguously attributed to the GaP or to the GaAs layer. For reasons of consistency we define the first As containing layer in x direction as the start of the quantum well and the first Ga layer which has neighboring P as end of the well. The thickness t with respect to the electron beam (along z-direction) is varied for all of the three above mentioned structures with the chosen values of 80, 184 and 376 ML (approximately 10, 25 and 50 nm). In addition, the y-direction is constructed to be periodic, therefore infinite in extension. This resembles the thin foil geometry of an actual TEM sample in cross-sectional measurements. The crystallographic directions of the cubic system are chosen to coincide with the reference system, therefore the epitaxial

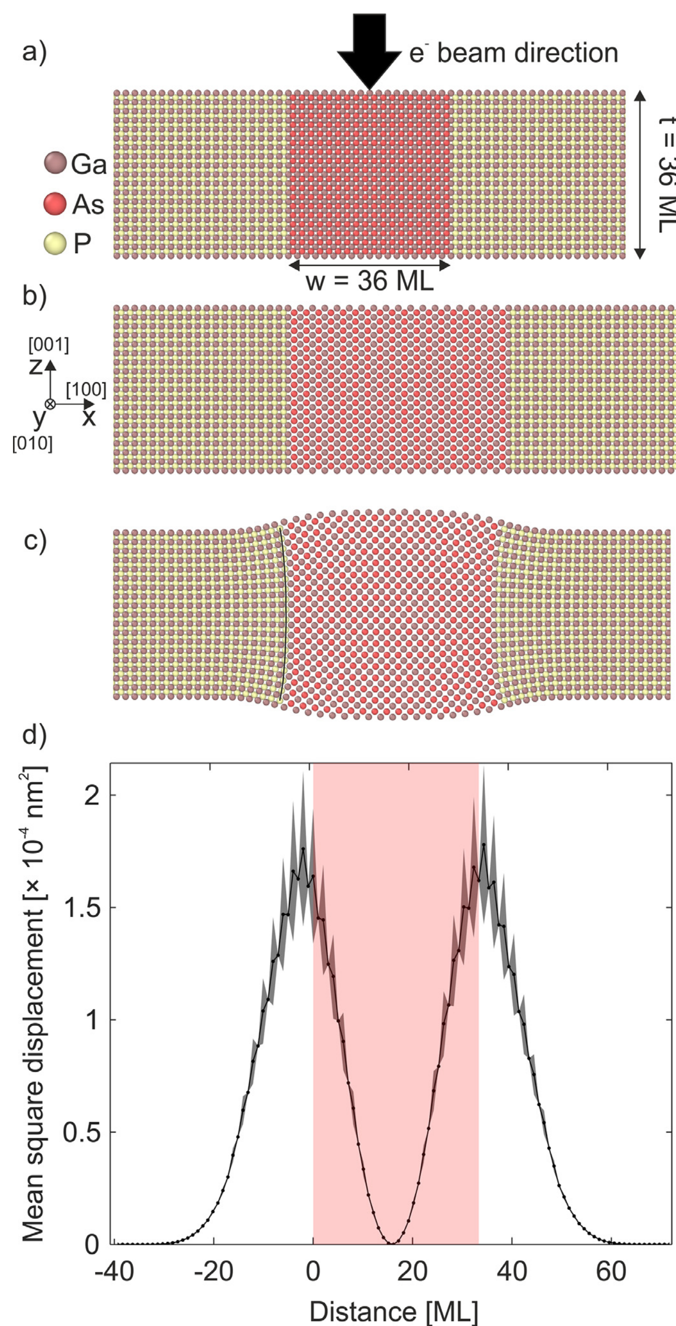

Fig. 1. Structural model of an unrelaxed GaP/GaAs heterostructure a). The direction of the electron beam is z. The same super cell after FE relaxation neglecting and allowing surface relaxation is shown in b) and c), respectively. For a better visualization of the effects, the displacement of the atoms is multiplied by a factor of 5. The bending of lattice planes is quantified via the mean square displacement depicted in d). The shaded red area indicates the position of the quantum well. The slight asymmetry is caused by the free top surface in positive x direction. (For interpretation of the references to colour in this figure legend, the reader is referred to the web version of this article.)

growth direction [100] is along the x-direction. The z-direction is transmitted by the electron beam and is identical to the [001] direction of the zinc blende crystal. For one structure the crystallographic [011] direction was chosen as viewing direction, to investigate the influence of the zone axis on the observed effects.

These initial super cells are relaxed in a two-step process. At first, the geometry is created as a continuous medium. The total structure is divided in smaller regions which are the basis for FE calculations solving the equations of linear elastic theory [16]. Since only complete pseudomorphic growth is considered, plastic deformation is neglected. The GaAs layer is set up in a condition of hydrostatic pressure, according to the lattice mismatch resulting from the free lattice constants. This procedure results in the well-known tetragonal distortion in epitaxial heterostructures when both x- and y-directions are nearly infinite (see Fig. 1b)).

Since the super cells are designed to be finite in both growth and transmission direction as well as periodic in y-direction the appropriate boundary conditions are chosen. It is noteworthy, that the x-direction is not considered to be periodic but fixed to the substrate and free at the top surface.

After relaxation of the initial stress due to the applied hydrostatic pressure the structure deforms according to the boundary conditions and the elastic properties which introduced in a fully anisotropic manner and taken from [29]. In a second step, a super cell with actual atom decoration is created and the displacement field due to relaxation is applied. This atomistic super cell is then refined using a VFF approach using the mesoscopic deformation as starting parameters. We have observed excellent agreement between the simulated surface deformation and experimental atomic force microscopy measurements in the case of (GaIn)(NAs) on GaAs [30].

To reduce the time needed for the relaxation, highly optimized molecular dynamics/energy minimization codes (such as LAMMPS [31]) could be used. To this end the Keating potential used in VFF has to be implemented like it was done e.g. in [32].

In addition to the GaP/GaAs heterostructures, hypothetical structures were created, where the GaP was replaced by GaAs while retaining the lattice constant of GaP. These structures serve as a reference to separate between the influence of the chemical composition and the lattice plane bending on the ADF intensity.

The derived relaxed as well as unrelaxed super cells served as input for ADF STEM multislice simulations in the frozen phonon (FP) approach [33] utilizing the STEMsalabim software [34]. This software package is based on the multislice code of Kirkland [35] and is optimized to perform well on highly parallelized computing clusters. Since the effect of elastic surface relaxation is of considerable length, as will be shown in detail in the next section, the image simulation of large areas is mandatory and the use of efficient simulation software inevitable. The simulation parameters were chosen to model a probe C_S-corrected JEOL JEM 2200FS microscope operating at 200 kV. A convergence semi-angle of 24 mrad was set and residual geometric aberrations of $\Delta f = -2$ nm, $C_S = 2$ µm and $C_5 = 5$ mm were assumed. The angular detection range of the ADF detector was varied systematically. For each sample geometry a defocus series consisting of 7 weighted defoci centered on the optimum defocus was calculated to model the effect of chromatic aberration [6]. For each defocus 10 individual phonon configurations were averaged. In each configuration, the atoms were randomly displaced with mean square displacements of 6.36×10^{-05} nm^2 and 7.73×10^{-5} nm^2 for P and As and 7.17×10^{-5} nm^2 and 9.09×10^{-5} nm^2 for Ga in GaP and GaAs, respectively, according to their Debye-Waller factors from [36]. A Lorentzian source distribution with a width of 38 pm was applied to the simulations according to [37] modeling the effect of spatial incoherence. Considering these parameters, 2 dimensional quantitative agreement between simulation and experiment was achieved [37]. This allows the extraction of meaningful data from the simulation at each position, e.g. at the position of the atomic columns and the regions in between.

3. Results

We will start with an introduction of the observable effects and the used nomenclature. For an exemplarily chosen combination of QW width w and TEM sample thickness t we will demonstrate the influence of lattice plane bending on HR STEM images of strained interfaces and discuss the impact on the angular dependence of the scattering process. We will systematically investigate the influence of the samples̓ geometric properties, i.e. w and t on the surface relaxation and the resulting ADF images. On a final stage we will derive parameters which enable the quantification of strained interfaces.

Fig. 1a) shows a structural model of the initial QW structure with a width of w = 36 ML, without any relaxation method applied. The TEM sample thickness with respect to the impinging electron beam is t = 36 ML. This is rather thin for an actual TEM sample but can be readily created by low energy ion milling [38] and serves the illustration of the occurring effects. The tetragonally distorted super cell depicted in Fig. 1b) was retrieved by applying periodic boundary conditions along y and z, whereas the cell was allowed to relax along x. For a better visualization of the effect, the displacement of the atoms is multiplied by a factor of 5. The additional surface relaxation of the thin TEM sample was accounted for by allowing the FE relaxation along x and z and retaining the periodicity along the y direction only. The resulting super cell is drawn in Fig. 1c). Again the displacement of the atoms is multiplied by a factor of 5 for visualization purposes. With mean square atom displacements in the range of 10^{-4} nm^{-2}, the magnitude of the surface relaxation is rather large. For comparison, the maximum displacements caused by phonons at room temperature is 9.09×10^{-5} nm^{-2} for As. Due to the additional free surface the QW expands along the z direction. This bulging was investigated e.g. [39,40] and directly measured via atomic force microscopy (AFM) in [30]. At this stage we want to note that in the case of tensile strained materials, analogously an indentation is formed at the free surface.

The fact that the lattice planes are no longer perfectly aligned with respect to the impinging electron beam but are bent, is more important for the imaging in TEM than the deformation of the surface along the z axis. One bent lattice plane in the left GaP barrier is highlighted with a black line in Fig. 1c). The center part of the QW remains straight as the strain of the two opposite interfaces compensates. Moreover, a reduction of the elongation along the x axis can be observed, which results from the relaxation at the additional free surface. The magnitude of the lattice plane bending can be quantified via the resulting mistilt angle as done e.g. in [15], or via the lateral mean square displacement M of each atomic column. The value M_i for the i-th column is determined via:

$$M_i = \sum_{k=1}^{N} \frac{(x_k - \overline{x_i})^2}{N} + \sum_{k=1}^{N} \frac{(y_k - \overline{y_i})^2}{N}, \quad (1)$$

where $\overline{x_i}$ and $\overline{y_i}$ are the mean x and y coordinates of the respective atomic column and N denotes the number of atoms in this column. It is noteworthy that any displacement along the z axis is not taken into account here. Moreover, the second y dependent sum is zero in the case of surface relaxation due to the periodic boundary conditions along this direction, whereas in the case of non-planar structures like quantum dots the sum will be non-zero. The course of the displacements across the QW of this example structure is drawn in Fig. 1d). The red shaded area indicates the position of the QW. The origin of the x axis is chosen at the lower

interface of the QW. Here and in the following, the shaded area around the curve denotes the standard deviation calculated for the lattice planes along the y direction. In the GaP barrier on the left hand side M has values in the order of 10^{-9} nm^2 which is in the order of the numerical noise. Towards the interface, M increases by 5 orders of magnitude to a maximum value of 1.7×10^{-4} nm^2, yielding a displacement of 13 pm. As the deformation is compensated for the QW center, M drops to zero and rises near the upper interface. Besides a slight asymmetry, caused by the free top surface in positive x direction, the mean displacement is analogous to the lower surface. It is worth noting that the static atomic displacements (SADs) introduced by the lattice plane bending are comparable to those of substitutional atoms like N introduced in GaAs, which are ∼30 pm for a single Ga-N bond and ∼9 pm for a TEM sample containing 3% of N [41,42]. The SADs resulting from this change of composition also have been shown to have a significant effect on TEM and STEM imaging [41,43].

In the following we will investigate the effect of the aforementioned bending on ADF imaging. Therefore, we create super cells consisting of t = 184 ML (∼25 nm) in z direction and a QW layer width w = 38 ML. Besides the surface relaxed super cell, we model a purely tetragonally distorted QW layer. The resulting HAADF image of the tetragonally distorted super cell is shown in Fig. 2a). To model HAADF imaging conditions the simulated intensity was integrated over an angular range of 74-174 mrad. To minimize the calculation effort, the actual width of the simulated region in y direction was one unit cell, as marked by the dashed rectangle in Fig. 2a). The simulated image was repeated periodically along the y-axis for presentation afterwards. To further reduce the simulation time, the GaP barrier on the right hand side was omitted, as the effects which are studied are anyhow almost symmetrical (cf. Fig. 1 d)).

The analogue simulations for the surface relaxed super cell can be found in Fig. 2b). Both images are aligned to each other with respect to the lower interface. Qualitatively the images look very similar, even on a common intensity scale. Hence, the significant influence of the relaxation on the intensity will be highlighted via the following quantitative evaluation. To this end the group III lattice and the group V lattice will be evaluated separately. The corresponding intensity profiles were derived by averaging the intensity in a circle with a diameter of 25 pm (= 2.9 pixels) around each atomic column. We decided for this averaging approach rather than a summing approach, like e.g. the frequently used PICS method [25], because the intensity averaged around the column positions is more sensitive with respect to the tilted lattice planes. For the determination of the chemical composition across an interface this sensitivity is commonly regarded as a disadvantage, but for our study it is actually advantageous, since the effect of bending shall be investigated and the chemical composition is fixed anyways. The understanding of the bending in this model system allows to address interfaces in more complex materials, where additional SADs, e.g. induced by Nitrogen, are present. However, it should be noted that the circular averaging approach is more sensitive to the actual aberrations, especially the probe size. To account for this, reasonable values for an aberration corrected STEM were assumed [37]. The evaluation analogue to Fig. 2 but applying the PICS procedure is shown in Fig. S3 to allow the comparison of our results to others from the literature. As expected the effect of the lattice plane bending is partially compensated for in the PICS approach.

Additionally to the group III positions (Fig. 2c)) and the group V positions (Fig. 2d)), the positions between the atomic columns, i.e. the background (BG) positions, are evaluated (Fig. 2e)). The respective positions are marked in the unit cell shown as inset in Fig. 2c). From a simple point of view one would not expect that the QW is visible in the intensity profile of the group III lattice

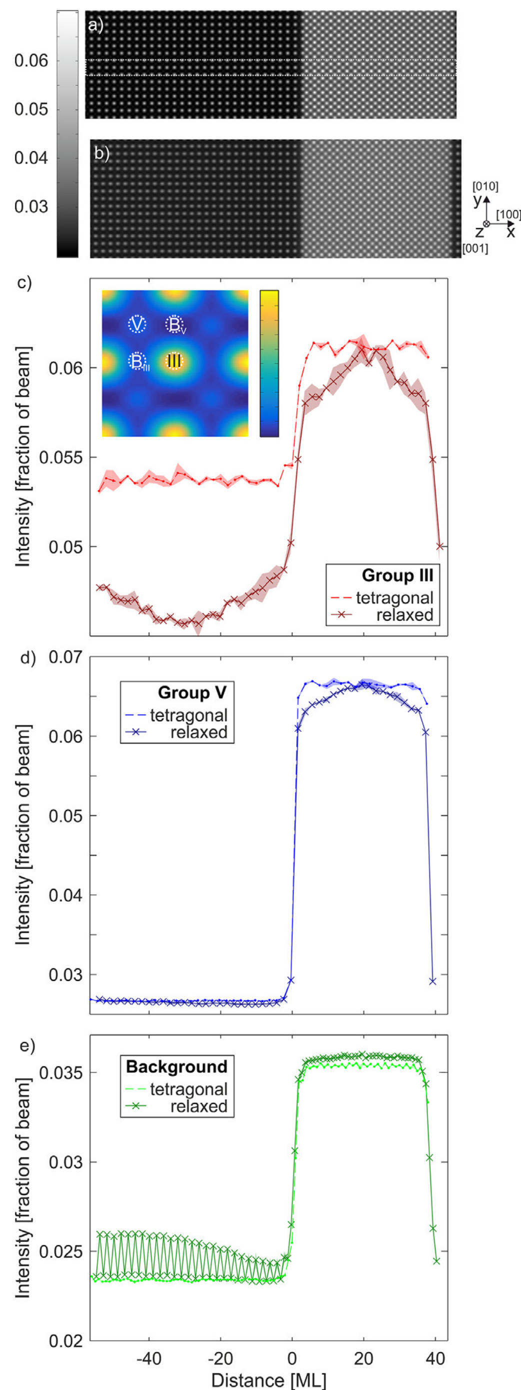

Fig. 2. Simulated ADF images of a tetragonally distorted a) and surface relaxed super cell b) in high angle regime (74-174 mrad). The intensity profiles of the group III sublattice positions are drawn in c) for the tetragonally distorted (broken red line) and relaxed (solid dark red line) super cell. Analogous graphs for the group V sublattice and the background positions are drawn in d) and e), respectively. (For interpretation of the references to colour in this figure legend, the reader is referred to the web version of this article.)

(Fig. 2c)), since the sublattice is occupied exclusively by Ga atoms throughout the entire heterostructure. However, the QW is clearly visible in the profile derived from the tetragonally distorted super cell (broken red line) by its higher intensity. This contrast can be caused by several reasons, i.e. the different interatomic distances of GaP and GaAs, the different Debye-Waller factors of Ga in GaP and GaAs and most prominently by the increased background intensity caused by the neighboring heavy columns. This “cross-talk” could be removed by background subtraction [44,45] or deconvolu-

tion [46]. Here we stick to the raw data as the influence of surface relaxation should be investigated. It is worth noting at this stage that even at the tetragonally distorted interface the STEM intensity does not switch digitally between the one of GaP and GaAs under realistic imaging conditions. Rather a transition over 4 ML (2 group III + 2 group V) is observable. This is caused by the finite probe size due to residual geometric aberrations as well as chromatic aberration and the finite source size. Additionally, broadening of the beam within the ~25 nm thick sample smears out the intensity profile. This highlights the necessity of adequate image simulations for the quantitative interpretation of experimental images.

For comparison, the corresponding profile for the surface relaxed super cell is drawn as solid dark red line in addition to the unrelaxed profile in Fig. 2c). The influence on the intensity is rather significant. The intensity in the GaP barrier is reduced by approximately 15%. Moreover, an intensity gradient across the QW is observable, ending in the same intensity for relaxed and unrelaxed profiles directly at the center. The intensity reduction occurs due to the displaced atomic columns and the resulting de-channelling [20,21] as will be investigated quantitatively later on. The analogue evaluation for the group V sublattice is shown in Fig. 2d). The difference between the intensity from the tetragonally distorted (broken blue line) and the surface relaxed (solid dark blue line) cell is most prominent in the region of the QW, where the intensity decreases by approximately 9%. This is of particular importance as the intensity gradient could be misinterpreted as a change in chemical composition across the QW. In contrast to the group III sublattice, the group V intensities in the GaP barrier seem to be rather unaffected by the relaxation. This is most likely due to the already very low intensity of the P columns. Dependent on the imaging conditions and the sample thickness the P intensity rises above the background level or not [37]. We assume that the effect of the lattice plane bending on the group V intensities will be more distinct in materials where there is not such a big difference in atomic numbers, e.g. (GaIn)As in GaAs. This assumption was verified exemplarily by evaluating a virtual structure, where the P atoms in GaP were replaced by As retaining the displacement field of GaAs in GaP (cf. Fig. S1).

The intensity evaluation of the background positions is shown in Fig. 2e). Here, the QW is clearly visible due to its increased intensity in the profile derived from the tetragonally distorted super cell (broken green line). This intensity rise (~1% of the impinging beam) is caused by the additional TDS of the heavy As columns, in analogy to the evaluation of the group III sublattice. The first thing that catches the eye in the corresponding relaxed profile (solid dark green line) is the intensity undulation in the GaP barrier. This reveals a different intensity depending on whether the position is situated between two group-III (B_{III}) or two group-V atoms (B_V) in growth direction x, which can be seen in more detail in the false color plot of a magnified unit cell shown as inset in Fig. 2c). This can be explained by the different amount of intensity de-channeled from the bent group III and group V atomic columns, respectively. The intensity at the B_{III} positions is significantly increased, as intensity from the neighboring bent Ga columns is present. In contrast to that, the intensity of the B_V positions is rather unaffected and the shape of the profile is retained. This can be understood since the intensity from the neighboring P columns is very low. For the virtual GaAs/GaAs structure the intensity on both background positions is increased and the intensity undulation between B_{III} and B_V is reduced drastically (cf. Fig. S1).

All in all, the total intensity is reduced resulting in the dark contrast at the interface in non-atomically resolved images as described e.g. in [15].

The quantitative correlation between intensity reduction and displacements M will be investigated in the following. To this end, we will use the group III columns because here the effect of the lattice plane bending can be seen most clearly. We have plotted the intensity difference derived from the relaxed and unrelaxed super cell $(I_{unrelaxed}-I_{relaxed})/I_{unrelaxed}$ as red line in Fig. 3 as a quantitative measure for the impact of the lattice plane bending. The plot illustrates the course of the intensity discussed above, i.e. a decreased intensity in the barrier and a gradient across the QW. We want to note here that the maximum intensity change of around 17% is located in the GaP barrier at x = −34 ML which is several nm away from the actual interface. This has strong implications for experiments, as these regions are often used as a reference as will be discussed in Section 3.2.

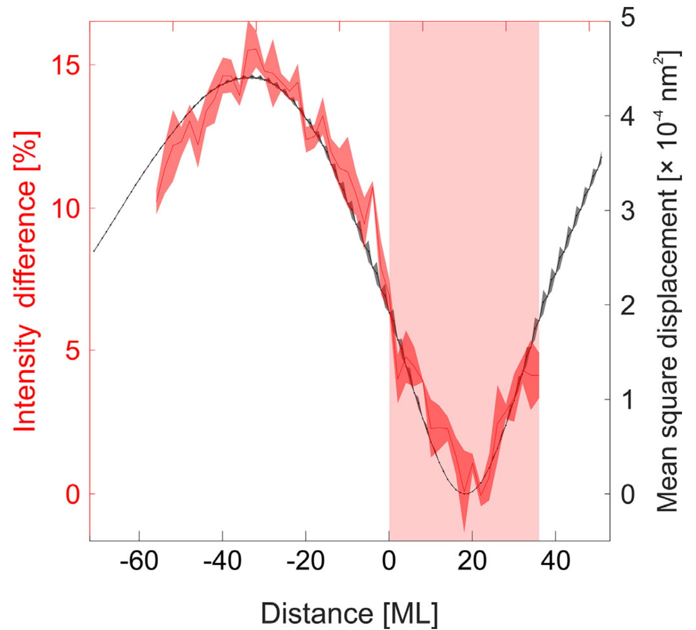

Fig. 3. Intensity difference of the relaxed and unrelaxed super cell for the group III sublattice (red line). The corresponding mean square displacement M of the atomic columns is drawn as black line. The shaded red area indicates the position of the quantum well. (For interpretation of the references to colour in this figure legend, the reader is referred to the web version of this article.)

We want to emphasize that in our simulations a finite source size and chromatic aberration were taken into account. In case of fully coherent simulations neglecting these effects, the influence of the lattice plane bending on the intensity is even more severe, which can be seen in the corresponding evaluation shown in Fig. S2. The intensity ratio is increased by a factor of 2.9 resulting in the unrelaxed intensity being up to 60% higher than relaxed one. Therefore, the discussed effects will be even more important for the next generation of aberration corrected microscopes. The profile of the atoms´displacements across the heterostructure is drawn as black line in Fig. 3. This curve exhibits the same shape as the intensity ratio, with a distinct maximum of 4.4×10^{-4} nm^2 (i.e. 21 pm displacement) in the barrier at x = −34 ML and zero displacement at x = 18 ML, i.e. the center of the QW. The two curves correlate perfectly with a proportionality factor c of 3.4×10^4%/nm^2, which was derived by dividing the red curve by the black one. In other words a displacement of 10 pm will result in an intensity change of 3.4% and to change the intensity by 1% the column has to be displaced by 5 pm. As mentioned before the effect is more pronounced in the coherent simulation, where a proportionality of $c^{III}{}_{coh} = 9.9 \times 10^4$%/nm^2 was found. A similar correlation was found for the group V sublattice in coherent simulations, in which the P intensity rises above the background level in GaP and in the virtual GaAs/GaAs heterostructure (cf. Fig. S1).

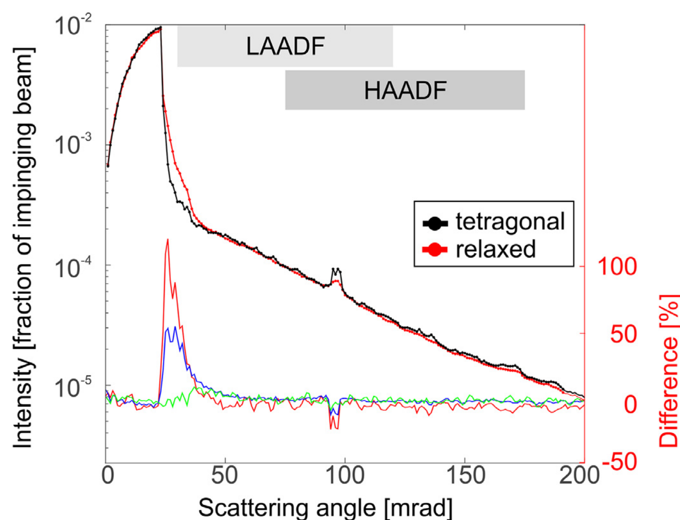

Fig. 4. Angular dependence of the scattered intensity for the tetragonally distorted (black data points) and surface relaxed super cell (red data points). Please read left y axis. The differences are drawn for the whole cell (blue line) and the lattice planes exhibiting the highest (red line) and lowest (green line) displacements, respectively. Please read right y axis. (For interpretation of the references to colour in this figure legend, the reader is referred to the web version of this article.)

With the knowledge of this proportionality constant, simulations neglecting the effect of lattice plane bending could be adapted or experimental images could be corrected to compensate for the bending effects. This is particularly beneficial as the necessary FE simulations are computationally cheap, whereas FP ADF multislice simulations are very demanding, see e.g. [47]. In order to give a measure for the relevant timescales, we choose the largest heterostructure considered in this study, i.e. a 360 ML thick sample containing an 80 ML thick GaAs QW. While the FE relaxation of the super cell was done in minutes, the HAADF simulation took 42 h on 256 cores for one defocus and full set of phonons. The speed of the relaxation can be further increased, if efficient parallel energy minimization codes like LAMMPS are used. Moreover, the strength and the range of the lattice plane bending strongly depends on the actual sample geometry (see chapter 3.2), therefore, more or less each STEM measurement of a strained interface has to be simulated independently, which makes a systematic compensation approach on basis of the FE relaxation even more favorable.

However, the exact value of the proportionality constant c depends on the applied imaging conditions, especially the used detector range, as well as sample parameters. A systematic study of the influencing factors is, however, beyond the scope of this work and will be performed in the future.

The remaining question, where the “missing” intensity is going to will be answered in the following.

3.1. Angular dependence

Already before we highlighted the similar magnitude of the atom displacements caused by the surface relaxation and caused by the incorporation of elements with different covalent radii, e.g. N in GaAs. For Ga(NAs) it has been shown that the consideration of the SADs induced by N is essential for the explanations of contrast reversals [41]. Due to the increased diffuse Huang scattering [22,23], low angle ADF (LAADF) measurements can be used to detect even small amounts of N in GaAs [48]. Therefore, one can expect a significant angular dependence in the case of surface relaxation, too.

To investigate this, the scattered intensity is drawn against the scattering angle in Fig. 4. The angular ranges used for retrieving the images in Fig. 2 (HAADF) and 5 (LAADF), respectively, are highlighted by grey rectangles. The reference curve derived from the tetragonally distorted super cell is represented by the black data points (read left y axis). The corresponding dependence derived from the surface relaxed super cell is represented by red data points. Both curves run parallel for most angles, they only differ at two distinct angular ranges. This can be seen in more detail in the difference plots shown in the lower part of Fig. 4. The blue curve depicts the intensity difference, i.e. $(I_{relaxed}-I_{unrelaxed})/I_{relaxed}$, derived from the whole super cell. The right y axis quantifies the deviation in percent. At low angles (∼25-50 mrad) the intensity of the relaxed cell is increased significantly by around 50%. The bent (disordered) lattice planes result in additional diffuse Huang scattering. Additionally, a drop of intensity is visible at around 100 mrad, which is the region of the first order Laue zone (FOLZ). This reduction is not surprising as the disorder is expected to smear out the Bragg reflections. To underpin that this intensity change is caused by the bent lattice planes, the analogue difference plots are drawn for the most distorted plane only (red line) and the undistorted plane in the center of the QW (green line). Indeed, the intensity difference is severe (∼100% at low angles) for the bent plane and almost negligible at the undistorted one.

To summarize the angular dependence briefly, intensity at high scattering angles is reduced by de-channeling caused by the displacements, whereas the intensity at lower angles is increased due to diffuse Huang scattering [22,23].

The consequences of this angular dependence for ADF imaging using different angular ranges, i.e. different camera lengths, is summarized in Figs. 2 and 5. In analogy to Fig. 2, the simulated images of the tetragonally distorted as well as the surface relaxed super cell are depicted for the LAADF regime (35–140 mrad) in Fig. 5a) and b), respectively. We choose this angular region because recent studies show quantitative agreement between FP simulations and experimental data for scattering angles above 35 mrad, whereas for lower angles significant discrepancies were observed [49]. The influence of the lattice bending on the intensity will be quantified via the intensity profiles depicted in Fig. 5c)-e). Despite the expectable change of the intensity scale, the intensity profiles extracted from the unrelaxed super cell (broken lines) look similar to the ones derived at high scattering angles (compare Fig. 2), i.e. a nearly abrupt intensity transition from GaP to GaAs is visible. However, the intensity profiles derived from the relaxed super cells (dark solid lines) drastically differ from the ones of the unrelaxed cell as well as from the analogue profiles derived at high scattering angles (compare Fig. 2). For explanatory reasons we will detail the differences on the basis of the background intensity depicted in Fig. 5e) at first. The intensity is clearly increased at the positions at which the lattice planes are strongly bent. This results in an intensity curve in the shape of the letter M, which is complementary to the shape observed at high scattering angles. Once more an undulation of the intensity is observable in the GaP caused by the large Z difference of Ga and P. This distinct BG intensity also overlays the profiles of group III (Fig. 5c)) and V (Fig. 5d)) and partially compensates for the intensity loss on the column positions. The intensity increase observed at the background positions is even higher for lower scattering angles. Assuming for example an angular detector range from 30-120 mrad, the background intensity becomes dominating leading to the M-shape being observable on the group III and V sublattices as well. In total, at low scattering angles an intensity increase is observable at the interfaces like already shown in for uncorrected STEM measurements [41,48].

3.2. Variation of geometrical parameters

As already stated before, the lattice plane bending drastically complicates the derivation of quantitative data from strained inter-

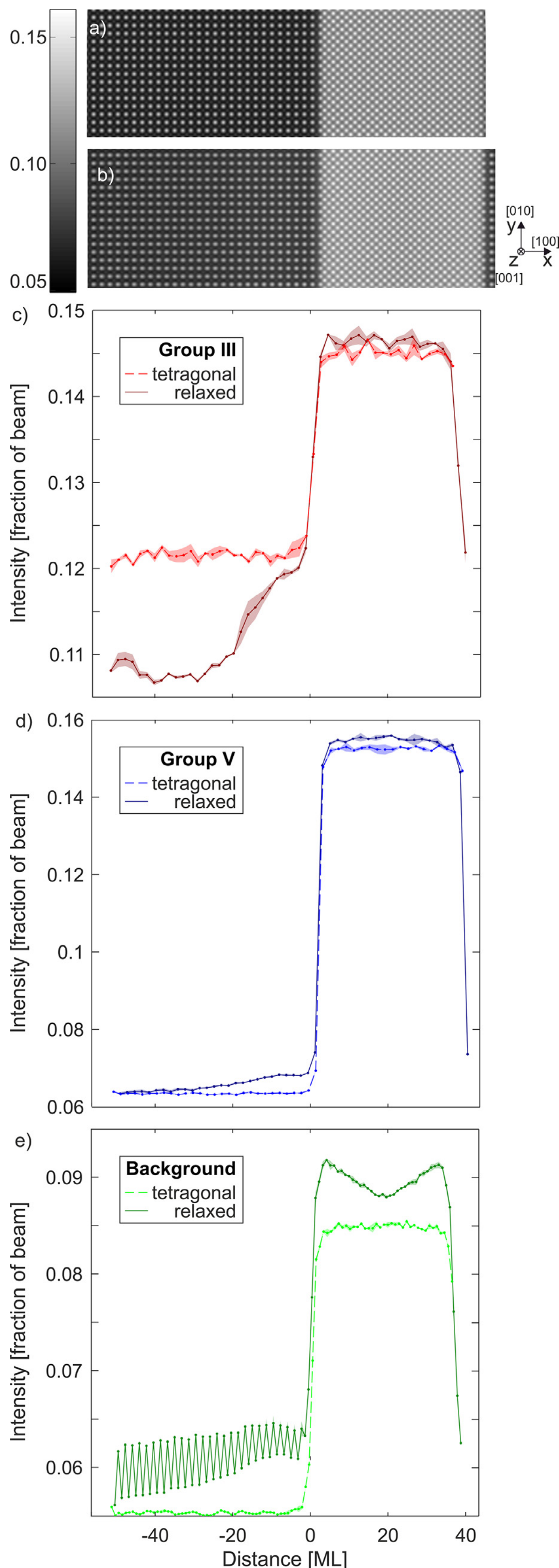

Fig. 5. Simulated ADF images of a tetragonally distorted a) and surface relaxed super cell b) in low angle regime (35-140 mrad). The intensity profiles of the group III sublattice positions are drawn in c) for the tetragonally distorted (broken red line) and relaxed (solid dark red line) super cell. Analogous graphs for the group V sublattice and the background positions are drawn in d) and e), respectively. (For interpretation of the references to colour in this figure legend, the reader is referred to the web version of this article.)

faces. At the previously discussed example structure, the maximum distortion was situated several nm away from the actual interface. In the following we will study how this depends on the sample geometric properties, namely QW width w (along x=[100] direction) and TEM sample thickness t (along z=[001] direction).

The results from 9 different sample geometries are summarized in Fig. 6. The QW width w increases from left to right from 22 to 37 and 74 ML. The position of the QW is marked by the red shaded area. Analogously the values for t increase from top to bottom, from 80 to 184 and 375 MLs, respectively. Like in the previous chapters we will look at the simulated STEM intensity on the group III column across the interface (red lines, read right y axis) as well as the mean square displacement for each corresponding atom column (black lines, read left y axis) in the following. To be able to compare samples with different thicknesses, the intensities are normalized to the intensities of pure GaP with the corresponding thickness, following the equation $I_{norm} = (I - I_{GaP})/I_{GaP}$. The mean square displacements for the different super cells are drawn on a common y scale which is determined by the highest values present, i.e. the values for the thickest sample and the widest QW (Fig. 6i)). In this super cell the maximum total strain energy which is proportional to $w \times t$ is accumulated.

For all super cells displayed, there is a perfect correlation between the displacements and the change of intensity: Firstly, the x position of the maximum displacement coincides with the maximum intensity drop. Secondly, the higher the displacement values, the more severe the intensity reduction. The quality of the correlation is highlighted exemplarily by the blue graph in Fig. 6e), which represents the intensity difference caused by the relaxation, i.e. $(I_{unrelaxed} - I_{relaxed})/I_{unrelaxed}$ in analogy to Fig. 3. Moreover, there are several other interesting trends visible, which will be discussed on the basis of the displacements first.

At a fixed TEM sample thickness (e.g. Fig. 6a)-c)), the thinner the QW, the smaller the maximum displacement. In addition, the x position of the maximum shifts away from the actual interface which may be explained by a compensation effect of the opposing interfaces.

Another observation is that for thicker TEM samples (e.g. from c) to f) and i)), the displacement field shifts away from the interface and broadens. For example in cell i), the maximum of the displacement is at x = -75 ML and it is still present at x = -250 ML. The long range of the displacement field again points out the necessity of large super cells and highly parallelized STEM simulations. For the two thicker QWs, also the magnitude of the displacement rises with increasing TEM sample thickness. This is not apparent for the thinnest QW (a), d) and g)), most likely due to a compensation of the effects of the opposing interfaces. It is worth noting that the degree of surface relaxation is reduced if the sample is thinned along [011] instead of [001]. A comparison between the two zone axes for a sample geometry comparable to the one evaluate in Fig. 6a) can be found in Fig. S4. A disadvantage of the [011] zone axis is that the distance between the group III and V atomic columns is smaller in this projection, therefore cross talk is more likely.

Finally, the two main consequences of the plane bending for ADF measurements will be highlighted briefly. Firstly, whenever the displacement field significantly reaches into the QW (see e.g. Fig. 6i)), the shape of the intensity curve is significantly altered from a box profile. If not accounted for, this can lead to a misinterpretation in terms of chemical composition. This means a thicker sample may be more favorable because the intensity drop is shifted into the barrier. Secondly, the bending significantly reaches into the barrier. This is of special importance as these regions often serve as reference for e.g. sample orientation, determining the chemical composition of the QW or during strain mapping, as they are regarded as undisturbed. For both problems, the computation-

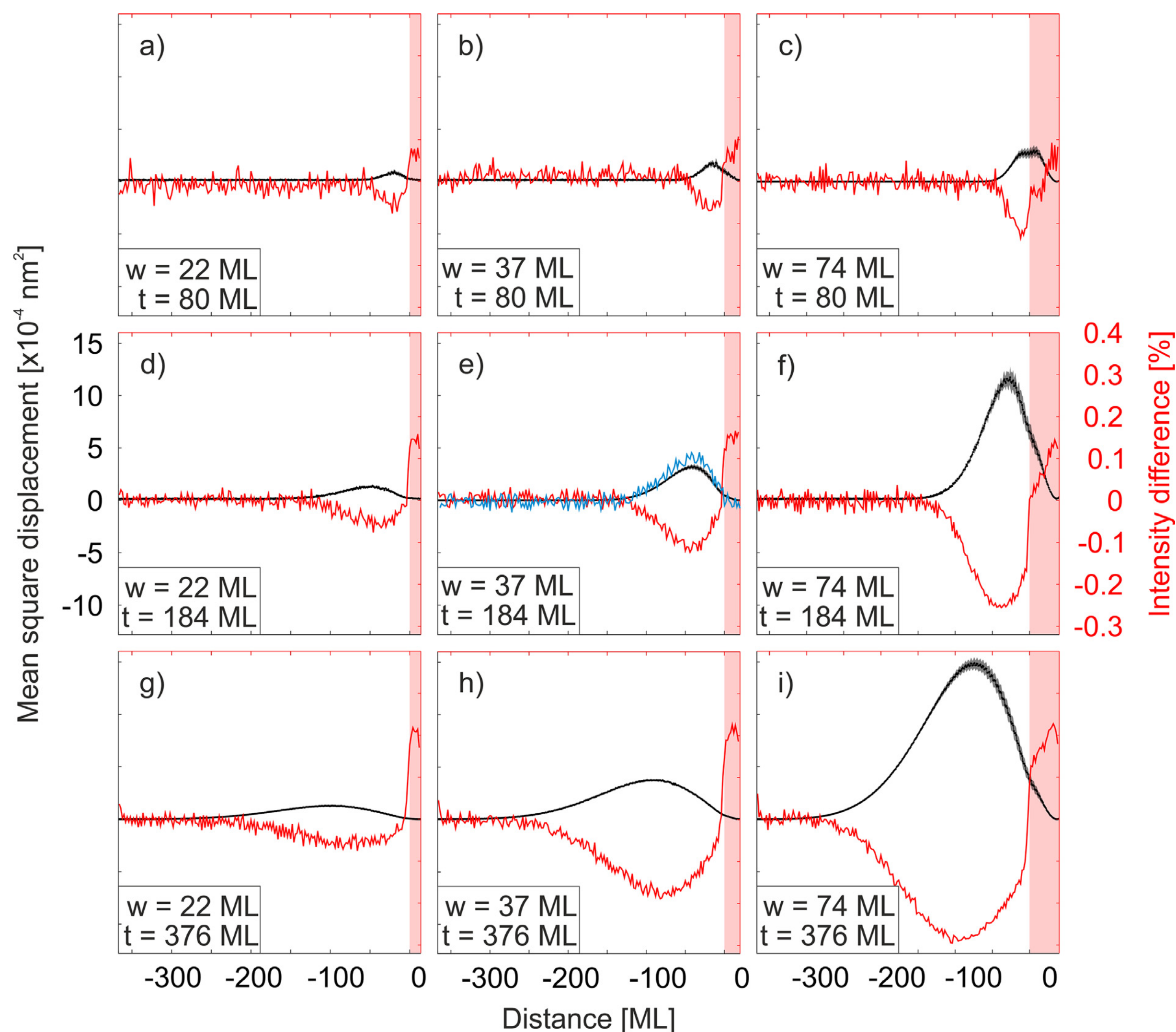

Fig. 6. Systematic variation of the sampleś geometric properties. The quantum well width w increases from left to right, whereas the TEM sample thickness increases from top to bottom. The displacements of the atomic columns are drawn as black lines (read left y axis). The normalized group III intensities are drawn as red lines (read right y axis). The shaded red area indicates the position of the quantum well. The blue curve in e) represents the intensity difference between the surface relaxed and tetragonally distorted super cell. (For interpretation of the references to colour in this figure legend, the reader is referred to the web version of this article.)

ally cheap FE relaxation can be used to localize the distorted regions, find undisturbed ones or on a final stage even to correct "spoiled" data. Anyhow, for real samples, some additional factors have to be considered. Firstly, any additionally present SADs (e.g. introduced by substitutional atoms) superimpose the effect of lattice bending giving rise to additional de-channeling. But since in our approach the FE and the VFF relaxations are performed consecutively, both effects may be differentiated from one another. Secondly, for heterostructures in which the chemical composition fluctuates the composition will influence the bending and the bending will influence the determination of the composition. This means, the problem has to be solved self-consistently. In this case, the average composition will be a good starting point for the simulation of the bending. The average composition can be determined from unbent regions, e. g. the center part of the QW.

4. Conclusions

Lattice plane bending significantly influences ADF images of strained interfaces. This impedes an accurate orientation of the sample, the quantitative evaluation of intensities as well as strain mapping.

Where and how much sample is bent can be estimated from FE relaxation of adequate super cells. FP simulations reveal a reduced intensity in HAADF images caused by de-channeling of electrons from the atomic column positions. Simultaneously, additional diffuse scattering takes place at the bent lattice planes resulting in an increased intensity at low scattering angles. Simulations neglecting the influence of chromatic aberration reveal that the discussed effects will be even more important for the next generation of aberration corrected microscopes.

The intensity reduction of an atomic column in HAADF measurements is directly proportional to its mean square displacement. The computationally cheap FE relaxation can be used to localize the distorted regions and on a final stage even to correct the reduced intensity, whereby a quantitative evaluation of the chemical composition across the interface becomes feasible.

Acknowledgements

This work was supported by the German Science Foundation (GRK 1782: "Functionalization of Semiconductors" and SFB 1083: "Structure and Dynamics of Internal Interfaces").

Supplementary materials

Supplementary material associated with this article can be found, in the online version, at doi:10.1016/j.ultramic.2017.04.019.

References

[1] Q. Xu, Y. Ji, D.D. Krut, J.H. Ermer, M.D. Escarra, Transmissive concentrator multijunction solar cells with over 47% in-band power conversion efficiency, Appl. Phys. Lett. 109 (2016) 193905, doi:10.1063/1.4967376.

[2] H. Tan, A. Furlan, W. Li, K. Arapov, R. Santbergen, M.M. Wienk, M. Zeman, A.H.M. Smets, R.A.J. Janssen, Highly efficient hybrid polymer and amorphous silicon multijunction solar cells with effective optical management, Adv. Mater. 28 (2016) 2170–2177, doi:10.1002/adma.201504483.

[3] N. Wang, L. Cheng, R. Ge, S. Zhang, Y. Miao, W. Zou, C. Yi, Y. Sun, Y. Cao, R. Yang, Y. Wei, Q. Guo, Y. Ke, M. Yu, Y. Jin, Y. Liu, Q. Ding, D. Di, L. Yang, G. Xing, H. Tian, C. Jin, F. Gao, R.H. Friend, J. Wang, W. Huang, Perovskite light-emitting diodes based on solution-processed self-organized multiple quantum wells, Nat. Photonics. 10 (2016) 699–704, doi:10.1038/nphoton.2016.185.

[4] S.J. Pennycook, Z-contrast stem for materials science, Ultramicroscopy. 30 (1989) 58–69, doi:10.1016/0304-3991(89)90173-3.

[5] N.D. Browning, S.J. Pennycook, Direct experimental determination of the atomic structure at internal interfaces, J. Phys. D. Appl. Phys. 29 (1996) 1779–1798, doi:10.1088/0022-3727/29/7/013.

[6] C. Dwyer, C. Maunders, C.L. Zheng, M. Weyland, P.C. Tiemeijer, J. Etheridge, Sub-0.1 nm-resolution quantitative scanning transmission electron microscopy without adjustable parameters, Appl. Phys. Lett. (2012) 100, doi:10.1063/1.4711766.

[7] J.M. Lebeau, S. Stemmer, Experimental quantification of annular dark-field images in scanning transmission electron microscopy, Ultramicroscopy 108 (2008) 1653–1658, doi:10.1016/j.ultramic.2008.07.001.

[8] A. Rosenauer, K. Gries, K. Müller, M. Schowalter, A. Pretorius, A. Avramescu, K. Engl, S. Lutgen, Measurement of composition profiles in III-nitrides by quantitative scanning transmission electron microscopy, J. Phys. Conf. Ser. 209 (2010) 12009, doi:10.1088/1742-6596/209/1/012009.

[9] C. Dwyer, R. Erni, J. Etheridge, Measurement of effective source distribution and its importance for quantitative interpretation of STEM images, Ultramicroscopy. 110 (2010) 952–957, doi:10.1016/j.ultramic.2010.01.007.

[10] D.T. Nguyen, S.D. Findlay, J. Etheridge, The spatial coherence function in scanning transmission electron microscopy and spectroscopy, Ultramicroscopy. 146 (2014) 6–16, doi:10.1016/j.ultramic.2014.04.008.

[11] K. Kuramochi, T. Yamazaki, Y. Kotaka, M. Ohtsuka, I. Hashimoto, K. Watanabe, Effect of chromatic aberration on atomic-resolved spherical aberration corrected STEM images, Ultramicroscopy. 110 (2009) 36–42, doi:10.1016/j.ultramic.2009.09.003.

[12] K.A. Mkhoyan, S.E. Maccagnano-Zacher, E.J. Kirkland, J. Silcox, Effects of amorphous layers on ADF-STEM imaging, Ultramicroscopy. 108 (2008) 791–803, doi:10.1016/j.ultramic.2008.01.007.

[13] M.M.J. Treacy, The effects of elastic relaxation on transmission electron microscopy studies of thinned composition-modulated materials, J. Vac. Sci. Technol. B Microelectron. Nanom. Struct. 4 (1986) 1458, doi:10.1116/1.583473.

[14] L. De Caro, A. Giuffrida, E. Carlino, L. Tapfer, Elastic stress relaxation in HRTEM specimens of strained semiconductor heterostructures and its influence on the image contrast, Microsc. Microanal. Microstruct. 6 (1995) 465–472, doi:10.1051/mmm:1995137.

[15] V. Grillo, The effect of surface strain relaxation on HAADF imaging, Ultramicroscopy. 109 (2009) 1453–1464, doi:10.1016/j.ultramic.2009.07.010.

[16] L. De Caro, A. Giuffrida, E. Carlino, L. Tapfer, Effects of the elastic stress relaxation on the HRTEM image contrast of strained heterostructures, Acta Crystallogr. Sect. A Found. Crystallogr. 53 (1997) 168–174, doi:10.1107/S0108767396012378.

[17] A. Rosenauer, D. Gerthsen, V. Potin, Strain state analysis of InGaN/GaN - sources of error and optimized imaging conditions, Phys. Status Solidi. 203 (2006) 176–184, doi:10.1002/pssa.200563519.

[18] L. De Caro, L. Tapfer, A. Giuffrida, Finite-size effects in one-dimensional strained semiconductor heterostructures, Phys. Rev. B. 54 (1996) 10575–10584, doi:10.1103/PhysRevB.54.10575.

[19] Z. Yu, D.A. Muller, J. Silcox, Study of strain fields at a-Si/c-Si interface, J. Appl. Phys. 95 (2004) 3362–3371, doi:10.1063/1.1649463.

[20] A. Amali, P. Rez, J.M. Cowley, High angle annular dark field imaging of stacking faults, Micron 28 (1997) 89–94, doi:10.1016/S0968-4328(97)00001-2.

[21] D.D. Perovic, C.J. Rossouw, A. Howie, Imaging elastic strains in high-angle annular dark field scanning transmission electron microscopy, Ultramicroscopy. 52 (1993) 353–359, doi:10.1016/0304-3991(93)90046-Z.

[22] J.M. Cowley, Y. Huang, De-channelling contrast in annular dark-field STEM, Ultramicroscopy. 40 (1992) 171–180, doi:10.1016/0304-3991(92)90058-R.

[23] K. Huang, X-Ray Reflexions from Dilute Solid Solutions, Proc. R. Soc. A Math. Phys. Eng. Sci. 190 (1947) 102–117, doi:10.1098/rspa.1947.0064.

[24] A. Rosenauer, T. Mehrtens, K. Müller, K. Gries, M. Schowalter, P. Venkata Satyam, S. Bley, C. Tessarek, D. Hommel, K. Sebald, M. Seyfried, J. Gutowski, A. Avramescu, K. Engl, S. Lutgen, Composition mapping in InGaN by scanning transmission electron microscopy, Ultramicroscopy. 111 (2011) 1316–1327, doi:10.1016/j.ultramic.2011.04.009.

[25] E. H, K.E. MacArthur, T.J. Pennycook, E. Okunishi, A.J. D'Alfonso, N.R. Lugg, L.J. Allen, P.D. Nellist, Probe integrated scattering cross sections in the analysis of atomic resolution HAADF STEM images, Ultramicroscopy. 133 (2013) 109–119, doi:10.1016/j.ultramic.2013.07.002.

[26] P.N. Keating, Effect of invariance requirements on the elastic strain energy of crystals with application to the diamond structure, Phys. Rev. 145 (1966) 637–645, doi:10.1103/PhysRev.145.637.

[27] H. Döscher, P. Hens, A. Beyer, L. Tapfer, K. Volz, W. Stolz, GaP-interlayer formation on epitaxial GaAs(100) surfaces in MOVPE ambient, J. Cryst. Growth. (2016), doi:10.1016/j.jcrysgro.2016.10.055.

[28] T. Grieb, K. Müller, E. Cadel, A. Beyer, M. Schowalter, E. Talbot, K. Volz, A. Rosenauer, Simultaneous, quantification of indium and nitrogen concentration in InGaNAs using HAADF-STEM, Microsc. Microanal. 20 (2014) 1740–1752, doi:10.1017/S1431927614013051.

[29] I. Vurgaftman, J.R. Meyer, L.R. Ram-Mohan, Band parameters for III–V compound semiconductors and their alloys, J. Appl. Phys. 89 (2001) 5815, doi:10.1063/1.1368156.

[30] J. Belz, A. Beyer, T. Torunski, W. Stolz, K. Volz, Direct investigation of (sub-) surface preparation artifacts in GaAs based materials by FIB sectioning, Ultramicroscopy. 163 (2016) 19–30, doi:10.1016/j.ultramic.2016.01.001.

[31] S. Plimpton, Fast parallel algorithms for short-range molecular dynamics, J. Comput. Phys. 117 (1995) 1–19, doi:10.1006/jcph.1995.1039.

[32] T. Grieb, K. Müller, R. Fritz, V. Grillo, M. Schowalter, K. Volz, A. Rosenauer, Quantitative chemical evaluation of dilute GaNAs using ADF STEM: avoiding surface strain induced artifacts, Ultramicroscopy. 129 (2013) 1–9, doi:10.1016/j.ultramic.2013.02.006.

[33] R.F. Loane, P. Xu, J. Silcox, Thermal vibrations in convergent-beam electron diffraction, Acta Crystallogr. Sect. A Found. Crystallogr. 47 (1991) 267–278, doi:10.1107/S0108767391000375.

[34] J.O. Oelerich, L. Duschek, J. Belz, A. Beyer, S.D. Baranovskii, K. Volz, STEMsalabim: a high-performance computing cluster friendly code for scanning transmission electron microscopy image simulations of thin specimens, Ultramicroscopy. 177 (2017) 91–96, doi:10.1016/j.ultramic.2017.03.010.

[35] E.J. Kirkland, Advanced Computing in Electron Microscopy, Springer U.S, Boston, M.A., 2010, doi:10.1007/978-1-4419-6533-2.

[36] M. Schowalter, A. Rosenauer, J.T. Titantah, D. Lamoen, Computation and parametrization of the temperature dependence of Debye-Waller factors for group IV, III-V and II-VI semiconductors, Acta Crystallogr. A. 65 (2009) 5–17, doi:10.1107/S0108767308031437.

[37] A. Beyer, J. Belz, N. Knaub, K. Jandieri, K. Volz, Influence of spatial and temporal coherences on atomic resolution high angle annular dark field imaging, Ultramicroscopy. 169 (2016) 1–10, doi:10.1016/j.ultramic.2016.06.006.

[38] A. Lotnyk, D. Poppitz, U. Ross, J.W. Gerlach, F. Frost, S. Bernütz, E. Thelander, B. Rauschenbach, Focused high- and low-energy ion milling for TEM specimen preparation, Microelectron. Reliab. 55 (2015) 2119–2125, doi:10.1016/j.microrel.2015.07.005.

[39] F. Lelarge, C. Priester, C. Constantin, A. Rudra, K. Leifer, E. Kapon, Strain mapping of V-groove InGaAs/GaAs strained quantum wires using cross-sectional atomic force microscopy, Appl. Surf. Sci. 166 (2000) 290–294, doi:10.1016/S0169-4332(00)00410-4.

[40] F. Lelarge, O. Dehaese, E. Kapon, C. Priester, Strain relaxation at cleaved surfaces studied by atomic force microscopy, Appl. Phys. A Mater. Sci. Process. 69 (1999) 347–351, doi:10.1007/s003390051012.

[41] V. Grillo, K. Mueller, K. Volz, F. Glas, T. Grieb, A. Rosenauer, Strain, composition and disorder in ADF imaging of semiconductors, J. Phys. Conf. Ser. 326 (2011) 12006, doi:10.1088/1742-6596/326/1/012006.

[42] O. Rubel, I. Németh, W. Stolz, K. Volz, Modeling the compositional dependence of electron diffraction in dilute GaAs- and GaP-based compound semiconductors, Phys. Rev. B. 78 (2008) 75207, doi:10.1103/PhysRevB.78.075207.

[43] V. Grillo, E. Carlino, F. Glas, Influence of the static atomic displacement on atomic resolution Z-contrast imaging, Phys. Rev. B. 77 (2008) 54103, doi:10.1103/PhysRevB.77.054103.

[44] D.O. Klenov, S. Stemmer, Contributions to the contrast in experimental high-angle annular dark-field images, Ultramicroscopy. 106 (2006) 889–901, doi:10.1016/j.ultramic.2006.03.007.

[45] Y. Kotaka, Essential experimental parameters for quantitative structure analysis using spherical aberration-corrected HAADF-STEM, Ultramicroscopy. 110 (2010) 555–562, doi:10.1016/j.ultramic.2009.12.008.

[46] K. Watanabe, Y. Kotaka, N. Nakanishi, T. Yamazaki, I. Hashimoto, M. Shiojiri, Deconvolution processing of HAADF STEM images, Ultramicroscopy. 92 (2002) 191–199, doi:10.1016/S0304-3991(02)00132-8.

[47] C. Dwyer, Simulation of scanning transmission electron microscope images on desktop computers, Ultramicroscopy. 110 (2010) 195–198, doi:10.1016/j.ultramic.2009.11.009.

[48] T. Grieb, K. Müller, R. Fritz, M. Schowalter, N. Neugebohrn, N. Knaub, K. Volz, A. Rosenauer, Determination of the chemical composition of GaNAs using STEM HAADF imaging and STEM strain state analysis, Ultramicroscopy. 117 (2012) 15–23, doi:10.1016/j.ultramic.2012.03.014.

[49] K. Müller-Caspary, O. Oppermann, T. Grieb, F.F. Krause, A. Rosenauer, M. Schowalter, T. Mehrtens, A. Beyer, K. Volz, P. Potapov, Materials characterisation by angle-resolved scanning transmission electron microscopy, Sci. Rep. 6 (2016) 37146, doi:10.1038/srep3714.

6.1.5 Publication 5

Citation

Influence of spatial and temporal coherences on atomic resolution high angle annular dark field imaging
A. Beyer, J. Belz, N. Knaub, K. Jandieri, K. Volz, Ultramicroscopy **169**, p.1–10, 2017,
DOI: 10.1016/j.ultramic.2016.06.006

Abstract

Aberration-corrected (scanning) transmission electron microscopy ((S)TEM) has become a widely used technique when information on the chemical composition is sought on an atomic scale. To extract the desired information, complementary simulations of the scattering process are inevitable. Often the partial spatial and temporal coherences are neglected in the simulations, although they can have a huge influence on the high resolution images.

With the example of binary gallium phosphide (**GaP**) we elucidate the influence of the source size and shape as well as the chromatic aberration on the high angle annular dark field (**HAADF**) intensity. We achieve a very good quantitative agreement between the frozen phonon simulation and experiment for different sample thicknesses when a Lorentzian source distribution is assumed and the effect of the chromatic aberration is considered. Additionally the influence of amorphous layers introduced by the preparation of the TEM samples is discussed.

Taking into account these parameters, the intensity in the whole unit cell of GaP, i.e. at the positions of the different atomic columns and in the region between them, is described correctly. With the knowledge of the decisive parameters, the determination of the chemical composition of more complex, multinary materials becomes feasible.

Contributions

Jürgen Belz and Nikolai Knaub contributed experimental data and prepared samples for the experiment. Andreas Beyer and Jürgen Belz designed the experiment and wrote software for the evaluation. Kachaber Jandieri calculated the amorphous layer and was involved in construction of the super cells. Kerstin Volz supervised the research and secured funding.

Reprinted from *Ultramicroscopy **169**,1–10,2016*, Copyright 2016, with permission from Elsevier.

Ultramicroscopy 169 (2016) 1–10

Contents lists available at ScienceDirect

Ultramicroscopy

journal homepage: www.elsevier.com/locate/ultramic

Influence of spatial and temporal coherences on atomic resolution high angle annular dark field imaging

Andreas Beyer *, Jürgen Belz, Nikolai Knaub, Kakhaber Jandieri, Kerstin Volz

Materials Science Center and Faculty of Physics, Philipps-Universität Marburg, Hans-Meerweinstraße 6, 35032 Marburg, Germany

ARTICLE INFO

Article history:
Received 23 February 2016
Received in revised form
18 May 2016
Accepted 19 June 2016
Available online 21 June 2016

Keywords:
HAADF imaging
Spatial coherence
Temporal coherence
Quantitative STEM
Image simulation
III/V semiconductors

ABSTRACT

Aberration-corrected (scanning) transmission electron microscopy ((S)TEM) has become a widely used technique when information on the chemical composition is sought on an atomic scale. To extract the desired information, complementary simulations of the scattering process are inevitable. Often the partial spatial and temporal coherences are neglected in the simulations, although they can have a huge influence on the high resolution images.

With the example of binary gallium phosphide (GaP) we elucidate the influence of the source size and shape as well as the chromatic aberration on the high angle annular dark field (HAADF) intensity. We achieve a very good quantitative agreement between the frozen phonon simulation and experiment for different sample thicknesses when a Lorentzian source distribution is assumed and the effect of the chromatic aberration is considered. Additionally the influence of amorphous layers introduced by the preparation of the TEM samples is discussed.

Taking into account these parameters, the intensity in the whole unit cell of GaP, i.e. at the positions of the different atomic columns and in the region between them, is described correctly. With the knowledge of the decisive parameters, the determination of the chemical composition of more complex, multinary materials becomes feasible.

© 2016 Elsevier B.V. All rights reserved.

1. Introduction

Modern semiconductor devices are usually built from complex compound materials. In the field of III/V semiconductors the binary materials GaN, GaP and GaAs are alloyed with one or more additional elements from the group III or V of the periodic table to meet the demands of the respective application. For example (GaIn)N, Ga(NAsP) and (GaIn)(NAs) can be used for LED, Laser and solar cell applications, respectively [1–5].

In all these materials the exact control of the chemical composition on each sublattice is crucial to achieve the desired functionality. Hence, adequate methods to determine the composition are needed, as e.g. conventionally used X-ray diffraction alone is not applicable anymore for materials consisting of more than three constituents. Moreover, its lateral resolution is limited and local fluctuations in composition cannot be detected.

In this task, (scanning) transmission electron microscopy ((S)TEM) has proven as a valuable tool to deliver the desired information. Due to the intuitive interpretation in terms of Z contrast, the high angle annular dark field (HAADF) technique is frequently applied [6]. In the last decade sub-angstrom resolution became possible due to the introduction of aberration correctors [7,8]. Nevertheless, the absolute composition of a sample is not always derivable directly in both low and high resolution imaging. This makes an adequate simulation of the scattering process inevitable. Here the multi slice algorithm in the frozen phonon (FP) approximation has shown to reproduce the experimental data very accurately [9].

By normalizing the experimental data to intensity of the impinging beam, e.g. via a detector scan [10], it is possible to compare simulations and experiment on the same intensity scale. Taking into account the sensitivity of the used detector quantitative results could be derived for various material systems [11–13].

Nevertheless, when high resolution information is sought, some additional challenges need to be faced. Depending on the studied specimen and its thickness, cross scattering from neighboring columns occurs and the measured HAADF intensity does not necessarily reflect the chemical composition at a certain position [14,15]. Moreover, amorphous layers due to sample preparation become increasingly important in the thin samples investigated in high-resolution STEM (HRSTEM) [16].

Most importantly, the resolution and especially the contrast are higher in the simulated than in the experimental data, even if the present geometric aberrations are included. This discrepancy is

* Corresponding author.
E-mail address: andreas.beyer@physik.uni-marburg.de (A. Beyer).

http://dx.doi.org/10.1016/j.ultramic.2016.06.006
0304-3991/© 2016 Elsevier B.V. All rights reserved.

caused by the partial spatial and temporal coherence of the electrons. The partial temporal coherence is mainly caused by the chromatic aberration and energy spread of the electrons in the TEM [17]. The influence of the chromatic aberration on the STEM has been investigated for example in [18,19].

The spatial coherence is related to the source size [20], i.e. the fact that the real electron source is not a point like emitter but has a finite dimension. The effect of the partial spatial coherence can be treated by convoluting the simulated images with an effective source distribution; see e.g. [21–23]. The shape of the source distribution is discussed controversially in the literature, as Gaussian, Lorentzian or combinations of both are used [21,24]. Nevertheless, the exact shape can have a huge impact on the appearance of the HAADF images and the application of a wrong distribution can lead to a wrong quantification of the chemical composition at an atomic scale.

If all the influencing parameters are accounted for in the simulation, the question remains how to compare simulated and experimental results with each other? Often only qualitative comparisons are carried out or intensity profiles are compared to simulations. In other approaches, some of the spatially resolved information available in a HRSTEM image is neglected by averaging the experimental intensity over a certain region, e.g. the Voronoi cell of an atomic column [25–27].

In this contribution we present a method to derive quantitative two-dimensional data, i.e. a representative unit cell of the investigated crystal, from experimental images, which can be compared to complementary simulations. We show the influence of the chromatic aberration and the choice of the source distribution on the simulated HAADF intensity. By comparing simulated and experimental data quantitatively for different sample thicknesses we deduce which source distribution has to be applied to the simulations to reproduce the experimental data correctly. Furthermore, we investigate how the presence of amorphous layers due to sample preparation affects the drawn conclusions. Although the influences of temporal coherence, spatial coherence and amorphous layers on STEM investigations have been investigated individually before, the interplay of these effects has not been studied yet. With the correct consideration of all of them we achieve excellent agreement throughout the whole two-dimensional unit cell.

We chose binary GaP as model material because of its inherently fixed stoichiometric composition. Moreover, because of the relative big difference in atomic number of the two constituents, the contrast within a unit cell is higher than for materials consisting of elements with similar atomic number like for example GaAs. Therefore, assumptions in the simulation can be checked and amended.

The conclusions drawn from the simple GaP system can then be used for future evaluation of more complex ternary or multinary materials.

2. Material and methods

Commercially available GaP wafers (Crystec) were used for this study. Electron transparent samples were prepared by conventional mechanical grinding and consecutive argon ion milling using the Gatan PIPS. The incident angle of the ions was chosen to 4° for bottom and top side, resulting in a wedge-shaped sample. The final ion energy was reduced to 1.7 kV in order to minimize the thickness of the amorphous layers at the sample surfaces introduced by the ion bombardment. Please note that the final ion energy of 1.7 kV is not suitable to create a sample fully free from amorphous layers, this energy was rather chosen to create a layer with a defined thickness to investigate its influence on the HAADF intensity. A more detailed description of the applied sample preparation and the resulting (sub-) surface damage is given in [28]. The GaP [010] zone axis was chosen as viewing direction because in this projection the group III and group V sub-lattice exhibit the largest spatial separation of around 0.19 nm.

The STEM investigation was carried out in a double C_S-corrected JEOL JEM 2200FS operating at 200 kV. A condenser aperture of 24 mrad and a detector range of 73–173 mrad were chosen for the HAADF measurements. Atomic-resolution image series were acquired at different positions of the sample exhibiting different TEM sample thicknesses. The individual images of the series were aligned non-rigidly utilizing the 'Smart align'-software [29] in order to reduce the influence of experimental noise and scan distortions on the images. The aligned images were normalized with respect to the impinging beam following the approach described in [30] to be able to compare experiment and simulation on an absolute intensity scale. The radial sensitivity of the used HAADF detector was determined via a detector scan [10] and taken into account.

Complementary image simulations were carried out utilizing the frozen phonon approximation of the STEMSIM code [31]. A residual spherical aberration of 2 µm was measured during the experiments with the help of the corrector software and taken into account in the simulations. A value of 5 mm was assumed for the fifth order spherical aberration coefficient C_5. Additionally the influence of the chromatic aberration was taken into account by summing over a simulated defocus series with 7 different defocus values. The weight of each defocus was determined by a Gaussian function with a full width half maximum (FWHM) of Δz_{CC}, which is connected to the chromatic aberration coefficient C_C by [18]

$$\Delta z_{CC} = 2C_c \frac{dE}{E_0} \sqrt{(2 log 2)}. \quad (1)$$

For the JEOL JEM 2200FS microscope with a C_C of 1.5 mm and a dE of 0.42 eV follows a Δz_{CC} of 7.5 nm at 200 kV acceleration voltage. For each defocus 10 phonon configurations were used. The total number of 70 phonon configurations showed to be a good trade-off between the convergence of the HAADF intensity and the simulation time.

The supercell for the intensity simulations consisted of 5 × 5 GaP unit cells in the *x*-*y*-plane and 92 unit cells in the z direction corresponding to a final thickness of approximately 50 nm.

Additionally, the intensity of amorphous GaP was simulated. Here a supercell of the same dimensions as for crystalline case was derived by the software to simulate the atomic packing in Ideal Amorphous Solids (IAS) [32–34]. This software generates the spherical amorphous structure that satisfies the basic requirements for amorphous solids. It contains none of the elements of symmetry such as mirror, rotation or glide and retains the stoichiometry. The density of amorphous material was adjusted by uniform deformation of IAS sphere and was chosen to 4.94 10^{22} atoms/cm^3, i.e. the same value as for the crystalline GaP. Finally, the supercell of desired rectangular geometry was cut from generated IAS sphere. More realistic models for amorphous layers require very complicated and time-consumable calculations in frames of Molecular Dynamic (MD) simulations [35]. Furthermore, the resulting structure is extremely sensitive to the initial conditions such as the initial temperature and the quenching rate. We believe that the theory of IAS is a sufficient approach for adequate theoretical interpretation of STEM images obtained in our experimental studies. Experimental and simulated data were compared utilizing MATLAB scripts as will be discussed in the result sections.

3. Results

This manuscript is organized as follows: with the example of the simulated thickness dependent HAADF intensity we demonstrate why it is important to apply the correct source distribution to the simulations and why GaP is the adequate material to determine it. In the next step an experimental HAADF measurement of GaP is presented. On its basis we will show how quantitative data from the images were obtained, which can be compared to simulations. By performing this comparison for different sample thicknesses we derive the correct simulation parameters to achieve an optimum agreement between simulation and experiment. Applying these parameters even the small intensities within the GaP unit cell, i.e. the P columns and the background, are described correctly and one can make use of the whole available data.

Even if all geometric aberrations are included in a simulation correctly, the observed experimental resolution is worse than in the simulation. The recognized reason for this discrepancy is the partial spatial coherence, also referred to as the source size, which can be taken into account by convoluting the simulated data with an effective source distribution. Nevertheless, its shape is discussed controversially in the literature [21,24]. Most commonly a symmetrical two-dimensional Gaussian distribution, given by

$$S_G = e^{\left(-\frac{x^2}{2\sigma}-\frac{y^2}{2\sigma}\right)}, \tag{2}$$

is used to convolute the simulation. Here x and y are the spatial coordinates and σ describes the width of the distribution. Besides this simple Gaussian assumption, also a Lorentzian distributions of the form

$$S_L = \frac{\sigma}{\left(x^2 + y^2 + \sigma^2\right)^{3/2}}. \tag{3}$$

is possible and also a combination of both has been discussed [21,24]. In the following we apply the two pure distributions, i.e. Gaussian and Lorentzian, to investigate the influence on the simulated HAADF intensity of GaP. Exemplary profiles of the source distributions are drawn in Fig. 1(a). The width σ was chosen arbitrarily as 55 pm for both distributions. The convolution is performed via a multiplication in the Fourier space which is equivalent but computationally less expense. The individual source distributions were normalized to keep the mean value of the simulation unaffected, which was shown mathematically e.g. in [36].

The simulated thickness dependence of the HAADF intensity for the two different source distributions is summarized in Fig. 1 (b). A ball and stick model of the GaP unit cell is shown as an inset. The Ga atoms are represented by red circles while the P atoms are represented by black ones. The position between the atoms, where the background intensity is derived, is marked by a blue cross. The colors of the thickness dependent intensity curves for the different positions in the unit cell are chosen according to the same color scheme. The different source distributions can be distinguished by their line styles, i.e. Gaussian distribution is shown as solid line and Lorentzian as dashed line. As stated before, the mean intensity of the whole unit cell (represented by the green curves) is independent from the applied source distribution and the curves overlap perfectly for the individual source shapes. A similar behavior can be observed for the intensity at the position of the Ga columns (red curves), which is nearly independent from the assumed source distribution. However, the lower intensities, i.e. at the background positions (blue curves) and at the P columns (black curves) are affected by the different source distributions. In the case of the group-V positions, the intensity assuming a Lorentzian distribution (dashed line) is significantly higher than the intensity assuming Gaussian one (solid line). This is most likely caused by the different amount of intensity that is transferred from the neighboring Ga columns to the P columns. While the Gaussian distribution drops to zero quite fast, the Lorentzian distribution has much wider tails which affect the neighboring P columns, as can be seen in the profiles presented in Fig. 1(a). To demonstrate the impact of this different behavior, the ratio of group V to background intensity for the individual distributions is drawn in (c), the line styles are kept the same as in (a) and (b). In this representation values above 1 mean that P column is brighter than the background and therefore is visible, whereas values below 1 mean that the P column is invisible.

The thickness dependencies of both curves are similar. The high ratio values at thin samples may be caused by the very small background intensity at these thicknesses, where almost no diffuse scattering takes place. For larger thicknesses the ratio increases again monotonically, as the intensity on the group-V column positions increases stronger with the thickness than the intensity on the background positions, presumably due to the channeling conditions.

Besides this similar course, the two curves have a significant horizontal offset to each other, which has a severe effect on the visibility of the P columns. Applying a Lorentzian distribution the P columns are visible for all sample thicknesses. In contrast to that

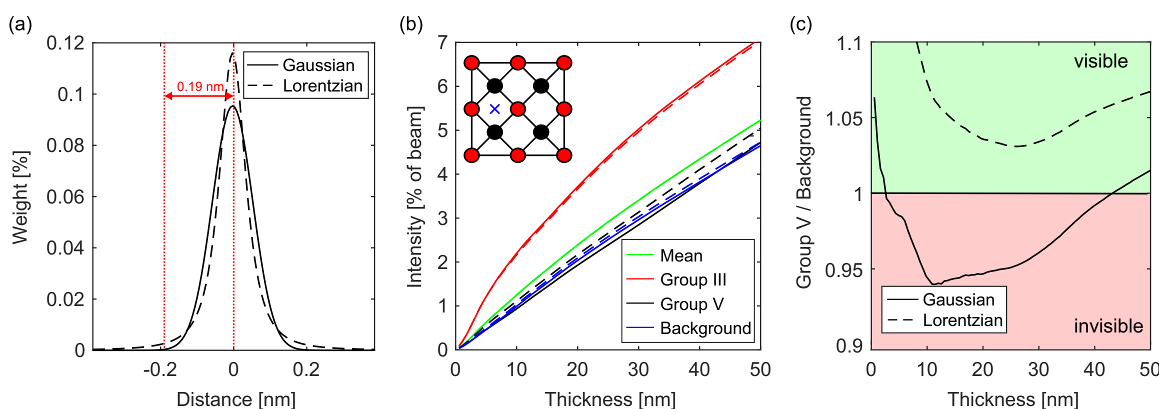

Fig. 1. One-dimensional profiles through the two-dimensional Gaussian (solid line) and Lorentzian (dashed line) source distributions with a fixed width of 55 pm (a). For comparison the inter-atomic distance of GaP is marked by red dotted lines. The simulated thickness dependencies for the two source distributions are shown in (b), i.e. Gaussian (solid line), Lorentzian (dashed line). The group III intensities (red curves) and the mean intensities (green curves) exhibit no significant difference and overlap for the individual source shapes. The lower intensities, i.e. at the group V (black curves) and the background positions (blue curves) are significantly affected by the different source distributions. For a clearer visualization the ratio of group V to background is drawn in (c). (For interpretation of the references to color in this figure legend, the reader is referred to the web version of this article.)

the P columns remain invisible for most of the thicknesses in the Gaussian case. For a mixed source distribution, which is omitted here for reasons of clarity, it depends very strongly on the sample thickness whether P atoms are visible or not.

It is worth noting that in these simulations the effect of chromatic aberration was already taken into account. Neglecting C_C, the discussed trends are even more pronounced because of the increased contrast [18,19]. For the data shown in Fig. 1 the width of the distributions was arbitrarily chosen to 55 pm. If this value is lowered the two curves shift upwards to visibility. When σ is increased, the curves shift downwards and the P column remains invisible.

The described effect may be minor for binary materials which have a smaller difference in atomic number like e.g. GaAs and even less pronounced for materials in diamond structure like Si, where both sublattices are occupied by the same element. In these cases the amount of intensity transferred from one sublattice to the other cancels out.

Nevertheless, as soon as a ternary/multinary material is studied, the choice of the right source distribution is important if quantitative information on atomic resolution is aimed for. Keeping for example GaP as host material, especially in the case of a partially occupied group V sublattice, like e.g. Ga(PAs) or Ga(NP), the determination of the chemical composition from HAADF imaging is not possible, unless the correct source distribution is applied.

Summarizing the conclusions drawn from Fig. 1, we think GaP with its combination of heavy and light scatterers is the adequate material to investigate which source distribution is the correct one.

The intensity data presented in Fig. 1 were derived from three representative positions of the unit cell only. For a more thorough comparison the whole cell should be evaluated. In two dimensions the actual shape of source distribution may have a significant influence on the appearance of the atomic columns. In the simulations the two-dimensional data is directly assessable. In the following we will exemplarily show the procedure how quantitative two-dimensional data can be derived from one experimental image. The other experimental data presented later on in this manuscript are derived in the same manner.

Fig. 2(a) depicts a representative HAADF image of a GaP crystal in [010]-projection. The presented image is an average of 7 individual images which were non-rigidly aligned with respect to each other in order to improve the signal-to-noise ratio. The sample thickness at this region is (19.5 ± 0.5) nm. An exemplary unit cell is marked by the white frame and shown in higher magnification as an inset. The bright Ga atoms are clearly visible while the P columns are only fairly visible.

The whole image consists of 830 individual group-III columns, which were averaged as described in [37] to achieve a mean unit cell which is representative for the whole field of view. In the averaged unit cell, depicted in (b), the P columns are clearly visible due to the further increased signal-to-noise ratio. Additionally, this averaging procedure provides the spatially resolved standard deviation of the intensity (STD_I), i.e. the variation of the intensity at each position (x, y) within the 830 unit cells, which is depicted in (c). Please note that in this graph the intensity values are multiplied by a factor of ten to keep the intensity scale of the other images. The STD_I exhibits a donut-like shape caused by an increased variance in a ring centered on the Ga-column positions. This could be caused by an imperfect alignment of the individual unit cells. However, this potential reason was excluded by evaluating simulated images in the same manner. In this case the determined STD_I does not exhibit this donut shape and its amplitude is significantly reduced to about 10^{-8} which is in the same order of magnitude as the numeric noise. Therefore, we assume that the

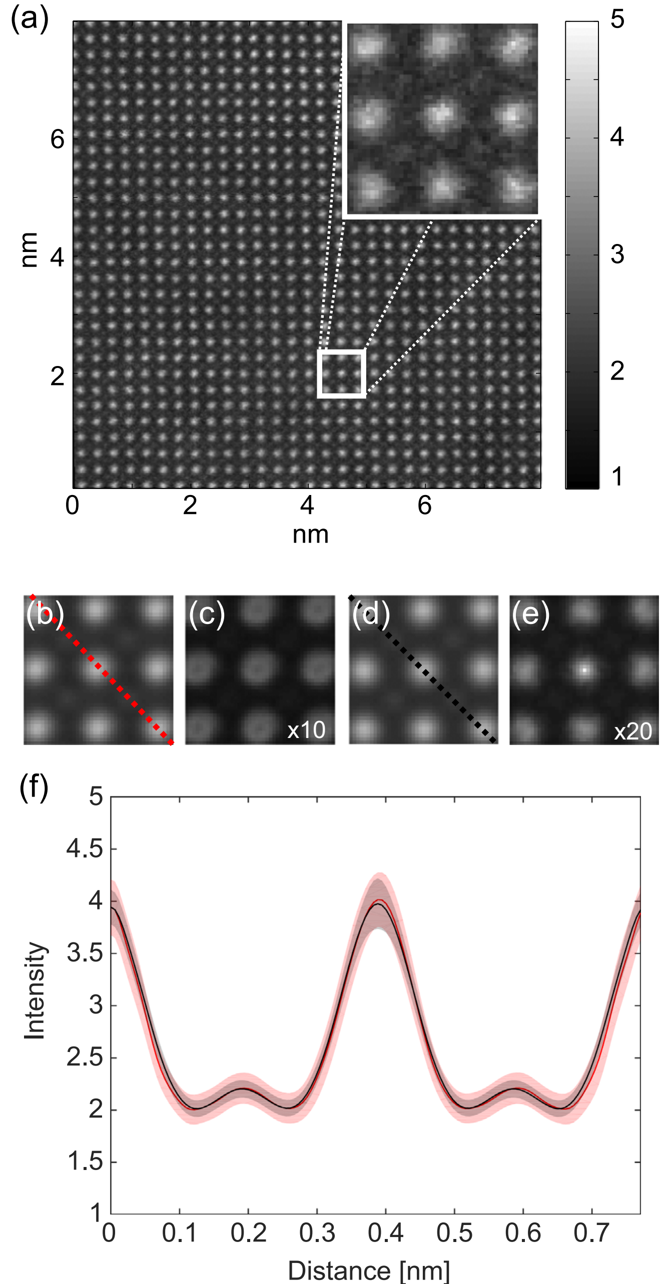

Fig. 2. Experimental HAADF image of a thin (19.5 nm) GaP sample (a). An exemplary unit cell is marked by a white frame and shown in higher magnification as an inset. The average of all 830 unit cells present in the picture and the corresponding spatially resolved standard deviation of the intensity are shown (b) and (c), respectively. The analogue figures applying a 4 fold rotational averaging are depicted in (d) and (e). The red and black dotted lines mark the positions of the intensity profiles across the diagonal of the unit cell, which are shown in (f). The shaded regions represent the standard deviation. While the profiles of the averaged unit cell (red curve) and the additionally rotation averaged unit cell (black curve) show no significant difference, the standard deviation is clearly reduced in the latter case. (For interpretation of the references to color in this figure legend, the reader is referred to the web version of this article.)

width of the atomic columns in the experimental image changes due to scan distortions or a change of astigmatism over the field of view. In order to minimize this effect we can exploit the fourfold symmetry of the investigated GaP by rotating each individual unit cell in the experimental image in steps of 90° and average over the four orientations. It has to be noted that this procedure could result in artefacts if non-rotational symmetric aberrations, e.g. astigmatism, are present to a huge extend. In the experimental data

presented here this is not the case. This averaging approach is similar to the ones proposed in [38,39] for complete images rather than the sub images which are utilized here. The analogue figures applying this fourfold rotational averaging are depicted in (d) and (e), this time the intensity values in (e) had to be multiplied by twenty to keep the intensity scale of the other images. The averaged image in (e) shows no obvious difference to the not rotated image in (b), only a slightly reduced background yielding in a better visibility of the P columns is observable. Nevertheless there is a major effect on the STD_I. In comparison to (c) its amplitude is reduced by nearly a factor of two and there is no apparent donut shape. Now the STD_I has its maximum value at group-III columns, which is most likely caused by the small changes in sample thickness.

The red and black dotted lines in (b–e) mark the positions of the intensity profiles across the diagonal of the unit cell, which are shown in (f).The shaded areas represent the standard deviation. As already discussed in the two-dimensional representation, the profiles of the averaged unit cell (red curve) and the additionally rotation averaged unit cell (black curve) show no significant difference, but the STD_I is significantly reduced in the latter case. The remaining STD_I is most likely caused by the aforementioned local thickness inhomogeneties, amorphous layers introduced during the sample preparation and experimental noise. Due to the highly increased signal-to-noise ratio, the averaged unit cell can be used to derive important quantities from the measured sample. Besides the pure intensity that will be used further on in this manuscript, e.g. the width of the atomic columns or the inter-atomic distances can be measured, if the lateral dimensions are calibrated correctly.

The clear visibility of the P columns in the thin sample and the shape of the column are already a hint that the actual source distribution is a Lorentzian rather than a Gaussian one. Nevertheless, to definitely answer the question, which source distribution is the appropriate one, a quantitative comparison of the experimental and simulated data will be performed for different sample thicknesses in the following.

The results of this comparison are summarized in Fig. 3. In the first row the experimental unit cells, which were derived by the procedure described before, are depicted. The sample thicknesses t of the investigated regions was determined to be (19.5 ± 0.5) nm (a) and (28.2 ± 0.5) nm (b), respectively. These values were derived by comparing the mean intensities of (2.33 ± 0.03) % and (3.20 ± 0.03) %, which are independent from the actual source distribution, to the thickness dependent simulations shown in Fig. 1(b). This method was verified to lead to correct thickness values for the used microscope utilizing different methods and sample materials [28,37,40].

Comparing the two experimental unit cells it becomes obvious that the P columns are visible at the different thicknesses, moreover, the relative intensity of the P columns increases and they become visible more clearly with increasing thickness. This is in agreement with the simulations shown in Fig. 1(b), where the Ga intensity saturates, whereas the P intensity increases in a linear manner with respect to the thickness, due to the difference in absorption of the different columns [6].

The simulated unit cells using different simulation parameters are shown in the leftmost column ((c), (f), (i), and (l)). The intensity is given in percent of the impinging beam for the simulated as well as the experimental data. The simulated data is shown for the thin sample only for reasons of clarity; moreover, the images would look very similar when they are drawn in their individual intensity scale.

The respective differences between simulated intensity I_{Sim} and experimental intensity I_{Exp} are shown color coded normalized to the experimental intensity in the center of the figure. Hence, the units of the intensity scale are given in percent deviation from the experimental data. The color limits of the deviation are chosen symmetrically around zero. In the applied color scheme blue corresponds to the case that the simulated intensity is higher than the experimental one, whereas red indicates that the simulated intensity is too low. The red numbers represent the absolute difference $\Delta_{absolute}$ of simulation and experiment in fractions of the impinging beam given by

$$\Delta_{absolute} = \sqrt{\frac{\sum_{x,y}^{Nx,Ny}\left(\mathrm{I}_{\mathrm{Exp}}(x, y) - \mathrm{I}_{\mathrm{Sim}}(x, y)\right)^2}{N_x N_y}}, \quad (4)$$

where x and y are the pixels in the image ranging from 1 to N_x and N_y, respectively. The blue numbers represent the relative difference $\Delta_{relative}$ which is additionally normalized to the experimental intensity I_{Exp}

$$\Delta_{relative} = \sqrt{\frac{\sum_{x,y}^{Nx,Ny}\left[\left(\mathrm{I}_{\mathrm{Exp}}(x, y) - \mathrm{I}_{\mathrm{Sim}}(x, y)\right)/I_{\mathrm{Exp}}(x, y)\right]^2}{N_x N_y}}. \quad (5)$$

It is important to distinguish between these two values because $\Delta_{absolute}$ strongly depends on the high intensities, i.e. strong scatterers which are in this case the Ga columns. Taking its value to determine the goodness of the agreement between simulation and experiment could lead to very good agreement on the Ga columns but a poor resemblance of the low intensities, in this case the P columns. Therefore we decided to choose $\Delta_{relative}$ as a figure of merit and minimize $\Delta_{relative}$ rather than $\Delta_{absolute}$.

In the second row of Fig. 3(c–e) the comparison between the experiments and the simulations, including the residual geometric aberrations as determined by the corrector software prior to the measurements, is shown for the different thicknesses. As discussed several times before, the simulations exhibit a significantly higher contrast than the experimental data. The intensity at the positions of the atomic columns is up to twice as high in the simulation as in the experiment, whereas the intensity at the background is significantly lower as can be seen by the blue and yellow colors in the difference plots, respectively. Interestingly the deviations become smaller for the thicker sample, which may be caused by the spreading of the beam within the sample which increases with sample thickness.

In addition to the geometric aberrations, the chromatic aberration was taken into account in the third row of Fig. 3(f–h). As expected the contrast is decreased, the maximum for example is reduced by around 20% which is in agreement with [18,19]. This results in the reduction of $\Delta_{relative}$ and $\Delta_{absolute}$ for both investigated thicknesses. Nevertheless, the discrepancy is still rather high, because the tremendous effect of the spatial coherence is neglected.

The spatial coherence was taken into account by applying a Gaussian source distribution in the fourth row of Fig. 3(i–k). The width parameter σ was varied to achieve the minimum $\Delta_{relative}$ according to Eq. (5). The resulting value of σ is shown in the individual plots. For both thicknesses the differences $\Delta_{relative}$ and $\Delta_{absolute}$ become significantly smaller and the intensity scale is the same for simulation and experiment leading to a qualitative agreement. Nevertheless, the quantitative comparison shows some distinct differences.

The difference is especially high at the positions of the group-V sublattice. In contrast to the experimental data (a), the P columns are not visible at all in the simulation of the thin sample (i), for the higher sample thickness P becomes more visible in accordance with Fig. 1, resulting in a slight reduction of $\Delta_{relative}$ for the thicker sample. Here $\Delta_{relative}$ was chosen as a criterion to determine the optimum σ, hence the resulting σ is slightly wider than the experimental column width to compensate for the missing intensity on group-V sublattice. If $\Delta_{absolute}$ was chosen as criterion instead the poor representation of the P columns would become even worse.

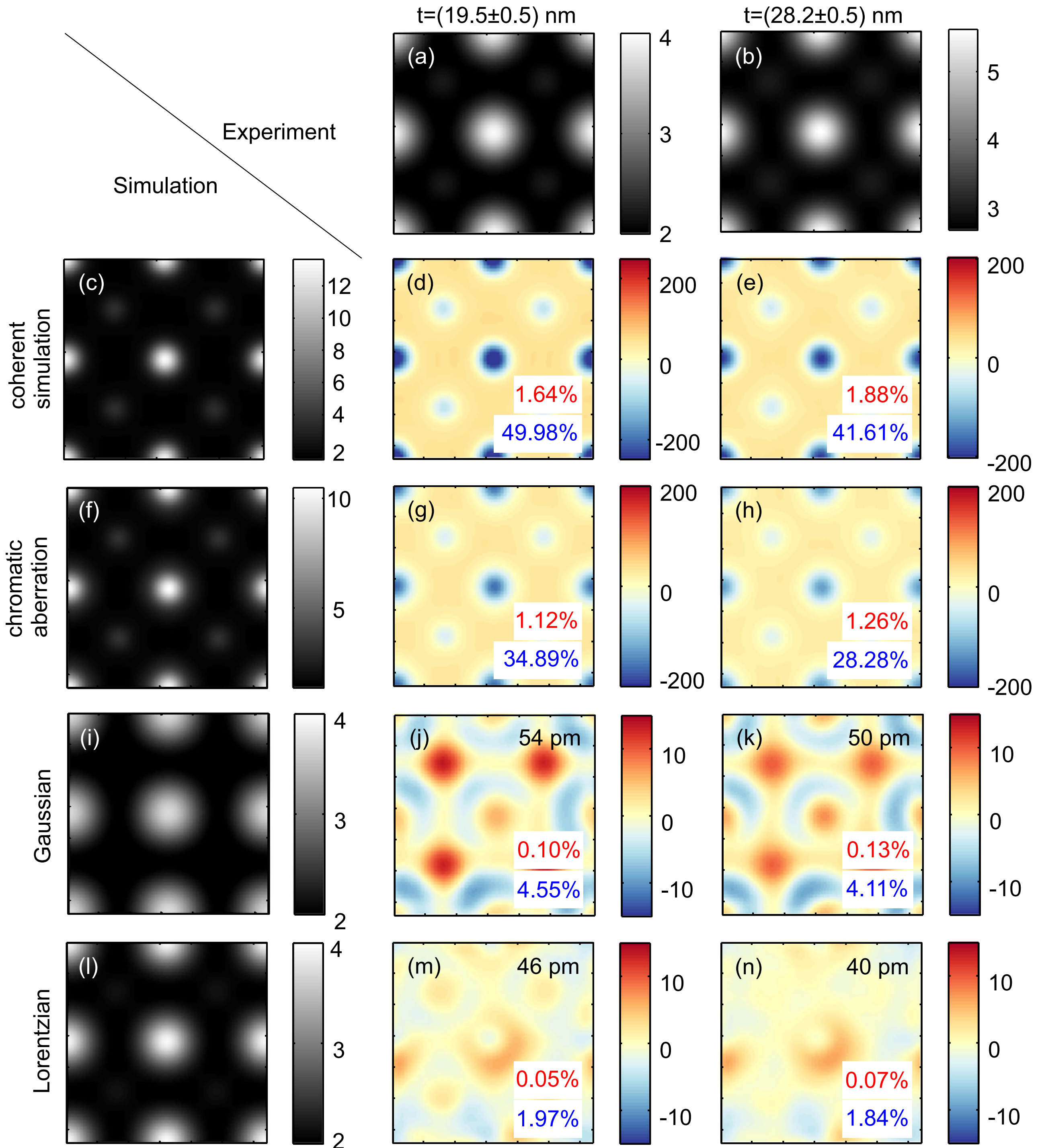

Fig. 3. Comparison of simulation and experiment: The first row ((a) and (b)) depicts the experimental unit cells for the two investigated thicknesses. For reasons of clarity, the corresponding simulated unit cells are shown for the thin sample only in the leftmost column. The individual images represent the simulation including geometric aberrations (c), additionally taking into account the chromatic aberration (f) and applying the source distribution as a Gaussian (i) and a Lorentzian (l). The grayscale is given in percent of the impinging beam. The corresponding differences between simulation and experiment normalized to the experimental intensity are shown color coded in (d) and (e), (g) and (h), (j) and (k) and (m) and (n), respectively. The units of the intensity scale are given in percent deviation and are chosen symmetrically around zero. The red numbers represent the absolute error in fractions of the impinging beam while the blue ones represent the relative error which is normalized to the intensity. The width of the distribution yielding the best agreement between simulation and experiment is indicated in the individual plots. (For interpretation of the references to color in this figure legend, the reader is referred to the web version of this article.)

The last row of Fig. 3(l–n) depicts the analogue evaluation utilizing a Lorentzian source distribution. No difference can be seen between the experimental (a) and simulated unit cell (l) with the naked eye. The good agreement is underpinned by the difference images. In contrast to the Gaussian case even the difference at the group-V sublattice is very low. The discrepancy $\Delta_{relative}$ for the thin and the thick sample (n) is below 2% which is rather small, given that the STD_I is higher. Moreover, the discrepancy is especially high in a ring around the group-III columns where also the experimental STD_I has its maximum (compare Fig. 2(c)).

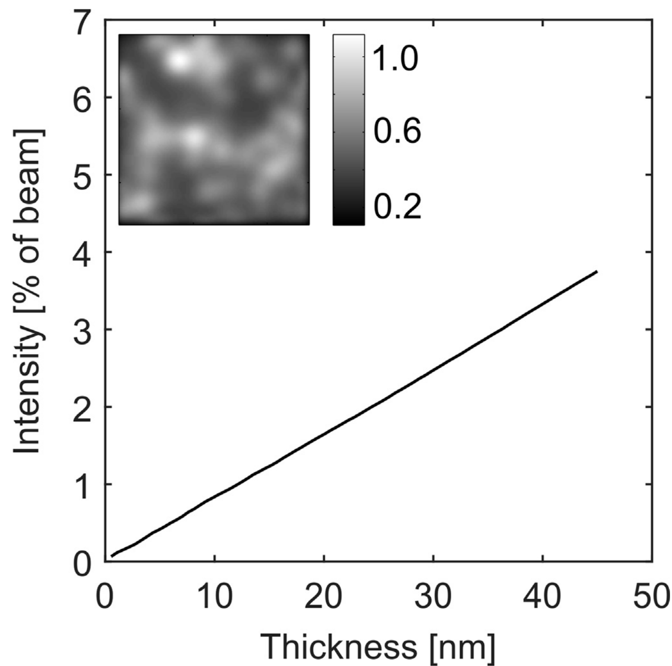

Fig. 4. Simulated thickness dependent HAADF intensity of amorphous GaP. The axes are chosen according to Fig. 1 for better comparability. A region corresponding to an unit cell of crystalline GaP with a thickness of 7 nm is shown as inset.

The analogue data utilizing a combination of Gaussian and Lorentzian source distribution are not shown for reasons of clarity. Nevertheless, as this distribution is a mixture of the two previously discussed cases, the results show an intermediate behavior. The intensity at the group-V positions is significantly underestimated in the simulations, but not as drastic as in the Gaussian case. With a maximum $\Delta_{relative}$ of 3.2% the discrepancy is quite low for both thicknesses.

The main conclusions from Fig. 3 shall be recapitulated briefly: the application of a source distribution is inevitable to match the simulated intensity and the experimental one. On the absolute intensity scale the choice of the distribution seems irrelevant as the discrepancy $\Delta_{absolute}$ is below 0.13% of the impinging beam for all investigated distributions and sample thicknesses. Considering the relative discrepancy $\Delta_{relative}$ it becomes obvious that especially for thin samples, the intensity at the P column is significantly underestimated for all source distributions but the Lorentzian one. This is not a cosmetic issue only but will lead to significant errors when determining the chemical composition of a ternary material. Our findings are in agreement with the ones from Maunders et al. [41], where a source distribution with extended tails was found rather than a Gaussian distribution. It is worth noting that when neglecting the chromatic aberration, the above discussion for the different source distributions remains valid, but the respective optimum σ of the distributions need to be adjusted because the chromatic aberration already leads to a small widening [18]. Additionally the values for $\Delta_{absolute}$ and $\Delta_{relative}$ are significantly higher without taking into account the chromatic aberration. The consideration of the sensitivity of the used HAADF detector also has no impact on the choice of the most suitable source distribution. When the sensitivity is applied to the simulations, the agreement between simulation and experiment is slightly improved and the values of σ for which the best agreement is achieved are slightly increased by around 3 pm.

To minimize the discrepancy between simulation and experiment σ was treated as a fitting parameter. Therefore, the optimum σ is different for each source distribution, which is caused by the specific shape of the respective distribution. Additionally, for a fixed distribution the values for σ differ for the different thicknesses, which is unexpected. The source distribution and its width should not change as the decisive parameters are fixed above the sample plane. Nevertheless, a trend is observable, the thinner the sample the bigger is the σ which has to be applied. In other words, for thin samples the experimental column width is too wide and a wider source distribution has to be applied to the simulations to match the experimental data. Hence a source of beam spreading may has been neglected in the simulations so far. The potential reasons for this will be discussed in the following.

On the one hand the relative thickness variation is higher for thin samples, due to the wedge shape caused by the sample preparation. The resulting change in intensity and effective defocus due to the different heights of the sample surface with respect to the electron beam could lead to a widening of the atomic columns in the experimental images. But the STD_I does not change significantly for the different sample thicknesses, therefore we do not think this is the decisive factor. On the other hand, the presence of amorphous layers introduced by the ion milling during TEM sample preparation may significantly influence the measured intensity for thin samples. The influence of such layers was studied in more detail e.g. in [16].

To investigate the impact of these amorphous layers on the HAADF intensity in this manuscript, the theoretical structure of amorphous GaP was determined utilizing the IAS software [32–34]. The structures found were used as input for STEM intensity simulations. The derived thickness dependent HAADF intensity of amorphous GaP is shown in Fig. 4. The axes were kept the same like in Fig. 1 to allow easy comparability. As expected, the amorphous GaP exhibits a smaller intensity than crystalline GaP, presumably due to the missing channelling effect in the disordered structure. The inset shows a simulated image of amorphous GaP with a thickness of 7 nm, the lateral dimensions correspond to the size of a unit cell of crystalline GaP. In analogy to Fig. 1a Lorentzian source distribution with $\sigma = 55$ pm was applied to the simulated image. In this image the spread of intensity is much smaller than for crystalline GaP. Nevertheless, some intensity maxima are visible which are most likely caused by several atoms which are aligned along the beam path by chance. An intensity distribution like this could be the reason for the cloudy contrast which is faintly observable in the experimental image shown in Fig. 1(a). Even though the intensity of amorphous GaP is rather small, its influence becomes notable for thin TEM samples. Moreover, the layer may change the relative intensities within a unit cell significantly and cause dechanneling. Therefore, amorphous layers need to be taken into account in the simulation, if they are present.

To treat the influence of the amorphous layers on the total HAADF intensity, supercells consisting of crystalline and amorphous material have to be created and used for intensity simulations, as it was done e.g. in [16]. There it was found that the amorphous layers result in an additional beam spread. Moreover the HAADF intensity showed to be sensitive to the set defocus value. Therefore, the defocus has to be set to the crystalline part of the supercell to achieve optimum contrast in the simulated images. To create a supercell which reproduces the structure of our investigated sample, the right fractions of crystalline and amorphous material have to be determined. We assume a 7 nm thick (2×3.5 nm at bottom and top surface) amorphous layer because this reflects the actual width of the layer we observed in a previous study for GaAs under the very same preparation conditions by cutting a cross section of a prepared sample with the help of a focused ion beam (FIB) [28]. Moreover, this size is in line with the TEM observations for Silicon [42]. An equivalent thickness of amorphous GaP leads to a HAADF intensity of 0.61%. If we assume that the experimental intensity is a simple sum of crystalline and amorphous contributions, the formerly derived integral thickness

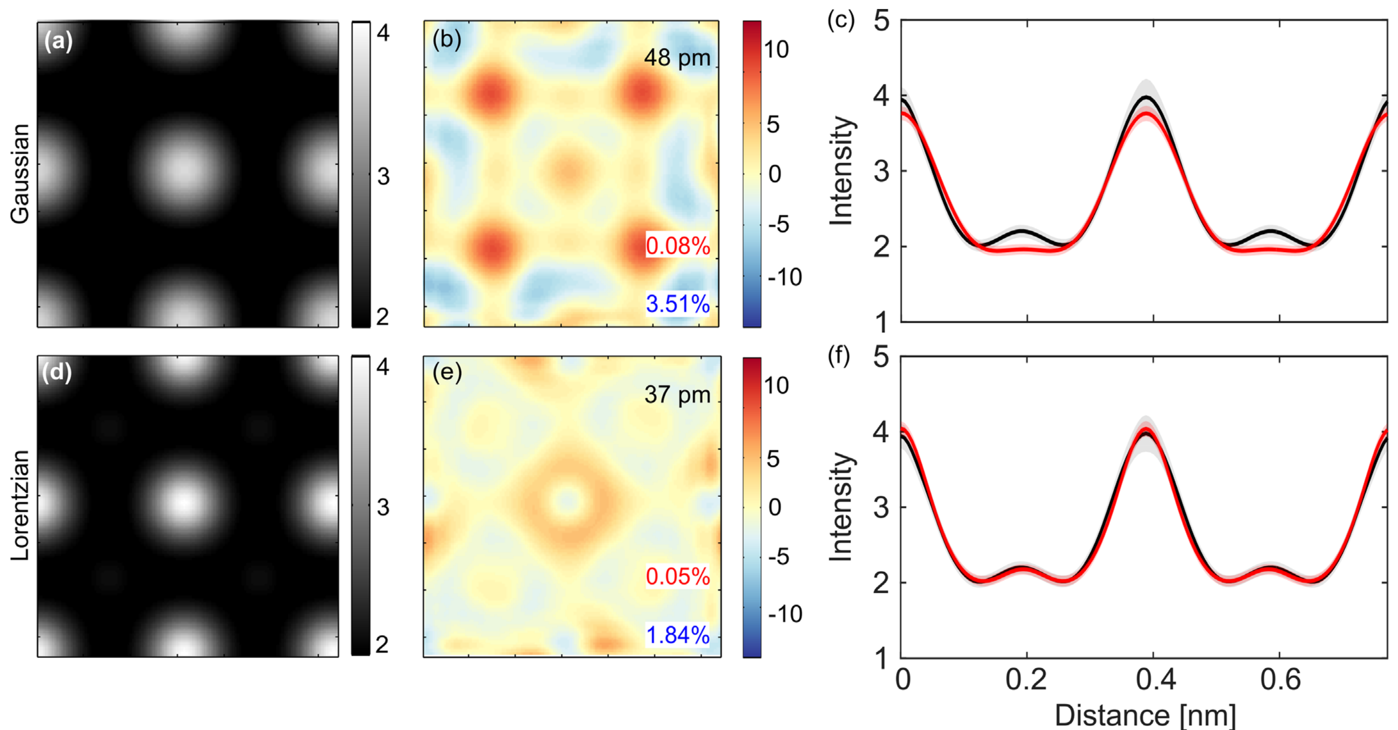

Fig. 5. Influence of amorphous layers: Simulated unit cells of 14.2 nm crystalline GaP sandwiched between two 3.5 nm thick amorphous GaP layers assuming Gaussian (a) and Lorentzian (d) source distribution. The corresponding differences are shown in (b) and (e), respectively. The intensity profiles depicted in (c) and (f) highlight that the best fit still is achieved for the Lorentzian distribution. The experimental curves are drawn in black and the simulated ones in red. (For interpretation of the references to color in this figure legend, the reader is referred to the web version of this article.)

of the thin sample (19.5 nm) has to be corrected to a crystalline thickness of only 14.2 nm. Accordingly, the crystalline fraction of the thick sample is reduced from 28 nm to only 23 nm.

In Fig. 5 the simulated HAADF images resulting from this supercell are shown for the different source distributions in (a) and (d), respectively. The depicted unit cells are an average of a simulation with a larger field of view of 5 × 5 unit cells, which was averaged in analogy to the experimental images depicted in Fig. 2. Although the previous findings suggest the source distribution to be a Lorentzian one, it still makes sense to check whether the presence of amorphous layers could change the previous conclusions, i.e. due to the additional beam spread.

The according difference plots show a clearly reduced $\Delta_{relative}$ and $\Delta_{absolute}$ for the Gaussian (b) and the Lorentzian case (e) compared to the analogue plots neglecting the amorphous layers (Fig. 3(j) and (m)). The values of σ which have been applied are shown in the individual plots. The improved fit for the Gaussian distribution could be explained by the fact that the amorphous layer lifts intensity uniformly, which has a similar effect as the extended wings of the Lorentzian distribution. Nevertheless, the best match is still achieved with the pure Lorentzian distribution, because only when this is applied the intensity on the P columns is well reproduced. This becomes very obvious in the line profiles acquired in a 45° angle across the unit cells, which are shown in the rightmost column of Fig. 5. In the Gaussian case (c) the experimental curve (black) and the simulated one (red) are in quite good agreement, except for the group V positions, where the experimental intensity is significantly higher. The shaded area around each plot corresponds to the STD_I of the data. Please note that now the simulated curves exhibit a finite STD_I as well, due to the averaging over the 5 × 5 unit cells.

For the pure Lorentzian distribution, simulation and experiment agree within the error bars for the whole intensity profile (f). Small discrepancies are visible only at the positions where the STD_I is increased nevertheless, i.e. at the central group III atom. More important than the observed improved fit, when the amorphous layers are taken into account, is the effect on the values of σ, for which this best fit is achieved. As the background of the simulated intensity is lifted by the amorphous layers, the σ which has to be applied to reproduce the experiment is much smaller in both source distributions compared to the case without the amorphous layers (see Fig. 3). Moreover the values of 48 pm and 37 pm for the Gaussian and Lorentzian type, respectively, agree better to the corresponding values of the thicker sample depicted in Fig. 3.

To ensure that the effect of the amorphous layer actually is smaller for the thicker sample, as stated before, the analogue evaluation for this sample is shown in Fig. 6. Considering the Lorentzian distribution in fact the change in σ which is occurs when the amorphous layer is accounted for is smaller but still observable (thin sample: 46 pm → 37 pm, thick sample: 40 pm → 34 pm). Similar is true for the Gaussian case. In presence of the amorphous layer, the resulting σ for thin and thick sample differ by less than 3 pm for both source shapes, which is in margin of error.

We conclude that a Lorentzian distribution with a width of approximately 36 pm has to be applied to simulated data in order to reproduce the experimental data. Applying the right source distribution, the whole unit cell will be described correctly and can be used to gain valuable information. These findings will be used in future to be able to evaluate the chemical composition of ternary/multinary materials like Ga(PAs) on each sublattice. Moreover, our findings once more show the influence of the sample preparation on the experimental HAADF images. To allow an unambiguous evaluation of thin samples, the thickness of the amorphous layers introduced by the preparation has to be reduced. Therefore the final milling energy has to be reduced below 1.7 KeV or other preparation techniques which do not involve ion milling have to be applied.

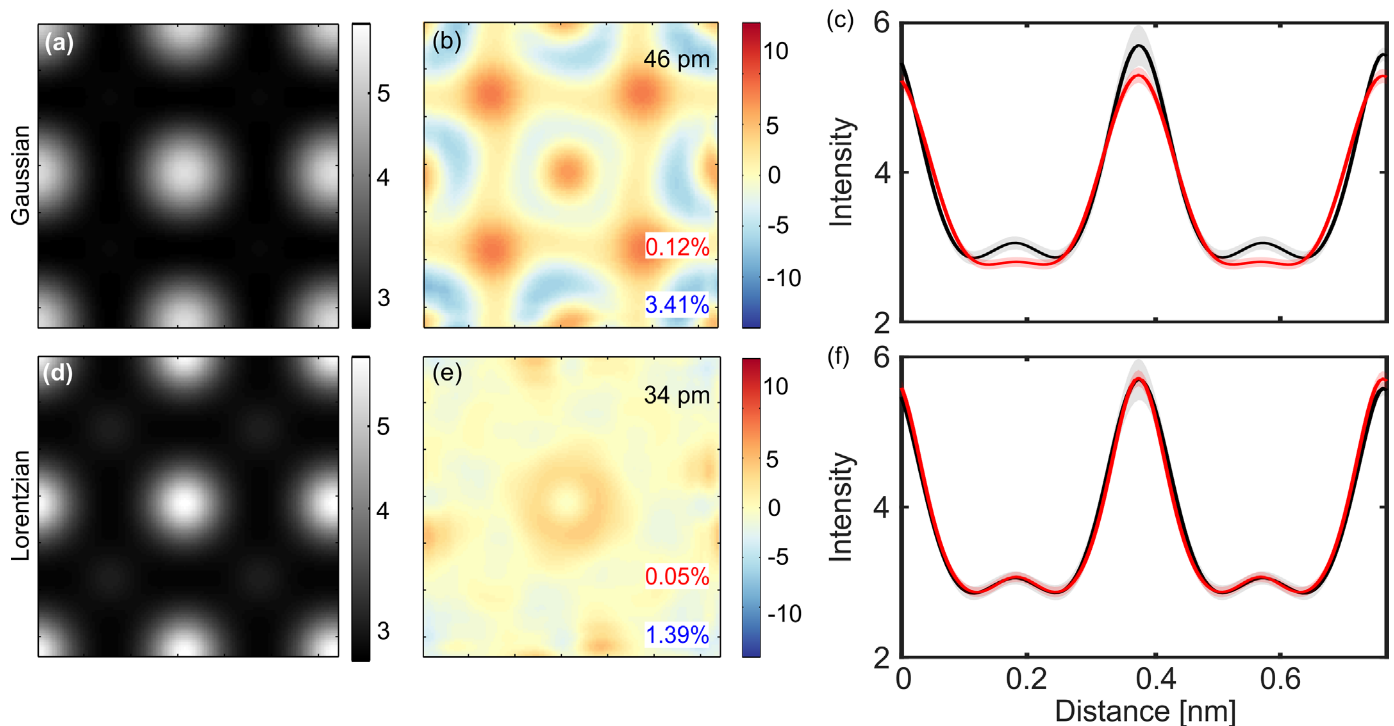

Fig. 6. Influence of amorphous layers: simulated unit cells of 23 nm crystalline GaP sandwiched between two 3.5 nm thick amorphous GaP layers assuming Gaussian (a) and Lorentzian (d) source distribution. The corresponding differences are shown in (b) and (e), respectively. The intensity profiles depicted in (c) and (f) highlight that the best fit still is achieved for the Lorentzian distribution. The experimental curves are drawn in black and the simulated ones in red. (For interpretation of the references to color in this figure legend, the reader is referred to the web version of this article.)

4. Summary

In modern multinary semiconductor materials the exact control of the chemical composition on each sublattice is crucial to achieve the desired functionality. Aberration-corrected STEM has proven as a valuable tool to provide information on the atomic scale. Nevertheless, partial spatial and temporal coherences can have a tremendous impact on the atomic resolution images and may hamper the analysis of the chemical composition. We chose GaP due to the high difference in atomic number of its constituents to visualize the individual effects in experimental and simulated images.

By quantitatively comparing experimental and simulated HAADF data for different thicknesses, we have shown that by applying a Lorentzian shaped source distribution, the experimental data are reproduced best. Compared to the effect of spatial coherence the effect of temporal coherence is minor. It was shown that for thin samples amorphous layers introduced by the sample preparation influence the HAADF intensity. Taking into account these amorphous layers, the width of the source distribution could be determined to approximately 36 pm. Applying the right source distribution, the intensity in the whole GaP unit cell is described correctly. With this knowledge the determination of the chemical composition of more complex, multinary materials becomes feasible.

Acknowledgements

This work was supported by the German Science Foundation (DFG) in the framework of SFB 1083: “Structure and Dynamics of Internal Interfaces”. NK acknowledges financial support by the DFG in the framework of GRK 1782: “Functionalization of Semiconductors”.

References

[1] M.-H. Kim, M.F. Schubert, Q. Dai, J.K. Kim, E.F. Schubert, J. Piprek, et al., Origin of efficiency droop in GaN-based light-emitting diodes, Appl. Phys. Lett. 91 (2007) 183507, http://dx.doi.org/10.1063/1.2800290.
[2] B. Kunert, K. Volz, J. Koch, W. Stolz, Direct-band-gap Ga(NAsP)-material system pseudomorphically grown on GaP substrate, Appl. Phys. Lett. 88 (2006) 182108, http://dx.doi.org/10.1063/1.2200758.
[3] P. Ludewig, S. Reinhard, K. Jandieri, T. Wegele, A. Beyer, L. Tapfer, et al., MOVPE growth studies of Ga(NAsP)/(BGa)(AsP) multi quantum well heterostructures (MQWH) for the monolithic integration of laser structures on (001) Si-substrates, J. Cryst. Growth 438 (2016) 63–69, http://dx.doi.org/10.1016/j.jcrysgro.2015.12.024.
[4] S.R. Kurtz, D. Myers, J.M. Olson, Projected performance of three-and four-junction devices using GaAs and GaInP, in: Conf. Rec. IEEE Photovolt. Spec. Conf., 1997, pp. 875–878.
[5] M. Wiemer, V. Sabnis, H. Yuen, 43.5% efficient lattice matched solar cells, Proc. SPIE 8108 (2011) 810804–810805, http://dx.doi.org/10.1117/12.897769.
[6] S. Pennycook, D. Jesson, High-resolution Z-contrast imaging of crystals, Ultramicroscopy 37 (1991) 14–38, http://dx.doi.org/10.1016/0304-3991(91)90004-P.
[7] M. Haider, S. Uhlemann, E. Schwan, R. Harald, B. Kabius, K. Urban, Electron microscopy image enhanced, Nature 392 (1998) 768–769, http://dx.doi.org/10.1038/33823.
[8] O.L. Krivanek, N. Dellby, A.R. Lupini, Towards sub-Å electron beams, Ultramicroscopy 78 (1999) 1–11, http://dx.doi.org/10.1016/S0304-3991(99)00013-3.
[9] R.F. Loane, P. Xu, J. Silcox, Thermal vibrations in convergent-beam electron diffraction, Acta Crystallogr. Sect. A Found. Crystallogr. 47 (1991) 267–278, http://dx.doi.org/10.1107/S0108767391000375.
[10] J.M. LeBeau, S. Stemmer, Experimental quantification of annular dark-field images in scanning transmission electron microscopy, Ultramicroscopy 108 (2008) 1653–1658, http://dx.doi.org/10.1016/j.ultramic.2008.07.001.
[11] A. Rosenauer, K. Gries, K. Müller, A. Pretorius, M. Schowalter, A. Avramescu, et al., Measurement of specimen thickness and composition in Al(x)Ga(1-x)N/GaN using high-angle annular dark field images, Ultramicroscopy 109 (2009) 1171–1182, http://dx.doi.org/10.1016/j.ultramic.2009.05.003.
[12] T. Grieb, K. Müller, R. Fritz, M. Schowalter, N. Neugebohrn, N. Knaub, et al., Determination of the chemical composition of GaNAs using STEM HAADF imaging and STEM strain state analysis, Ultramicroscopy 117 (2012) 15–23, http://dx.doi.org/10.1016/j.ultramic.2012.03.014.
[13] S.I. Molina, D.L. Sales, P.L. Galindo, D. Fuster, Y. González, B. Alén, et al., Column-by-column compositional mapping by Z-contrast imaging, Ultramicroscopy 109 (2009) 172–176, http://dx.doi.org/10.1016/j.ultramic.2008.10.008.
[14] J. Fertig, H. Rose, Resolution and contrast of crystalline objects in high-

resolution scanning transmission electron microscopy, Optik (Stuttgart) 59 (1981) 407–429.
[15] P.D. Nellist, S.J. Pennycook, Incoherent imaging using dynamically scattered coherent electrons, Ultramicroscopy 78 (1999) 111–124, http://dx.doi.org/10.1016/S0304-3991(99)00017-0.
[16] K.A. Mkhoyan, S.E. Maccagnano-Zacher, E.J. Kirkland, J. Silcox, Effects of amorphous layers on ADF-STEM imaging, Ultramicroscopy 108 (2008) 791–803, http://dx.doi.org/10.1016/j.ultramic.2008.01.007.
[17] R. Erni, High-Resolution Transmission Electron Microscopy, in: Aberration-Corrected Imaging Transm. Electron Microsc., Imperial College Press, 2010, pp. 13–43. doi:10.1142/9781848165373_0002.
[18] K. Kuramochi, T. Yamazaki, Y. Kotaka, M. Ohtsuka, I. Hashimoto, K. Watanabe, Effect of chromatic aberration on atomic-resolved spherical aberration corrected STEM images, Ultramicroscopy 110 (2009) 36–42, http://dx.doi.org/10.1016/j.ultramic.2009.09.003.
[19] C. Dwyer, C. Maunders, C.L. Zheng, M. Weyland, P.C. Tiemeijer, J. Etheridge, Sub-0.1 nm-resolution quantitative scanning transmission electron microscopy without adjustable parameters, Appl. Phys. Lett. (2012), http://dx.doi.org/10.1063/1.4711766.
[20] C.B. Williams, D.B. Carter, Transmission Electron Microscopy, 1st ed., Springer, 1996.
[21] D.T. Nguyen, S.D. Findlay, J. Etheridge, The spatial coherence function in scanning transmission electron microscopy and spectroscopy, Ultramicroscopy 146 (2014) 6–16, http://dx.doi.org/10.1016/j.ultramic.2014.04.008.
[22] C. Dwyer, R. Erni, J. Etheridge, Measurement of effective source distribution and its importance for quantitative interpretation of STEM images, Ultramicroscopy 110 (2010) 952–957, http://dx.doi.org/10.1016/j.ultramic.2010.01.007.
[23] C. Dwyer, R. Erni, J. Etheridge, Method to measure spatial coherence of subangstrom electron beams, Appl. Phys. Lett. 93 (2008) 021115, http://dx.doi.org/10.1063/1.2957648.
[24] J. Verbeeck, A. Béché, W. Van den Broek, A holographic method to measure the source size broadening in STEM, Ultramicroscopy 120 (2012) 35–40, http://dx.doi.org/10.1016/j.ultramic.2012.05.007.
[25] A. Rosenauer, T. Mehrtens, K. Müller, K. Gries, M. Schowalter, P. Venkata Satyam, et al., Composition mapping in InGaN by scanning transmission electron microscopy, Ultramicroscopy 111 (2011) 1316–1327, http://dx.doi.org/10.1016/j.ultramic.2011.04.009.
[26] H. E, K.E. MacArthur, T.J. Pennycook, E. Okunishi, A.J. D'Alfonso, N.R. Lugg, et al., Probe integrated scattering cross sections in the analysis of atomic resolution HAADF STEM images, Ultramicroscopy 133 (2013) 109–119, http://dx.doi.org/10.1016/j.ultramic.2013.07.002.
[27] E.C. Cosgriff, V. Nicolosi, J.N. Coleman, P.D. Nellist, Quantification of ADF STEM images of molybdenum chalcogenide nanowires, J. Phys. Conf. Ser. 26 (2006) 280–283, http://dx.doi.org/10.1088/1742-6596/26/1/067.
[28] J. Belz, A. Beyer, T. Torunski, W. Stolz, K. Volz, Direct investigation of (sub-) surface preparation artifacts in GaAs based materials by FIB sectioning, Ultramicroscopy 163 (2016) 19–30, http://dx.doi.org/10.1016/j.ultramic.2016.01.001.
[29] L. Jones, H. Yang, T.J. Pennycook, M.S.J. Marshall, S. Van Aert, N.D. Browning, et al., Smart Align—a new tool for robust non-rigid registration of scanning microscope data, Adv. Struct. Chem. Imaging 1 (2015) 8, http://dx.doi.org/10.1186/s40679-015-0008-4.
[30] D.S. He, Z.Y. Li, A practical approach to quantify the ADF detector in STEM, J. Phys. Conf. Ser. 522 (2014) 012017, http://dx.doi.org/10.1088/1742-6596/522/1/012017.
[31] A. Rosenauer, M. Schowalter, STEMSIM - a new software tool for simulation of STEM 2007, Microsc. Semicond. Mater. 120 (2008) 170–172, http://dx.doi.org/10.1007/978-1-4020-8615-1_36.
[32] L.-T. To, D.J. Daley, Z.H. Stachurski, On the definition of an ideal amorphous solid of uniform hard spheres, Solid State Sci. 8 (2006) 868–879, http://dx.doi.org/10.1016/j.solidstatesciences.2006.02.042.
[33] C.-Y. Lee, Z.H. Stachurski, T. Richard Welberry, The geometry, topology and structure of amorphous solids, Acta Mater. 58 (2010) 615–625, http://dx.doi.org/10.1016/j.actamat.2009.09.040.
[34] Z.H. Stachurski, On structure and properties of amorphous materials, Materials (Basel) 4 (2011) 1564–1598, http://dx.doi.org/10.3390/ma4091564.
[35] A.A. Valladares, J.A. Díaz-Celaya, J. Galván-Colín, L.M. Mejía-Mendoza, J. A. Reyes-Retana, R.M. Valladares, et al., New approaches to the computer simulation of amorphous alloys: a review, Materials (Basel) 4 (2011) 716–781, http://dx.doi.org/10.3390/ma4040716.
[36] J.M. Lebeau, S.D. Findlay, L.J. Allen, S. Stemmer, Position averaged convergent beam electron diffraction: theory and applications, Ultramicroscopy 110 (2010) 118–125, http://dx.doi.org/10.1016/j.ultramic.2009.10.001.
[37] A. Beyer, R. Straubinger, J. Belz, K. Volz, Local sample thickness determination via scanning transmission electron microscopy defocus series, J. Microsc. (2015), http://dx.doi.org/10.1111/jmi.12284.
[38] X. Sang, J.M. LeBeau, Revolving scanning transmission electron microscopy: correcting sample drift distortion without prior knowledge, Ultramicroscopy 138 (2014) 28–35, http://dx.doi.org/10.1016/j.ultramic.2013.12.004.
[39] C. Ophus, J. Ciston, C.T. Nelson, Correcting nonlinear drift distortion of scanning probe and scanning transmission electron microscopies from image pairs with orthogonal scan directions, Ultramicroscopy 162 (2016) 1–9, http://dx.doi.org/10.1016/j.ultramic.2015.12.002.
[40] H. Han, A. Beyer, K. Jandieri, K.I. Gries, L. Duschek, W. Stolz, et al., Quantitative characterization of the interface roughness of (GaIn)As quantum wells by high resolution STEM, Micron 79 (2015) 1–7, http://dx.doi.org/10.1016/j.micron.2015.07.003.
[41] C. Maunders, C. Dwyer, P.C. Tiemeijer, J. Etheridge, Practical methods for the measurement of spatial coherence—A comparative study, Ultramicroscopy 111 (2011) 1437–1446, http://dx.doi.org/10.1016/j.ultramic.2011.05.011.
[42] M.J. Süess, E. Mueller, R. Wepf, Minimization of amorphous layer in Ar+ ion milling for UHR-EM, Ultramicroscopy 111 (2011) 1224–1232, http://dx.doi.org/10.1016/j.ultramic.2011.03.004.

6.2 Presentations and Further Publications

- Microscopy of Semiconductor Materials (MSM), 2015, Cambridge, UK, Poster presentation:
  Determination of Ion Beam Induced Artifacts in TEM Sample Preparation of Strained Semiconductor Heterostructures by means of FIB Target Preparation

- Microscopy Conference (MC), 2015, Göttingen, GER, Poster presentation:
  (S)TEM Investigation of Coherently Strained (GaIn)(NAs) Heterostructures with Respect to Finite Thickness Effects

- Microscopy and Microanalysis (M&M), 2017, St.Louis, USA, Oral presentation:
  On the Effects of Column Occupancy and Static Atomic Disorder on the Analysis of Chemical Ordering in Ga(P,Bi) Compounds

- PICO, 2017, Kasteel Vaalsbroek, NL, Poster presentation:
  Atom Counting Reconstruction for Antiphase Boundaries of Gallium Phosphide on Silicon

Further Publications

[1] J. Belz, A. Beyer, L. Nattermann, and K. Volz, "On The Effects of Column Occupancy and Static Atomic Disorder on the Analysis of Chemical Ordering in Ga(P(1-x)Bix) Compounds," *Microscopy and Microanalysis*, vol. 23, no. S1, pp. 1474–1475, 2017.

[2] A. Beyer, R. Straubinger, J. Belz, and K. Volz, "Local sample thickness determination via scanning transmission electron microscopy defocus series," *Journal of Microscopy*, vol. 262, no. 2, pp. 171–177, 2016. [Online]. Available: `http://doi.wiley.com/10.1111/jmi.12284`

[3] P. Farin, M. Marquardt, W. Martyanov, J. Belz, A. Beyer, K. Volz, and A. Lenz, "Three-dimensional structure of antiphase domains in GaP on Si (001)," *Journal of Physics: Condensed Matter*, 2019.

[4] M. Feifel, J. Ohlmann, J. Benick, T. Rachow, S. Janz, M. Hermle, F. Dimroth, J. Belz, A. Beyer, K. Volz *et al.*, "MOVPE Grown Gallium Phosphide-Silicon Heterojunction Solar Cells," *IEEE Journal of Photovoltaics*, vol. 7, no. 2, pp. 502–507, 2017.

[5] M. Feifel, J. Ohlmann, J. Benick, M. Hermle, J. Belz, A. Beyer, K. Volz, T. Hannappel, A. W. Bett, D. Lackner, and F. Dimroth, "Direct growth of III-V/Silicon triple-junction solar cells with 19.7% efficiency," *IEEE Journal of Photovoltaics*, 2018.

[6] R. M. France, M. Feifel, J. Belz, A. Beyer, K. Volz, J. Ohlmann, D. Lackner, and F. Dimroth, "Single- and dual-variant atomic ordering in GaAsP compositionally graded buffers on GaP and Si substrates," *Journal of Crystal Growth*, vol. 506, no. October 2018, pp. 61–70, 2019. [Online]. Available: `https://doi.org/10.1016/j.jcrysgro.2018.10.007`

[7] W. Guo, Y. Mols, J. Belz, A. Beyer, K. Volz, A. Schulze, R. Langer, B. Kunert, W. Guo, Y. Mols, J. Belz, A. Beyer, K. Volz, A. Schulze, R. Langer, and B. Kunert, "Anisotropic relaxation behavior of InGaAs / GaAs selectively grown in narrow trenches on (001) Si substrates," vol. 025303, no. 001, pp. 0–12, 2017.

[8] H. Han, A. Beyer, J. Belz, A. König, W. Stolz, and K. Volz, "Quantitative atomic resolution at interfaces: Subtraction of the background in STEM images with the example of (Ga,In)P/GaAs structures," *Journal of Applied Physics*, vol. 121, no. 2, 2017.

[9] H. Han, A. Beyer, J. Belz, A. König, W. Stolz, and K. Volz, "Correlation of interface morphology and composition in gainp/gaas with growth conditions," in *European Microscopy Congress 2016: Proceedings*. Wiley Online Library, 2016, pp. 573–574.

[10] J. O. Oelerich, L. Duschek, J. Belz, A. Beyer, S. D. Baranovskii, and K. Volz, "STEMsalabim: A high-performance computing cluster friendly code for scanning transmission electron microscopy image simulations of thin specimens," *Ultramicroscopy*, vol. 177, pp. 91–96, 2017. [Online]. Available: http://dx.doi.org/10.1016/j.ultramic.2017.03.010 http://www.online.uni-marburg.de/stemsalabim/

[11] R. Straubinger, M. Widemann, J. Belz, L. Nattermann, A. Beyer, and K. Volz, "Thermally introduced bismuth clustering in ga (p, bi) layers under group v stabilised conditions investigated by atomic resolution in situ (s) tem," *Scientific reports*, vol. 8, no. 1, p. 9048, 2018.

Bibliography

[1] Z. W. Wang, Z. Y. Li, S. J. Park, A. Abdela, D. Tang, and R. E. Palmer, "Quantitative Z-contrast imaging in the scanning transmission electron microscope with size-selected clusters," *Phys. Rev. B*, vol. 84, p. 073408, Aug 2011. [Online]. Available: https://link.aps.org/doi/10.1103/PhysRevB.84.073408

[2] J. M. Lebeau, S. D. Findlay, L. J. Allen, and S. Stemmer, "Quantitative atomic resolution scanning transmission electron microscopy," *Physical Review Letters*, vol. 100, no. 20, p. 206101, may 2008. [Online]. Available: http://link.aps.org/doi/10.1103/PhysRevLett.100.206101

[3] W. Hagen, "Tetragonal distortion in heteroepitaxial layers: Ge on GaAs," *Journal of Crystal Growth*, 1978.

[4] H. Krömer, "Polar-on-nonpolar epitaxy," *Journal of Crystal Growth*, vol. 81, no. 1-4, pp. 193–204, 1987.

[5] A. Beyer, J. Ohlmann, S. Liebich, H. Heim, G. Witte, W. Stolz, and K. Volz, "GaP heteroepitaxy on Si(001): Correlation of Si-surface structure, GaP growth conditions, and Si-III/V interface structure," *Journal of Applied Physics*, vol. 111, 04 2012.

[6] A. Beyer and K. Volz, "Advanced Electron Microscopy for III/V on Silicon Integration," *Advanced Materials Interfaces*, vol. 6, 05 2019.

[7] K. Volz, A. Beyer, W. Witte, J. Ohlmann, I. Nemeth, B. Kunert, and W. Stolz, "GaP-nucleation on exact Si (0 0 1) substrates for III/V device integration," *Journal of Crystal Growth*, vol. 315, no. 1, pp. 37–47, jan 2011. [Online]. Available: https://www.sciencedirect.com/science/article/pii/S0022024810007669?via{%}3Dihub

[8] O. Rubel, I. Nemeth, W. Stolz, and K. Volz, "Modeling the compositional dependence of electron diffraction in dilute GaAs- and GaP-based compound semiconductors," *Physical Review B - Condensed Matter and Materials Physics*, 2008.

[9] S. Ushiba, K. Masui, N. Taguchi, T. Hamano, S. Kawata, and S. Shoji, "Size dependent nanomechanics of coil spring shaped polymer nanowires," *Scientific Reports*, vol. 5, pp. 1–5, 2015. [Online]. Available: http://dx.doi.org/10.1038/srep17152

[10] M. Treacy, “The effects of elastic relaxation on transmission electron microscopy studies of thinned composition-modulated materials,” *Journal of Vacuum Science and Technology B: Microelectronics and Nanometer Structures*, vol. 4, no. 6, pp. 1458–1466, nov 1986. [Online]. Available: http://scitation.aip.org/content/avs/journal/jvstb/4/6/10.1116/1.583473

[11] L. De Caro, A. Giuffrida, E. Carlino, and L. Tapfer, “Elastic Stress Relaxation in HRTEM Specimens of Strained Semiconductor Heterostructures and its Influence on the Image Contrast,” *Microscopy Microanalysis Microstructures*, vol. 6, no. 5-6, pp. 465–472, 1995. [Online]. Available: http://www.edpsciences.org/10.1051/mmm:1995137

[12] O. Zienkiewicz, R. Taylor, and D. Fox, Eds., *The Finite Element Method for Solid and Structural Mechanics*, seventh edition ed. Oxford: Butterworth-Heinemann, 2014. [Online]. Available: http://www.sciencedirect.com/science/article/pii/B9781856176347000168

[13] E. Rutherford, “The scattering of alpha and beta particles by matter and the structure of the atom,” *The London, Edinburgh, and Dublin Philosophical Magazine and Journal of Science*, vol. 21, no. 125, pp. 669–688, 1911.

[14] E. J. Kirkland, *Advanced computing in electron microscopy.* Springer Science and Business Media, 2010.

[15] P. A. Doyle and P. S. Turner, “Relativistic Hartree-Fock X-ray and electron scattering factors,” *Acta Crystallographica Section A*, vol. 24, no. 3, pp. 390–397, May 1968. [Online]. Available: https://doi.org/10.1107/S0567739468000756

[16] A. Weickenmeier and H. Kohl, “Computation of absorptive form factors for high-energy electron diffraction,” *Acta Crystallographica Section A*, 1991.

[17] I. Lobato and D. Van Dyck, “A complete comparison of simulated electron diffraction patterns using different parameterizations of the electron scattering factors,” *Ultramicroscopy*, 2015.

[18] P. Rez, “Electron Beam Interactions with Solids for Microscopy,” *Microanalysis and Microlithography (Scanning Electron Microscopy Inc., USA, 1984)*, 1984.

[19] W. L. Bragg, “The Structure of Some Crystals as Indicated by Their Diffraction of X-rays,” *Proceedings of the Royal Society A: Mathematical, Physical and Engineering Sciences*, 1913.

[20] R. F. Egerton, *Electron energy-loss spectroscopy in the electron microscope.* Springer Science and Business Media, 2011.

[21] O. L. Krivanek, T. C. Lovejoy, N. Dellby, and R. Carpenter, “Monochromated STEM with a 30 meV-wide, atom-sized electron probe,” *Microscopy*, vol. 62, no. 1, pp. 3–21, 01 2013. [Online]. Available: https://doi.org/10.1093/jmicro/dfs089

[22] P. Debye, “Interferenz von Röntgenstrahlen und Wärmebewegung,” *Annalen der Physik*, vol. 348, no. 1, pp. 49–92, 1913. [Online]. Available: https://onlinelibrary.wiley.com/doi/abs/10.1002/andp.19133480105

[23] M. Schowalter, A. Rosenauer, J. T. Titantah, and D. Lamoen, “Computation and parametrization of the temperature dependence of Debye-Waller factors for group IV, III-V and II-VI semiconductors,” *Acta Crystallographica Section A: Foundations of Crystallography*, vol. 65, no. 1, pp. 5–17, 2008.

[24] Brydson, Rik, Ed., *Aberration-Corrected Analytical Transmission Electron Micrscopy*. 2011 John Wiley and Sons, Ltd, 2011.

[25] F. F. Krause, D. Bredemeier, M. Schowalter, T. Mehrtens, T. Grieb, and A. Rosenauer, “Using molecular dynamics for multislice TEM simulation of thermal diffuse scattering in AlGaN,” *Ultramicroscopy*, vol. 189, pp. 124 – 135, 2018. [Online]. Available: http://www.sciencedirect.com/science/article/pii/S0304399118300056

[26] D. A. Muller, B. Edwards, E. J. Kirkland E, and J. Silcox, “Simulation of thermal diffuse scattering including a detailed phonon dispersion curve,” *Ultramicroscopy*, 2001.

[27] A. Sommerfeld, “Zur Elektronentheorie der Metalle auf Grund der Fermischen Statistik,” *Zeitschrift für Physik*, vol. 47, no. 1, pp. 1–32, Jan 1928. [Online]. Available: https://doi.org/10.1007/BF01391052

[28] R. Erni, *Aberration-corrected imaging in transmission electron microscopy: An introduction*. World Scientific Publishing Company, 2010.

[29] H. Busch, “Berechnung der Bahn von Kathodenstrahlen im axialsymmetrischen elektromagnetischen Felde,” *Annalen der Physik*, vol. 386, no. 25, pp. 974–993, 1926. [Online]. Available: https://onlinelibrary.wiley.com/doi/abs/10.1002/andp.19263862507

[30] O. Scherzer, “Über einige Fehler von Elektronenlinsen,” *Zeitschrift fuer Physik*, vol. 101, no. 9, pp. 593–603, Sep 1936. [Online]. Available: https://doi.org/10.1007/BF01349606

[31] M. Haider, “Correction of the spherical aberration of a 200kV TEM by means of a hexapole corrector,” *Optik*, vol. 99, pp. 167–179, 1995.

[32] O. Krivanek, N. Dellby, and A. Lupini, "Towards sub-Ångstroem electron beams," *Ultramicroscopy*, vol. 78, no. 1, pp. 1 – 11, 1999. [Online]. Available: http://www.sciencedirect.com/science/article/pii/S0304399199000133

[33] O. Scherzer, "Sphärische und chromatische Korrektur von Elektronen-Linsen," *Optik*, 1947.

[34] M. Born and E. Wolf, *Principles of optics: electromagnetic theory of propagation, interference and diffraction of light*. Elsevier, 2013.

[35] H. Rose, "Correction of aberrations, a promising means for improving the spatial and energy resolution of energy-filtering electron microscopes," *Ultramicroscopy*, vol. 56, no. 1, pp. 11 – 25, 1994. [Online]. Available: http://www.sciencedirect.com/science/article/pii/0304399194901422

[36] M. Haider and P. Hartel and H. Mueller and S. Uhlemann and J. Zach, "Current and future aberration correctors for the improvement of resolution in electron microscopy," *Philosophical Transactions of the Royal Society A: Mathematical, Physical and Engineering Sciences*, vol. 367, no. 1903, pp. 3665–3682, 2009.

[37] H. Rose, "Outline of a spherically corrected semiaplanatic medium-voltage transmission electron microscope," *Optik*, vol. 85, pp. 19–24, 1990.

[38] H. Rose, *Geometrical charged-particle optics*. Springer, 2009.

[39] O. Krivanek, G. Corbin, N. Dellby, B. Elston, R. Keyse, M. Murfitt, C. Own, Z. Szilagyi, and J. Woodruff, "An electron microscope for the aberration-corrected era," *Ultramicroscopy*, vol. 108, no. 3, pp. 179 – 195, 2008. [Online]. Available: http://www.sciencedirect.com/science/article/pii/S0304399107002331

[40] N. Dellby, O. Krivanek, and M. Murfitt, "Optimized quadrupole-octupole C3/C5 aberration corrector for STEM," *Physics Procedia*, vol. 1, no. 1, pp. 179–183, 2008.

[41] B. Kabius, P. Hartel, M. Haider, H. Mueller, S. Uhlemann, U. Loebau, J. Zach, and H. Rose, "First application of Cc-corrected imaging for high-resolution and energy-filtered TEM," *Journal of electron microscopy*, vol. 58, no. 3, pp. 147–155, 2009.

[42] B. Kabius and H. Rose, "Novel aberration correction concepts," *Advances in imaging and electron physics*, vol. 153, pp. 261–281, 2008.

[43] I. Ross and T. Walther, "Configuring a 300kV cold field-emission gun for optimum analytical performance," in *Journal of Physics: Conference Series*, vol. 371. IOP Publishing, 2012, p. 012012.

[44] P. Nellist and S. Pennycook, "Accurate structure determination from image reconstruction in ADF STEM," *Journal of Microscopy*, vol. 190, no. 1-2, pp. 159–170, 1998.

[45] D. He and Z. Li, "A practical approach to quantify the ADF detector in STEM," *Journal of Physics: Conference Series*, vol. 522, p. 012017, 2014. [Online]. Available: http://stacks.iop.org/1742-6596/522/i=1/a=012017?key=crossref.2adcd06e33a5b3dc4617812435c8fdd5

[46] J. O. Oelerich, L. Duschek, J. Belz, A. Beyer, S. D. Baranovskii, and K. Volz, "STEMsalabim: A high-performance computing cluster friendly code for scanning transmission electron microscopy image simulations of thin specimens," *Ultramicroscopy*, vol. 177, pp. 91 – 96, 2017. [Online]. Available: http://www.sciencedirect.com/science/article/pii/S030439911630300X

[47] C. R. Hall and P. B. Hirsch, "Effect of thermal diffuse scattering on propagation of high energy electrons through crystals," *Proceedings of the Royal Society of London. Series A. Mathematical and Physical Sciences*, vol. 286, no. 1405, pp. 158–177, 1965.

[48] J. S. Reid, "Debye-Waller factors of zincblende-structure materials - a lattice dynamical comparison," *Acta Crystallographica Section A*, vol. 39, no. 1, pp. 1–13, Jan 1983. [Online]. Available: https://doi.org/10.1107/S010876738300001X

[49] N. Gopi Krishna and D. B. Sirdeshmukh, "Compilation of temperature factors of hexagonal close packed elements," *Acta Crystallographica Section A*, vol. 54, no. 4, pp. 513–514, Jul 1998. [Online]. Available: https://doi.org/10.1107/S0108767398004176

[50] D. B. Williams and C. B. Carter, "The transmission electron microscope," in *Transmission electron microscopy*. Springer, 1996, pp. 3–17.

[51] D. Van Dyck and A. de Jong, "Ultimate resolution and information in electron microscopy: general principles," *Ultramicroscopy*, vol. 47, no. 1-3, pp. 266–281, nov 1992. [Online]. Available: http://linkinghub.elsevier.com/retrieve/pii/030439919290202U

[52] P. Geuens and D. Van Dyck, "The S-state model: A work horse for HRTEM," *Ultramicroscopy*, vol. 93, no. 3-4, pp. 179–198, 2002.

[53] J. J. Hu and N. Tanaka, "A study of the validity of the image deconvolution method on the basis of channelling theory for thicker crystals," *Ultramicroscopy*, vol. 80, no. 1, pp. 1–5, 1999.

[54] P. Voyles, J. Grazul, and D. Muller, "Imaging individual atoms inside crystals with ADF-STEM," *Ultramicroscopy*, vol. 96, no. 3, pp. 251 – 273, 2003. [Online]. Available: http://www.sciencedirect.com/science/article/pii/S0304399103000925

[55] L. Dieterle, B. Butz, and E. Müller, "Optimized Ar-ion milling procedure for TEM cross-section sample preparation," *Ultramicroscopy*, vol. 111, no. 11, pp. 1636 – 1644, 2011. [Online]. Available: http://www.sciencedirect.com/science/article/pii/S0304399111002087

[56] J. Belz, A. Beyer, T. Torunski, W. Stolz, and K. Volz, "Direct investigation of (sub-) surface preparation artifacts in GaAs based materials by FIB sectioning," *Ultramicroscopy*, vol. 163, pp. 19–30, 2016. [Online]. Available: http://dx.doi.org/10.1016/j.ultramic.2016.01.001

[57] COMSOL AB, "COMSOL Multiphysics v5.3," Stockholm, Sweden. [Online]. Available: www.comsol.com

[58] MATLAB, "version R2015a - R2016b," Natick, Massachusetts, 2015. [Online]. Available: https://www.mathworks.com/products/matlab.html

[59] I. Vurgaftman, J. R. Meyer, and L. R. Ram-Mohan, "Band parameters for III-V compound semiconductors and their alloys," *Journal of Applied Physics*, vol. 89, no. 11 I, pp. 5815–5875, 2001.

[60] D. Madouri, A. Boukra, A. Zaoui, and M. Ferhat, "Bismuth alloying in GaAs: a first-principles study," *Computational Materials Science*, 2008.

[61] Y. Cai, L. Zhang, Q. Zeng, L. Cheng, and Y. Xu, "Infrared reflectance spectrum of BN calculated from first principles," *Solid State Communications*, 2007.

[62] S. Q. Wang and H. Q. Ye, "First-principles study on elastic properties and phase stability of III-V compounds," *Physica Status Solidi (B) Basic Research*, 2003.

[63] P. Capper and C. Elliott, *Infrared detectors and emitters: materials and devices*. Springer Science / Business Media, 2013, vol. 8.

[64] S. Nikanorov, Y. A. Burenkov, and A. Stepanov, "Elastic properties of Si," *Sov Phys Solid State*, vol. 13, no. 10, pp. 2516–2518, 1972.

[65] P. N. Keating, "Effect of invariance requirements on the elastic strain energy of crystals with application to the diamond structure," *Physical Review*, 1966.

[66] V. Grillo, E. Carlino, and F. Glas, "Influence of the static atomic displacement on atomic resolution Z-contrast imaging," *Physical Review B - Condensed Matter and Materials Physics*, vol. 77, no. 5, p. 054103, feb 2008. [Online]. Available: http://link.aps.org/doi/10.1103/PhysRevB.77.054103

[67] T. Grieb, K. Müller, E. Cadel, A. Beyer, M. Schowalter, E. Talbot, K. Volz, and A. Rosenauer, "Simultaneous quantification of indium and nitrogen concentration in InGaNAs using HAADF-STEM," *Microscopy and Microanalysis*, 2014.

[68] T. G. Ramesh and S. Ramaseshan, “Determination of the static displacement of atoms in a binary alloy system using anomalous scattering,” *Acta Crystallographica Section A*, 1971.

[69] A. J. Shalindar, P. T. Webster, B. J. Wilkens, T. L. Alford, and S. R. Johnson, “Measurement of InAsBi mole fraction and InBi lattice constant using Rutherford backscattering spectrometry and X-ray diffraction,” *Journal of Applied Physics*, 2016.

[70] P. L. Galindo, S. Kret, A. M. Sanchez, J.-Y. Laval, A. Yanez, J. Pizarro, E. Guerrero, T. Ben, and S. I. Molina, “The peak pairs algorithm for strain mapping from hrtem images,” *Ultramicroscopy*, vol. 107, no. 12, pp. 1186–1193, 2007.

[71] M. Hÿtch, E. Snoeck, and R. Kilaas, “Quantitative measurement of displacement and strain fields from hrem micrographs,” *Ultramicroscopy*, vol. 74, no. 3, pp. 131–146, 1998.

[72] W. Guo, Y. Mols, J. Belz, A. Beyer, K. Volz, A. Schulze, R. Langer, B. Kunert, W. Guo, Y. Mols, J. Belz, A. Beyer, K. Volz, A. Schulze, R. Langer, and B. Kunert, “Anisotropic relaxation behavior of InGaAs / GaAs selectively grown in narrow trenches on (001) Si substrates,” vol. 025303, no. 001, pp. 0–12, 2017.

[73] A. Beyer, R. Straubinger, J. Belz, and K. Volz, “Local sample thickness determination via scanning transmission electron microscopy defocus series,” *Journal of Microscopy*, vol. 262, no. 2, pp. 171–177, 2016. [Online]. Available: http://doi.wiley.com/10.1111/jmi.12284

[74] A. Beyer, L. Duschek, J. Belz, J. O. Oelerich, K. Jandieri, and K. Volz, “Influence of surface relaxation of strained layers on atomic resolution ADF imaging,” *Ultramicroscopy*, vol. 181, pp. 8–16, 2017.

[75] J. Belz, A. Beyer, and K. Volz, “Atomic-scale 3D reconstruction of antiphase boundaries in GaP on (001) silicon by STEM,” *Micron*, vol. 114, pp. 32 – 41, 2018. [Online]. Available: http://www.sciencedirect.com/science/article/pii/S0968432818302130

[76] S. Pennycook and D. Jesson, “High-resolution Z-contrast imaging of crystals,” *Ultramicroscopy*, vol. 37, no. 1-4, pp. 14–38, aug 1991. [Online]. Available: http://linkinghub.elsevier.com/retrieve/pii/030439919190004P

[77] H. Bluhm, U. D. Schwarz, F. Herrmann, and P. Paufler, “Study of the influence of native oxide layers on atomic force microscopy imaging of semiconductor surfaces,” *Applied Physics A Solids and Surfaces*, vol. 59, no. 1, pp. 23–27, jul 1994. [Online]. Available: http://link.springer.com/10.1007/BF00348415

[78] V. Grillo, K. Müller, K. Volz, F. Glas, T. Grieb, and A. Rosenauer, “Strain, composition and disorder in ADF imaging of semiconductors,” *Journal of Physics: Conference Series*, vol. 326, p. 012006, nov 2011. [Online]. Available: http://stacks.iop.org/1742-6596/326/i=1/a=012006?key=crossref.f2391226520c819238ec4d78655fb138

[79] J. F. Ziegler, M. Ziegler, and J. Biersack, “SRIM – The stopping and range of ions in matter (2010),” *Nuclear Instruments and Methods in Physics Research Section B: Beam Interactions with Materials and Atoms*, vol. 268, no. 11, pp. 1818 – 1823, 2010, 19th International Conference on Ion Beam Analysis. [Online]. Available: http://www.sciencedirect.com/science/article/pii/S0168583X10001862

[80] U. Mühle, J. Huang, M. Löffler, A. Than, L. Kwakman, H. Mulders, and E. Zschech, “Determination of the Ga penetration during FIB machining using atom probe tomography and ToFSIMS,” in *Microscopy Conference 2015 (MC 2015) - Proceedings* , Michael Laue, Ed., Regensburg, 2015. [Online]. Available: https://epub.uni-regensburg.de/32876

[81] J. Huang, M. Löffler, W. Moeller, and E. Zschech, “Ga contamination in silicon by Focused Ion Beam milling: Dynamic model simulation and Atom Probe Tomography experiment,” *Microelectronics Reliability*, vol. 64, pp. 390 – 392, 2016. [Online]. Available: http://www.sciencedirect.com/science/article/pii/S002627141630230X

[82] K. Momose, H. Yonezu, Y. Fujimoto, K. Ojima, Y. Furukawa, A. Utsumi, and K. Aiki, “Hardening Effect of GaP_{1- x}N_x and GaAs_{1-x}N_x Alloys by Adding Nitrogen Atoms,” *Japanese Journal of Applied Physics*, vol. 41, no. Part 1, No. 12, pp. 7301–7306, dec 2002. [Online]. Available: http://stacks.iop.org/1347-4065/41/7301

[83] M. Schaffer, B. Schaffer, and Q. Ramasse, “Sample preparation for atomic-resolution STEM at low voltages by FIB,” *Ultramicroscopy*, vol. 114, pp. 62–71, mar 2012. [Online]. Available: http://www.ncbi.nlm.nih.gov/pubmed/22356790

[84] F. Lelarge, O. Dehaese, E. Kapon, and C. Priester, “Strain relaxation at cleaved surfaces studied by atomic force microscopy,” *Applied Physics A: Materials Science and Processing*, vol. 69, no. 3, pp. 347–351, sep 1999. [Online]. Available: http://link.springer.com/10.1007/s003390051012

[85] G. T. Martinez, L. Jones, A. De Backer, A. Beche, J. Verbeeck, S. Van Aert, and P. D. Nellist, “Quantitative STEM normalisation: The importance of the electron flux,” *Ultramicroscopy*, vol. 159, no. P1, pp. 46–58, 2015.

[86] J. M. Lebeau, S. D. Findlay, L. J. Allen, and S. Stemmer, “Standardless atom counting in scanning transmission electron microscopy,” *Nano Letters*, vol. 10, no. 11, pp. 4405–4408, nov 2010. [Online]. Available: http://www.ncbi.nlm.nih.gov/pubmed/20945926

[87] G. T. Martinez, A. Rosenauer, A. De Backer, J. Verbeeck, and S. Van Aert, "Quantitative composition determination at the atomic level using model-based high-angle annular dark field scanning transmission electron microscopy," *Ultramicroscopy*, vol. 137, pp. 12–19, feb 2014. [Online]. Available: http://www.ncbi.nlm.nih.gov/pubmed/24270003

[88] D. P. Basile, R. Boylan, B. Baker, K. Hayes, and D. Soza, "Fibxtem - Focussed ion beam milling for TEM sample preparation," *MRS Online Proceedings Library Archive*, vol. 254, 1991.

[89] D. V. Dyck and M. Op de Beeck, "A simple intuitive theory for electron diffraction," *Ultramicroscopy*, vol. 64, no. 1, pp. 99 – 107, 1996. [Online]. Available: http://www.sciencedirect.com/science/article/pii/0304399196000083

Acronyms

2XS – double cross-section

ADF – annular dark-field
AFM – atomic force microscopy
AP – antiphase
APB – antiphase boundary
APD – antiphase domain

CAD – computer-aided design

DWF – Debye-Waller factor
DS – double-sector

EELS – electron energy loss spectroscopy
EWF – exit wave field

FEA – finite elements analysis
FT – Fourier transform
FIB – focused ion beam
FEG – field emitting gun

GaP – gallium phosphide
GaAs – gallium arsenide
Ga(P,Bi) – gallium phosphide bismide
Ga(P,As) – gallium phosphide arsenide
(Ga,In)As – gallium indium arsenide
(Ga,In)(N,As) – gallium indium nitride arsenide
Ga(N,As) – gallium nitride arsenide
GPA – geometric phase analysis

HAADF – high angle annular dark-field
HR-STEM – high resolution scanning transmission electron microscope/microscopy
HR-TEM – high resolution transmission electron microscope/microscopy
HR-XRD – high resolution X-ray diffraction

LAADF – low angle annular dark-field
MAADF – medium angle annular dark-field
MOVPE – metal-organic vapor phase epitaxy
MSD – mean square displacement
ML – monolayer
MP – mainphase

PV – plan view
PACBED – position averaged convergent beam electron diffraction
QW – quantum well

SAD – static atomic displacement
STEM – scanning transmission electron microscope/microscopy
SS – single-sector

TEM – transmission electron microscope/microscopy
TDS – thermal diffuse scattering
VFF – valence force field
XS – cross-section

ZLF – zero-loss filtered

List of Figures

2.1 The mainphase crystal of GaP is separated from the APD by the APB. The origin of this defect is the monoatomic step on the silicon surface. The boundary contains P-P and Ga-Ga bonds that are not present in ideal binary crystals. 4
2.2 The longitudinal spherical aberration leads to a lateral blurring of the image from P_0 at the gaussian image plane P_1. 10
2.3 The wave aberration function leads to an imperfect wave front that leads to a image spread at P_1. 11
2.4 The electron beam is focused by the condensor lens (system) and the angular acceptance angle is limited by an aperture. The sharply focused beam is scanned across the specimen and the dark-field is integrated by an ADF detector. Each scan position is correlated to a digital image pixel representing this integrated intensity value. 15

3.1 a) The conventional cross-section preparation of hard materials like inorganic semiconductors typically requires cutting of the initial bulk material (here: a wafer). Small pieces are then combined face-to-face with epoxy adhesive and put into a titanium support ring. This TEM specimen is then mechanically thinned to below about 100 microns and carefully polished to assure homogeneous ion beam etching. b) The polished specimen is introduced into the PIPS and etched by a broad argon ion beam from the bottom and top side until a small hole is created. 22
3.2 a) The target site (here: the thin edges of a conventionally prepared TEM specimen) are coated by electron beam deposition of tungsten and a following gallium ion deposition of additional protective layers. b, c) The target site is cut by ion beam milling and attached to a transfer manipulator by tungsten soldering. d) The thick lamella is transferred to a TEM compatible copper holder and e) thinned with successively reduced ion polishing steps until a thickness of less then 50 nm is reached f). Illustration modified from 6.1.1. 24

3.3 a) The secondary electron image shows a mechanically thinned wedge of material glued onto a copper support ring. b) After ion beam milling with successivly lower ion energies the resulting specimen contains electron transparent regions for high resolution microscopy. 25

4.1 Comparison between an idealized sample geometry of a typical cross-section preparation and an more realistic model with added complexity. 32
4.2 a) The high resolution ADF image of a 2XS that shows the initially thinned surface (vertical) and the unaffected surface that was protected by an excessive epoxy layer throught the preparation (horizontal). Their respective intensity profiles along the b) protected GaAs material as well as c) the damaged GaAs regions indicate a significant difference of these regions regarding crystal quality. Both profiles are shown for different acquisition angles (from an image series) and are aligned to each other. 33
4.3 a) The simulated topological profile for cross-sections of (Ga,$In_{30\%}$)($N_{1.5\%}$,As) QWs in a GaAs matrix with a thickness of 20 nm, 50 nm and 100 nm and the corresponding AFM data are shown. The green region indicates the free surface whereas the grey regions show embedded quantum wells. b) Illustration of the different strain contents causing the bulging effect in different regions as shown in a). 35
4.4 a) Overview TEM micrograph showing a 2XS specimen. b) The (projected) strain of several regions within a QW is shown as measured by GPA. The strain is shown as a fraction of its value for infinitely thick samples. c) Shows the calculated values for projected strains derived by a *nanowire* simulation with geometries derived from the overview micrograph in a). . 37
4.5 Illustration of a cross-section of simplified APBs. The location is changed from left to right revealing the different chemical compositions of each individual column as usually measured along the [001] direction. 41
4.6 The averaged intensities from all simulations of group-III and -V sub-lattice positions with a MP/AP ratio from 0% to 100% are shown for a) a single thickness of about 35 nm and b) a set of different thicknesses. 42
4.7 The reconstruction of two APBs from two HAADF images (a&d) with containing about 22 000 and 55 000 atom columns, respectively. The reconstructed atom positions are shown in b) and e) in plan view. The depth location of the APB ranging from 0 nm to 35 nm is color coded from blue to yellow, respectively. Another perspective on the reconstructed volume is shown in c and f, where the mainphase atoms are removed for visual clarity. 43

4.8 a) The average intensity of a simulated phosphorous column with the addition of a single bismuth atom is plotted over the position of this single impurity with respect to the top surface (black). The blue line references a pure phosphorous column without bismuth substitution. Additionally, the depth profile of the simulated electron probe is shown (orange). 45
4.9 a) The intensity profile with an extension of varying defocus positions for a source with perfect coherence b) only partial coherence is shown. The pronounced ridge of intensity with optimum defocus (as depicted in fig. 4.8 is included at around -2 nm defocus. 45

List of Tables

3.1 Material databases used for continuum elastic strain relaxation by COMSOL. 27

Jürgen Belz

Scientific Curriculum Vitae

10/2014 – 10/2019	**Dr. rer. nat.** , *Philipps-University Marburg*, Thesis: Analysis of Strain Relaxation, Ion Beam Damage and Instrument Imperfections for Quantitative STEM Characterizations.
10/2006 – 07/2014	**Diplom(Physics)**, *Philipps-University Marburg*, Thesis: Untersuchung tetragonaler Verzerrung an Halbleiter-Heterostrukturen mittels hochauflösender Transmissionselektronenmikroskopie. Grade: **"Good"**
08/1996 – 07/2006	**Abitur**, *Gustav-Stresemann-Gymnasium Bad Wildungen.* Grade **1.7**